Thin Nanostructured Crystalline TiO_2 Films and Their Applications in Solar Cells

Dissertation zur Erlangung des Grades

`Doktor der Naturwissenschaft´

am Fachbereich Chemie und Pharmazie

der Johannes Gutenberg Universität Mainz

Yajun Cheng

Geboren in Jiangsu, China

Mainz, June 2007

學而不思則罔，思而不學則殆

—— 孔子

"Learning without thought is labor lost; thought without learning is perilous"

Confucius

Contents

Abbreviations

AFM	Atomic Force Microscopy
ATRP	Atom transfer radical polymerization
B	Baseline of the decaying autocorrelation function
BA	Born approximation
d	Film thickness
D	Diffusion coefficient
DLS	Dynamic light scattering
DWBA	Distorted wave Born approximation
DMF	N, N-dimethylformamide
ED	Electron diffraction
EQE	External quantum efficiency
f	Volume fraction of a block in the block copolymer
FESEM	Field emission scanning electron microscopy
FF	Filling factor
FTO	Fluorine doped Tin Oxide
g_1	Normalized electric field autocorrelation function
g_2	Autocorrelation function of the dynamic light scattering intensity
G	Gibbs free energy
GISAXS	Grazing incidence small angle x-ray scattering
H	Enthalpy
HRTEM	High resolution transmission electron microscopy
I	Ionization potential
I_{inc}	Intensity of incident light
IPCE	Incident photon-electron conversion efficiency
IQE	Internal quantum efficiency
I_{sc}	Short circuit current
ITO	Indium doped Tin Oxide
k_B	Boltzmann constant

k_i	Wave vector
k_{zi}	Z-component of the wave vector of wave *i*
MEH-PPV	Poly (2-methoxy-5-2′ ethylhexyloxy)-p-phenylenevinylene)
M_n	Number average molecular weight
M_w	Weight average molecular weight
n	Refractive index
N	Degree of polymerization
OOP	Out-of-plane
P3HT	Poly (3-hexylthiophene)
PDI	Polydispersity index
PEDOT/PSS	Poly (3, 4-ethylenedioxythiophene)/poly (styrene sulfonate)
PEO	Poly (ethylene oxide)
PEO-b-PPO-b-PEO	Poly (ethylene oxide)-*block*-poly (propylene oxide)-*block*-poly (ethylene oxide)
PEO-b-PS-b-PEO	Poly (ethylene oxide)-*block*-poly (styrene)-*block*-poly (ethylene oxide)
PHB-b-PEO	Poly (ethylene-*co*-butylene)-*block*-poly (ethylene oxide)
P_{inc}	Incident power of light
PMMA-b-PEO	Poly (methyl-methacrylate)-*block*-poly (ethylene oxide)
PMMA	Poly (methyl-methacrylate)
PS-b-PAA	Poly (styrene)-*block*-poly (acrylic acid)
PS-b-PEO	Poly (styrene)-*block*-poly (ethylene oxide)
PS-b-PI	Poly (styrene)-*block*-poly (isoprene)
q	Scattering vector
r	Amplitude of the fraction of the reflected x-ray beam
R	Intensity of the reflected x-ray beam
R_g	Radius-of-gyration
r_H	Hydrodynamic radius
r_{ij}	Segment-segment separation
rpm	Rotation per minute
S	Form factor

S	Entropy
Si	Silicon
S (q)	Total interference function
SEM	Scanning electron microscopy
SFM	Scanning force microscopy
T	Temperature
t_{ij}	Fresnel transmission coefficient from medium *i* to *j*
Tg	Glass transition temperature
TTIP	Titanium (IV) tetraisopropoxide
V_{oc}	Open circuit voltage
V_p, I_p	Intersection values of the rectangle square possessing the largest area in the region defined by the *I-V* curve
XRD	X-ray diffraction
Z	Number of nearest-neighbor contacts
α	Segment polarizability or experimentally determined enthalpy due to segment contact
α_c	Critical angle
α_i	Incidence angle
α_f	Exit angle
β	Entropy loss due to segment contact or Coherence factor
χ	Flory-Huggins segment-segment Interaction parameter
δ	Real part of the refractive index
ε_{AB}	Contact energy between *A* and B segments
ϕ	Phase angle
η	Viscosity coefficient
$\eta(\varepsilon_r)$	Efficiency for absorption of incident photon of energy ε_r
λ	Wavelength
θ_c	Critical angle of total external reflection
θ	Scattering angle

σ	Surface roughness
τ	Characteristic decay time
T	Relaxation rate of the decaying autocorrelation function

Chapter1. Introduction

Synthesis of nanostructured TiO_2 thin films has attracted considerable interest in the past decade due to their intriguing physical properties and promising applications in photocatalysis, [1-33] photocoltaics, [34-51] gas sensing, [52-56] and Li ion battery materials. [57-67] Especially, since the report of TiO_2 base dye-sensitized solar cells with global power efficiency around 10% in the early 1990's, [68] tremendous research activities have been initiated in both academic and industrial fields. [34-51] The TiO_2 layer plays an important role in dye-sensitized solar cells. On one hand, it is used as a substrate for the adsorption of dye molecules on the surface; on the other hand, it provides a media for the transportation of electrons. [38, 40, 43, 68-78] The performance of TiO_2 based dye-sensitized solar cells significantly depends on the morphology and crystallinity of the nanostructured TiO_2. The morphology including the shape, size, size distribution, and spacing size between nanostructures controls the surface-to-volume ratio of the TiO_2 films, which determines the active-site density on the surface available for surface reactions and interfacial charge carrier transfer rate. Furthermore, different morphologies can provide varied charge carrier transportation routes and as a result influence electron-hole pair recombination probabilities. [79-84] It is therefore very important to prepare TiO_2 thin films with controllable morphologies. Besides the morphology, crystallinity of TiO_2 nanostructures is another important factor in the solar cells because it determines the electronic structure to influence the electron adsorption and transportation in the TiO_2 films. [37, 46] Generally TiO_2 has three different crystallographic polymorphs, anatase, rutile, and brookite. [85] In many of the functional materials, anatase makes the most important contributions to the performance because of its thermodynamically metastable characteristics and preferred formation in nano-scale systems. Compared to anatase, rutile is more thermodynamically stable and chemically inert and brookite commonly does not form a pure crystallographic phase and in many cases coexists with anatase and/or rutile as a labile, metastable state. [37, 46] Finally, the overall macroscopic size of the homogeneous structured titania films is another important requirement for their use in device applications. For example, for dye-sensitized solar cell devices in the laboratory scale, the films should fulfill the prerequisite to cover substrates with area of a few square millimeters homogeneously. [86] To summarize, for the purpose of applications of titania thin films in dye-sensitized solar cell devices, it is crucial to prepare titania films with controlled morphologies of anatase phase on an mm^2 scale.

There have been numerous reports about the synthesis of nanoscale titania materials with varied morphologies including nanoparticles, nanorods, mesoscale network structures, nanotubes, and lamellae. [84, 87-100] The main preparation recipes apply Titanium inorganic salts or Titanium alkoxides as Titanium sources, which are hydrolyzed and condensed to form Ti-O- networks in the presence of small molecule surfactants or block copolymers as structure directing agents.[87, 93, 100-125] The Pluronic family of PEO-PPO-PEO triblock copolymer has been widely used as a template. [92, 100, 108, 123-132] However, compared to the Pluronic copolymers, other kinds of block copolymers have been mainly used to template non titania systems,[133-145] and until recently only a limited number of results about templating titania nanostructures have been reported. [116, 120, 146-153] For example, PHB-b-PEO (H $(CH_2CH_2CH_2CH\ (CH_3)\text{-}CH_3)_{66}(OCH_2CH_2)_{86}H$) diblock copolymer has been used as the structure-directing agent to prepare crystalline titania mesoporous structures; [116] PS-b-PEO has also been applied as a template to synthesize foam like bicontinuous titania nanostructures. [150] Our group recently also reported the results using PS-b-PEO as a template to synthesize nanocomposite films composed of ordered titania nanoparticles. [146, 148, 149] Toluene and isopropanol were used as the solvents, in which the block copolymer could undergo microphase separation to form micelles in the solution and the Titanium sol-gel precursor was subsequently incorporated into the micelles. After spin coating composite films consisting of ordered nanoparticles were achieved.

With respect to the structure formation process, Eisenberg and coworkers have intensively studied the self-assembly behavior of amphiphilic block copolymer PS-b-PAA or PS-b-PEO in solution, where PAA and PEO are the minority parts of the block copolymer. [154-181] The block copolymers are dissolved into 1, 4-dioxane, or DMF, which is a good solvent for both blocks, followed by slow addition of water, a selectively poor solvent for the PS block. As a result of the slow addition so-called crew-cut micelles with large PS cores and thin PEO or PAA coronas are formed in solution. The morphologies of the crew-cut micelles are controlled by a force balance between different factors: the stretching degree of the core-forming block, the interfacial force between the core and surrounding solvents, and interactions between the coronas. Eisenberg and coworkers have adjusted the solution components to tune the force balance and obtained rich morphologies such as spherical micelles, [175-177] cylinder micelles, [168, 176, 178] lamellae, [175, 179] and vesicles. [175, 180, 181] However, the structures consist of only a pure organic polymer and lack a functional inorganic part. Furthermore, the obtained structures are present in solution, whereas in many applications the structures are required to be present in the form of dry films.

In this Ph. D study a new strategy has been developed using amphiphilic block copolymer as a templating agent coupled with sol-gel chemistry to control the morphologies of TiO_2 thin films via a good-poor solvent pair induced phase separation process (**Scheme 1**). Based on the knowledge how to control the morphology, nano structured TiO_2 thin films with different morphologies are introduced into dye-sensitized solar cells to study the effect of the morphology on the performance of the solar cells.

Amphiphilic diblock copolymers like PS-b-PEO, PMMA-b-PEO, and triblock copolymer of PEO-b-PS-b-PEO have been applied as templating agents. For example, The PS-b-PEO block copolymer with a PEO minor constitution part is first dissolved in 1, 4-dioxane, which is a good solvent for both blocks, followed by successive addition of 37% concentrated HCl solution and Titanium tetraisopropoxide (TTIP).

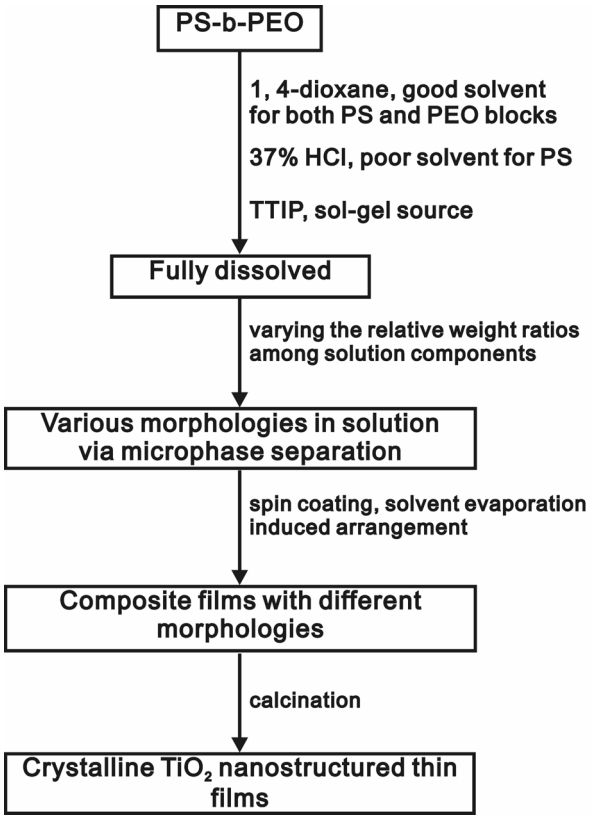

Scheme 1. *Sample preparation procedure for TiO_2 films with varied morphologies.*

Because both HCl and TTIP are poor solvents for the hydrophobic PS block, micelles are formed in the solution. A complex force balance will control the shape and size of the micelles. The interfacial interactions between block copolymer and the used solvent, and the stretching of the

polymeric chains balance to give an equilibrium lyotropic structure. Furthermore, TTIP can be incorporated into the hydrophilic PEO domain through coordination bonds. If this occurs, the delicate force balance of the lyotropic system is perturbed and as a result phase boundaries are shifted. Within the confined environment of PEO domain, TTIP acts as a precursor for TiO_2 because it is hydrolyzed and condensed into TiO_2 through sol-gel process. Concentrated HCl acts as a catalyst for the hydrolysis and condensation of TTIP, which makes the sol-gel reaction proceeding within the confined environment formed by the block copolymer. The morphologies in the solution can be transferred into titania-block copolymer composite films via spin coating process, where a solvent evaporation induced arrangement is accompanied to reorganize the nano structures on the substrate.

Chapter2. Fundamentals

2.1 Microphase Separation of Block-copolymers in Bulk Phase

The amphiphilic block copolymer is composed of both hydrophobic and hydrophilic blocks, which are linked by covalent bonds. This constraint leads to the formation of microphase separated structures on length scales below 100 nanometers. The equilibrium block copolymer phase behavior is governed by five factors: molecular architecture, segment-segment interaction, degree of polymerization, composition, [182] and external parameters including temperature, shear force, electric field, and magnetic field.

2.1.1 Molecular Architectures of Block Copolymers

The block copolymer made from two different monomers mainly have three different types of molecular architectures: branched block copolymer, grafted block copolymer, and linear block copolymer (**Scheme 2**). [182] In the bulk phase separation process, the polymer melt where materials have been heated above the glass transition temperature, T_g, is very viscous, which makes the polymer hard to reach the equilibrium state. Thus the molecular architecture plays an important role in the morphology evolution because it strongly influences the polymer viscosity. [182]

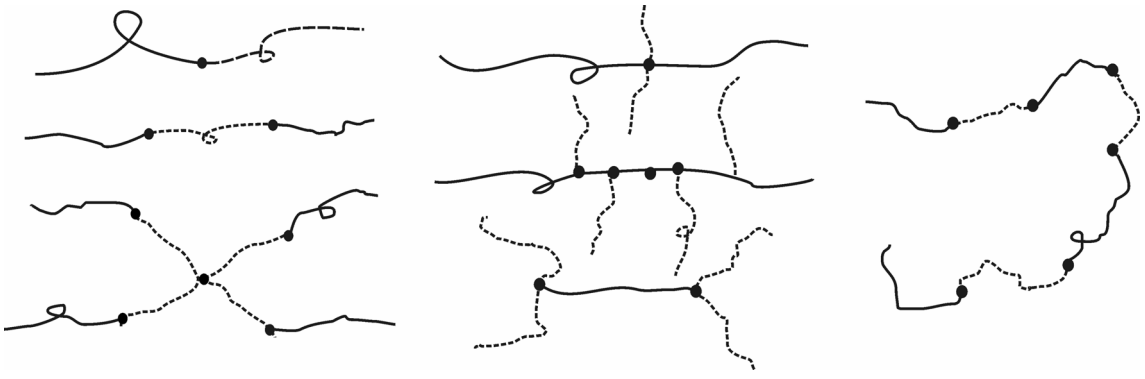

Branched block copolymers **Grafted block copolymers** **Linear block copolymers**

Scheme 2. *Typical molecular architectures of the block copolymers composed of two distinct monomers.* [182]

Besides the molecular architecture, the bulk phase behavior of the block copolymer is further controlled by three other intrinsic structural factors: segment-segment interaction, degree of polymerization, and composition.

2.1.2 Segment-segment Interaction

In the case of diblock copolymer, the particular combination of monomer A and B determines the sign and magnitude of the energy mixing, which can be approximated by the Flory-Hugggins segment-segment interaction parameter χ. [183, 184]

$$\chi = \frac{1}{k_B T}\left[\varepsilon_{AB} - \frac{1}{2}\left(\varepsilon_{AA} + \varepsilon_{BB}\right)\right] \qquad \textbf{Eq. 1}$$

In this equation, ε_{AB} represents the contact energy between *A* and *B* segments, and k_B is the Boltzmann constant. A negative value of χ indicates that there is a favorable interaction between A and B segment. Consequently, the A-B contact lowers the overall system energy compared to the sum of A-A and B-B contacts. On the contrary, the positive χ values occur when the A-B contacts increases the overall system energy.

In a specific case of the nonpolar polymer segment like polyethylene, polystyrene, and polyisoprene, the contact energy can be described in terms of dispersive interactions, that is, van der Waals force. [184]

$$\varepsilon_{ij} = \sum_{i,j} \frac{3}{4} \frac{I_i I_j}{I_i + I_j} \frac{\alpha_i \alpha_j}{r^6_{ij}} \qquad \textbf{Eq. 2}$$

Where r_{ij} is the segment-segment separation, and α and *I* are the segment polarizability and ionization potential respectively.

Based on the assumption that there is neither net volume change nor entropy loss after A-B segment contact, a new formula to describe the χ parameter can be derived through the combination of **Eq. 1** and **Eq. 2** as following: [182]

$$\chi = \frac{3}{16} \frac{I}{k_B T} \frac{Z}{V} \frac{2}{}\left(\alpha_A - \alpha_B\right)^2 \qquad \textbf{Eq. 3}$$

Where a cubic lattice is assumed with $I_i=I_j=I$ and all but the Z nearest-neighbor contacts are neglected. However, the assumptions for **Eq. 3** are rarely realized in practical cases because very likely the total volume and entropy of the system may be modified upon A-B segment contact. Therefore, a modified and practical formula of χ is further derived as **Eq. 4**. *[185-187]*

$$\chi = \alpha T^{-1} + \beta \qquad \textbf{Eq. 4}$$

Where α represents experimental determined enthalpy, and β describes the entropy loss.

2.1.3 Degree of Polymerization

The Flory-Huggins parameter only describes the interaction energy between individual monomer pair. To calculate the total mixing energy of the polymer blocks, a total degree of polymerization of the block copolymer, N, should be counted, where $N=N_A+N_B$ (N_A, N_B, degree of polymerization of block A and B respectively). Consequently, the total energy of mixing is calculated as χN with the total degree of polymerization N. *[188]*

2.1.4 Composition of Block Copolymer

Besides the monomer pair and degree of polymer of polymerization, the volume ratio of individual blocks in the block copolymer, f, will influence the shape and symmetry of the microphase separated structures. Varying the composition f will put unequal packing and stretching constraint on both blocks, leading to the formation of different ordered-phase symmetries over certain composition range. *[189, 190]*

2.1.5 External Parameters

Besides the factors stemming from the intrinsic chemical structure of the block copolymer, some external parameters can also affect the microphase separation behavior. For example, temperature, shear field force, electric field, and magnetic field. *[191-201]*

2.1.6 Principle Governing the Block Copolymer Microphase Separation

The collective contribution of polymer architecture, segment-segment interaction, and degree of polymerization, composition, and external parameters to the equilibrium phase of the block copolymer can be generally formalized as the system Gibbs free energy via the components of enthalpy, *H*, and entropy, *S*, as in **Eq. 5**. [183, 202]

$$G = H - TS \qquad \textbf{Eq. 5}$$

In the situation where no extra external field is applied (no electric, magnetic, and shear field; temperature fixed), the Gibbs energy is only determined by the thermodynamic parameters derived from the intrinsic chemical structure of the block copolymer, that is,χ, *N*, and *f*. The equilibrium microphase separated structure of the block copolymer is determined by the minimum overall system Gibbs energy.

In the situation of amphphilic block copolymer composed of a hydrophobic block A and hydrophilic block B, the positive χ value between A and B blocks indicates that the decrease A-B segment contact results in a decrease system enthalpy *H*. Consequently, microdomains composed of individual A and B blocks tend to be formed. However, an entropy loss will be accompanied with the aggregation of A and B blocks due to two reasons: first, the joints of the A-B blocks have to be localized in the interface region; second, the stretching degree of the polymer chain is increased to maintain a uniform density within the domain. [182] From the point view of the block copolymer structure, the overall effects of the enthalpy and entropy are mainly determined by the combination of χN and *f*.

2.1.7 A Special Case of the Block Copolymer Microphase Separation

In the special case of a block copolymer with f=1/2, when $\chi N \ll 10$, entropic factors dominate and only a spatially homogeneous state exists in the bulk block copolymer (**Figure 1**). [203, 204] By slight increasing either χ or *N* to the region $\chi N < 10$, the free energy balance is shifted leading to a local composition fluctuation in a length scale comparable to the radius-of-gyration of the block copolymer ($R_g^2 = R^2_{g,A} + R^2_{g,B}$). [205] With $\chi N \approx 10$, there is a balance between entropy and enthalpy. Further increase of χN leads to a first-order transition from disordered to ordered structures. In this step, entropy favors

mixing, but disordered structures are formed due to the energy cost of A-B segment contacts. [203, 205] When χN is further increased to >10, sharper microdomain boundaries are formed as the number of A-B segment-segment contacts decrease at the price of increasing entropy. As χN>>10, the energy facors dominate and ordered microphase separated structures are formed with narrow interface and nearly flat composition profile. [204]

In the situation where f is not ½, the block copolymer composition *f* mainly influences the packing and symmetry of the microphase separated structures. Except in the case near to the order-to-disorder transition, *f* is almost uncorrelated with χN. [204] The impact of the composition *f* on the microphase behavior originates from the unequal packing and stretching constraints on the individual block in the block copolymer, leading to different ordered structures over certain composition range. For example, the block copolymer of polystyrene-block-polyisoprene (PS-b-PI) has several different ordered phases found over a large composition range (**Figure 2**). [189, 190]

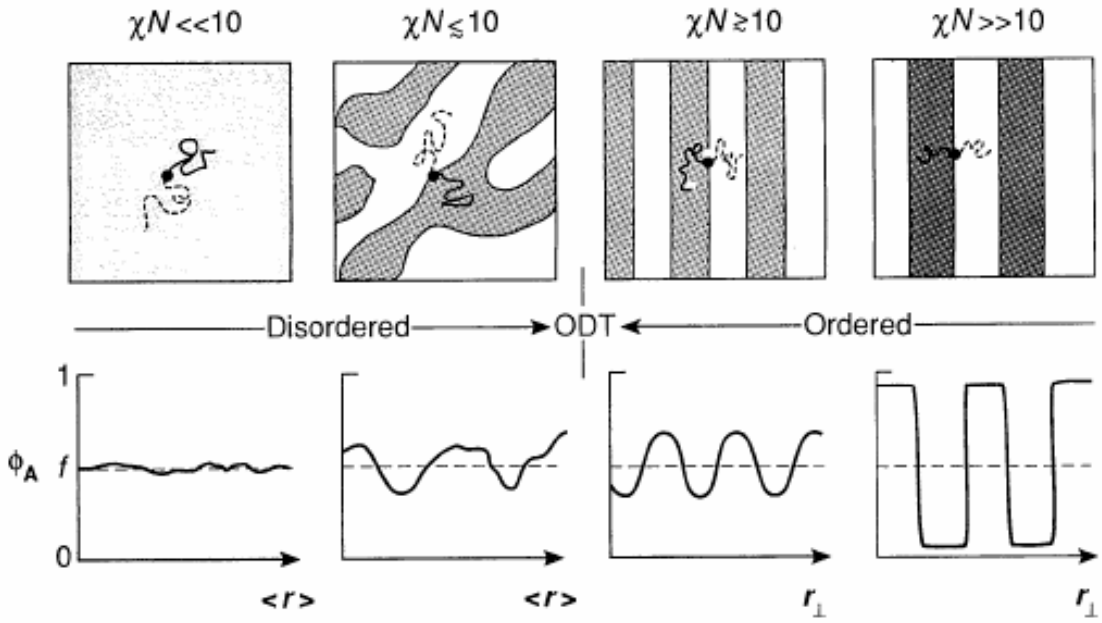

Figure 1. *Evolution of structure with the combined parameter χN for a symmetric diblock copolymer with f=0.5. When χN~10, small variations in system entropy (~N^{-1}) or energy (~χ) leads to ordered ($\chi N \geq 10$) or disordered (($\chi N \leq 10$) states. A homogeneous composition profile (ϕA versus r) results when entropic factors dominate ($\chi N << 10$), whereas a strongly microphase segregated pattern characterizes the limit when energetic factors prevail ($\chi N >> 10$).* [182]

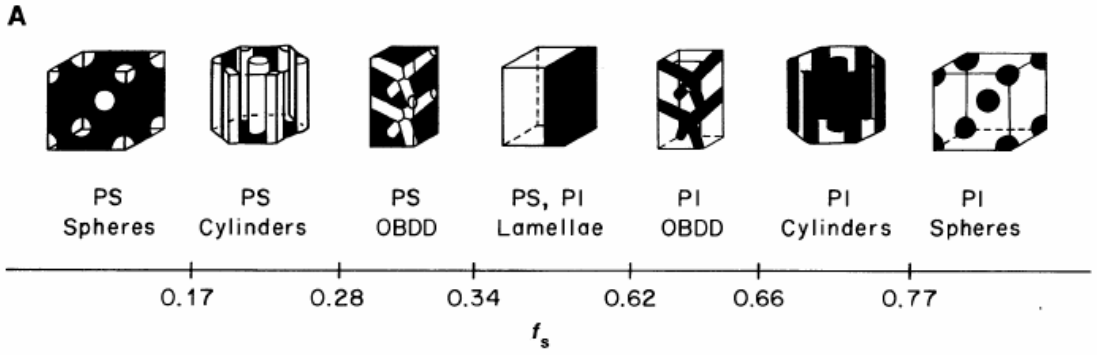

Figure 2. *(A) Effect of varying composition on the order-phase symmetry in polystyrene-b-polyisoprene (PS-b-PI) diblock copolymer, f_s refers to the overall volume fraction of polystyrene. (B) Phase diagram for polystyrene-b-polyisoprene (PS-b-PI) diblock copolymers. Ordered phases correspond to those illustrated in (A).*[182]

2.2. Atomic Force Microscope (AFM)

Atomic force microscopy (AFM), which is also called scanning force microscopy (SFM), was invented by Gerd Binig, Calvin Quate and Christoph Gerber in 1986. [206] AFM can image not only conducting samples but also insulating samples. It can be used in a wide range of environments, for example, vacuum, air, liquids, under heating and pressure. Through AFM, it is not only possible to image samples on the substrate, but also possible to measure the force-distance curve between tip and samples. AFM can be operated in different modes, for example, contact mode and tapping mode. [206-208] However, the tapping mode has several distinct advantages over the contact mode: first, it can avoid the friction force; second, the destruction of the sample surface by the tip is to be diminished due to the significant reduction of the contact time and intensity between the tip and sample. Therefore, tapping mode is much more frequently used to image samples than contact mode. [207, 208]

2.2.1 Measurement Principle of AFM

In AFM measurement, the sample is scanned underneath the tip, which is mounted to a cantilever spring (**Scheme 2**). [208] When the tip is brought close to the sample, surface force between the tip and the sample leads to a deflection of the cantilever according to Hook's Law. Depending on the situation, forces that are measured in AFM include mechanical contact force, Van der Waals forces,

capillary forces, chemical bonding, and so on. Typically, the deflection is measured using a laser spot reflected from the top of the cantilever into an array of photodiodes.

2.2.1.1 Operation Mode of AFM

Contact mode: In contact mode, the tip will touch the sample surface, however, the force between the tip and sample surface is very small, in the order of 0.1nN to 100nN. In order to achieve such a small force, the spring constant of the cantilever must also be very small and typical spring constants are 1N/m. There are two different kinds of contact modes, constant height mode and constant force mode. In the constant height mode, the height of the sample is kept constant and the deflection of the cantilever is recorded. The image is plotted by the deflection of the cantilever versus *x* and *y*. The advantage of constant height mode is that the scan rate is relatively fast. In the constant force mode, the deflection of the cantilever is sensed and a feedback loop keeps the deflection, and hence, the force is kept constant. Therefore the image is plotted by the height of the sample versus *x* and y. The quality of the images obtained from constant force mode is better than those from constant height mode because the information obtained from constant force mode is more close to the topography than that in constant height mode.

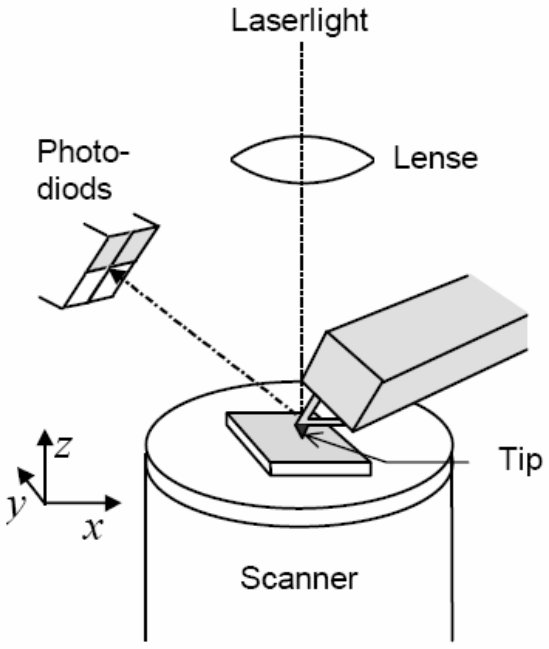

Scheme 2. *The schematic view of the working mechanism of AFM* [208]

Tapping mode: The cantilever is externally oscillated at or close to its resonance frequency. The oscillation amplitude, phase and resonance frequency are modified by tip-sample interaction forces. These changes in oscillation with respect to the external reference oscillation provide information about the sample. The tapping mode can be operated with either frequency modulation or amplitude modulation. In frequency modulation, changes in the oscillation frequency provide information about tip-sample interactions; however, in amplitude modulation, changes in the oscillation amplitude or phase provide the feedback signal for imaging. In principle, the change in the oscillation is related to the height information of the sample surface (height image), and the oscillation phase change is determined by the types of materials on the surface (phase image).

In the practical scanning process of amplitude modulation, the tip is engaged to the sample surface until the fixed predetermined shift of the amplitude ΔA is reached. [209] The image of the sample is reflected as an iso-ΔA surface. In the case where the sample has the same interactions with the tip in the whole scan region, the iso-ΔA surface reflects the real height image. However, if the sample has different interactions with the tip in the whole scan region, then the iso-ΔA surface will not correspond directly to the real height of the sample. In this case, the soft and hard properties of the sample in different regions need to be taken into account for the interpretation of the iso-ΔA surface into real sample surface height profile.

2.3. X-ray Reflectivity

X-ray reflectivity is a versatile characterization method to study the electron density gradient perpendicular to the film interface. The principle of x-ray reflectivity is based on the interaction between x-ray and matters on the surface and inside the film while x-ray penetrates the film. Therefore, x-ray reflectivity enables it possible to reveal the structure information beneath the film surface, which is difficult to achieve via scanning probe microscopy methods. [210-214] A brief working process of a reflectivity experiment is as following. A highly collimated x-ray beam is illuminating a sample with a very small incidence angle followed by the reflection of the x-ray beam from the surface. During the reflectivity experiment, the angle of incidence is varied and the intensity of the reflected x-ray is monitored as the function of the incident angle. The plot of reflectivity versus scattering angle shows three different contributions: [210, 214]

1. a sharp edge at the critical angle of total external reflection.

2. a characteristic overall power-law decay.
3. a modulation pattern due to the presence of surface layers.

From the shape and decay of the modulation patterns further information about the number, thickness, and interfacial properties of surface layers in the sample can be extracted.

2.3.1 Reflection from a Single Surface

2.3.1.1 Snells Law

If an x-ray beam hits a surface two things may happen (**Scheme 3**): [210, 214]

1. The x-ray beam is reflected at the surface, cos (θ_0) = cos (θ);
2. The x-ray beam is refracted governed by the Snells law: n_0 cos (θ_0) = $n_1$cos (θ_1); (n_0, n_1, the refractive indexes in medium 0 and 1 respectively)

2.3.1.2 Fresnel's Law

The critical angle of total external reflection θ_c is given by [210, 212, 214]

$$n_0 \cos(\theta_c) = n_1 \qquad \textbf{Eq. 6}$$

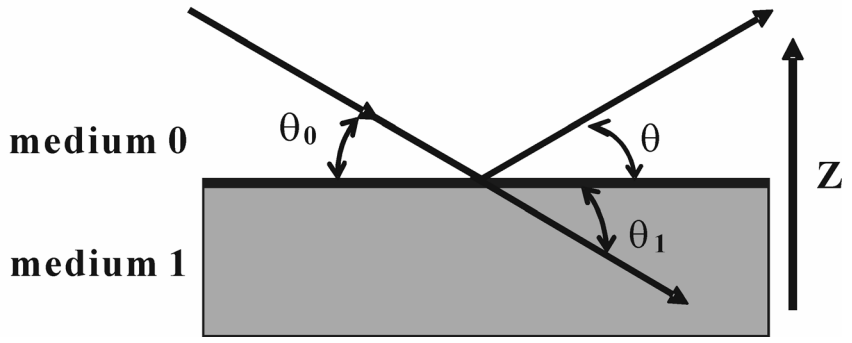

***Scheme 3**. Reflection and refraction of an X-ray at a single surface*[214]

By combing Snell law with the critical angle expression, the following equation is obtained:

$$n_1^2 \sin^2(\theta_1) = n_0^2 \sin^2(\theta_0) - n_0^2 \sin^2(\theta_c) \text{ or } k_{z1} = (k_{z0}^2 - k_{zc}^2)^{1/2} \qquad \textbf{Eq. 7}$$

where k_{zi} is the z-component of the wave vector of wave *i*.
The amplitude of the fraction of the reflected x-ray beam r is: [210-214]

$$r = \frac{k_{z0} - k_{z1}}{k_{z0} + k_{z1}} \qquad \textbf{Eq. 8}$$

And therefore the intensity of the fraction of the reflected x-ray beam is:

$$R = \left| \frac{k_{z0} - k_{z1}}{k_{z0} + k_{z1}} \right|^2 \qquad \textbf{Eq. 9}$$

The expression of the intensity R is called Fresnel's law. Both r and R are normalized quantities, which are normalized with respect to the amplitude and intensity of the incident wave.

2.3.1.3 Reflectivity from a single layer (two interfaces)

In the case of reflectivity from a single layer, it is similar to the reflectivity from a single surface except the consideration of reflection and refraction of x-ray beam inside the layer. In order to calculate the reflected intensity, it is needed to introduce two definitions. The first is r_{ij}, the Fresnel reflection coefficient, which describes the fraction of the amplitude reflected upon traversal from media i to j. The second is t_{ij}, the Fresnel transmission coefficient, which represents the fraction of the amplitude transmitted from medium i to medium j. The general value is given by [210-214]

$$r_{ij} = \frac{k_{zi} - k_{zj}}{k_{zi} + k_{zj}} \qquad t_{ij} = \frac{2k_{zj}}{k_{zi} + k_{zj}} \qquad \textbf{Eq. 10}$$

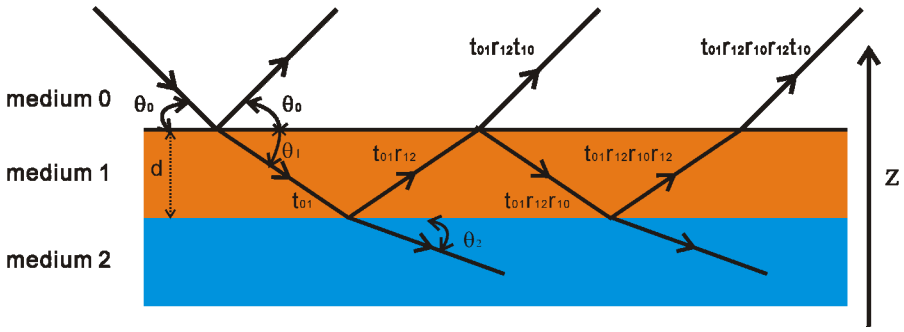

Scheme 4. *Schematic view of multiple internal reflections and refractions in the single layer*[214]

In **Scheme 4** it shows the amplitude yields at different reflection and diffraction steps. Besides the amplitude change, there is also a phase shift with respect to the incident wave. The phase shift is 2ϕ where

$$\phi_i = \frac{2\pi}{\lambda} n_1 \sin(\theta_1) d = k_{z1} d \qquad \textbf{Eq. 11}$$

The sum of the total amplitude yields

$$r = \frac{r_{01} + r_{12} e^{-i2\phi_i}}{1 + r_{10} r_{12} e^{-i2\phi_i}} \qquad \textbf{Eq. 12}$$

And the sum of the intensity R is

$$R = \left| \frac{r_{01} + r_{12} e^{-i2\phi_i}}{1 + r_{10} r_{12} e^{-i2\phi_i}} \right|^2 \qquad \textbf{Eq. 13}$$

The reflectivity R shows a beating pattern, which is called Kiessig fringes. Between the maxima the phase shift of the internally reflected waves is 2π and the waves interfere constructively. rom this fact it is possible to make a crude estimation of the film thickness d from the interval Δq between two maxima via $d \approx \frac{2\pi}{\Delta q}$ *[213, 214]* **Eq. 14**

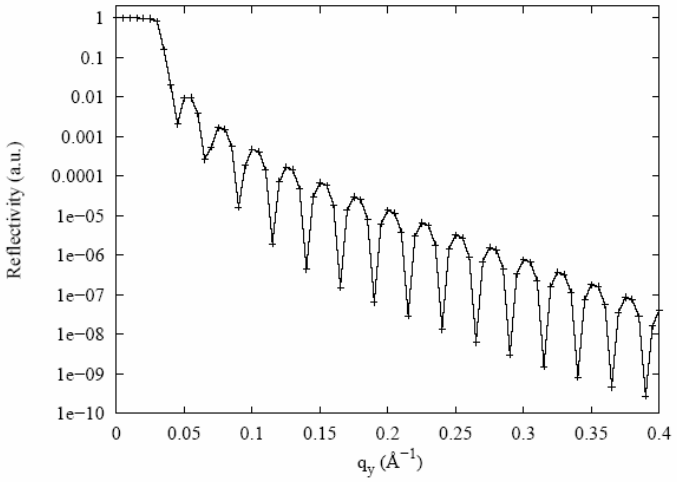

***Figure 3**. Simulated reflectivity profile of a silicon wafer with a 25nm polystyrene layer (σ_{rms} =5Å surface roughness for both interfaces).*[214]

In **Figure 3** it shows a typical simulated reflectivity profile. The thickness of the polystyrene layer covered on Silicon wafer is 25nm obtained from the above equation.

2.4. Grazing Incidence Small Angle X-ray Scattering (GISAXS)

Grazing incidence small angle x-ray scattering (GISAXS) is a powerful tool to study the lateral structure over large length scale on the surface. Compared to imaging techniques, for example, Atomic force microscope (AFM), or scanning electron microscopy (SEM), the GISAXS technique has the main advantages in the following aspects. First, the direct imaging techniques are highly local characterization methods, which normally can only cover the area over maximum a few square micrometers; however, the GISAXS experiment allows it possible to give lateral structure information over a large length scale up to a few millimeters parallel to the substrate. Second, GISAXS can determine the structure of the buried and inner layer in the film because x-ray can penetrate the film, which is usually difficult for the imaging techniques.[209, 215-223]

The scattering geometry of the GISAXS method is described in **Scheme 5**. [215] A monochromatic x-ray beam with a wave factor k_i is generated from the x-ray source and hits the surface with a very small incidence angle α_i respect to the surface. The *z* axis is normal to the sample plane, where *x* axis is in the direction parallel to the beam and *y* axis perpendicular to the *x* axis in the surface plane. The x-ray is scattered along k_f in the direction of (α_f, θ_f) due to any electron density fluctuation in the x-ray illuminated area on the surface. Due to a reason of tradition, the scattering in the *y* axis direction is called Out-of-Plane (OOP) scattering and consequently, the scattering along both *x* and *y* axis is called in-plane scattering.

The definition of the scattering vector in *x*, *y*, and *z* direction is defined as following: [215, 224]

$$q_{x,y,z} = \frac{2\pi}{\lambda}\begin{bmatrix} \cos(\alpha_f)\cos(\theta_f) - \cos(\alpha_i) \\ \cos(\alpha_f)\sin(\theta_f) \\ \sin(\alpha_f) + \sin(\alpha_i) \end{bmatrix} \qquad \textbf{Eq. 15}$$

And the intensity of the scattered x-ray beam is described as

$$I(\vec{q}) = \left\langle |F|^2 \right\rangle S(q_{\parallel}) \qquad \textbf{Eq. 16}$$

Where F is the form factor and S (q) is the total interference function. The interference function S (q) describes the spatial arrangement and further lateral correlation of the objects on the surface.

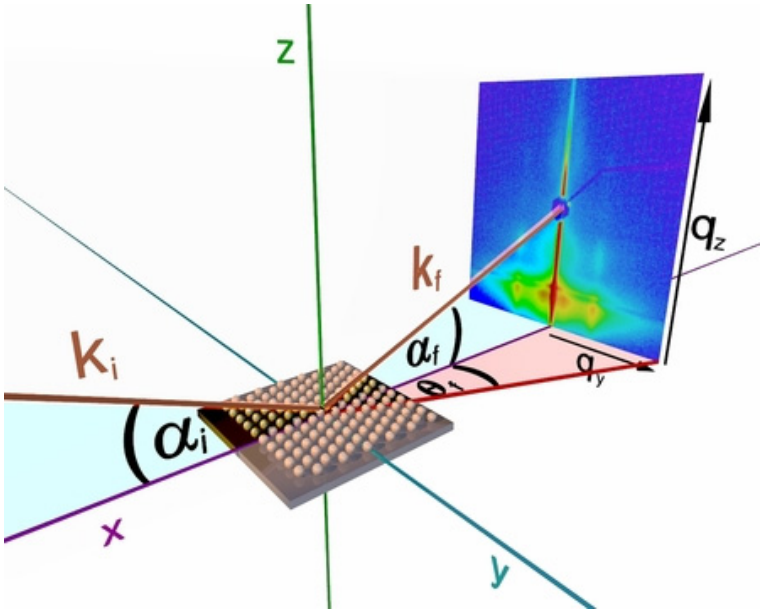

Scheme 5. *The scattering geometry of grazing incidence small angle x-ray scattering* [215]

It is the Fourier transform of the object position autocorrelation function. In a simple Born approximation (BA), F is the Fourier transform of the shape function of the objects defined as

$$F(\vec{q}) = \int_V \exp(i\vec{q}\cdot\vec{r})d^3r \qquad \textbf{Eq. 17}$$

However, in practice due to the effects of the reflection-refraction on the surface of the substrate, F has to be calculated based on a Distorted Wave Born Approximation (DWBA). The full calculation for the scattering cross section within the DWBA frame is illustrated including four different scattering events: The four scattering events interfere coherently to give an effective DWBA form factor, F_{DWBA} and the expression for the total cross section is described as **Eq. 18** [215, 224]

$$\frac{d\sigma}{d\Omega} \propto \left|F(\vec{q}_{\|}, K_{fz} - K_{iz}) + R(\alpha_i)F(\vec{q}_{\|}, K_{fz} + K_{iz}) + R(\alpha_f)F(\vec{q}_{\|}, -K_{fz} - K_{iz}) + R(\alpha_i)R(\alpha_f)F(\vec{q}_{\|}, -K_{fz} + K_{iz})\right|^2$$

Eq. 18

$$I(\vec{q}) = \left\langle \left| F_{\mathrm{DWBA}} \right|^2 \right\rangle S(q_{\parallel}) \qquad \textbf{Eq. 19}$$

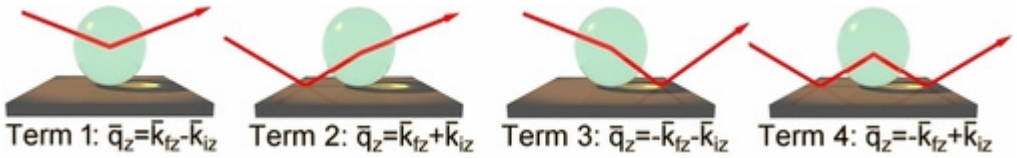

***Scheme 6**. Four scattering events accounted in the real grazing incidence small angle x-ray scattering [215]*

In experiment, to make x-ray scattering surface sensitive, a grazing incidence angle α is chosen between about half the critical angle α_c and several times the critical angle of the film material, where α_c is defined as following: [210]

$$\alpha_c = \sqrt{2\delta} \qquad \textbf{Eq. 20}$$

Where δ is the real part of the refractive index.

When the exit angle of the scattered beam is close to the critical angle, the intensity of the scatted beam is increased due to Vineyard effect, resulting in a bright band of intensity at the critical angle. This is also referred to as the Yoneda peak. The lateral structure information of the film is analyzed from the Out-of-Plane (OOP) scan along the Yoneda peak region in the direction of q_y. [215]

The actual choice of the grazing incidence angle depends on the system to be studied. For example, for free-standing quantum dots, an incident angle below α_c may be chosen to make the scattering exclusively surface-sensitive. In order to probe the internal structure of a polymer thin film of 100 nm thickness, the incident angle should be above α_c of the film, to ensure a full penetration of the sample. [215]

2.5. Dynamic Light Scattering (DLS)

Dynamic light scattering is a useful method to investigate hydrodynamic radius distribution of the aggregates in solution. When light hits small particles a Rayleigh scattering occurs in all directions

as long as the particles are smaller than around 250nm. If laser is used as the light source, which is monochromatic and coherent, then a time-dependent fluctuation in the scattering intensity can be observed. These fluctuations are due to the fact that the small molecules in solutions are undergoing Brownian motion and so the distance between the scatter centers in the solution is constantly changing with time. Consequently, there is a either constructive or destructive interference of the scattered laser light by the surrounding particles. The intensity fluctuation is related to the time scale of movement of the scatter centers, that is, the aggregates in the solution. *[225-228]*

The DLS experiment measures the intensity autocorrelation function, g_2 (q,τ), *[227, 228]*

$$g_2(q,\tau) = \langle I(q,0) \cdot I(q,\tau) \rangle = \lim_{T\to\infty} \int_0^T I(q,t) I(q,t+\tau) dt \qquad \textbf{Eq. 21}$$

which is an exponentially decaying function of the decay time, t(s), in a dilute of monodisperse particles. And the scattering vector is defined as: *[227, 228]*

$$q = (4\pi n / \lambda) \sin(\theta / 2) \qquad \textbf{Eq. 22}$$

Where n is refractive index of the solution and λ is the wavelength of the incident light and θ is the scattering angle.

g_2 (q,τ) is related to the normalized electric field autocorrelation function, g_1 (q,τ), via the Siegert relationship. *[227, 228]*

$$g_2(\tau) = B(1 + \beta |g_1(\tau)|^2) \qquad \textbf{Eq. 23}$$

Where B is the measured baseline of the decaying autocorrelation function and β is the coherence factor which can be used as an adjustable parameter in the data fitting.

In the case of monodisperse noninteracting particles in the solution, g_1 (τ) is described as a single exponential function as: *[227, 228]*

$$g_1(\tau) = \exp(-\Gamma \tau) \qquad \textbf{Eq. 24}$$

Where Γ is the relaxation rate of the decaying autocorrelation function (s^{-1}) and Γ is related to diffusion coefficient, D (m^2 s^{-1}), by *[227, 228]*

$$\Gamma = Dq^2 \qquad \textbf{Eq. 25}$$

And the hydrodynamic radius is calculated by the Stokes-Einstein equation: [226-228]

$$r_H = \frac{kT}{6\pi\eta D} \qquad \textbf{Eq. 26}$$

Where k is the Boltzmann constant and η is the viscosity coefficient.

2.6. Working Mechanism of Titania Based Dye-sensitized Solar Cells

The TiO_2 based solar cells provide a technically and economically alternative concept to present commercialized Silicon based solar cells. There has been a tremendous related work triggered by the report from Graetzel group in the early 1990's, where a TiO_2 based dye-sensitized solar cells with an energy efficiency ca. 7.1% was achieved. [68]

The TiO_2 based solar cells can de divided into two categories based on the type of charge carrier transport medium used, that is, liquid state dye-sensitized solar cells and solid state dye-sensitized solar cells. [34-51] While the liquid state solar cells use liquid electrolyte, for example, I^-/I_3^- pair, or ionic liquid as the charge transport; [34, 36, 40, 42, 43, 50, 229-244] the solid state dye-sensitized solar cells apply p-type semiconductor to transport charges. The p-type semiconductors include inorganic species like CuI, CuSCN, [36, 245, 246]or organic conjugated molecules, for example, Poly (3-hexythiophene) (P3HT), and poly (2-methoxy-5-2′-ethylhexyloxy)-p-phenylenevinylene) (MEH-PPV). [34-51, 147, 150, 247-263] Although the detailed working mechanisms of these two types of solar cells are different, the general working principle and the role of the TiO_2 in solar cells are similar, which will be addressed in the following.

2.6.1 Liquid State Dye-sensitized Solar Cells

Scheme 7 shows the device component and working mechanism of the liquid state dye-sensitized solar cells. [38] The solar cell device is of sandwich type. A conducting glass layer of Indium doped Tin Oxide (ITO) or Fluorine doped Tin Oxide (FTO) is used as an anode, and gold, carbon tape

or Platinum is used as a cathode. The surface of the conducting glass is deposited with a layer of TiO_2, which acts as an electron transport media. Furthermore, the TiO_2 film provides the surface for the adsorption of the dye molecules, for example, Ruthenium complex, or organic dye molecules. The redox couple of I^-/I_3^- pair in organic solvent is used as the electrolyte. *[34-36, 38, 40-46, 264]*

Under the illumination of sunlight the dye-molecules adsorbed on the TiO_2 layer are excited from the ground states. An electron is injected from the excited dye-molecule into the TiO_2 film, which migrates through TiO_2 to the anode electrode. A regeneration of the excited dye-molecules is conducted by the I^-/I_3^- redox pair and the redox pair can be further restored by electron donation from the external circuit. So in summary, there is no net chemical change in the whole process and the only change that happens is the conversion of sun light into electricity. The open circuit voltage of the solar cell is determined by the band gap between the Fermi level of TiO_2 and the band level of redox couple. *[38, 43]*

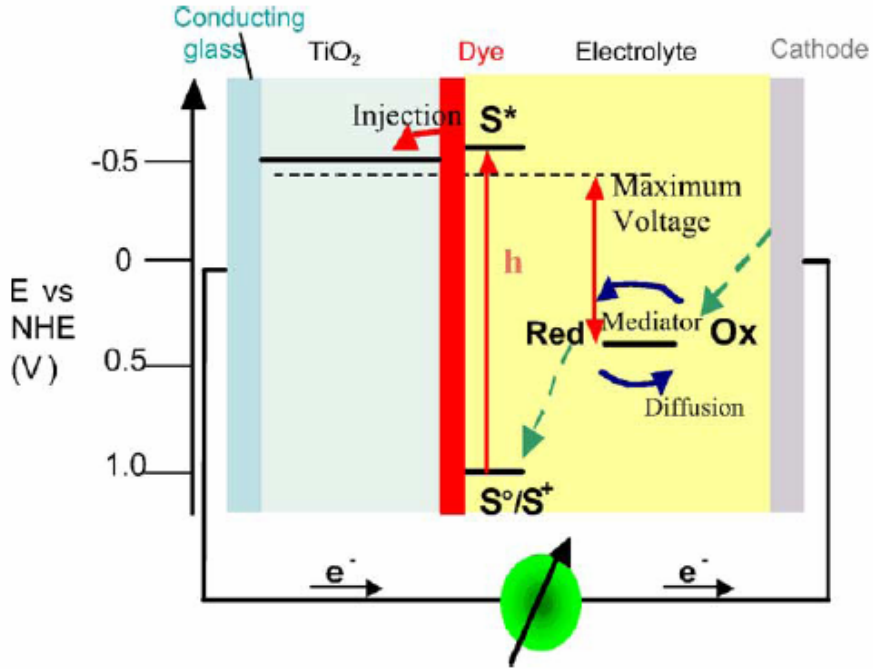

Scheme 7. *The structure components and working process of liquid state dye-sensitized solar cells* *[38]*

2.6.2 Solid State Dye-sensitized Solar Cells

Compared to liquid state dye-sensitized solar cells, the only different component in the solid state solar cell is the use of solid layer of hole conductor. As showed in **scheme 8**, the excited dye-

molecule releases an electron into the conduct band of TiO_2, where a hole is produced simultaneously. The hole is transported in the hole conductor media to the cathode. [43]

2.6.3 Performance Parameters of Solar Cells

The calculation of the solar cell efficiency relies on the determination of several key parameters from the *I-V* cure of the solar cell. A typical solar cell *I-V* curve is exhibited in **Scheme 9**. [265] There are several different kinds of efficiency definitions to evaluate the solar cell performance including global efficiency, external quantum efficiency and internal quantum efficiency. [44, 46]

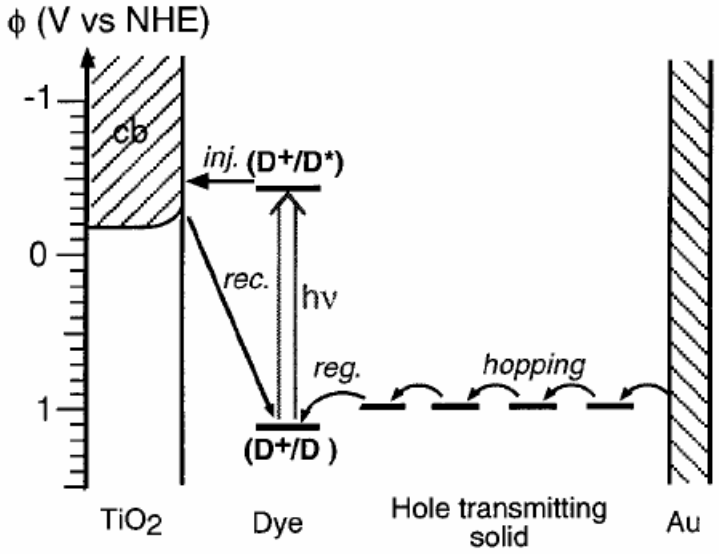

***Scheme 8**. The working process of solid state dye-sensitized solar cells* [43]

2.6.3.1 Global Efficiency

$$\eta_e = \frac{V_{oc}(V) \times I_{sc}(A/cm^2) \times FF}{P_{inc}(W/cm^2)} \qquad \textbf{Eq. 27}$$

Where V_{oc} is the open-circuit voltage, and I_{sc} is the short-circuit current, and P_{inc} is the incident power of light. FF is the filling factor of the solar cell, which is defined in the following way:

$$FF = \frac{V_p \times I_p}{V_{oc} \times I_{sc}} \qquad \textbf{Eq. 28}$$

Where V_p and I_p correspond to the intersection values of the rectangle square possessing the largest area in the region defined by the *I-V* curve.

2.6.3.2 External Quantum Efficiency

The external quantum efficiency (EQE) is the ratio of electrons delivered to external circuit per incident photon of a given wavelength. It is also called Incident photon-electron conversion efficiency (IPCE). The value is calculated using the following equation:

$$EQE\% = \frac{1240}{\lambda} \times \frac{I_{sc}(\mu A / cm^2)}{I_{inc}(W / m^2)} \qquad \textbf{Eq. 29}$$

Where I_{inc} is the intensity of incident light.

2.6.3.3 Internal Quantum Efficiency

The internal quantum efficiency (IQE) is the ratio of electrons delivered to external circuit per absorbed photon of a given wavelength. It is calculated as:

$$IQE = \frac{IPCE}{\eta(\varepsilon_r)} \qquad \textbf{Eq. 30}$$

Where $\eta(\varepsilon_r)$ is the efficiency for absorption of incident photon of energy ε_r

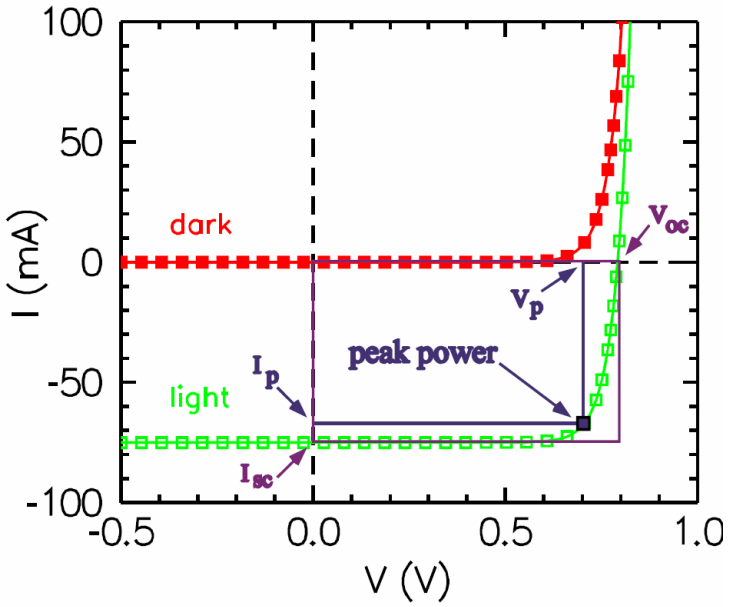

Scheme 9. *Typical I-V curve of solar cells* [265]

Chapter3. Experiment

3.1. Chemicals Sources

3.1.1 Block Copolymers

Three kinds of amphiphilic block copolymers were used as templates to control the morphology of the TiO_2 nanstructured films. They are polystyrene-*block*-poly (ethylene oxide) (PS-*b*-PEO), poly (methyl methacrylate)-*block*-poly (ethylene oxide) (PMMA-*b*-PEO), and poly (ethylene oxide)-*block*-polystyrene-*block*-poly (ethylene oxide) (PEO-*b*-PS-*b*-PEO) respectively. The molecular structures of the block copolymer are exhibited in **Scheme 10**. Detailed source and composition information are described in the following.

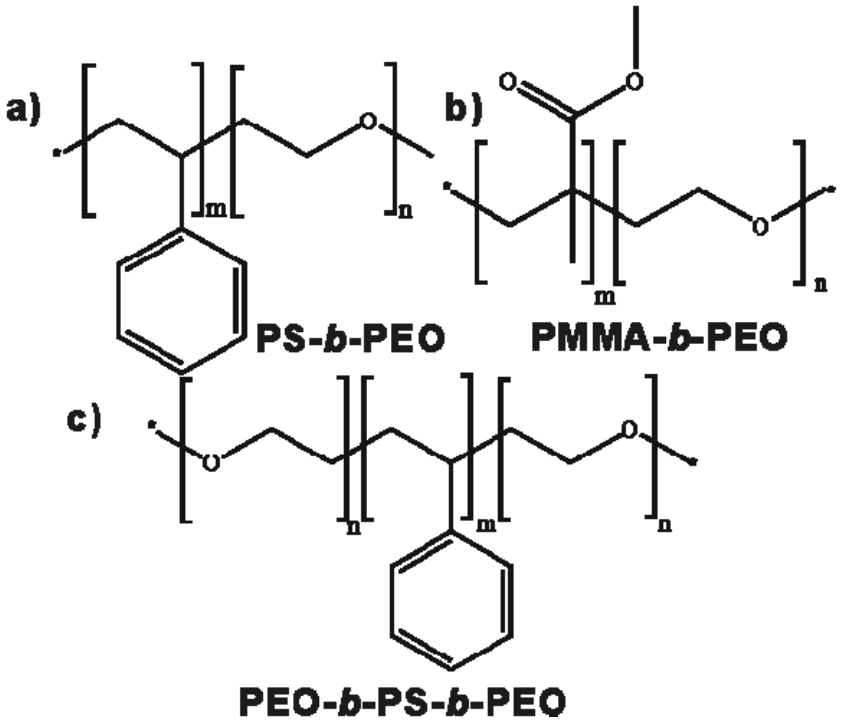

Scheme 10. The molecular structures of the amphiphilic block copolymers

PS-b-PEO diblock copolymer from two different sources was used in this thesis. A commercial one was obtained from Polymer Source Inc, whose number average molecular weight was 19k for PS and 6.4k for PEO respectively, with a polydispersity index (PDI) of 1.05. A second PS-b-PEO block

copolymer was synthesized in the Max-Planck-Institute for Polymer Research via the combination of anionic polymerization (PEO block) and Atomic Transfer Radical Polymerization (ATRP) (PS block). The number average molecular weight M_n of the PS and PEO blocks is 17.3k and 5.9k respectively with a polydispersity index of 1.14.

The asymmetric diblock copolymer of PMMA-*b*-PEO was synthesized in the Max-Planck Institute for Polymer Research via the combination of anionic polymerization (PEO block) and ATRP (PMMA block). The number average molecular weight is 57.7k for PMMA and 17.88k for PEO respectively with a polydispersity index of 1.22.

The symmetric triblock copolymer of PEO-*b*-PS-*b*-PEO was synthesized in MPI via sequential anionic polymerization according to standard literature recipe using naphthalene potassium as a bifunctional initiator. [266] The molecular weight of the middle PS block was determined by GPC of an aliquot taken from the reaction mixture before the addition of ethylene oxide: M_n=12.3k, M_w=20.0k and PDI=1.62. The molecular ratio of the PEO block is determined by H^1 NMR, through which the number average molecular weight of PEO block is determined to be 5.4k.

3.1.2 Other Chemicals

Table 1. The information of the chemicals used

Chemicals	Formula	Purity grade	Source
Titanium tetra-isopropoxide	$C_{12}H_{28}O_4Ti$	97%	Aldrich
Titanium tetra-isopropoxide	$C_{12}H_{28}O_4Ti$	≥95%	Fluka
1,4-dioxane	$C_4H_8O_2$	≥99.5%	Fisher Scientific
N, N-dimethyl formamide	C_3H_7NO	≥99.8%	Fisher Scientific
Hydrochloric acid	HCl	37%	Riedel-de Haën
Nitric acid	HNO_3	65%	Riedel-de Haën
Absolute ethanol	C_2H_5OH	>99.8%	Aldrich
Aceton	C_3H_6O	>99.5%	Riedel-de Haën
Isopropanol	C_4H_9OH	>99.8%	Riedel-de Haën
Chlorobenzene	C_6H_5Cl	≥99.5%	Fluka
Acetonitrile	C_2H_3N	99.99%	Fisher Scientific
tert-butyl alcohol	C_4H_9OH	≥99.5%	Riedel-de Haën

3-phenylpropionic acid	$C_9H_{10}O_2$	99%	Alfa Aesar
2, 2'-bipyridyl	$C_{10}H_8N_2$	99%	Aldrich
2, 2'-dipyridyl-4, 4'-dicarboxylic acid	$C_{12}H_8N_2O_4$	98%	Alfa Aesar
Dichloro(p-cymene) Ruthenium(II) dimer	$C_{20}H_{28}Cl4Ru_2$	98%	Alfa Aesar
Triton x-100			Alfa Aesar
PEDOT/PSS: Poly (3,4-ethylenedioxythiophene) poly (styrenesulfonate) (Baytron P)			Bayer
Alconox Powder			Aldrich

3.2. Sample Preparation

3.2.1 TiO_2 Films in the Morphology Phase Diagram Templated by PS-*b*-PEO

Sample solutions were prepared according to the following procedure. 0.040g PS-b-PEO (commercial) and 4.0g 1, 4-dioxane were mixed together, followed by the addition of appropriate amount of 37% concentrated HCl solution and TTIP (Aldrich) within 3 minutes. After complete addition the common solution was stirred for a period of time ranging from 30 minutes to one hour.

In order to compare the morphologies of the composite films to the morphologies of the pure block copolymer, solutions of pure block copolymers were prepared in the same procedure except that no TTIP is added. The weight ratios of the concentrated HCl solution over the sum of 1, 4-dioxane and HCl solution are varied from 0 to 10%.

Films were prepared on Si (100) substrate by spin coating for 120.0s using a Süss MicroTec Delta 80 spin coater under ambient conditions (temperature: 21°C; relative humidity: 35%-45%, rotation speed of 2000rpm, acceleration speed of 2000rpm/s, lid closed). In order to clarify the influence of humidity, samples were also spin coated with a speed of 2000rpm at 22.0°C and 0.0ppm absolute humidity in a glove box (P-6000 spin coater, Specialty Coating System Inc).

Films were calcined at 400°C for 4 hours in air with a ramp rate of 6.25°C/min starting from room temperature. After calcination, the samples were cooled to room temperature in the furnace. To study the effect of calcination temperature on the morphology, films were calcined at a temperature of

400, 500, and 600°C for 4 hours respectively with a ramp rate of 6.25°C/min. After calcination, the samples were cooled to room temperature in the furnace.

Samples for XRD measurement were prepared by putting a few drops of the solution onto 2.5cm×2.5cm Si (100) substrates, allowing the solution to dry under ambient conditions. Then the films were calcined in air at 200, 400, 500, 600 and 800°C for 4 hours respectively with the same recipe as above mentioned.

3.2.2 TiO_2 Films Templated by PS-*b*-PEO with Different Polymer Concentrations

Sample solutions were prepared according to the following procedure. For the samples with copolymer concentrations ranging from 0.25% to 2%, 0.01-0.08g PS-b-PEO (commercial) was mixed together with 4.0g 1, 4-dioxane, and 0.03g 37% HCl, and 0.12g TTIP (Aldrich). For the samples with a copolymer concentration of 4.0%, 0.0795g PS-b-PEO (commercial) was mixed with 2.0071g 1, 4-dioxane, and 0.0171g 37% HCl, and 0.0676g TTIP.

Sample solutions for the dynamic light scattering (DLS) experiment were prepared as following: 0.010 or 0.040g PS-b-PEO (commercial) was mixed with 4.00g 1, 4-dioxane, 0.037g conc. HCl, and 0.109g TTIP and stirred.

Films were prepared on Si (100) substrate by spin coating for 60.0s using a Süss MicroTec Delta 80 spin coater under ambient conditions (temperature: 21°C; relative humidity: 55%-65%, rotation speed of 2000rpm, acceleration speed of 2000rpm/s, lid open). To study the effect of the sol-gel reaction time on the morphologies, the stock solutions were spin coated after different stirring time ranging from *ca*. 40 min to 25 hours.

UV degradation was applied to the as-prepared films, which were prepared after different stirring time. The films were irradiated by UV light of a major wavelength 254nm with a dose of 25 J/cm^2 (XX-15S; UVP, Inc.) at room temperature for 6 hours in air to remove the organic matrix, leaving titania on the substrate. [146]

Calcination of the films was carried out at 400°C for 4 hours in air with a heating rate of 6.25°C/min starting from room temperature. After calcination, the samples were cooled to room temperature in the furnace.

3.2.3 TiO_2 Films Templated by PMMA-*b*-PEO

Samples were prepared in the following way: Nanovesicles: 0.0406g PMMA-b-PEO and 4.0091g 1.4-dioxane were mixed together, followed by the addition of 0.0910g 37% concentrated HCl solution and 0.0612g TTIP (Aldrich) within 4 minutes. After complete addition the common solution was stirred for one hour.

Nanoplatelets: 0.0414g PMMA-b-PEO and 4.0247g 1.4-dioxane were mixed together, followed by the addition of 0.1032g 37% concentrated HCl solution and 0.4812g TTIP (Aldrich) within 4 minutes. After complete addition the common solution was stirred for one hour.

Transition morphology between nanovesicles and nanoplatelets: 0.0404g PMMA-b-PEO and 4.0221g 1.4-dioxane were mixed together, followed by the addition of 0.1025g 37% concentrated HCl solution and 0.2461g TTIP (Aldrich) within 4 minutes. After complete addition the common solution was stirred for one hour.

Films were prepared on Si (100) substrate by spin coating for 30.0s using a Süss MicroTec Delta 80 spin coater at a rotation speed of 2000rpm, and acceleration speed of 2000rpm/s.

3.2.4 TiO_2 Films Templated by PEO-*b*-PS-*b*-PEO

Sample solutions for the titania films were prepared according to the following procedure. 0.0407g PEO-*b*-PS-*b*-PEO and 3.9971g DMF were mixed together, followed by the addition of 0.1525g 37% concentrated HCl solution. The mixture was turbid and stirred for 18 minutes. Thereafter 0.1307g TTIP (Aldrich) was added and the solution became clear. After complete addition the common solution was further stirred for *ca*. 20min.

Sample solution for the as-prepared film were prepared according to the following procedure: 0.0398g PEO-PS-PEO, 4.0225g DMF, 0.1346g TTIP, and 0.1498g 37% HCl were mixed together within 5 minutes and stirred for further 3 hours before spin coating.

Films were prepared on Si (100) substrate by spin coating using an open Süss MicroTec Delta 80 spin coater in a climatized lab with the ambient relative humidity around 60%. Films for the calcined samples were spun at a rotation speed of 500rpm, and acceleration speed of 500rpm/s for 180.0s. The films of the as-prepared sample were prepared with a rotation speed of 1000rpm, and

acceleration speed of 1000rpm/s for 60.0s. Calcination of the films was carried out at either 550 or 1000°C for 4 hours in air with a heating rate of 6.25°C/min from room temperature. After calcination, the samples were cooled spontaneously in the furnace to room temperature.

Samples for XRD measurement were prepared by putting a few drops of the solution onto 2.5cm×2.5cm Si (100) substrates, allowing the solution to dry under ambient conditions. The films were calcined in air at 550 and 1000°C for 4 hours respectively, following the time/temperature profile given below.

3.2.5 Solar Cell Device Fabrication

The SnO_2: F glass (FTO) (Hartford Glass Co., Inc.) was cleaned according to the literature with slight modification: rinsed with alconox solution (Aldrich, dissolved in MiliQ water with a concentration of 20mg/ml); rinsed with MiliQ, Aceton, ethanol, and isopropanol in sequence; ultrasonicated in isopropanol for 15min; finally Oxygen plasma cleaning for 10min(1mbar, 300W). [259]

The sol-gel solution for the TiO_2 barrier layer was prepared according to the literature. 10ml absolute ethanol was mixed together with 250µl MiliQ. The pH of the solution mixture was adjusted with concentrated nitric acid to 2-3. Finally, 750µl TTIP (Fluka) was added in the glove box and the solution was typically stirred in the glove box for 3 days. [259]

The TiO_2 barrier layer was prepared as following: before spin coating, the edge of the FTO glass was protected with the kapton tape. Then the sol-gel solution was spin coated in ambient conditions on either on Si (100) substrate or FTO glass with a rotation speed of 1000rpm and 60.0 seconds (Süss MicroTec Delta 80 spin coater). Before further spin coating with the polymer solution, vacuum of less than 100Pa was applied to the barrier layer for 5min in order to fix the barrier layer on the substrate.

PS-*b*-PEO synthesized in the Institute was used as a templating agent to control the morphologies of the TiO_2 films. The block copolymer-titania composite films were prepared on FTO glass, Si (100) substrate coated with barrier layer, and bare Si (100) substrate by spin coating for 60.0s (Süss MicroTec Delta 80 spin coater) under ambient conditions at a rotation speed of 1000rpm, acceleration speed of 1000rpm/s and close lid. The tape was removed after spin coating.

Calcination of the films was carried out at 450°C for 4 hours in air with a heating rate of 6.25°C/min starting from room temperature. After calcination, the samples were cooled to 200°C in the

furnace. The FTO glass was then put into a solution of 300μM Z907Na sensitizer (synthesized according to literature [76, 267]) and 300μM 3-phenylpropionic acid coadsorbent in acetonitrile and *tert*-butyl alcohol (volume ratio 1:1) for 6 hours, allowing the dye adsorption onto the TiO_2 surface. The FTO glass was then washed with ethanol in the glove box to remove the physically adsorbed dye molecules and it was further spin coated with 10mg/ml P3HT solution in chlorobenzene (1000rpm, 60.0s). The backside and edge of the FTO glass was cleaned with toluene, followed by annealing at 200°C for 2 hours in the glove box. After annealing a mix solution of PEDOT/PSS with 0.5% Triton x-100 was spin coated on the P3HT layer (2000rpm, 60.0s). The device was further annealed in glove box (Nitrogen environment) for 15min at 100°C. [268] Finally, 100nm Gold top electrode was deposited onto the FTO glass to form the device.

3.3. Sample Characterization

3.3.1 Atomic Force Microscope (AFM)

AFM images were recorded using a Digital Instruments Dimension™ 3100 scanning force microscope in tapping mode equipped with Olympus cantilevers (spring constant ranging between 33.2 – 65.7 N/m and resonant frequency of 277.3 – 346.3 kHz). The images were analyzed using the software of Nanoscope 5.12r5.

3.3.2 Scanning Electron Microscopy (SEM)

Scanning electron microscopy (SEM) images were obtained on field emission SEM (LEO 1530 "Gemini"). The accelerating voltage is 1kv if without special mention in the text. FFT pattern was obtained using the software of Image J 1.33U and areas of 512×512 pixels of the SEM images were randomly selected and studied.

3.3.3 Transition Electron Microscopy (TEM)

High resolution transmission electron microscopy (HRTEM) and electron diffraction (ED) measurements were conducted on a FEI Tecnai F20 electron microscope at an operating voltage of 200 kV. The 550°C sample was scratched from the spin coating film. The 1000°C sample was prepared by

scratching carefully the drop-casting film, followed by ultrasonication in ethanol to form a suspension, which was then dropped onto a carbon coated copper grid.

3.3.4 Film Thickness Measurement

The thickness of the titania-block copolymer film was measured by a Tencor P-10 surface profiler and the value was averaged from more than 6 data points.

3.3.5 Dynamic Light Scattering (DLS) Experiment

A frequency doubled, cw Nd: YAG-Laser (Coherent, Model Verdi 2W) was used at $\lambda = 532$ nm and up to 150 mW power on the sample cell. The scattering cell is mounted in the center of a goniometer (ALV, Langen, Germany) with all degrees of freedom adjustable. A Glan-polarizer selects only vertically polarized incident light. The scattered intensity is detected through a single mode optical-fiber, which contains a Y-coupler ending in two avalanche diodes (ALV, Langen, Germany) acting as single photon detector setup. The detected, scattered light is computed to correlation functions by a hardware correlator (6000/E if not mentioned especially in the text; ALV, Langen, Germany). The output of the two avalanche diodes (APD) enables us to do a pseudo cross correlation and by this to avoid the well known after pulsing of APDs leading to distortion of the correlation functions below 10 μs otherwise.

3.3.6 X-ray Diffraction (XRD)

θ-θ measurements were conducted on Siemens D500 (TiO_2 films in the morphology phase diagram) or D8 (TiO_2 films templated by PMMA-*b*-PEO or PEO-*b*-PS-*b*-PEO) diffractometer equipped with a Cu anode generated at a current of 30mA and a voltage of 30KV. Scans were taken in a 2θ range from 20° to 80° with a step size of 0.05° and integration time of 30.0s.

3.3.7 X-ray Reflectivity Measurement

X-ray reflectivity experiment was conducted using a surface XRD-TT3003 diffractometer equipped with Göbel mirror. The modeling of the experimental profiles was conducted using the

Parratt 32 software, version 1.5, provided by the Berlin Neutron Scattering Center at the Hahn-Meitner-Institute.

3.3.8 Grazing Incidence Small Angle X-ray Scattering (GISAXS) Measurement

GISAXS measurements were performed at the A2 and BW4 beamlines of the DORIS III storage ring at HASYLAB/DESY. Using a completely evacuated sample-detector pathway (1.09m for A2, 1.93m and 2.20m for BW4 respectively) and a wavelength of λ= 1.54Å for A2 and 1.38 Å for BW4 respectively. An in-plane resolution of 6.02×10^{-4} $Å^{-1}$ for A2 was achieved. Corresponding in-plane resolutions of 3.73×10^{-4} $Å^{-1}$ and 3.44×10^{-4} $Å^{-1}$ for BW4 was achieved respectively. The scattering image was analyzed in terms of out-of-plane (OOP) scans along the q_y-axis of the scattering image at a q_z values corresponding to the critical angle of TiO_2. For such cuts the transmission function of the incident and scattered waves only enter as constant scaling factors and do not depend on the precise functional shape of the transmission functions. In this way, the OOP scans are selective to the scattering information of a particular material, i.e. a given scattering length density, as they take advantage of the intensity increase of the transmission function at the critical angle.

3.3.9 Solar Cell Performance Characterization

The solar cell performance was recorded with a Keithley 236 Source-Measure Unit. A Tungsten-halogen lamp was employed as light source, supplying monochromatic light from 300nm to 700nm through a TRIAX 180 monochromator. Incident light intensity was determined by a calibrated silicon diode. The maximum intensity was 6 W/m^2 at ca. 600 nm.

3.3.10 Cyclovoltammetry

Cyclovoltammetry experiments were conducted to study the blocking property of the TiO_2 barrier layer. A typical three electrode experimental set-up was used (Ag|AgCl||sat KCl as a reference electrode, a TiO_2 coated FTO or bare FTO as a working electrode, and Pt wire as a counter electrode). The TiO_2 coated FTO was immersed into a solution of 0.1M aqueous solution of $Fe(CN)_6^{3-/4-}$ to observe the suppression of the redox peak relative to the bare working electrode. [259]

Chapter4. Results and Discussions

4.1. Overview

Three different kinds of amphiphilic block copolymers are used as templating agents to prepare nanostrcutred TiO_2-block copolymer composite films coupled with sol-gel chemistry. The applied block copolymers include PS-b-PEO, PMMA-b-PEO, and PEO-PS-PEO. A good-poor solvent pair induced phase separation process is introduced to achieve controllable microphase separation of the block copolymer in solution. Composite films are prepared by spin coating and crystalline nanostructured TiO2 films have been achieved via further calcination at high temperatures. On the base of morphology control, titania thin films with different morphologies are introduced into dye-sensitized solar cells to tune the performance of the solar cells. Detailed results and discussions will be addressed in the following subsections.

4.2. PS-b-PEO Templating System

4.2.1 Morphologies of Pure PS-b-PEO

Eisenberg and co-workers have intensively studied the crew-cut morphologies of pure amphiphilic block copolymer PS-b-PEO in solution. However, the polymers they used have extra short blocks of PEO, while the PEO block applied in this thesis has a significantly larger M_w. Furthermore, Eisenberg *et.al* used DMF as a good solvent and water a poor solvent. [156, 179] Here in this thesis, 1, 4-dioxane is used as a good solvent and concentrated HCl a poor solvent for the PS block. Because our studies are focused on films spin coated on Si substrates, first films of pure PS-b-PEO were prepared on Si substrate and the morphologies were studied with SEM or AFM, instead of the morphologies in solution. The results obtained on pure block copolymer films can thus be easily correlated to the morphologies of titania-block copolymer composite films.

The solutions with concentrated HCl ratios up to 2.84% are clear. With higher ratios the solutions become turbid, indicating the formation of micrometer sized aggregates in the solution. This puts an upper limit to the usable HCl concentration. For the films without acid and with 1.06% concentrated HCl, it is difficult to characterize the films with SEM because of the small sizes of the

structures. As an alternative way, AFM in tapping mode is used to study the morphologies of the films. From AFM, cylinder like structures can be observed. The spacing size between nanowires derived from power spectral density profiles are 22nm for both films (**4a** and **4b**).

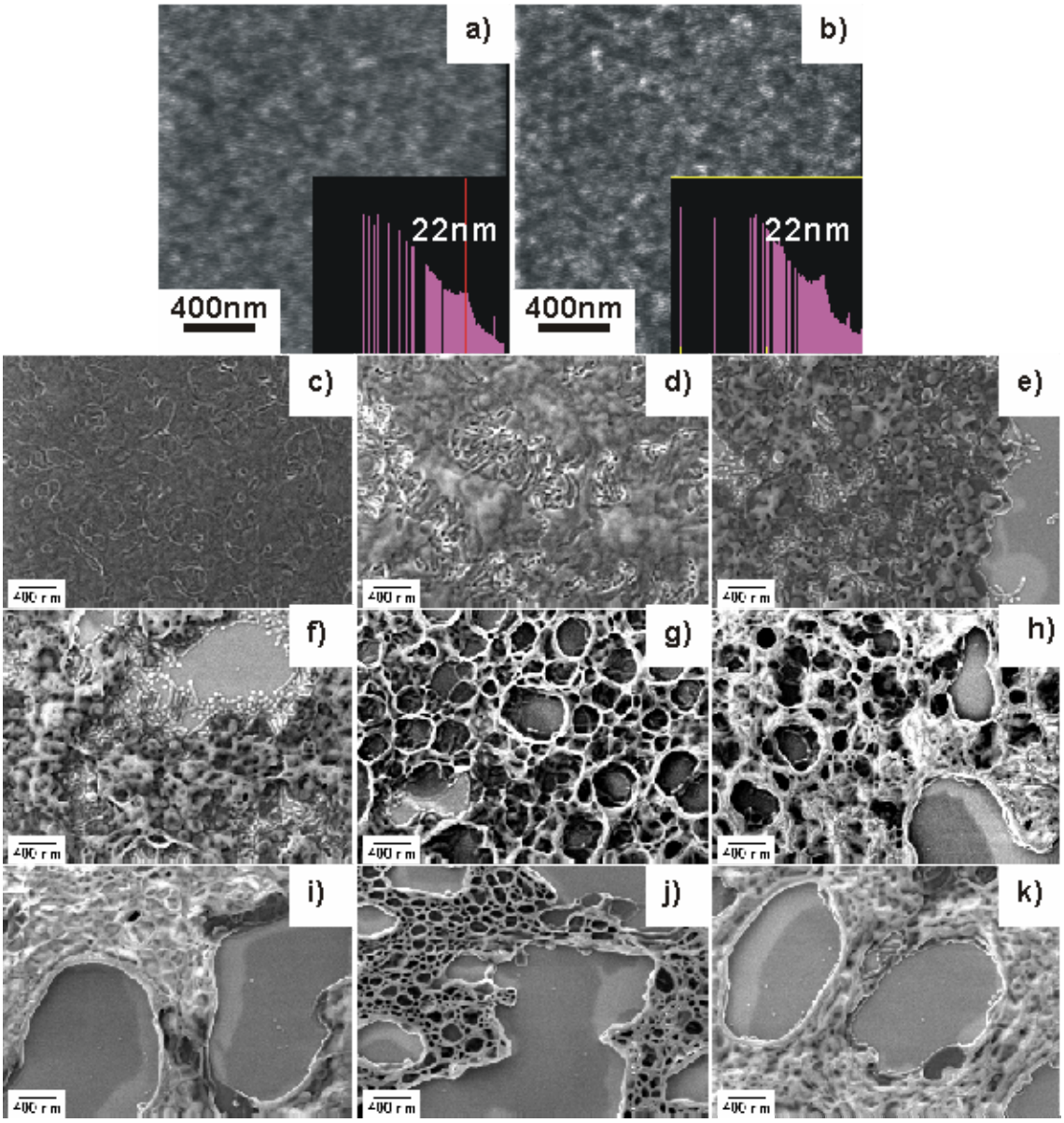

Figure 4. *AFM (**a** and **b**) height images and SEM images of the films spin coated from pure PS-b-PEO block copolymer in 1,4-dioxane with increasing weight ratios of concentrated HCl solution.* $W_{HCl/(HCl+1,4\text{-dioxane})}$ *is 1.06%, 2.08%, 2.84%, 4.09%, 4.96%, 5.97%, 6.92%, 8.05%, 8.92%, 9.88% for samples from **b** to **k** respectively. Height scale of AFM images: 5nm.The insets in image **a** and **b** are power spectral density profiles of their corresponding AFM images.*

With the HCl amount increased to 2.08%, nanowire structures can be seen in the SEM image (**Figure 4c**). However besides nanowires, lamellae structures are also present in the film. When the HCl content is further increased to 2.84%, the amount of nanowire structures is increased and the nanowires are partially covered by lamellae structures (**Figure 4d**). When the concentrated HCl solution weight ratio is 4.09% (**Figure 4e**) and 4.96% (**Figure 4f**), vesicle structures appear in the film, coexisting with the nanowire structures. With HCl content further increased to 5.97% (**Figure 4g**) and 6.92% (**Figure 4h**), vesicles of large size are formed. Huge size Vesicles and a large number of small size vesicles are present at HCl concentrations of 8.05% (**Figure 4i**), 8.92% (**Figure 4j**), and 9.88% (**Figure 4k**). The morphologies formed by pure block copolymer are similar to those present in the composite films, which will be discussed in the following. This similarity confirms the templating effect of block copolymer to control the morphologies of titania nanostructures.

4.2.2 Ternary Phase Diagram (1, 4-dioxane, HCl, and TTIP)

Figure 5 shows the phase diagram indicating the existence region of different morphologies. The morphologies are formed by simply varying the relative weight fractions between 1, 4-dioxane, 37% HCl, and TTIP. They include clustered nanoparticles, flake-like structures, nanowires and nanowire aggregates, nanodoughnut structures, collapsed vesicles, nanogranulas, worm-like aggregates, and foam-like structures.

In terms of composition, the phase space in which templated nanostructures are formed is limited by the amount of HCl solution. Micrometer sized precipitates of the block copolymer will appear in the solution at weight fraction (W_{HCl}) larger than 0.1. The same holds true for a TTIP weight fractions larger than 0.1, where films with a large number of cracks are formed. For this reason only the compositional region of the phase diagram shown in **Figure 5** is further investigated in this paper. The individual morphology formed within the investigated compositional region and their associated structure formation mechanisms are discussed in the following.

4.2.2.1 Clustered Nanoparticles

With very low weight fractions of both HCl (less than 0.005) and TTIP (from 0.005 to 0.02), clustered nanoparticles are formed. **Figure 6a** and **6c** show the AFM and SEM images of the clustered

nanoparticles before calcination respectively (film thickness: 38nm). The SEM image of the morphologies after calcination is shown in **Figure 6d**.

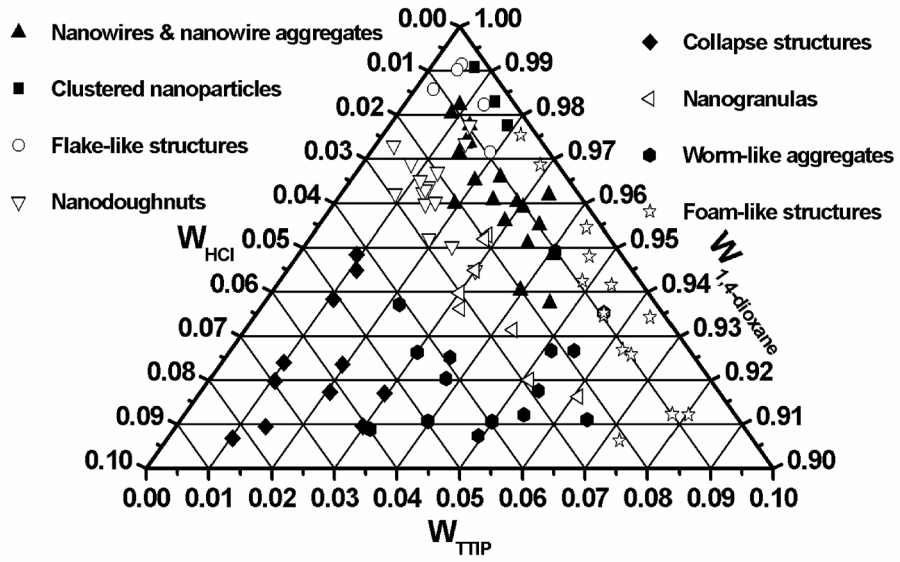

***Figure 5**. Phase diagram of TiO_2 films after calcination with varied morphologies (W: weight fraction).*

The ring-like FFT patterns of the images before and after calcination indicate that the nanoparticles are of a defined size but randomly distributed with respect to an orientation of their superstructure. Before calcination, the average center to center distance obtained from the AFM image is 41nm, which is in agreement with the value from the SEM image (42nm). After calcination, the center-to-center distance is 45nm. When the PS-b-PEO block copolymer is dissolved in 1, 4-dioxane, which is a good solvent for both PS and PEO blocks, the block copolymer will be fully dissolved and there are no self-assembly aggregates present in the solution. Along with the addition of concentrated HCl solution into the block copolymer solution, the interfacial energy between the PS block and solvent system is increased because the HCl solution is a poor solvent for PS block. In order to minimize the extra surface free energy, a spherical micelle structure is formed with a core of PEO block and corona of PS block. HCl solution and TTIP are incorporated into the hydrophilic PEO core, where TTIP is hydrolyzed and condensed into Ti-O- nanostructures. In solution, the spherical micelles may fuse together statistically, and as a result of fusion, the cores of the micelles will be linked together through the condensation process of Ti-O- nanostructures between neighboring cores. This linking process is, however, irreversible because of the formation of covalent bonds. Consequently, the linkages between the neighboring micelles are fixed and clustered nanoparticles are formed in the

solution. The presence of micelle aggregates in solution can be confirmed by dynamic light scattering results (See Supporting information **Figure S-1** in appendix). After spin coating, composite films composed of clustered nanoparticles are obtained on the Si (100) substrate, which are proved in **Figure 6c**. By comparing the SEM images before and after calcination (**Figure 6d**), it can be concluded that the clustered nanoparticle structures are retained after calcination.

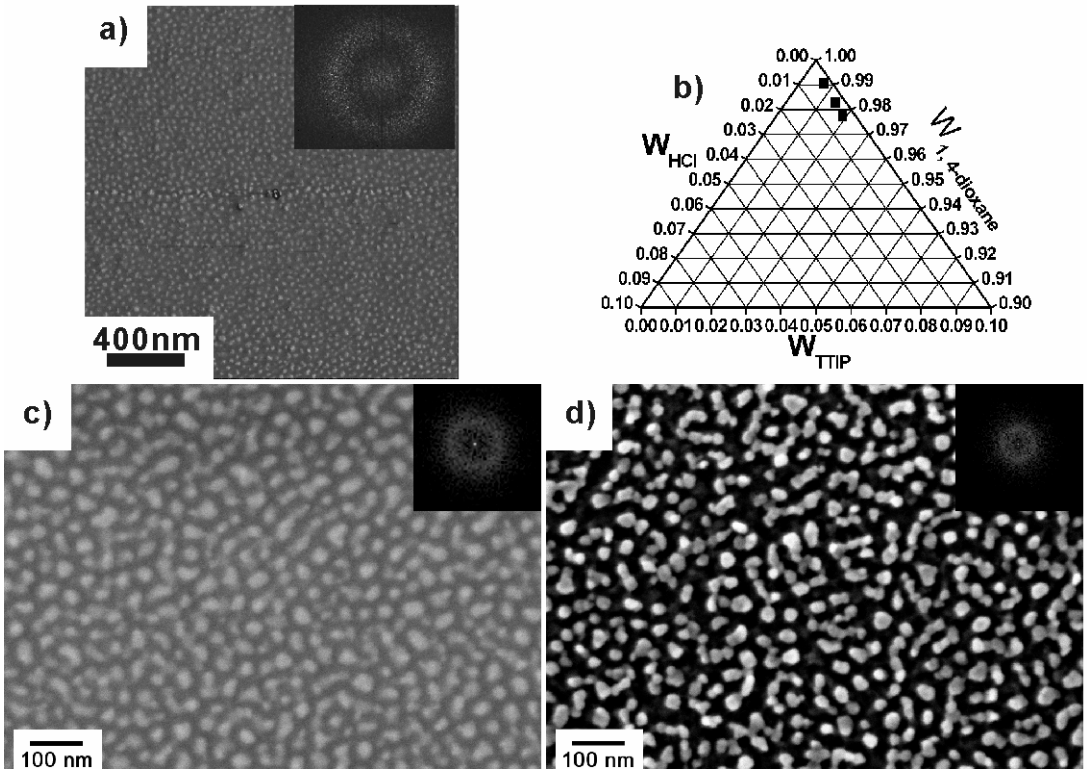

***Figure 6**. AFM and SEM images of TiO_2 films with clustered nanoparticles. **a**): AFM phase image before calcination, phase scale: 10°; **b**): compositional existence region in the phase diagram (W: weight fraction); **c**): SEM image before calcination; **d**): SEM image after calcination. The insets in the images are FFT patterns of the corresponding structures.*

4.2.2.2 Flake-like Structures

Figure 7b and **7c** show a flake like structure before and after calcination (film thickness before calcination: 41nm). With increasing weight fraction of HCl, the interfacial surface energy is further increased and in order to lower the surface energy, the clustered spherical micelles grow into isolated flakes with sizes ranging from tens to a few hundred nanometers. The flakes are actually three-

dimensional structures, as from SEM images it can be seen that the peripheral of the flakes extrude from the flake plane. Similar flake-like structures were also observed by Eisenberg in the solution of pure PS-b-PEO in DMF, where a so-called lamellae structure with protruding nanorods was formed. [175, 179] The flake like morphologies are also present in pure PS-b-PEO films (**Figure 7c** and **7d**), indicating the templating effects of the block copolymer.

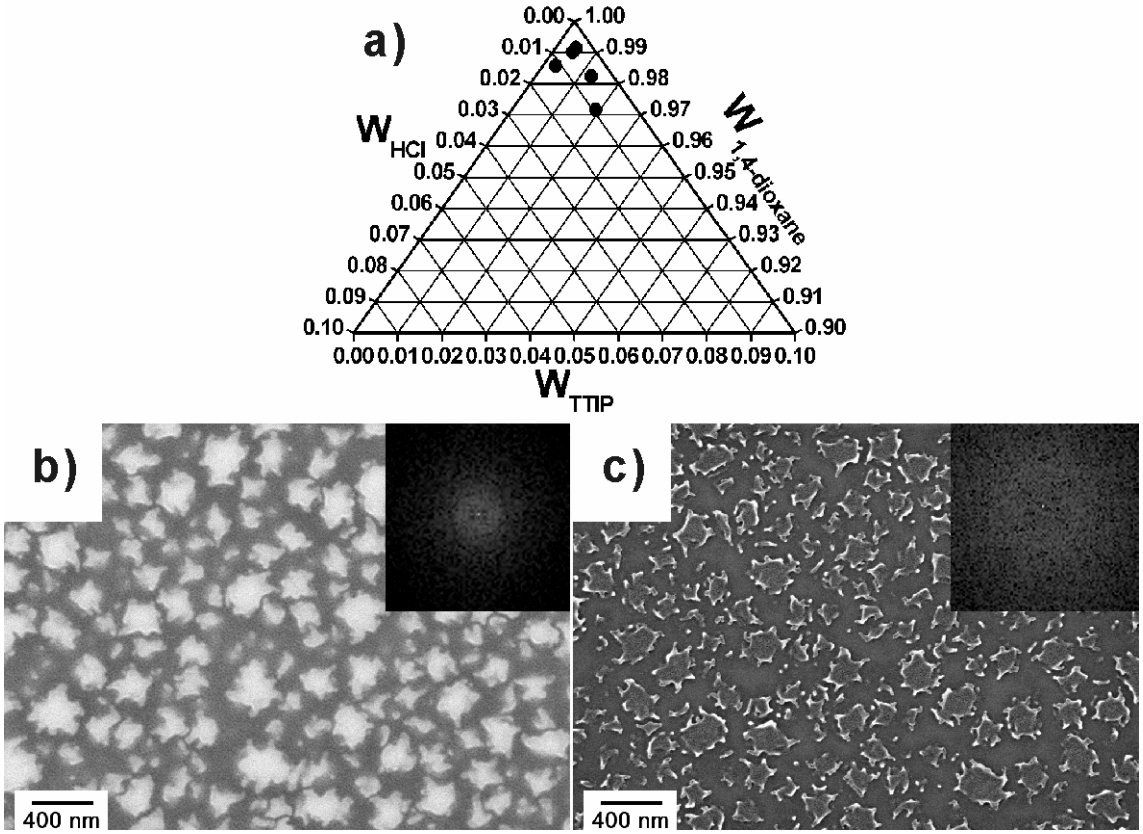

***Figure** 7. AFM and SEM images of TiO_2 films with flake-like morphologies. **a**): compositional existence region in the phase diagram (W: weight fraction); **b**): SEM image before calcination; **c**): SEM image after calcination. The insets in the images are FFT patterns of the corresponding structures.*

4.2.2.3 Nanowires

Figure 8a and **8c** show the AFM phase image and SEM image of the nanowire structures before calcination respectively (film thickness before calcination: 33nm). **Figure 8d** shows the SEM image of the nanowire structures after calcination. From the AFM image **Figure 8a** it can be seen that the titania-block copolymer composite nanowires are arranged in parallel over large length scales, which is also seen in the SEM image **Figure 8c**. The average spacing size of the nanowires is 51nm according to the FFT pattern of the AFM image, which is in accordance with the value obtained from the SEM image (52nm). What is interesting is that both AFM and SEM images before calcination show double-ring like FFT patterns. While the inner ring can be assigned to the spacing between neighboring nanowires, the outer ring corresponds to the second order of the first ring. From the presence of the second order ring it is concluded that the nanowires are closely packed leading to a strong ordering in a bundle consisting of several nanowires. For the SEM image **Figure 8d**, no clear ring-like FFT pattern can be observed, indicating a loss of order after calcination. The average diameter of the nanowires is 27nm, which is significantly smaller than the size before calcination. It is inferred that the cylinder micelles are formed in the solution from a comparison of our system with Eisenberg's reported results, where an amphilic block copolymer of PS-b-PAA is used and 1, 4-dioxane is applied as a good solvent for both PS and PAA blocks and water a poor solvent for the PS block. *[164, 168, 177, 178]* They obtained and proved the existence of cylinder micelles in the solution. In our case, instead of PS-b-PAA, another amphilic block copolymer of PS-b-PEO is used, which is assumed to behave qualitatively similarly as PS-b-PAA in solution. Although there is additional TTIP in the copolymer solution, which is different from Eisenberg's results, it is believed that the nanowires within the films cannot be formed directly from the spin coating process if there is no cylinder structure initially formed in the solution. Furthermore, the nanowire structures composed of pure PS-b-PEO polymer is observed in the copolymer film (**Figure 4c-4f**), which means that the copolymer does act as a template to control the formation of composite nanowire structures.

The formation mechanism of the titania-block-copolymer nanowires can be understood as following. With increasing amount of concentrated HCl solution, the solvent is becoming poorer and poorer for PS block leading to a continuously rising surface energy between the PS block and the solvent. In order to minimize the surface free energy, the spherical micelles will change the shape to decrease the specific surface area, leading to the formation of cylinder micelles in the solution. Besides

the HCl solution, the increasing amount of TTIP in the PEO core domains also makes a contribution to the morphology transformation because the hydrolysis and condensation of TTIP will release isopropanol at the price of water consumption, which is also a poor solvent for PS block. The overall reaction of hydrolysis and condensation leads to the net amount increase of hydrophilic solvent in the solution, which makes the solvent system increasingly poor for PS block. [269]

In AFM measurements different positions on the film were checked and the images recorded in different positions show comparable morphologies. SEM images at low magnification show that the surface is homogeneously covered with ordered nanowires (See supporting information **Figure S-2** in appendix). Therefore it can be concluded that the homogeneous films composed of ordered nanowire structures cover the surface of mm^2 scale.

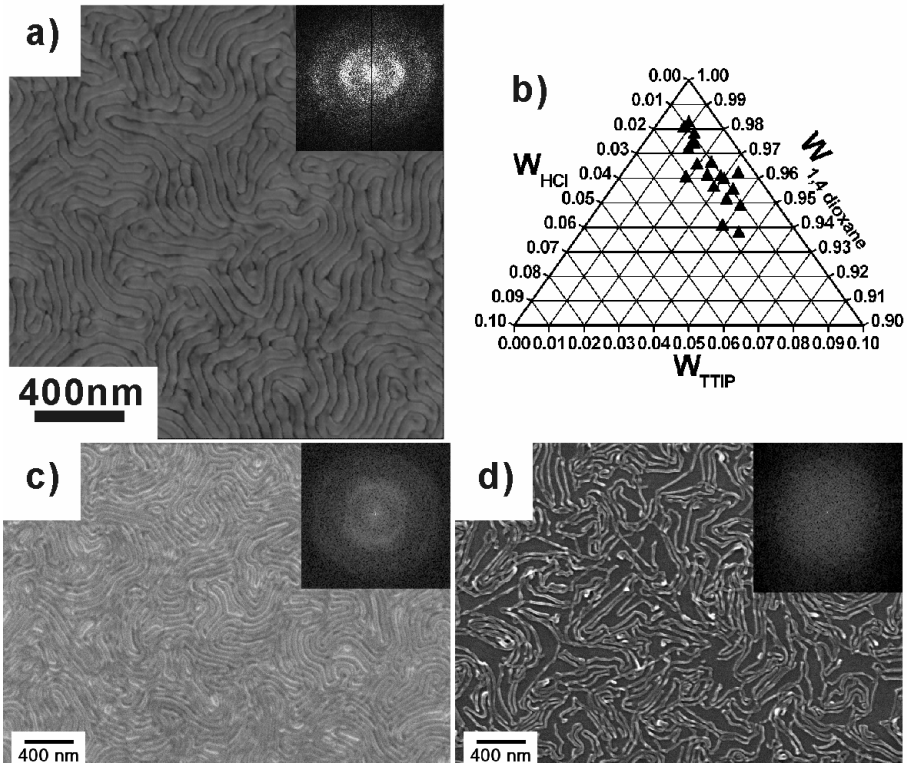

***Figure 8**. AFM and SEM images of TiO_2 films with nanowires. **a**): AFM phase image before calcination, phase scale: 20°; **b**): compositional existence region in the phase diagram (W: weight fraction); **c**): SEM image before calcination; d): SEM image after calcination. The insets in the images are fast Fourier transform (FFT) patterns of the corresponding images.*

After calcination, the organic block copolymer is burned off and only titania is left. From the SEM image after calcination, it can be seen that the nanowire structures are retained, which further confirms the existence of cylindrical micelles. By comparing the SEM images before and after calcination, it is found that the nanowires before calcination are arranged very tightly. However, after calcination, big gaps between the neighboring nanowires can be seen in the SEM image. This phenomenon corroborates our structural picture of the corona composed of PS. After calcination the coronas of the nanowires are burned away and gaps appear between neighboring nanowires. The assumption that the cylinder micelles have PS coronas can be proved by four facts: First, the SEM image before calcination has a lower contrast compared to the SEM image after calcination, indicating the presence of an organic block copolymer coverage on the nanowires before calcination. Second, in the SEM image after calcination, most of the nanowire structures are separated and only very minor parts of the nanowires are seemingly bound together. If the composite nanowires had an outer PEO corona, then the Ti-O- species within the PEO domains would tend to bind together during calcination due to the thermal driving force. Third, the size of the calcined nanowire structures is significantly decreased compared to the nanowire structures before calcination. Fourth, if PS blocks would form the nanowire cores, there would be porous structures formed after calcination because the inner PS cores would be totally burned off. However, the calcined structures obtained are solid nanowires and nanotubular like structures are not observed. Therefore, based on the above-mentioned facts and discussions, it is concluded that the composite nanowires have a core composed of PEO blocks and corona composed of PS blocks.

With increasing weight fraction of TTIP and fixed weight fraction of HCl, an interesting phenomenon of the titania nanowire structure evolution is observed (SEM images in **Figure 9** and corresponding AFM height and phase images in **Figure S-3** in appendix). The weight fraction of HCl is fixed at 0.01 and the weight fraction of TTIP is varied from 0.01 to 0.04. For the sample with TTIP weight fraction of 0.01, well-ordered nanowire structures are present in the film and there are almost no other side morphologies coexisting in the film (**Figure 9a1 and 9a2**). It's actually the sample shown in **Figure 8**. The sizes of the nanowires are uniform not only within a single nanowire, but also for different nanowires, which reflects the highly uniform characteristics of the cylinder micelles in solution. The double-ring like FFT pattern of the SEM image also indicates high order of the nanowire structures and the average spacing size of the nanowires is found to be 52nm from the FFT pattern. After calcination the morphologies of TiO_2 are almost purely nanowires, reflecting the corresponding structures before calcination.

When the TTIP weight fraction is increased to 0.015 (film thickness: 41nm before calcination), it can be seen that the order degree of the nanowires is decreased compared to the sample in **Figure 9a** and the size of the nanowires is no longer uniform (**Figure 9b1 and 9b2**).

In the image **Figure 9b1** there are some nanowires with obviously larger sizes than other nanowires and there are also some nanowires featuring nodular structures. The outer ring in the FFT pattern is broadened compared to the first sample, indicating less order of the nanowire structures in the film. The spacing size of the nanowires averaged from the inner ring of the FFT pattern is 52nm, which is in agreement with the sample in **Figure 9a**. Besides the main morphologies, there are some vesicle-like structures coexisting in the film, which will be discussed later. For the structures obtained after calcination, some nanowires containing nodules can still be observed, reminiscent of the protrusion features in the nanowires before calcination.

For the sample with TTIP weight fraction of 0.025 (film thickness before calcination: 35nm), many nanowire structures are forked (**Figure 9c1 and 9c2**). It can also easily be seen from the SEM image before calcination that the nanowire structures stack as a multilayer and a ring-like FFT pattern is still present before calcination. The corresponding spacing size between nanowire structures is 51nm. After calcination, TiO_2 nanowire structures with a large number of junctions are obtained. When the weight fraction of TTIP is further increased to 0.030 (film thickness before calcination is 43nm), the number of junctions is further increased compared to the sample with TTIP weight fraction of 0.025 (**Figure 9d1 and 9d2**). The ring-like FFT pattern of the image before calcination is further broadened compared to the samples with lower TTIP weight fractions and the average spacing between the nanowires is about 42nm, which is smaller than the first three samples in the series. After calcination, both nanowires and junctions are retained and a mesoscale network structure is formed. It can be found that the morphologies before and after calcination correspond very well. When the weight fraction of TTIP reaches 0.040 (film thickness before calcination: 46nm), there are many junctions of different sizes in the film and the nanowires are not the dominant structural elements any more (**Figure 9e1 and 9e2**). The ring-like FFT pattern in the SEM image before calcination is rather broadened and the spacing of the nanowire structures is further decreased to roughly 33nm. After calcination, a TiO_2 mesoscale network composed of nanowires and junctions is obtained. From the structure evolution it can be found that the morphologies evolve from pure nanowires via interconnected nanowires to mesoscale network structures due to increasing amount of junctions in the film. The mechanism of the morphology evolution can be rationalized by analyzing the role of TTIP in the system because for the above five samples, the relative weight fraction of HCl is always kept constant. The micelle core is

chemically reactive because the Ti-O- nanostructures inside the core can undergo further condensation with neighboring cores and the potential for further condensation is increased with increasing weight fraction of TTIP. Being mobile in solution, cylinder micelles may come close to each other and fuse together, which in pure block copolymer micelles is a statistical and dynamic event. However, in our system case, the cores will be linked covalently through the condensation of Ti-O- nanostructures

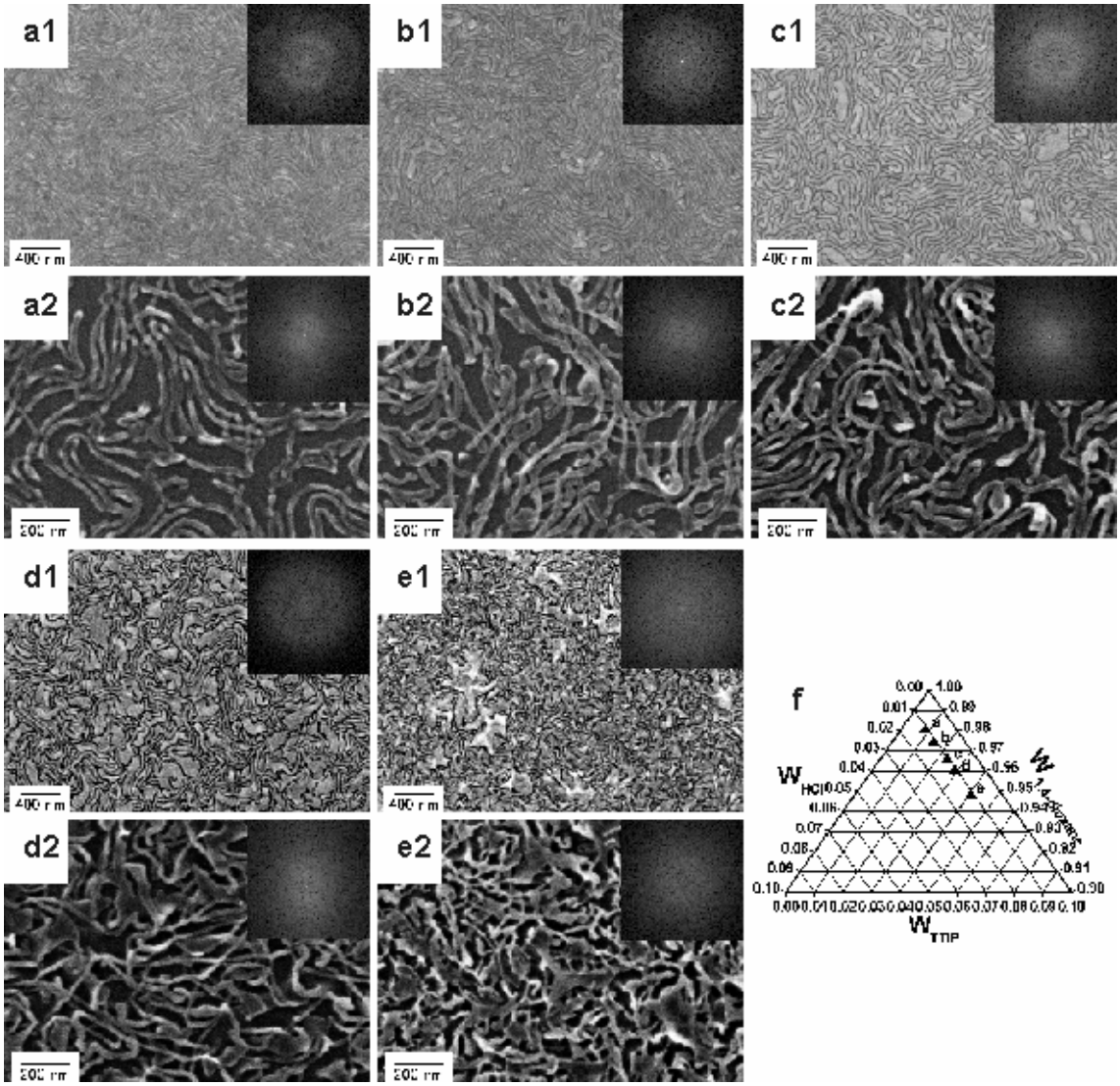

Figure 9. *SEM images of structure evolution with increasing weight fractions of TTIP in TiO_2 nanowire films.* ***a1***, ***b1***, ***c1***, ***d1***, *and* ***e1****: SEM images before calcination;* ***a2***, ***b2***, ***c2***, ***d2***, *and* ***e2****: SEM image after calcination;* ***f****: compositional existence points in the phase diagram with increasing TTIP weight fractions from* ***a*** *to* ***e*** *(W: weight fraction). The insets in the images are FFT patterns of the corresponding structures.*

between each other as a result of the micellar fusion. The increasing amount of TTIP in the micelle cores introduces more possibilities of the formation of linkages between cylinder micelles. Consequently, the number of junctions is increased with increasing W_{TTIP}. Compared to TTIP, an increase in the weight fraction of HCl retains the nanowire morphologies, where W_{TTIP} is 0.035 and W_{HCl} is 0.015 (**Figure 10**) (film thickness before calcination: 57nm). The ring-like FFT patterns before calcination correspond to a characteristic spacing of 38nm. If only the effect of TTIP is taken into account, the morphology should lie in the transition from **Figure 9d** to **Figure 9e**. However, from **Figure 10** it can be found that the nanowires are mainly connected by junction points, rather than junction planes as in **Figure 9d**. The total number of the junctions in **Figure 10** (*ca*. 248/μm^2) is increased compared to that in **Figure 9d** (ca. 96/μm^2). The increasing weight fraction of HCl solution retards the condensation of Ti-O- nanostructures. [270] Therefore it favors the formation of junction points rather than junction planes, which requires further condensation of Ti-O species in the solution.

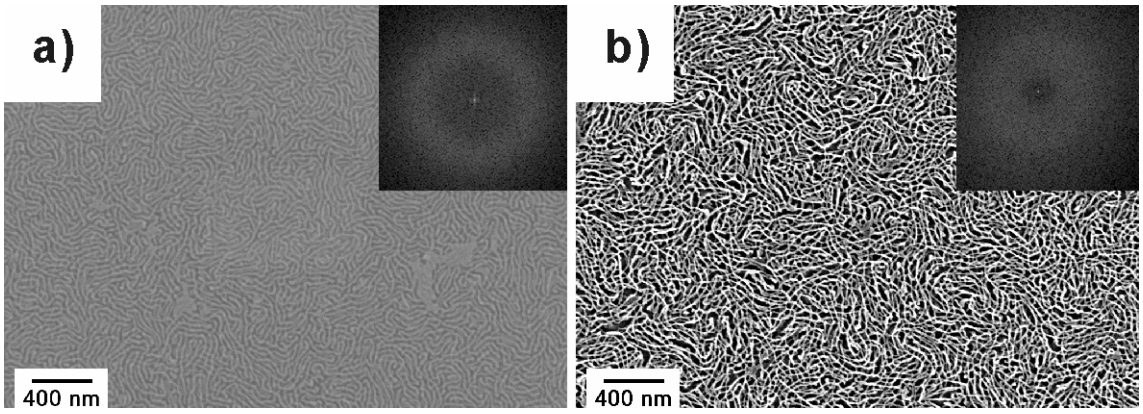

Figure 10. *SEM images of TiO_2 films with nanowire structures before (**a**) and after (**b**) calcination. The insets in the images are FFT patterns of the corresponding structures.*

4.2.2.4 Vesicle structures

With a further increase in the weight fraction of concentrated HCl solution, the nanowire structures will transform into vesicles. The shape and size of the vesicles will be determined by two factors: The volume ratio of HCl to the total amount of PS-b-PEO, 1, 4-dioxane and TTIP will determine the overall size of the vesicles, while the volume ratio of TTIP to the volume of PEO in PS-

b-PEO will determine the thickness of the titania shell of the vesicles. In this experiment, the amounts of PS-b-PEO and 1, 4-dioxane was always kept constant; therefore the morphology of the vesicle structures can be indicated by the relative weight fractions of HCl and TTIP. It is inferred that the TTIP component gets incorporated into the wall of the vesicles and eventually integrated via condensation since the titania is complexed to the PEO domain. The vesicle structures can be divided into three subgroups according to their specific morphologies either directly present in the film, for example, nanogranulas, or after calcination, for example, nanodoughnuts and collapsed vesicles. The reason for the presence of different morphologies is due to varied ratios of vesicle size to wall thickness, which can be modified by the weight fractions of HCl and TTIP in the solution.

4.2.2.4.1 Nanodoughnut Structures

Figure 11a and **Figure 11c** show AFM and SEM images of the vesicle structures before calcination respectively (film thickness: 49nm). After calcination, a three-dimensional nanodoughnut structure is formed, which is shown in **Figure 11d**. A ring-like FFT pattern of the SEM image before calcination indicates the average spacing size of the vesicles is 73nm, which is in agreement with the value obtained from AFM (71nm). It is noteworthy that the three-dimension characteristic reminiscent of very uniform vesicular structures can even be seen in the AFM image. A similar morphology transition trend was also observed by Eisenberg and coworkers, where PS-b-PAA in water solution can undergo the morphology transformation from nanowires to vesicles with increasing water amount. Here in our case the amount of concentrated HCl solution is increased leading to an increase in surface free energy between the PS blocks and surrounding solvents, which drives the morphology transformation from nanowires to vesicles in order to minimize the extra interfacial surface energy. During spin coating the vesicles formed in the solution are rearranged in an ordered fashion on the Si wafer substrate via a solvent evaporation induced arrangement process.

4.2.2.4.2 Collapsed Vesicles

With increasing weight fraction of the concentrated HCl solution and constant W_{TTIP} compared to the nanodoughnut samples, the vesicle structures still remain present in the film (**Figure 12b**) (film thickness before calcination: 56nm).

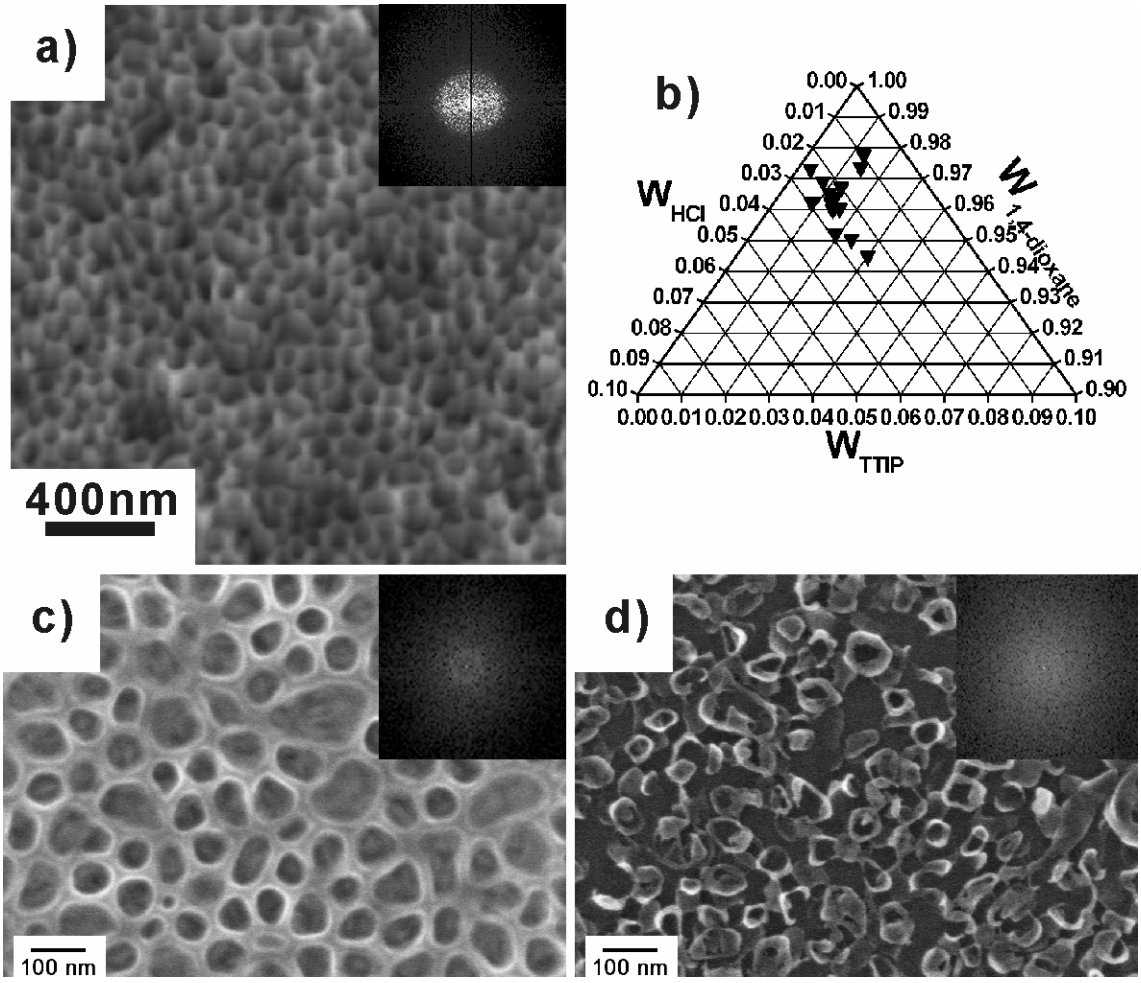

Figure 11. *AFM and SEM images of TiO_2 films with nanodoughnuts.* ***a****): AFM height image of the nanodoughnut structures before calcination, height scale: 40nm;* ***b****): compositional existence region in the phase diagram (W: weight fraction);* ***c****): SEM image before calcination;* ***d****): SEM image after calcination. The insets in the images are FFT patterns of the corresponding structures.*

However, the vesicle structures are different from the nanodoughnut structures in two aspects: first, the average size of the vesicles is larger than the nanodoughnut structure. Second, the ratio of vesicle size to wall thickness is increased. The increasing amount of HCl solution induces the formation of vesicles with large sizes to decrease the specific surface area. Vesicles with sizes of more than 200nm are due to the fusion of several small vesicles. Compared to the enlarged vesicle size, the wall thickness is nevertheless not increased, as the amount of TTIP swollen in the wall region of the vesicles is almost kept constant relative to the nanodoughnut samples. After calcination, the vesicle structures collapse

into disordered structures because of the increasing ratio of vesicle size to wall thickness, which turns the vesicle structures unstable during calcination. However, some parts of the vesicle walls can still be observed on the substrate after calcination, reminiscent of the vesicle structures before calcination (**Figure 12c**).

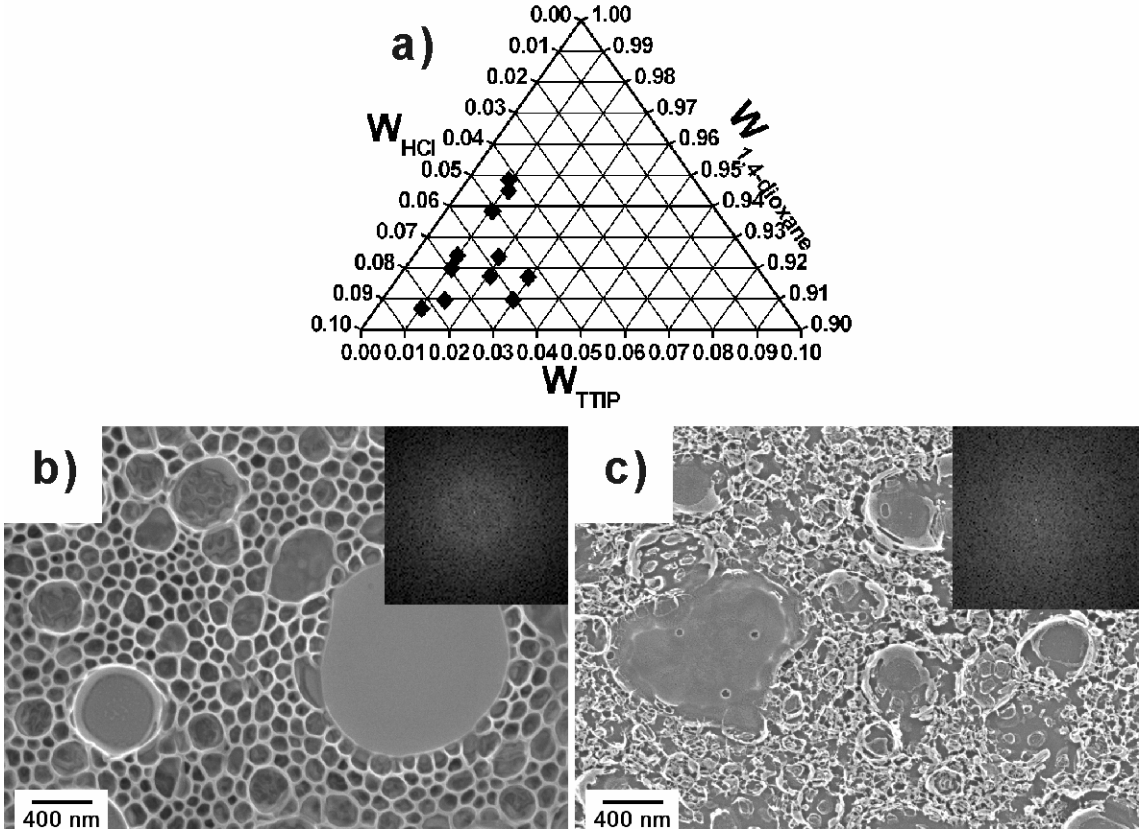

Figure 12. *SEM images of TiO_2 films with collapsed structures after calcination.* ***a****): compositional existence region in the phase diagram (W: weight fraction);* ***b****): SEM image before calcination;* ***c****): SEM image after calcination. The insets in the images are FFT patterns of the corresponding structures.*

4.2.2.4.3 Nanogranulas

Figure 13a shows the AFM image of nanogranulas before calcination and **Figure 13c** shows the corresponding SEM image (film thickness before calcination: 64nm). **Figure 13d** shows the SEM image of Nanogranulas after calcination. The formation mechanism of the nanogranulas can be

understood with the starting point of the vesicle structures. Compared to the nanodoughnut sample, the increasing amount of TTIP will thicken the wall of the vesicles, however, the overall size of the vesicles are not increased correspondingly because the W_{HCl} remains constant. As a consequence of the combined effects of HCl and TTIP, the ratio of vesicle size to wall thickness is decreased. The vesicle structures with thick walls are squashed into nanogranulas during spin coating because the solution is dried and compressed to form an ultra thin film. The small-depressed regions on the surface of the granular structures confirm the original vesicle structures.

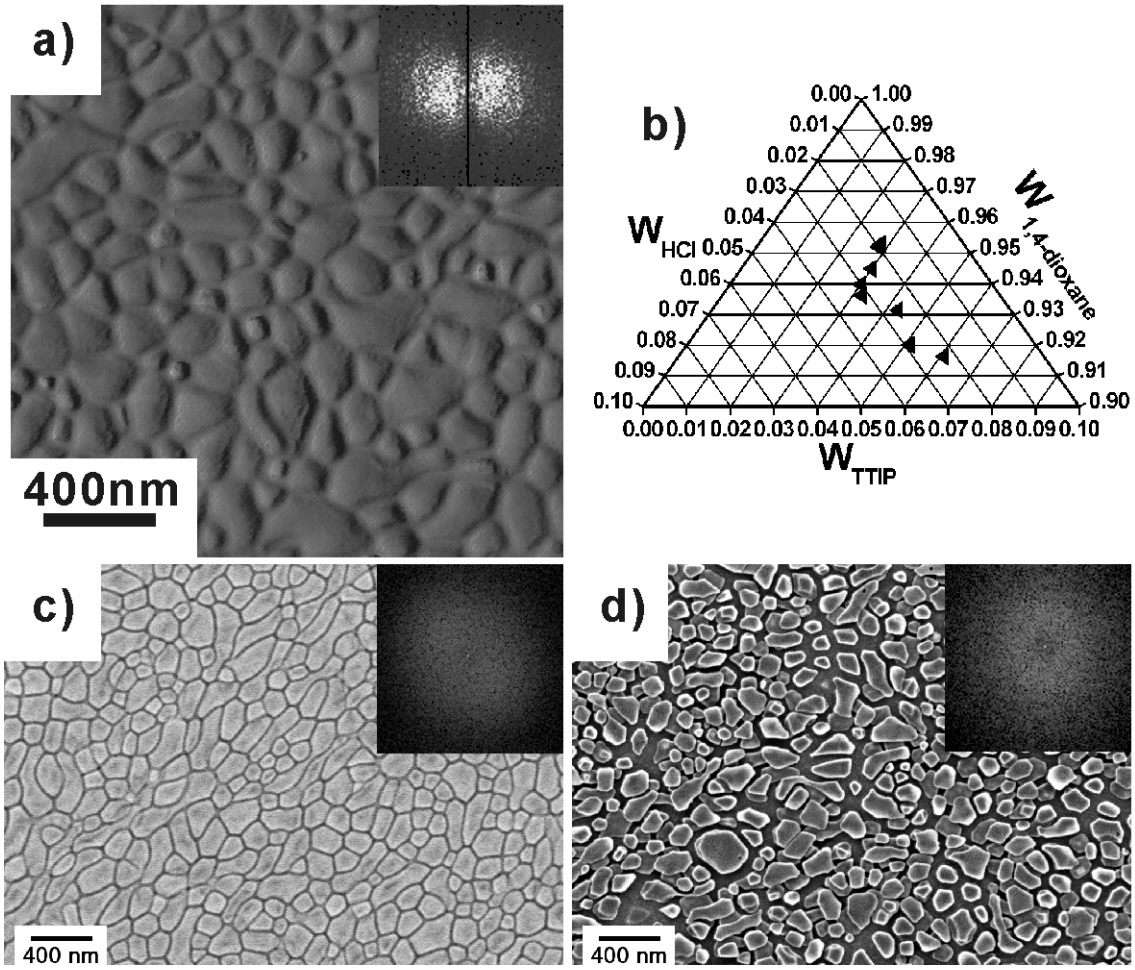

Figure 13. *AFM and SEM images of TiO_2 films with nanogranula structures.* ***a****): AFM phase image before calcination, phase scale: 30°;* ***b****): compositional existence region in the phase diagram (W: weight fraction);* ***c****): SEM image before calcination;* ***d****): SEM image after calcination. The insets in the images are FFT patterns of the corresponding structures.*

4.2.2.5 Worm-like Aggregates

When the surface energy between the PS block domain and the solvents outside the domain exceeds the stabilization energy limit of the micelles, a phase transition from micelles to reverse micelles happens in the solution. Consequently, worm-like aggregates, which are inverted cylinder micelle structures, are obtained. After calcination, the inner PS cores are burned away and holes are formed within the worm-like aggregates. **Figure 14b** and **14c** show the SEM images of worm-like aggregates before and after calcination (film thickness before calcination: 55nm). Both SEM images show ring-like FFT patterns and the corresponding characteristic spacing sizes are 44nm and 43nm respectively, which mean that the sizes of the structures are unchanged after calcination. However, there are holes present in the SEM image after calcination, whose formation mechanism will be discussed in the following.

Due to increasing amount of hydrophilic solvents the surface energy between the PS blocks and solvents exceeds the stabilization energy limit of the micelles and the micelle structures are no longer stable. As a result, an interesting phase transition from micelles to reverse micelles happens in the solution. The worm-like aggregates are inverted cylinder micelles consisting of PS cores and PEO coronas. TTIP and HCl solution are incorporated into the PEO coronas, and therefore a continuous phase is formed in which TTIP is hydrolyzed and condensed into Ti-O nanostructures. The assumption of the inverted cylinder micelles can be proved by analyzing the SEM images. First, there are holes present in the SEM image after calcination consistent with the removal of cylinder micelle cores composed of PS blocks after calcination. Second, the size of the worm-like structures remains constant in contrast to the significant size decrease in the nanowire samples, where the cylinder micelle coronas composed of PS blocks are burned off during calcination.

4.2.2.6 Foam-like Structures

Figure 15b and 15c show the SEM images of foam like structures before and after calcination (film thickness before calcination: 91nm). It can be seen that the foam like structures are basically formed in the region of the phase diagram with low weight fractions of HCl solution (**Figure 15a**). The foam-like structures are composed of skeleton containing large number of small sized structures. The low amount of concentrated HCl solution makes it possible to form large amount of small sized microphase-separated structures in the solution. And the high amount of TTIP incorporated into the

PEO domains make the PEO domains highly chemically reactive. It can undergo further hydrolysis and condensation reactions with other PEO domains when they are getting close induced by mutual collision, which is highly frequent in the solution because of the presence of large amount of small structures. As a result, three-dimensional random structures composed of mutually linked small sized structures are formed, which has a large specific surface area, leading to the formation of foam-like structures after calcination.

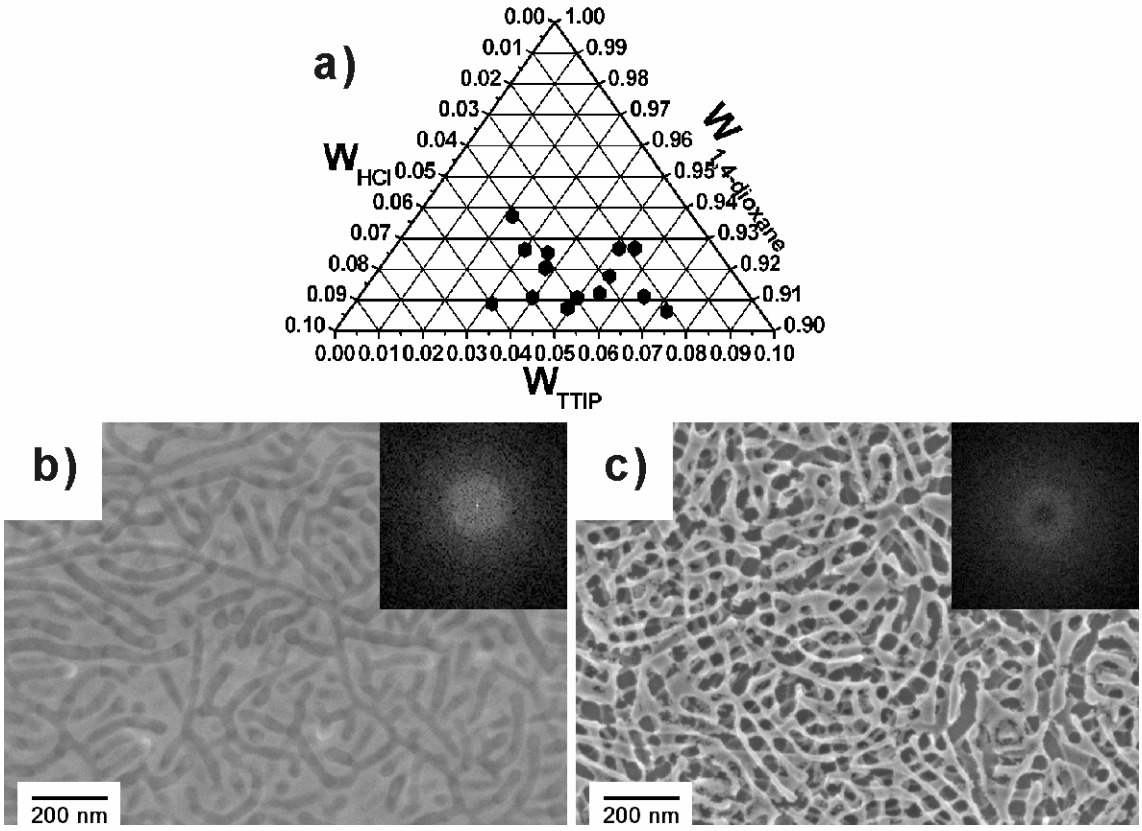

Figure 14. *SEM images of TiO_2 films with worm-like aggregates before and after calcination.* ***a****): compositional existence region in the phase diagram (W: weight fraction);* ***b****): SEM image before calcination;* ***c****): SEM image after calcination. The insets in the images are FFT patterns of the corresponding structures.*

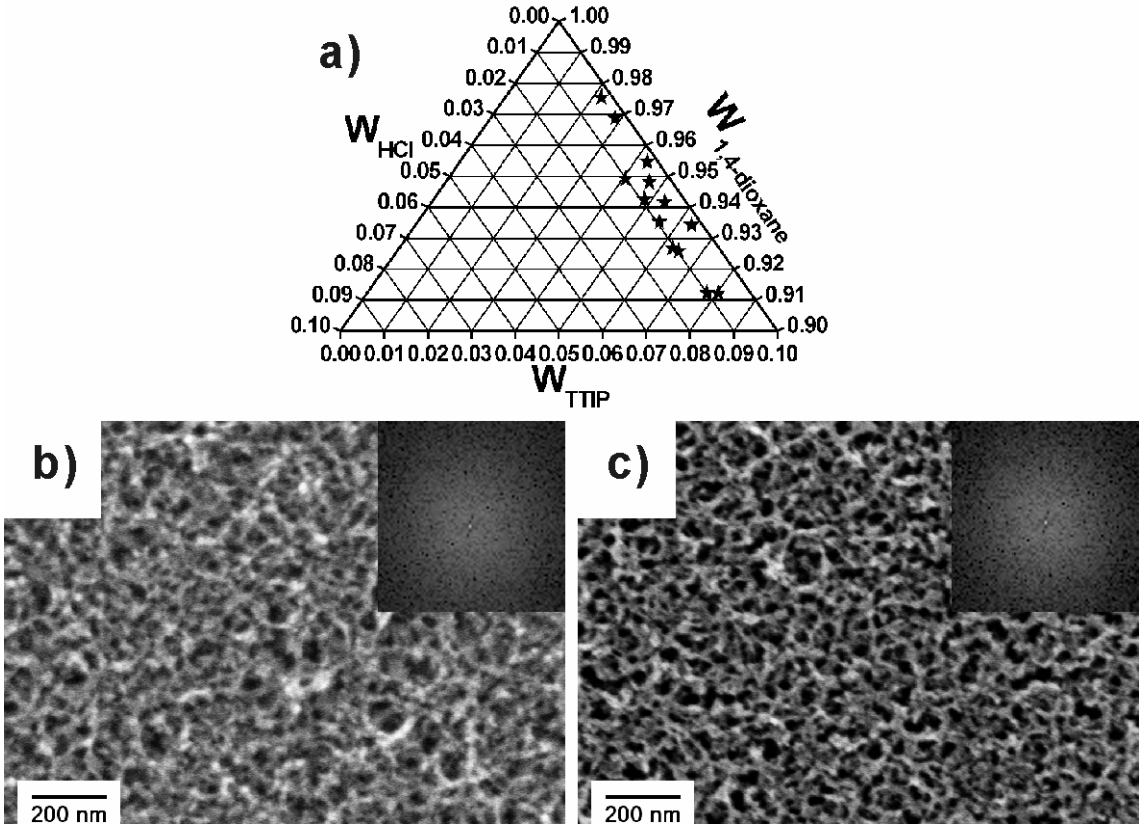

***Figure 15**. SEM images of TiO_2 films with foam-like structures before and after calcination. **a**): compositional existence region in the phase diagram (W: weight fraction); **b**): SEM image before calcination; **c**): SEM image after calcination. The insets in the images are FFT patterns of the corresponding structures.*

4.2.2.7 Summary of the Morphology Evolution

The total structure evolution in the investigated phase diagram can be summarized as follows. With low weight fractions of concentrated HCl solution and TTIP, clustered spherical micelles are formed in the solution (**Figure 16a**). The clustered spherical micelles can be transformed into diverse morphologies under different conditions. For example, with slightly higher weight fractions of HCl solution and comparable weight fractions of TTIP, flake-like structures are formed (**Figure 16b**). When the weight fraction of HCl solution is kept below 0.01 and the amount of TTIP is increased, a skeleton composed of large amount of small-sized structures is formed leading to the formation of foam-like structures after calcination.

With increasing weight fractions of HCl solution compared to the clustered nanoparticles and flake-like structures, cylinder micelles are formed (**Figure 16c**). The neighboring cylinder micelles can be linked to form junctions, whose number is increased with increasing amounts of TTIP, leading to the formation of mesoscale network of interconnected nanowires. Compared to nanowire structures, vesicles structures are formed with further increasing weight fractions of HCl (**Figure 16d**).

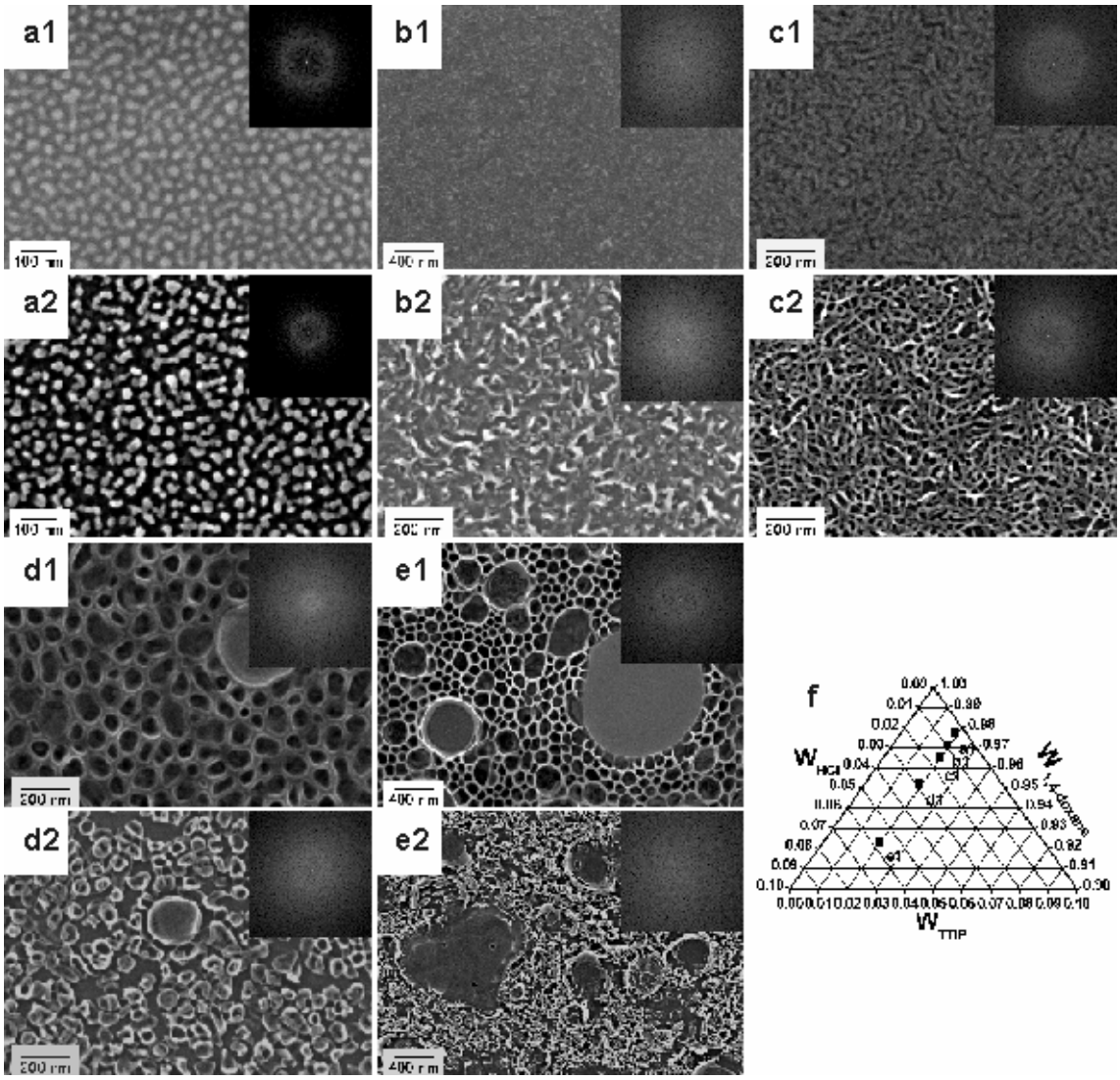

Figure 16*. SEM images of TiO_2 films with morphology evolution with increasing HCl weight fractions.* ***a1****,* ***b1****,* ***c1****,* ***d1****, and* ***e1****: SEM images before calcination;* ***a2****,* ***b2****,* ***c2****,* ***d2****, and* ***e2****: SEM images after calcination;* ***f****: the compositional existence regions in the phase diagram where the five structures are formed with increasing HCl weight fractions from* ***a*** *to* ***e*** *(W: weight fraction). The insets in the images are FFT patterns of the corresponding structures.*

Due to different ratios of vesicle size to wall thickness, different morphologies are present either directly in the dry film (nanogranulas), or after calcination (naodoughnuts and collapsed vesicles). If the HCl fraction is roughly less than 0.03, the vesicle structures in the film can survive calcination and nanodoughnut like structures can be obtained. If the weight fraction of HCl is increased (more than 0.04) and TTIP fraction remains unchanged, the vesicle structures collapse into disordered structures after calcination (**Figure 16e**). When the weight fraction of HCl is fixed relative to the nanodoughnuts and the amount of TTIP is increased, nanogranular structures are formed via the squashing process during spin coating.

4.2.2.8 XRD

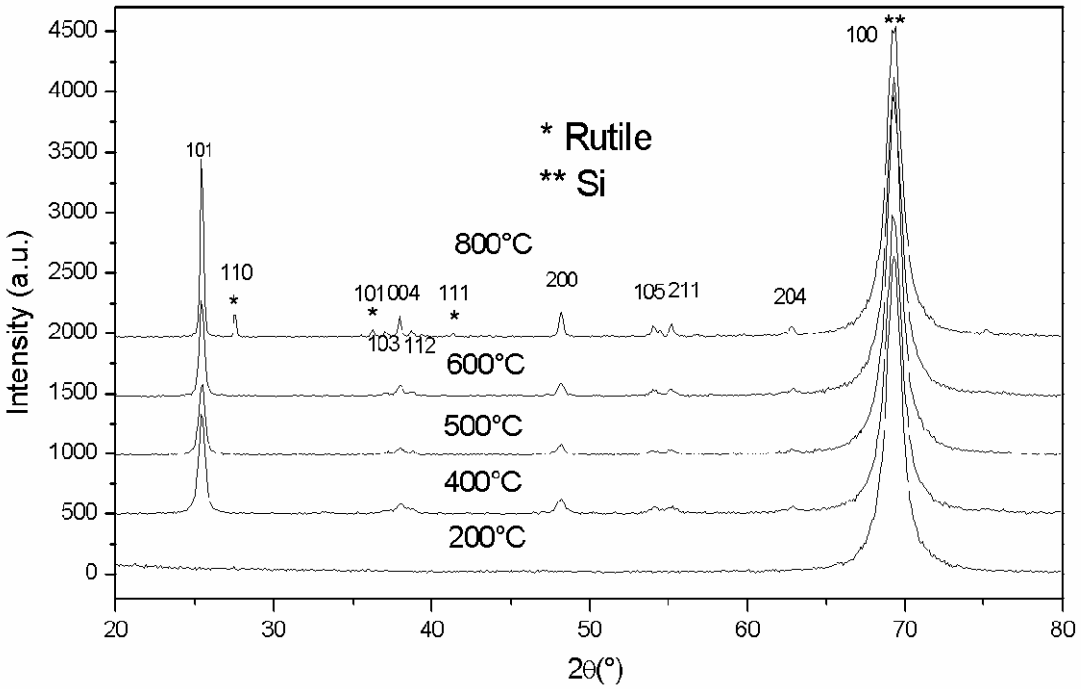

***Figure 17**. X-ray diffraction patterns of TiO_2 films on Si (100) substrate calcined at different temperatures for 4 hours.*

Figure 17 shows XRD results with different calcination temperatures (Sample composition: W_{TTIP}: 0.029; $W_{1,\ 4\text{-dioxane}}$: 0.963; W_{HCl}: 0.008). It can be seen that there is no crystallographic phase obtained after calcination at 200°C for 4 hours. Anatase phase appears when the calcination temperature increases to 400°C. At temperatures above 800°C, a rutile phase appears besides anatase. *[84, 271]*

From these results it is concluded that the varied morphologies obtained after calcination at 400°C for 4 hours are in the anatase phase.

4.2.3 Further Structural Investigation of Nanostructured TiO_2 Thin Films with Different Morphologies

Complete understanding of the TiO_2 film structure relies on the combination of imaging analysis and x-ray scattering techniques. The imaging analysis can provide detailed local structural information of the film and as a complementary method; x-ray scattering is a method to reveal the average component information over large length scale in the film. Furthermore, to build a complete 3D picture of the film, both structures in the direction normal and parallel to the substrate, that is, the vertical and horizontal structure of the films need to be studied. *[148, 149, 210, 272]* Potential characterization methods are listed in **Table 2**.

Table 2. Potential Film Structure Characterization Techniques

	Imaging analysis	x-ray scattering techniques
Horizontal structure	AFM, SEM, TEM	GISAXS
Vertical structure	SEM, TEM	x-ray reflectivity

In the following section, a detailed structure investigation of the film with above-mentioned different morphologies will be addressed.

4.2.3.1 Clustered Nanoparticles

4.2.3.1.1 Vertical Structure

The SEM side view image and x-ray reflectivity profiles of the TiO_2 film with clustered nanoparticles are exhibited in **Figure 18**. The SEM side view image (**a**) indicates that the film consists of a monolayer of clustered nanoparticles. However, the x-ray reflectivity profile (**b**) suggests that besides the nanoparticles monolayer, there is a second layer of TiO_2 beneath the nanoparticles. According to the fitting model of the experimental reflectivity curve, the upper nanoparticle layer has a thickness around 5.0nm and the bottom TiO_2 layer has a thickness ca. 3.5nm. Due to high roughness of

the film originating from the nanostructures, the oscillation of the reflectivity curve is smeared out, which is therefore a non-classical system for the x-ray reflectivity experiment. The smeared out reflectivity profile makes it difficult to fit the curve with highly defined parameters. To fit the curve, the nanostructured surface has to be assumed as a homogeneous layer with a high roughness. Consequently, the film thickness of the film is just an approximation to the real TiO_2 film.

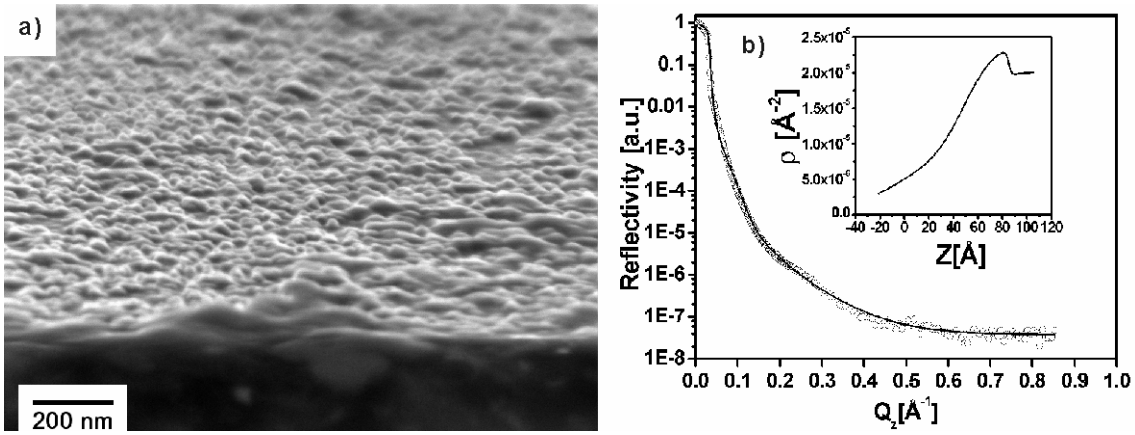

Figure 18. *SEM side view (**a**) and x-ray reflectivity experimental and simulation profiles (**b**) of the TiO_2 film composed of clustered nanoparticles. (Inset is the profile of scattering length density versus film thickness)*

4.2.3.1.2 Lateral Structure

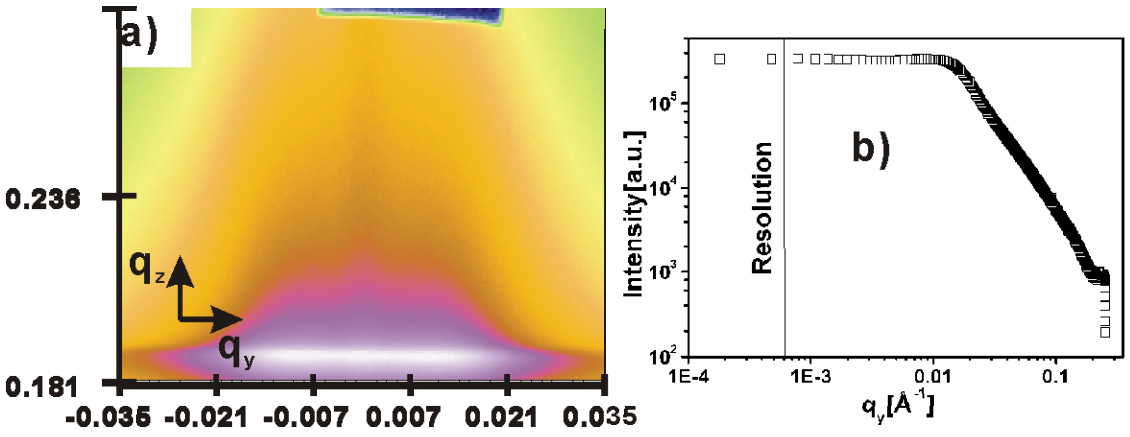

Figure 19*. GISAXS 2D image (**a**) and corresponding Out-Of-Plane (OOP) cut q_y (**b**).Beam line: A2*

The local horizontal structure of the film has been investigated with SEM as shown in **Figure 6d**. By using GISAXS, long range lateral structure information of the film can be revealed, as exhibited in **Figure 19**. [148, 149, 273] It shows a GISAXS 2D image of the film (**a**), where the lateral structure information can be extracted by the Out-of-Plane (OOP) cut along the critical angle region of TiO_2 in the direction of q_y (**b**). The peak in the OOP profile indicates a lateral inter-particle distance of 42nm, which is in agreement with the value from the local SEM analysis. The GISAXS results confirm that the clustered nanoparticles are deposited in a long range order in the film over a length scale of at least a few mm.

4.2.3.2 Flake

4.2.3.2.1 Vertical Structure

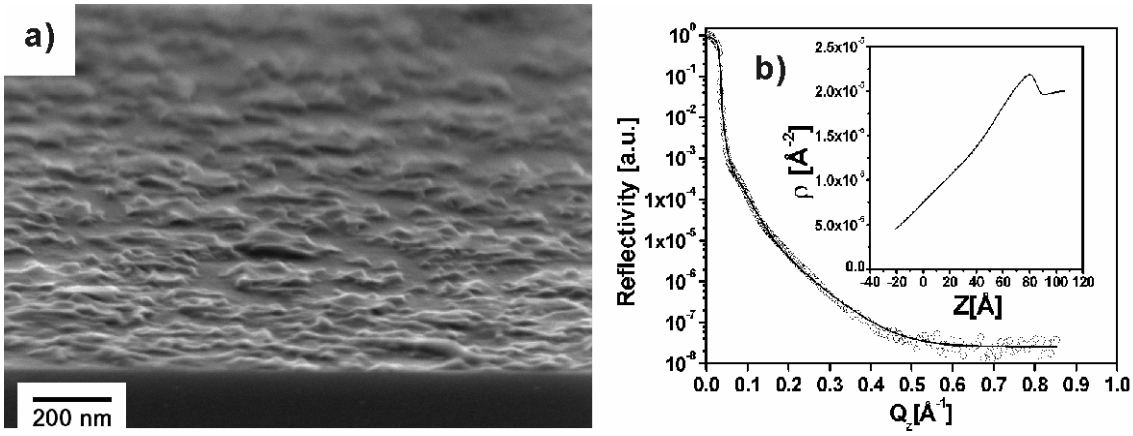

Figure 20. *SEM side view (**a**) and x-ray reflectivity experimental and simulation profiles (**b**) of the TiO_2 film composed of flake structures. (Inset is the profile of scattering length density versus film thickness).*

The SEM side view image confirms the flake-like structure on the substrate (**a**) and it further shows that the flake structure is monolayer on the substrate. Similar to the film with clustered nanoparticles, the x-ray reflectivity profile does not exhibit classic oscillation pattern due to high roughness of the film (**b**). The model used to fit the reflectivity profile consists of two layers: an upper flakes layer with a thickness ca. 6.0nm and a bottom TiO_2 layer with a thickness around 2.5nm, which has a similar thickness to the bottom layer in the film of clustered nanoparticles.

4.2.3.2.2 Lateral Structure

The lateral structure of the film is investigated by GISAXS and the result is shown in **Figure 21**. The OOP scan (**b**) based on the 2D image (**a**) indicates no long range order parallel to the substrate, which is reasonable because of the poor order of the flake structures on the substrate as proved by the SEM image in **Figure 7c**.

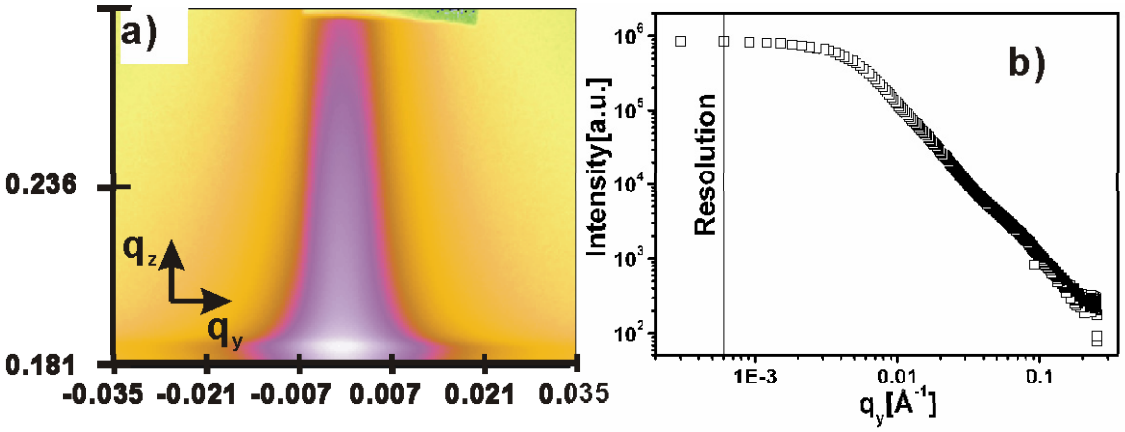

Figure 21. *GISAXS 2D image (**a**) and corresponding Out-Of-Plane (OOP) cut along q_y (**b**). Beam line: A2.*

4.2.3.3 Nanowires

4.2.3.3.1 Vertical Structure

A vertical structure evolution of the films composed of nanowires with increasing weight ratio of TTIP is shown in **Figure 22**. Samples **a-c** correspond to the samples **b-d** addressed in **Figure 9**. The SEM side view images show that the number of nanowires increases with the weight ratio of TTIP, which is in agreement with the top view SEM images in **Figure 9**. X-ray reflectivity measurement of the samples **a-c** show similar profiles but with an increasing film thickness of 13.5, 17.5, and 19.5nm respectively. Similar to films with clustered nanoparticles, and flakes, there are also thin TiO_2 layers beneath the nanowires with a thickness of 2.2, 2.5, and 3.5nm for samples **a-c** respectively.

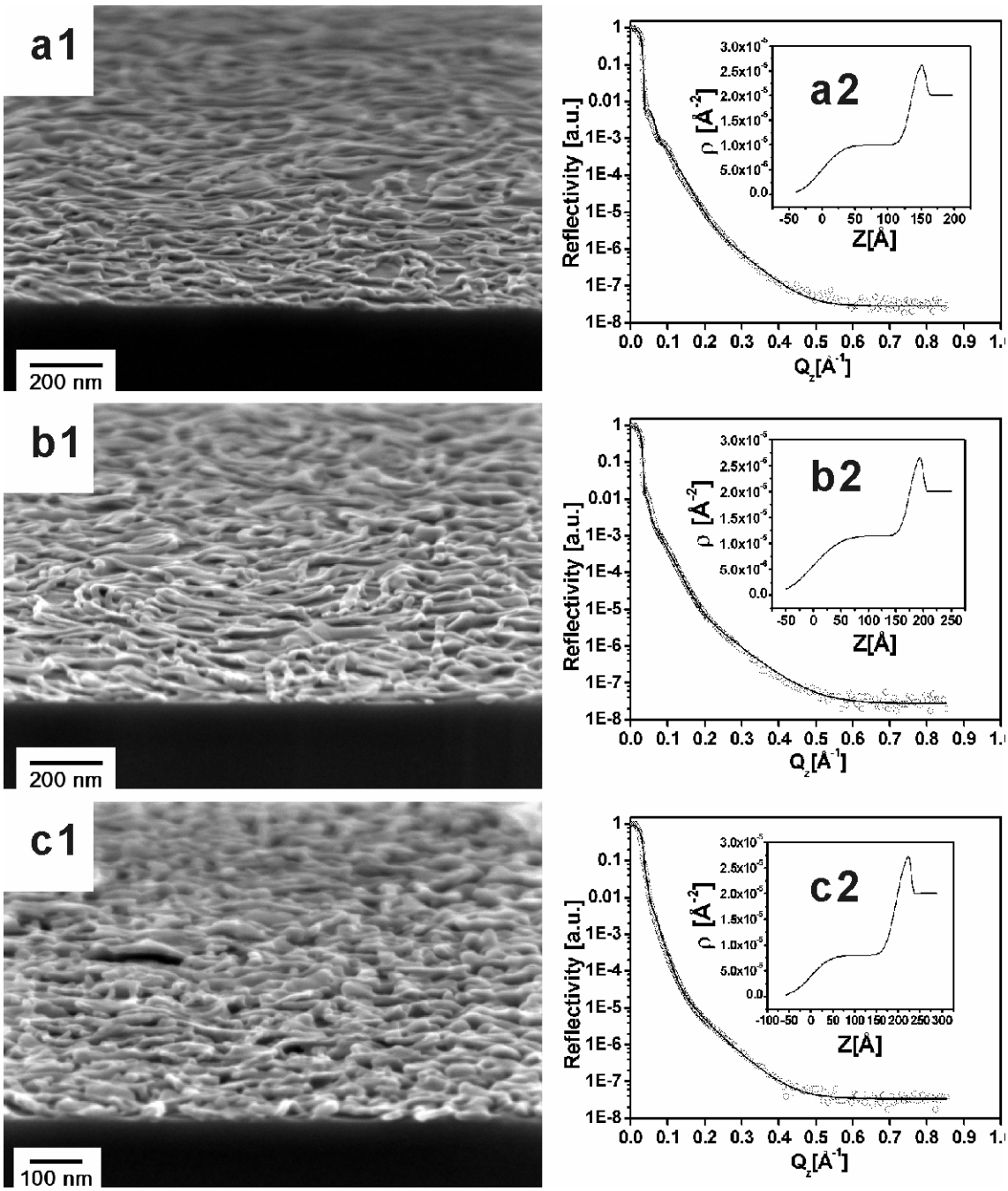

Figure 22. *SEM side view (**a1**, **b1**, **c1**) and x-ray reflectivity experimental and simulation profiles (**a2**, **b2**, **c2**) of the TiO_2 film with a nanowire structure evolution by increasing weight ratio of TTIP. (Inset is the corresponding profile of scattering length density versus film thickness). Sample **a**, **b**, and **c** corresponds to sample **b**, **c**, and **d** addressed in **Figure 9** respectively.*

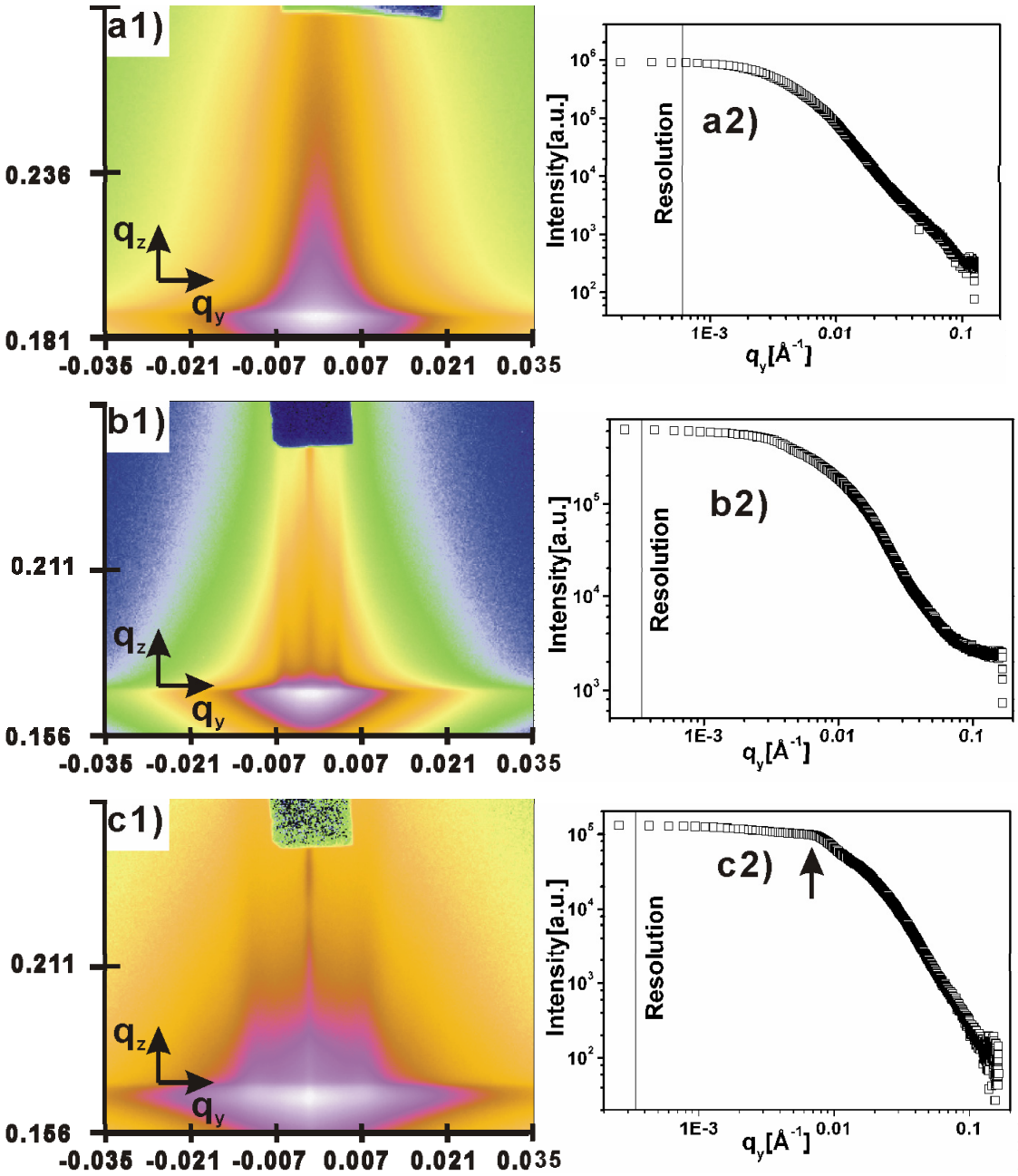

Figure 23. *GISAXS 2D images (**a1**, **b1**, and **c1**) and corresponding Out-of-Plane (OOP) cuts along q_y (**a2**, **b2**, and **c2**) of the nanowire films with increasing weight ratios of TTIP. The peak addressed in the thesis is marked by an arrow. Beam line: a, A2; b and c, Beamline: BW4.*

4.2.3.3.2 Lateral Structures

The GISAXS results in **Figure 23** exhibit a long range lateral structure evolution of the nanowire films from **a** to **c**. **Figure 23a** does not show an evident peak in the OOP profile indicating the loss of long range order of the nanowire structures in sample **a**. However, on the contrary to sample **a**, there is a long rang order present in the film **b**, which is confirmed by the existence of a peak in the OOP profile in **Figure23b**. Although it's very difficult to obtain the spacing size between nanowires from the SEM image of the nanowires after calcination due to a rather broad FFT pattern (**Figure 9c2**), the GISAXS peak indicates a characteristic distance of 51nm, which agrees with the spacing size between nanowires obtained from the SEM image before calcination (51nm in **Figure 9c1**). Similar to sample **b**, the weak peak in the GISAXS profile (**Figure 23c**) indicates a long range order of the lateral nanowire structures in the film **c** with a spacing size of 29nm between nanowires. However, compared to sample **b**, where the spacing size before and after calcination does not have a big change, here in sample **c**, the spacing size after calcination is dramatically reduced after calcination (before calcination: 42nm in **Figure 9d1**). The reason for the difference is probably due to the increasing number of the junction planes between nanowires in the film from film **b** to **c**.

4.2.3.4 Nanodoughnuts

4.2.3.4.1 Vertical Structure

The vertical structure of the film with nanodoughnut is shown in **Figure 24**, whose top view SEM image is shown in **Figure11d**. The SEM side view image (**a**) suggests a monolayer of nanodought and the fitting model of the x-ray reflectivity curve (**b**) includes a layer of nanodought with a thickness of 11.5nm and a bottom TiO_2 layer with a thickness of 2nm. Again the reflectivity profile does not have a clear oscillation pattern because of the rough surface originating from the nanostructured surface.

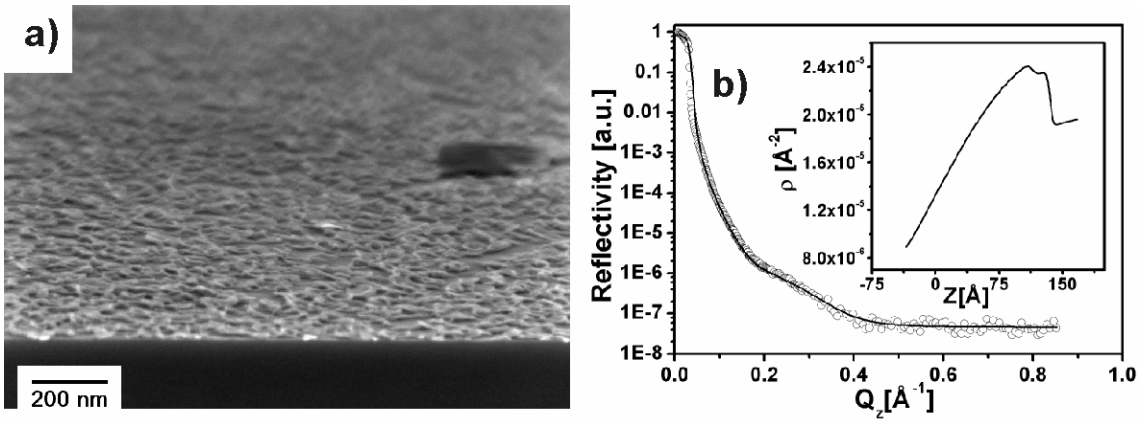

Figure 24. *SEM side view (**a**) and x-ray reflectivity experimental and simulation profiles (**b**) of the TiO_2 film composed of nanodoughnuts (Inset is the profile of scattering length density versus film thickness).*

4.2.3.4.2 Lateral Structure

Although the local SEM image does not show a nice order of the nanodoughnuts on the substrate (**Figure 11d**), the peak in the OOP scan (**a**) of the 2D GISAXS image (**b**) suggests there is a long range order in the film with an inter-nanodoughnut distance of 52nm. It means that even though there is a sever order loss of the composite film after calcination, partial long range order is still retained in the calcined TiO_2 film.

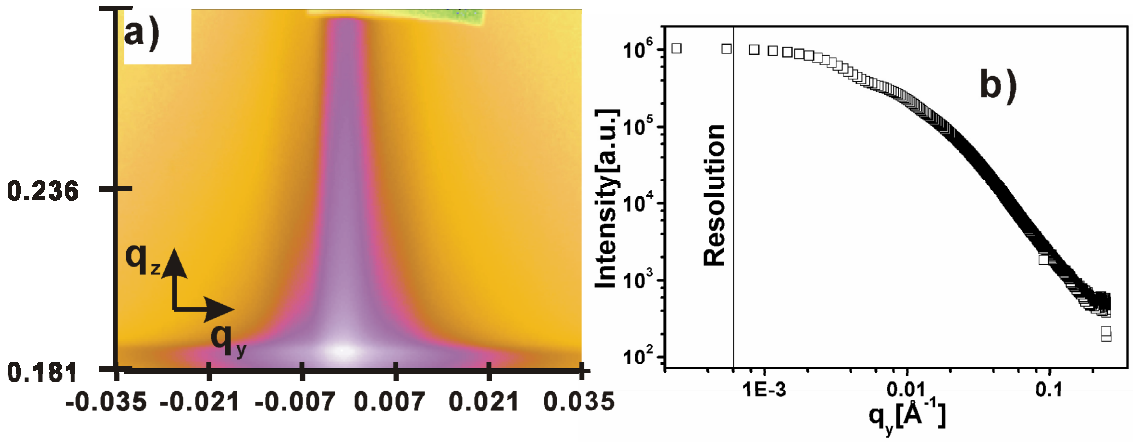

Figure 25. *GISAXS 2D image (**a**) and corresponding Out-of-Plane (OOP) cut along q_y (**b**) of the film with nanodoughnut structures. Beam line: A2.*

4.2.3.5 Nanogranulas

4.2.3.5.1 Vertical Structure

The SEM side view image in **Figure 26a** shows a layer with large number of nanogranulas on the substrate. The fitting model of the x-ray reflectivity profile suggests an upper nanogranular layer with a thickness around 45nm and a bottom TiO_2 layer with a thickness around 5.0nm.

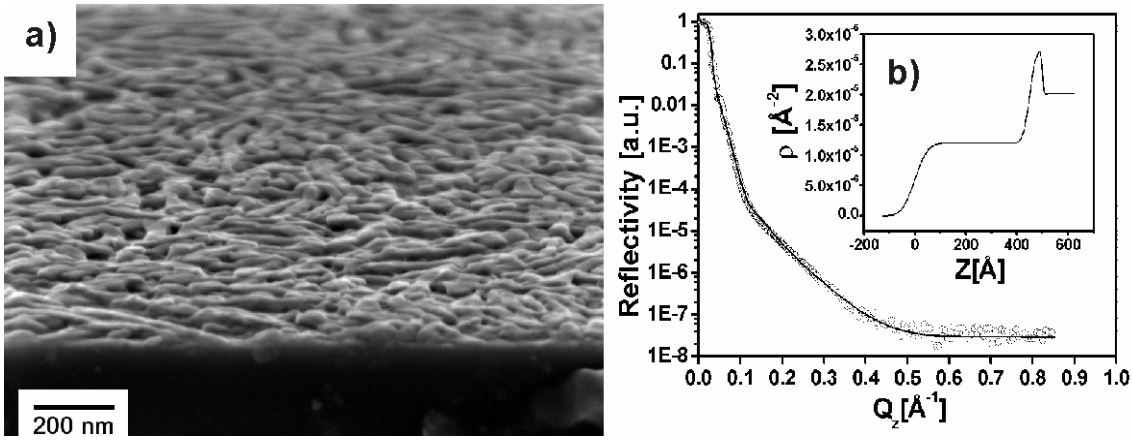

Figure 26. *SEM side view (**a**) and x-ray reflectivity experimental and simulation profiles (**b**) of the TiO_2 film composed of nanogranula structures (Inset is the profile of scattering length density versus film thickness).*

4.2.3.5.2 Lateral Structure

The SEM image (**a**) in **Figure 27** provides the local structure information about the film of nanogranulas. No long range order structure is present in the film as revealed by the GISAXS study (**b** and **c**).

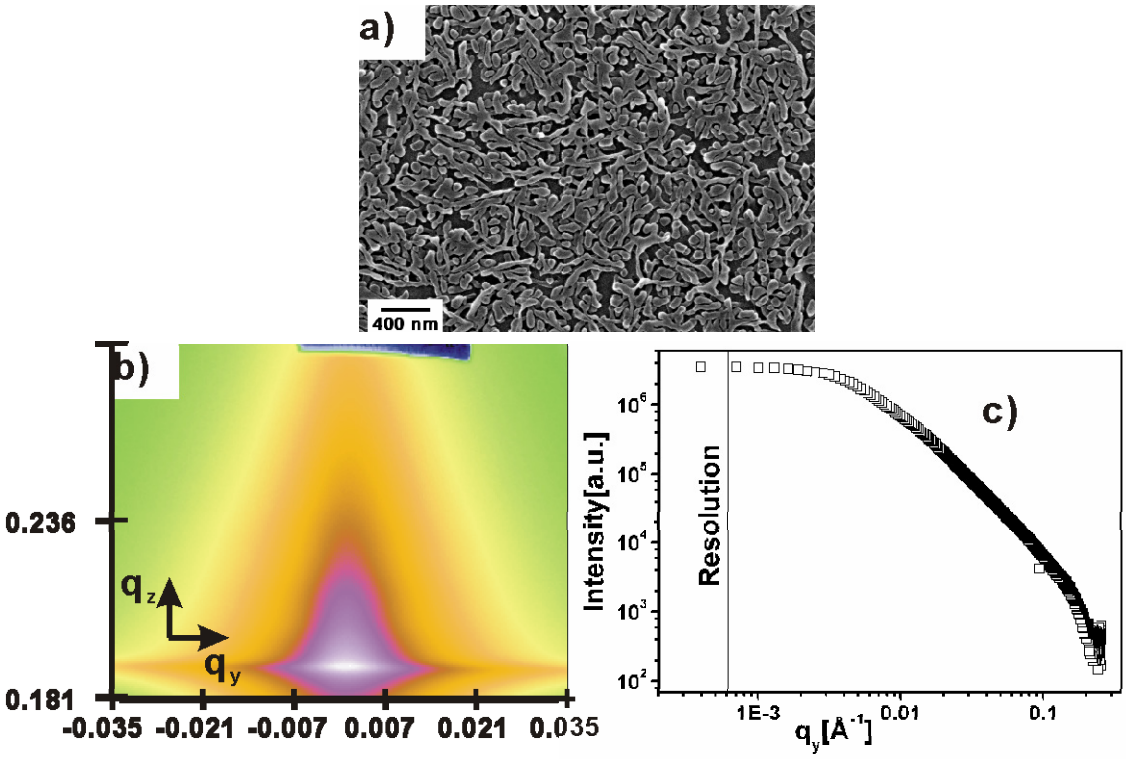

Figure 27*. SEM image (**a**) and GISAXS 2D image (**b**) and corresponding Out-of-Plane (OOP) cut along q_y (**c**) of the film with nanogranular structures. Beam line: A2.*

4.2.3.6 Worm-like structure

4.2.3.6.1 Vertical Structure

The SEM top view image in **Figure 28** (**a**) shows a worm-like structure on the substrate, which is confirmed by the side view image (**b**). The ring like FFT pattern of the SEM top view image indicates the narrow size distribution the worm-like structures (49nm).The x-ray reflectivity profiles indicate the worm structure layer has a thickness of 17.0nm and an additional bottom TiO_2 layer with a thickness of 1.1nm (**c**).

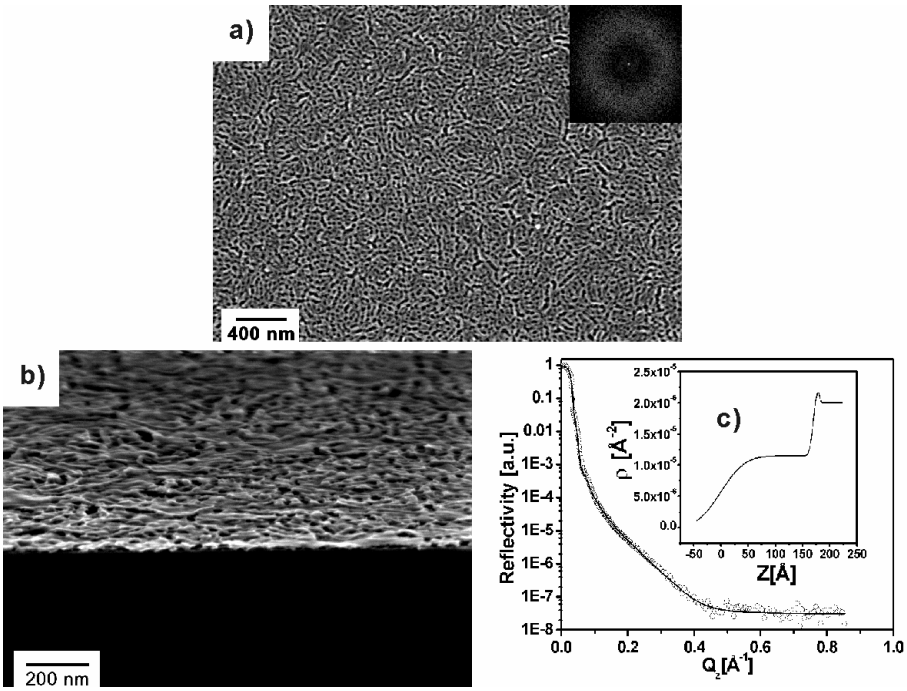

Figure 28. *SEM top view (**a**), side view (**b**) and x-ray reflectivity experimental and simulation profiles (**c**) of the TiO_2 film composed of nanogranula structures (Inset is the profile of scattering length density versus film thickness).*

4.2.3.6.2 Lateral Structure

The GISAXS profile of the worm-like structure in **Figure 29** indicates a long range order with a characteristic distance of 49nm (**a** and **b**), which agrees with the value obtained from the FFT pattern of the local SEM image (**Figure 28a**).

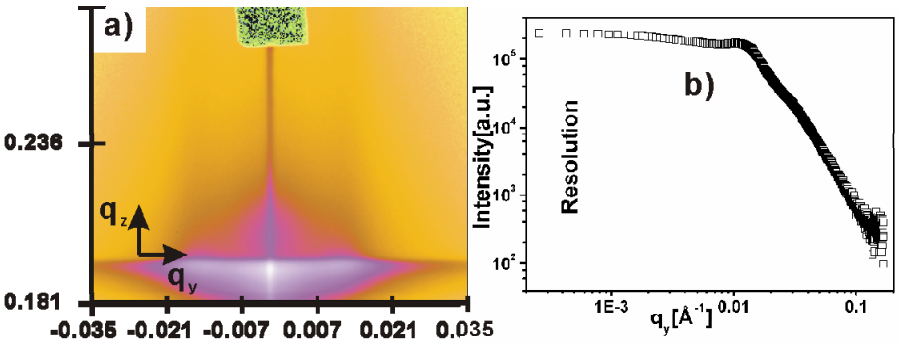

Figure 29*. GISAXS 2D image (**a**) and corresponding Out-Of-Plane (OOP) cut along q_y (**b**) of the film with worm-like structure. Beam line: BW4.*

4.2.3.7 Foam

4.2.3.7.1 Vertical Structure

The SEM side view image (**a**) in **Figure 30** confirms the foam like TiO_2 film, which is in agreement with the top view image in **Figure 15**. The oscillation peaks in the x-ray reflectivity profile indicate a film thickness of 34nm. Besides the foam layer, the bottom TiO_2 layer has a thickness of 3.5nm (**b**).

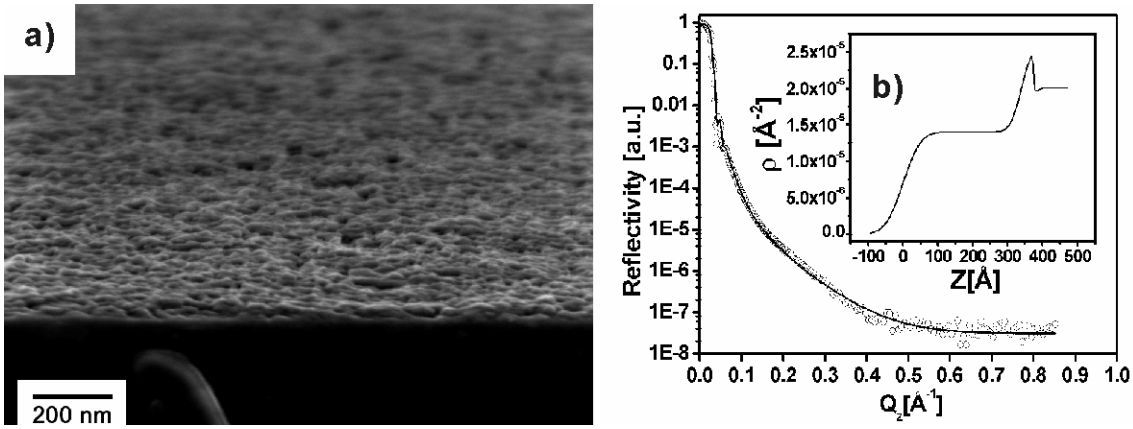

Figure 30. *SEM side view (**a**) and x-ray reflectivity experimental and simulation profiles (**b**) of the TiO_2 foam (Inset is the profile of scattering length density versus film thickness).*

4.2.3.7.2 Lateral Structure

The GISAXS measurement of the foam in **Figure 31** does not show a peak in the OOP cut curve, which means that there is no long range order within the foam. This is reasonable because according to the SEM image, the foam is composed of huge amount of randomly agglomerated nanoparticles exhibiting a broad range of lateral length scales.

4.2.3.8 Summary of the Structural Investigation of TiO_2 Films with Different Morphologies

The combination of the local imaging characterization and x-ray scattering techniques provide a way to build a 3D picture of the nanostructured TiO_2 film. The SEM side view images have proved if

the nanostructures are monolayer or multilayer on the substrate. For example, in the samples investigated in this section, clustered nanoparticles, flakes, nanodoughnut, nanogranulas are monolayer; nanowires can have structure evolution from monolayer to multilayer by increasing the amount of TTIP; worm like structures and foam are likely multilayer on the substrate. The x-ray reflectivity experiments provide the vertical structural information of the films, especially, the components and corresponding thickness normal to the substrate, which are difficult to be revealed by SEM side view experiments.

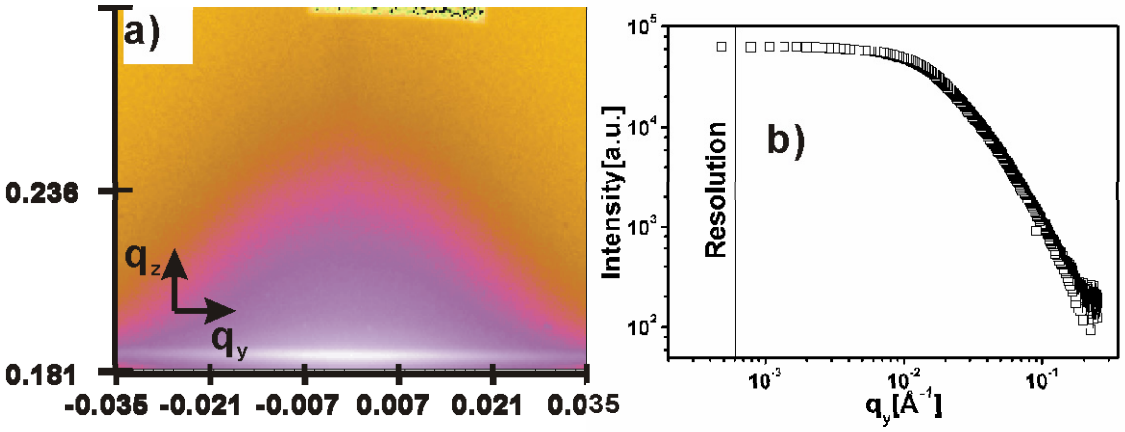

Figure 31. *GISAXS 2D image (**a**) and corresponding Out-Of-Plane (OOP) cut along q_y (**b**) of the film with foam structure. Beam line: A2.*

All of the x-ray reflectivity models suggest a thin TiO_2 layer on the surface of the substrate. The formation of the thin TiO_2 layer is likely due to the preferential wetting of the silicon oxide surface by the sol-gel solution and a subsequent reaction between the titania precursor and water molecules attached to the SiO_x surface.

The GISAXS experiments further investigate the lateral structural information over large length scale parallel to the substrate, which is very difficult to obtain by the local SEM characterization. The GISAXS prove that some of the nanostructured TiO_2 films have long range order with a characteristic distance in agreement with the SEM analysis. And those films with no long range order structures as shown in GISAXS also have poor order structures in the local SEM images. Consequently, a deep insight about the long range lateral structures of the films is achieved.

4.2.4 Influence of Various Parameters on Morphologies

4.2.4.1 Impact of Copolymer Concentration on Morphologies

Besides the parameter of relative weight ratios among 1, 4-dioxane, HCl, and TTIP, the block copolymer concentration is the fourth dimensional parameter to control the micellar morphologies. To understand how block copolymer concentration influences the morphologies, the relative ratios among 1, 4-dioxane, HCl, and TTIP need to be first fixed, while varying the block copolymer concentration in a systematic way. A specific weight ratio combination of the solution components is therefore chosen, where a nanovesicle structure is supposed to be formed with the copolymer concentration of 1%. The block copolymer concentration is varied from 0.25 wt. % to 4 wt. % and the morphology evolution is investigated. Sample solutions were prepared according to the following procedure. For the samples with copolymer concentrations ranging from 0.25 wt. % to 2 wt. %, 0.01-0.08g PS-b-PEO was mixed together with *ca*. 4.0g 1, 4-dioxane, and 0.03g 37%HCl, and 0.12g TTIP. For the samples with a copolymer concentration of 4.0%, 0.0795g PS-b-PEO was mixed with 2.0071g 1, 4-dioxane, and 0.0171g 37%HCl, and 0.0676g TTIP. The solutions were stirred for from 30min to 1hr before spin coating.

In **Figure 32** it shows the morphology of the film with a copolymer concentration of 0.25 wt. % before and after calcination. The SEM image before calcination (**Figure 32a**) shows a mesoporous like structure. But the nanoparticle like morphology in the AFM height image (**Figure 32b**) suggests that the "dark" region in the SEM image is composed of polystyrene block domain, which has lower electron density compared to the region composed of Ti-PEO domain. The AFM phase image (**Figure 32c**) further confirms the hardness difference between the soft PS domain and hard Ti-PEO domain. The morphology of the film can be described as nanovesicles with hard continuous Ti-PEO walls and soft interior PS/1, 4-dioxane filled pockets. The six-fold symmetry of the FFT patterns indicates that the nanovesicles are hexgonally packed. The additional presence of second order peak means that order of the hexagonal packing is high. The center-to-center value calculated from FFT is ca. 35nm. The SEM and AFM images after calcination (**Figure 32d** and **32e** respectively) show a mesoporous film because of the removal of PS block during calcination. The corresponding FFT pattern indicates that the film still retains its hexagonal packing. The side view image shows that the mesoporous film is a monolayer with holes penetrating through the whole film (**Figure 32f**). The low magnificantion SEM

images of the film before and calcination show that the film is quite homogeneous in a large length scale (See supporting information **Figure S-4** in appendix).

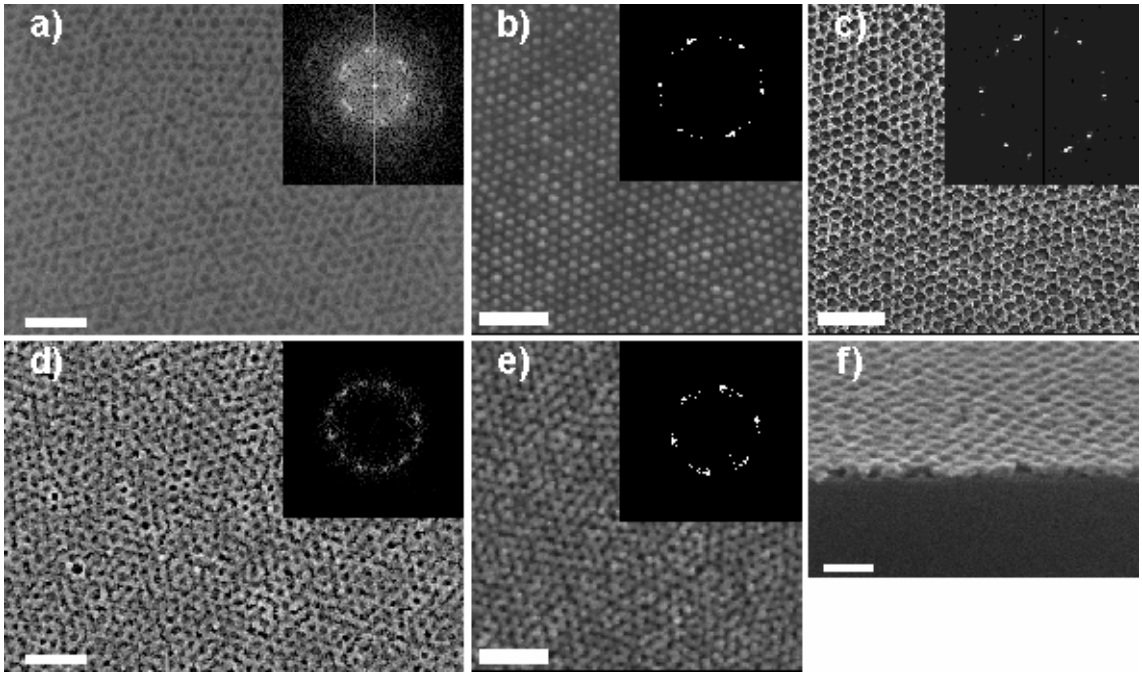

***Figure 32**: SEM and AFM images of the ordered mesoporous TiO_2 film before (**a**, **b**, **c**) and after (**d**, **e**, **f**) calcination at 400°C (Block copolymer concentration: 0.25wt. % PS-b-PEO in 1, 4-dioxane). SEM images: top view: **a**, **d**; side view: **f**. AFM images: height image: **b**, **e**; phase image: **c**; Height scale: 10nm; phase scale: 20°. Scale bar: **a**-**e**: 200nm; **f**: 80nm.*

The structures of the film with an increasing copolymer concentration of 0.5 wt. % is shown in **Figure 33**. Compared to the sample with the copolymer concentration of 0.25 wt. %, in the film with 0.50 wt. % copolymer, some nanovesicles are fused together and the order degree of the nanovesicle packing is decreased. In the FFT patterns, instead of six isolated dots, only a ring-like pattern is observed, indicating an isotropic orientation of the nanovesicles. The AFM and SEM image before calcination (**Figure 33a** and **33c**) correspond with each other quite well and fused nanovesicles are visible in both images. After calciantion, a mesoporous structure is formed and there are many larger pores formed in the film because of the fusion of nanovesicles (**Figure 33b** and **33d**). However, the ring-like FFT pattern of the SEM image after calcination indicates that the size distribution of the pores are narrow and the presence of a weak second order ring means that the structure is still highly ordered.

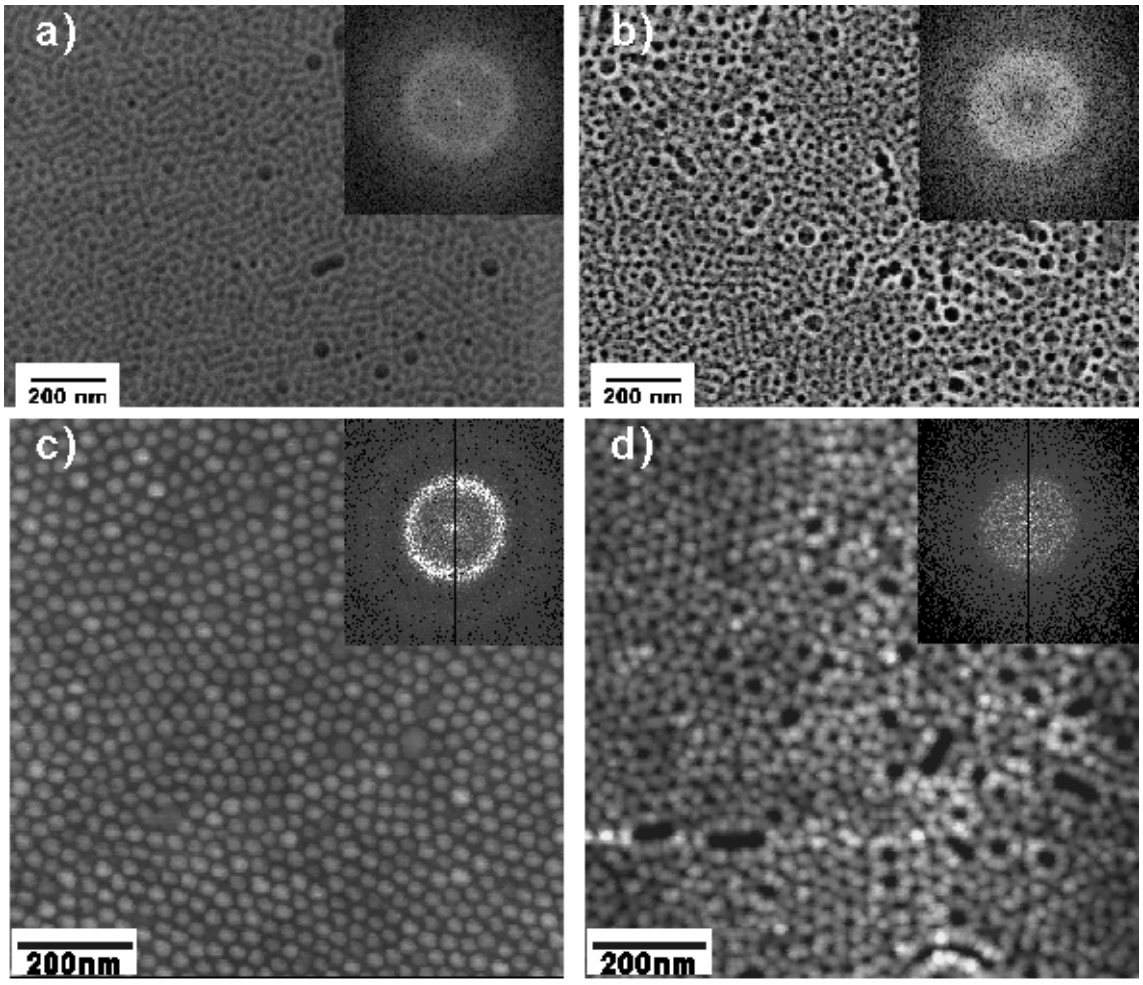

***Figure 33**: SEM and AFM height images of the ordered mesoporous TiO_2 film from 0.50 wt. % PS-b-PEO in 1, 4-dioxane. Before calcination: **a**, **c**; calcination at 400°C: **b**, **d**. SEM images: **a**, **b**; AFM height images: **c**, **d**; Height scale: 10nm.*

When the copolymer concentration is further increased to 1 wt. %, nanovesicle fusion is even more significant (before calcination: **Figure 34a and 34c**). As a result, the FFT pattern shows a rather broad ring-like FFT pattern, indicating the size distribution of the nanovesicles is very broad. After calcination, a mesoporous film with large pores is formed (**Figure 34b** and **34d**). The FFT pattern of the SEM image (**Figure 34b**) still exhibits a weak broad ring like pattern; however, the broad ring pattern for the corresponding AFM image is smeared out (**Figure 34d**).

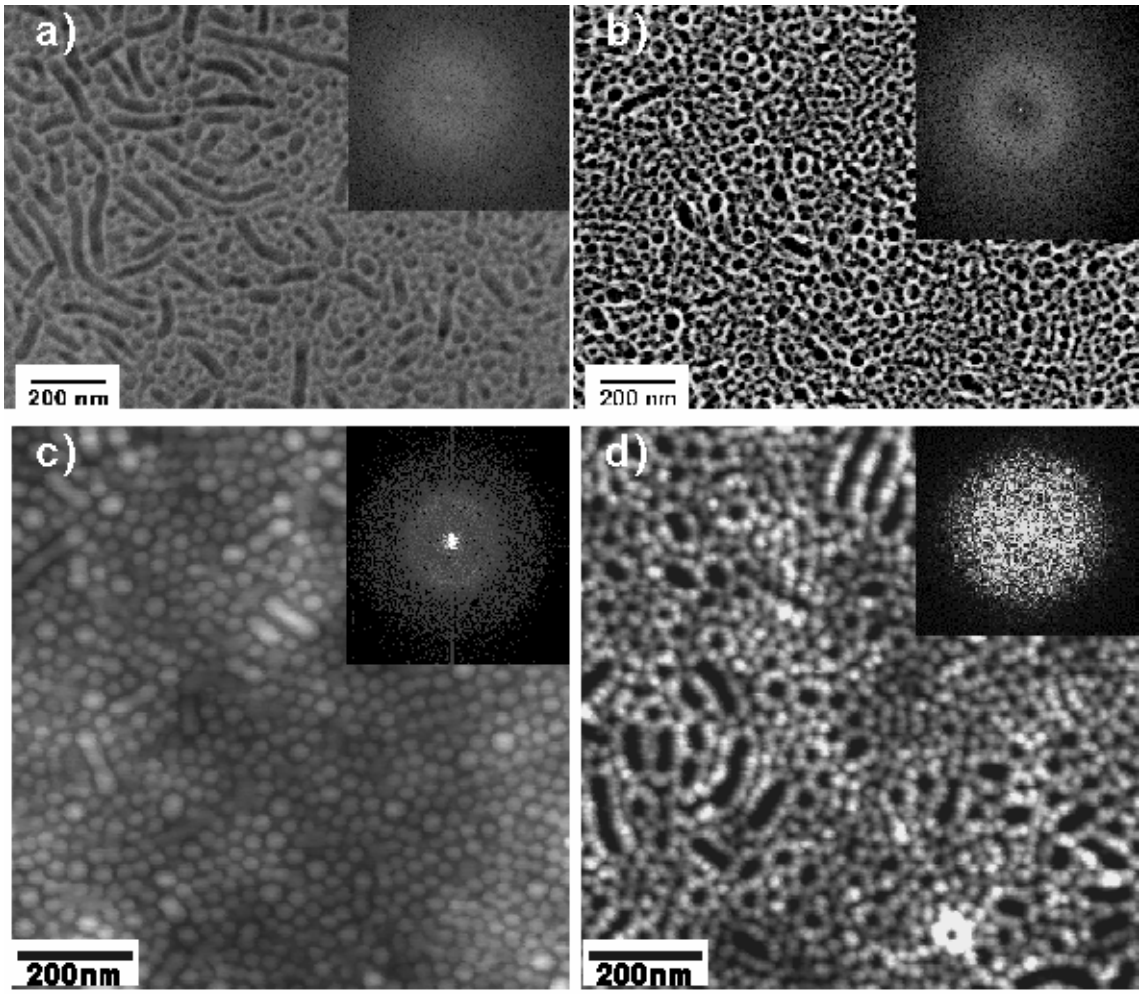

Figure 34. *SEM and AFM height images of the ordered mesoporous TiO_2 film from 1.0 wt. % PS-b-PEO in 1, 4-dioxane. Before calcination:* ***a, c****; calcination at 400°C:* ***b, d****. SEM images:* ***a, b****; AFM height images:* ***c, d****; Height scale: 10nm.*

When the copolymer concentration is increased to 2 wt. %, a clear-cut morphology transition from nanovesicles to lamellae is observed (**Figure 35a-35d**). The FFT pattern of the SEM image before calcination (**Figure 35a**) only shows a ring with very broad size distribution indicating the large size distribution and no orientation alignment of the lamellae. The AFM phase image (**Figure 35c**) also shows similar morphologies. After calcination, gaps are formed between TiO_2 lamellae (SEM: **Figure 35b**, AFM phase image: **Figure 35d**).

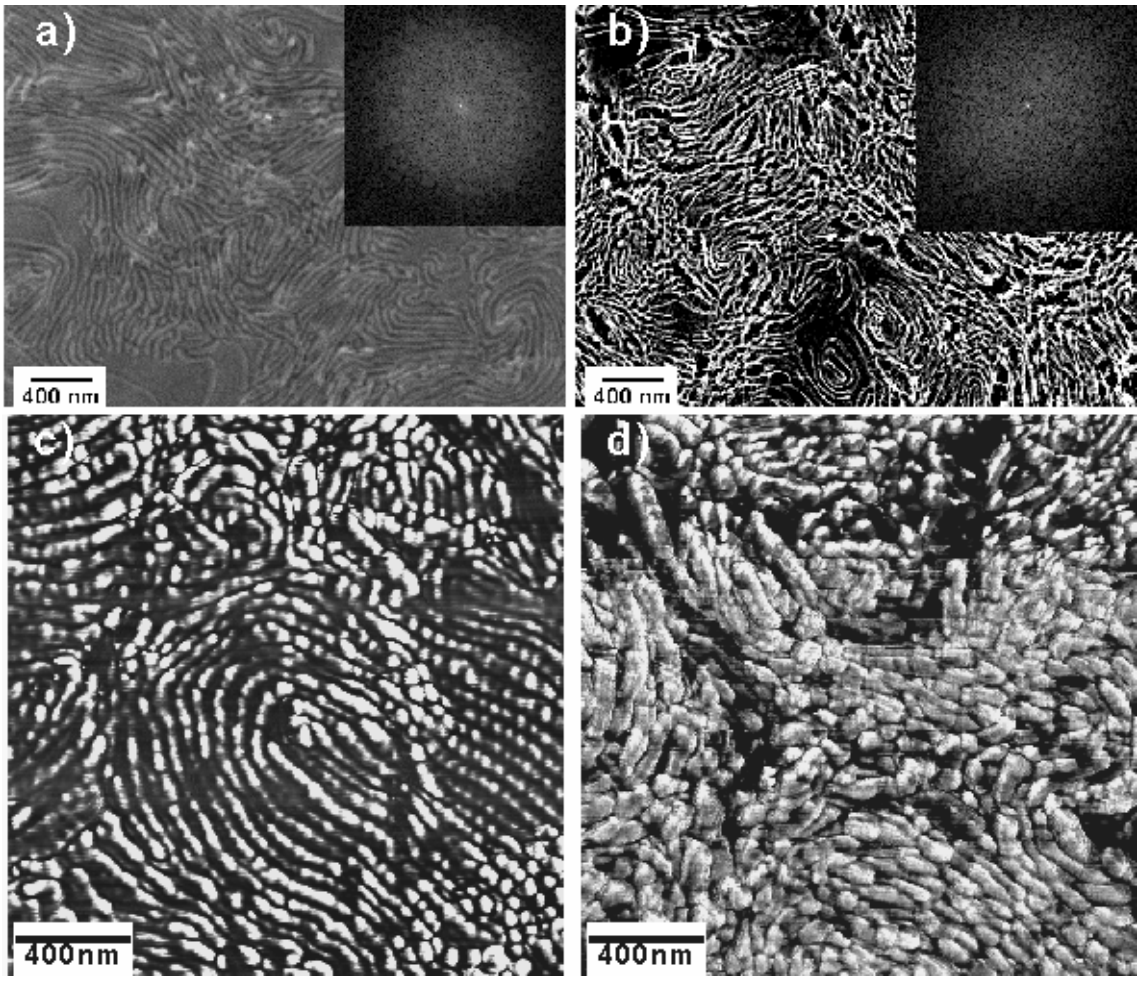

***Figure 35**: SEM and AFM phase images of the lamellae TiO_2 film with 2.0 wt. % PS-b-PEO in 1, 4-dioxane. Before calcination: **a, c**; calcination at 400°C: **b, d**. SEM images: **a, b**; AFM phase images: **c, d**; phase scales: 50°.*

When the copolymer concentration is further increased from 2 wt. % to 4 wt. %, the lamellae structure is even more obvious and ordered than the sample with 2 wt.% (before calcination: **Figure 36a**, **36c**; after calcination: **Figure 36b**, **36d**). The morphology evolution along with increasing copolymer concentration can be interpreted by analyzing the role of the block copolymer. With increasing copolymer concentration, the stretching degree of the PS block within the domain is strengthened, which is entropy unfavorable. In order to relax the stretching, the size of the nanovesicles is increased via a vesicle fusion process. [156, 274, 275] Stabilization of larger vesicles is due to a reduction of surface curvature and correspondingly reduced chain crowding. As a result of increasing block

copolymer concentration, the number and size (i.e. curvature radius) of nanovesicles is increased with increasing copolymer concentration from 0.25% to 1%. When the copolymer concentration is further increased to 2% and 4%, the curvature radius becomes so large that the nanovesicle morphology is not stable anymore and new lamellae morphology is formed. It should be pointed out that the lamellae phase is not observed in the morphology phase diagram with specific block copolymer concentration of 1%. Thus the variation of the block copolymer concentration expands the regime of available morphologies.

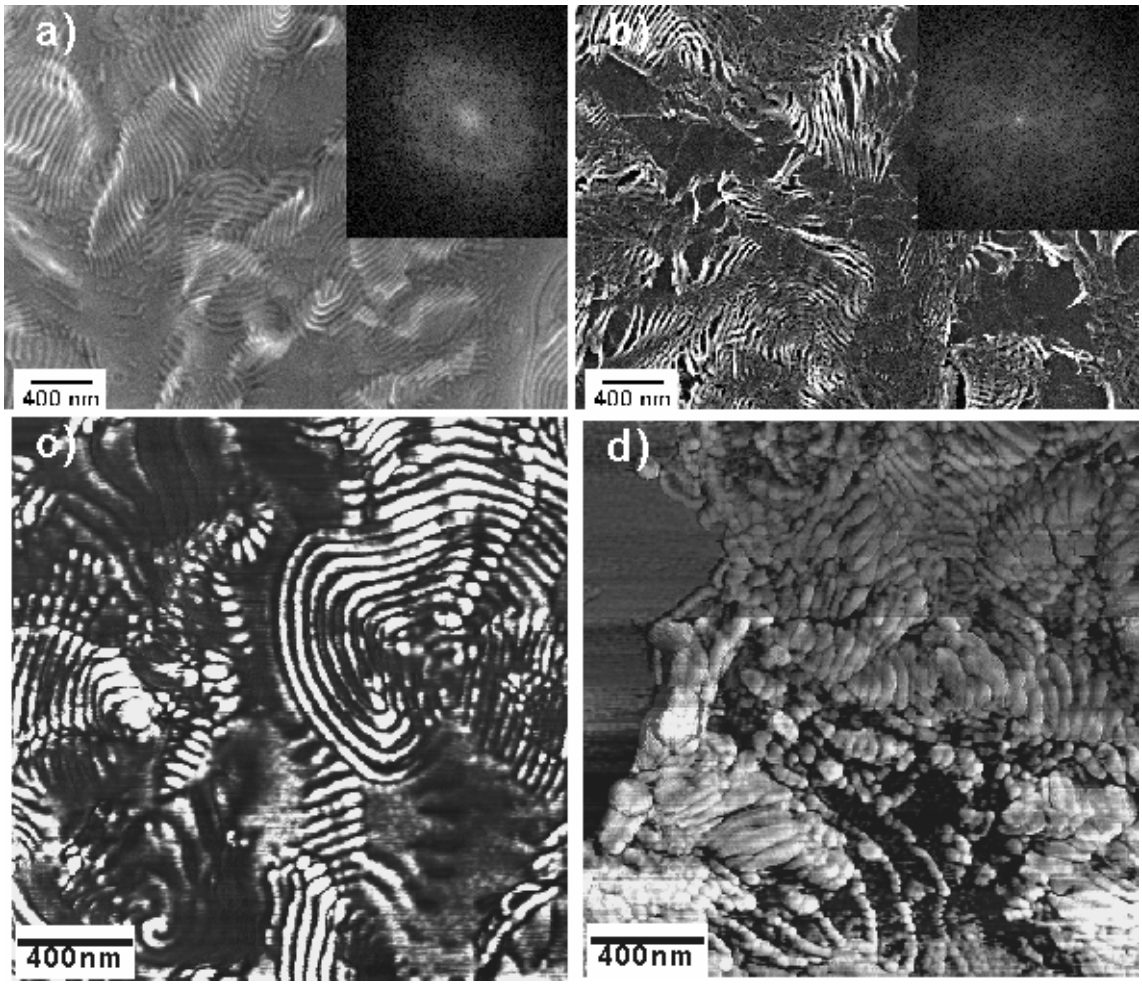

***Figure 36**: SEM and AFM phase images of the lamellae TiO_2 film with 4.0 wt. % PS-b-PEO in 1, 4-dioxane. Before calcination: **a**, **c**; calcination at 400°C: **b**, **d**. SEM images: **a**, **b**; AFM phase images: **c**, **d**; phase scales: **c**: 50°; **d**: 100°.*

4.2.4.2 Impact of Sol-gel Reaction Time on Morphologies

HCl plays an important role in the templating process, which guides the formation of titania nanostructures with a variety of morphologies. It acts not only as a catalyst for the hydrolysis of TTIP but also a retardant for the condensation. It is very important for a controlled nanostructure formation that the condensation step is retarded; otherwise the rapid and violent condensation will proceed beyond the templating boundary of the block copolymer to form unspecific large-scale structures. As a result the solution will be turbid because of the precipitation of Ti-O- species, where homogeneous films cannot be obtained via spin coating process.

The hydrolysis and condensation of TTIP is intrinsically a kinetic process and the structures will evolve along with time. Therefore it is important to study the influence of sol-gel reaction time on the morphology evolution. To elucidate the impact of reaction time in a systematic way, two series of solutions with different block copolymer concentrations of 0.25 wt. % and 1.0 wt. % are exploited. The stock solutions are the same as those addressed in the section of block copolymer concentration effect. The reaction time recorded ranges from ca. 0.5hr to 48hr. Morphologies of the films are investigated by AFM and SEM; as a complementary manner, the corresponding aggregate size evolution in solution is studied by dynamic light scattering (DLS).

With each specific sol-gel reaction time scale, structures of the as-prepared, calcined, and UV degraded films are studied by AFM and SEM respectively to make a good comparison about the morphology change. The integration of inorganic TiO_2 network and organic block copolymer in the as-prepared film weakens the electron density contrast in the SEM image, which makes the image not sharp enough to reveal probable tiny morphology evolution in the film. On the contrary, calcination treatment can remove the organic block copolymer to enhance the electron density contrast in the SEM image; however, the thermal drive force during calcination may cause severe agglomeration of the TiO_2 nanostructures, which actually already modify the morphologies of the films. Therefore, in a compromise way, UV degradation is conducted to remove partially the organic block copolymer to enhance the electron density contrast, while leaving the TiO_2 network in a relative intact way compared to calcination. [146] Results at three different reaction time scales ranging from *ca*. 0.5 hour to 25 hour are shown in the following and a complete time series results with a reaction time from 0.5 hour to 50 hour are presented in the appendix. In **Figure 37** it shows the AFM height images of the TiO_2-block copolymer composite films prepared from the stock solution with 0.25 wt. % PS-b-PEO. The sol-gel reaction time ranges from 40min to 48hr. The AFM images include the samples as-prepared (**a1**, **b1**,

c1), calcined at 400°C (**a2**, **b2**, **c2**) and UV degraded (**a3**, **b3**, and **c3**). The images indicate that until 3 hour sol-gel reaction, the structure of the nanovesicles in the film do not have a visible change. A complete study actually indicates that there is no structural change until 5 hour reaction (**Figure S-5** in appendix). However, after 25 hours reaction, there is a significant morphology change due to the nanovesicle fusion process, as proved in the AFM images.

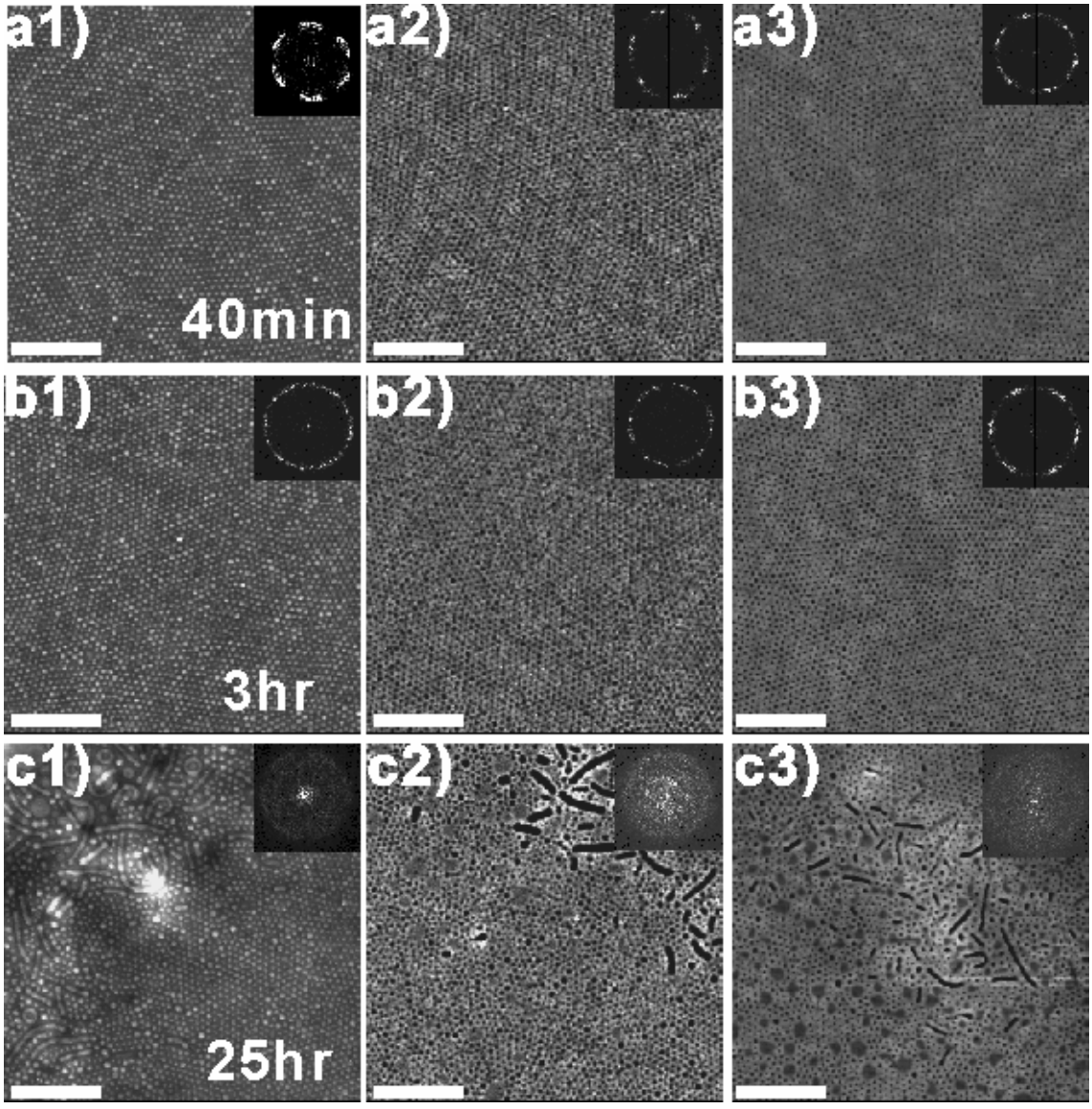

Figure 37*. AFM height images of the nanovesicles prepared with different sol-gel reaction time from a stock solution of 0.25 wt. % PS-b-PEO. As-prepared film:* ***a1****,* ***b1****, and* ***c1****; calcined at 400℃:* ***a2****,* ***b2****, and* ***c2****; UV degraded:* ***a3****,* ***b3****, and* ***c3****. Insets are corresponding FFT patterns of each image. Height scale: 10nm. Scale bar: 400nm.*

In a complementary way, **Figure 38** shows the corresponding SEM image of the as-prepared, calcined, and UV degraded films prepared with different sol-gel reaction time. The structures in the SEM images are in good agreement with the AFM images, where a significant morphology change happens after 25 hour reaction time (**Figure S-6** in appendix for the complete time scale).

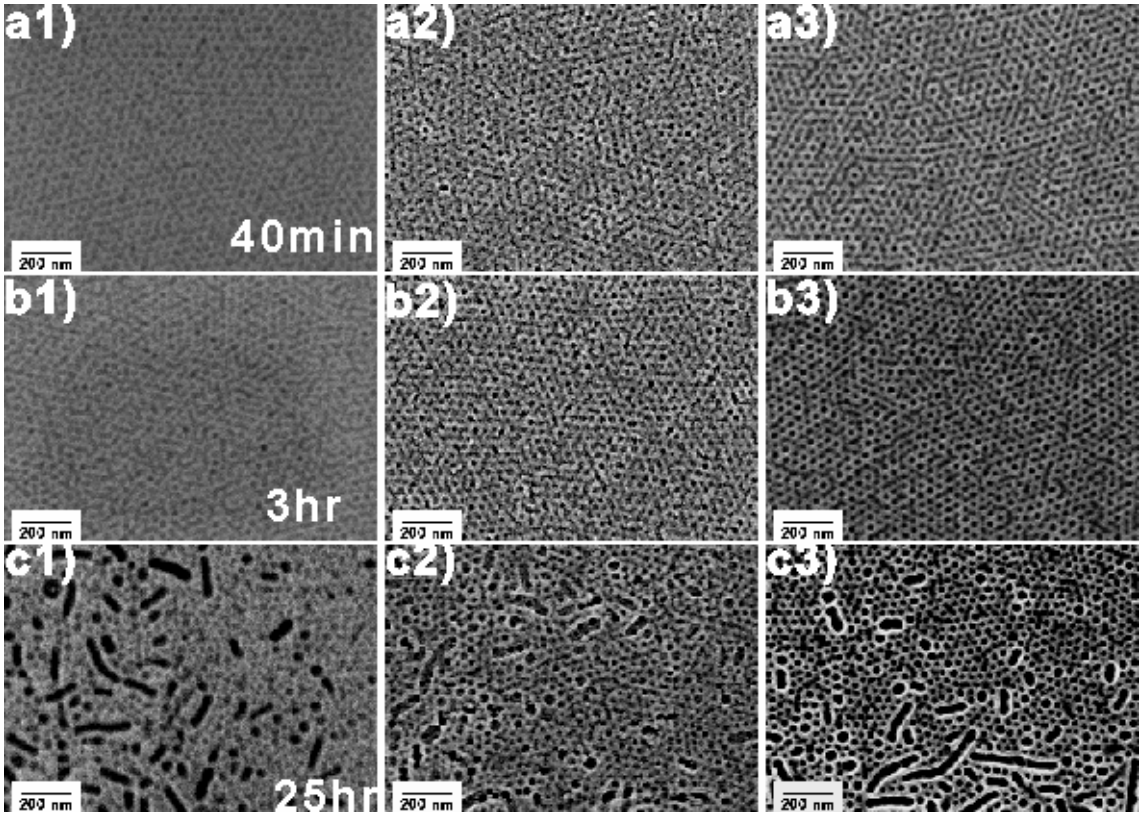

Figure 38. *SEM images of the nanovesicles prepared with different sol-gel reaction time from a stock solution of 0.25 wt. % PS-b-PEO. As-prepared film:* ***a1****,* ***b1****, and* ***c1****; calcined at 400 ℃:* ***a2****,* ***b2****, and* ***c2****; UV degraded:* ***a3****,* ***b3****, and* ***c3****.*

The aggregate size evolution in solution is investigated by dynamic light scattering experiments,a s shown in **Figure 39**. **Figure 39a** presents the correlation curve and **Figure 39b** is the corresponding size distribution profile. The results show that there is a clear size evolution after 25 hours (**Figure S-7** in appendix for the complete time scale).

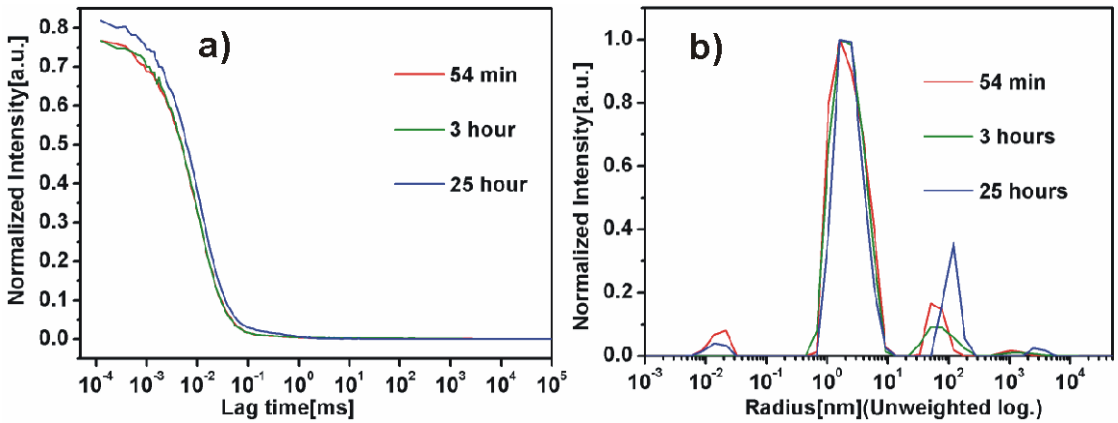

Figure 39. *Dynamic light scattering results of the aggregate size evolution with different sol-gel reaction time scales in the solution of 0.25 wt. % PS-b-PEO.* ***(a)****: correlation profile;* ***(b)****: corresponding size distribution profile.*

The morphology evolution of the films prepared from the solution with 1.0 wt. % is exhibited in the AFM height images in **Figure 40**. The time scale ranges from 51 min to 25 hours. A complete time range to 50 hours is exhibited in the appendix. To make a good comparison to reveal the structure evolution, as-prepared, calcined, and UV degraded films are studied. Similar to the system of 0.25 wt. % PS-b-PEO, until 3 hour reaction there is no clear morphology change. And after 25 hours, all of the as-prepared calcined, and UV degraded films present a significant structure evolution in the AFM images (**Figure S-8** in appendix for complete time scale AFM images).

Further SEM analysis in **Figure 41** confirms that within 3 hour sol-gel reaction, there is no clear morphology change. A further detailed study proves that actually the structure does not change until 5 hour reaction (**Figure S-9** in appendix). A significant morphology evolution is only observed after 25 hour reaction, which is in agreement with the AFM results.

Dynamic light scattering experiment reveals the corresponding size evolution in the solution in **Figure 42**. Within 3 hour reaction time the correlation curve and size distribution profiles are generally similar, indicating no size distribution evolution in the solution. However, after 25 hours, a big change in the DLS profiles is observed, which proves that the size evolution of the aggregates in the solution (**Figure S-10** in appendix for the DLS profiles in complete time scale).

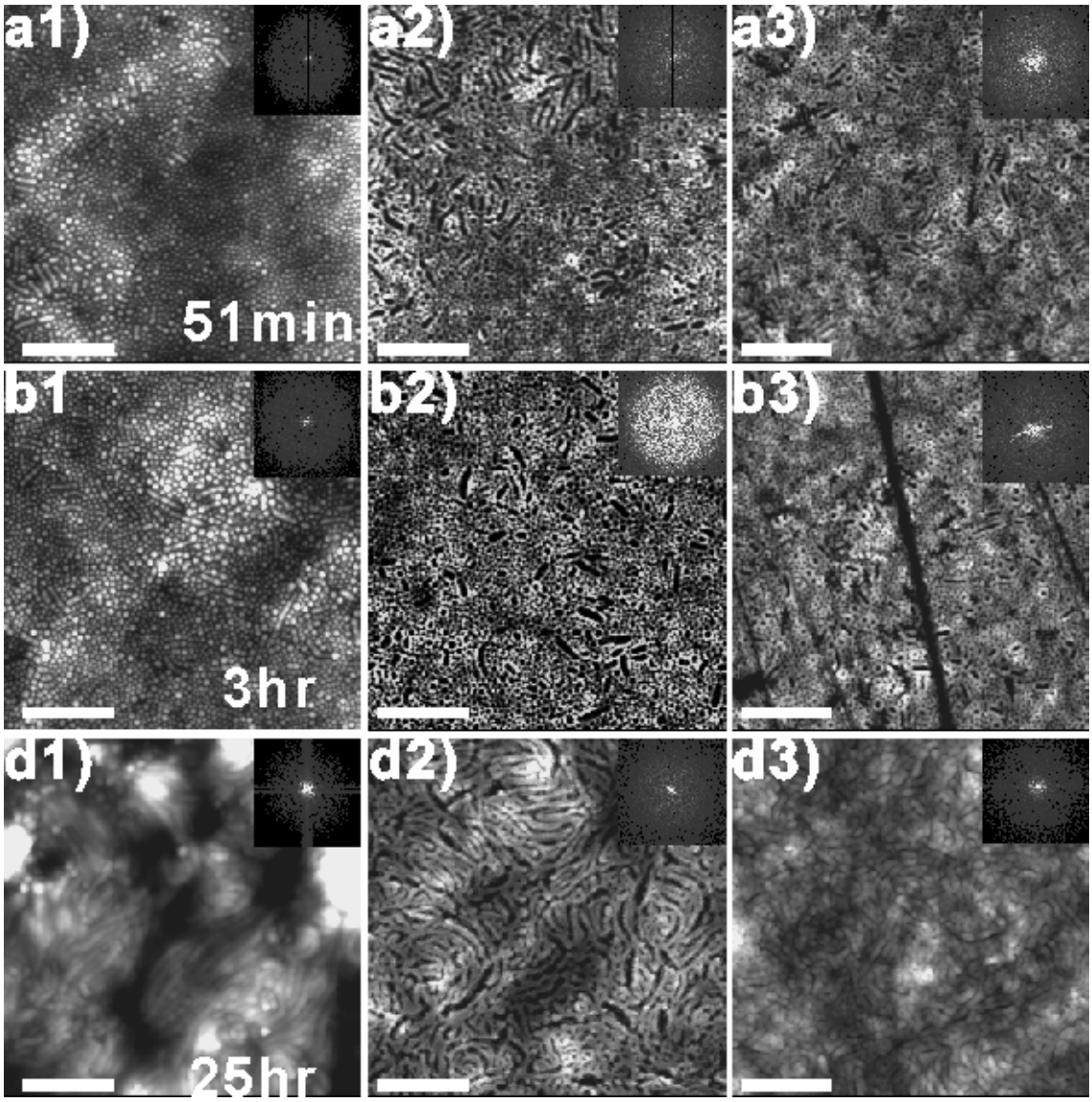

Figure 40. *AFM height images of the nanovesicles prepared with different sol-gel reaction time from a stock solution of 1.0 wt. % PS-b-PEO. As-prepared film:* ***a1***, ***b1***, *and* ***c1****; calcined at 400℃:* ***a2***, ***b2***, *and* ***c2****; UV degraded:* ***a3***, ***b3***, *and* ***c3***. *Insets are corresponding FFT patterns of each image. Height scale: 10nm. Scale bar: 400nm.*

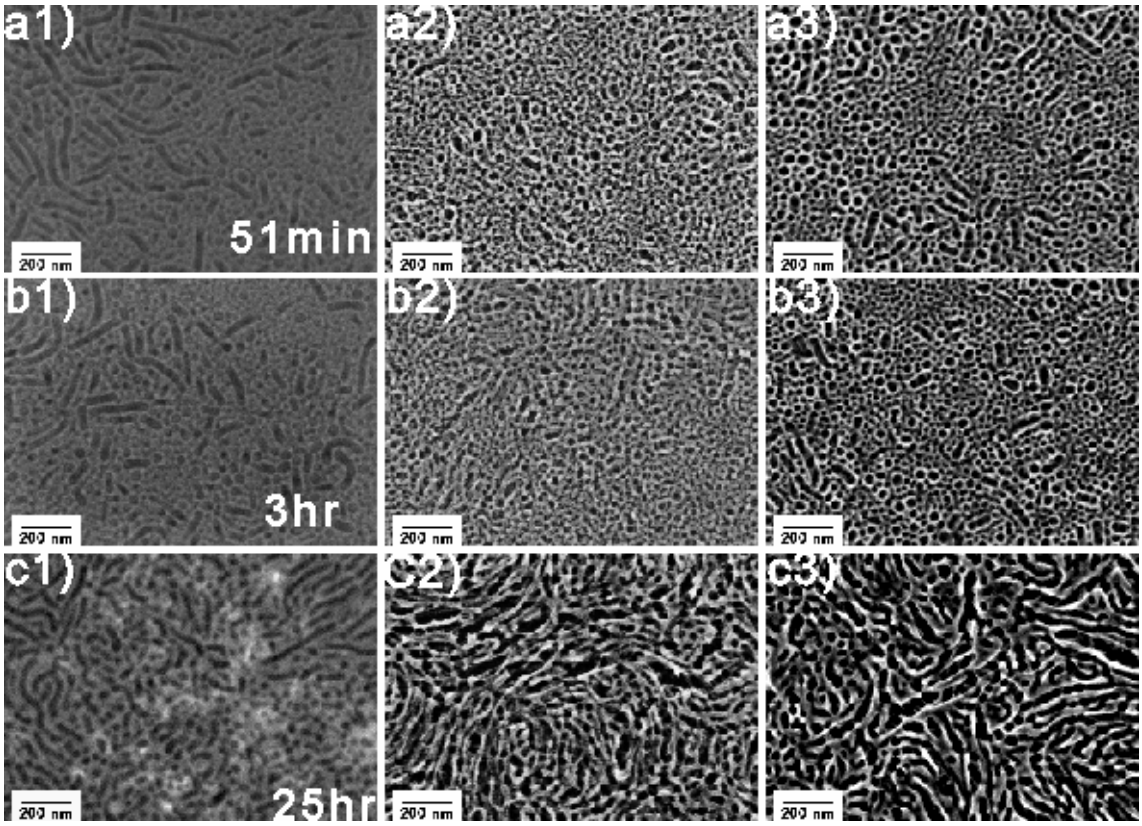

Figure 41. *SEM images of the nanovesicles prepared with different sol-gel reaction time from a stock solution of 1.0 wt. % PS-b-PEO. As-prepared film:* ***a1***, ***b1***, *and* ***c1****; calcined at 400℃:* ***a2***, ***b2***, *and* ***c2****; UV degraded:* ***a3***, ***b3***, *and* ***c3***.

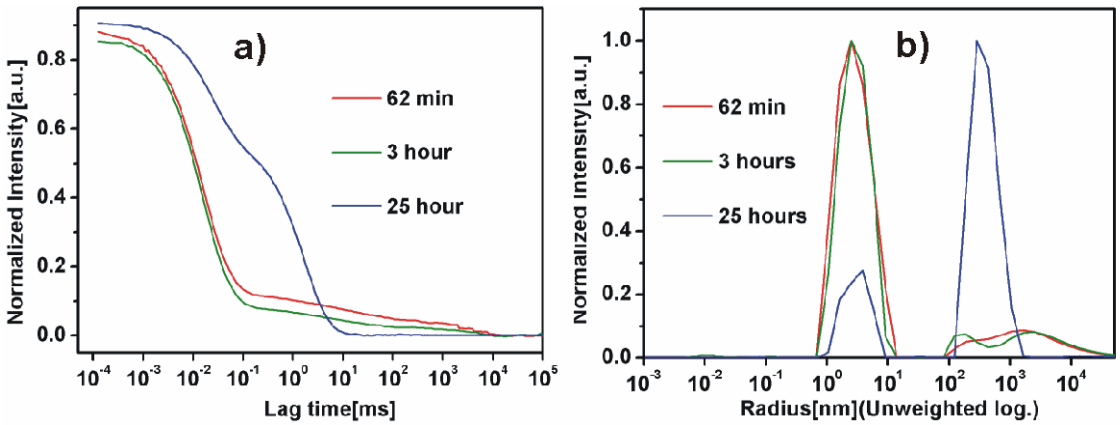

Figure 42. *Dynamic light scattering results of the aggregate size evolution with different sol-gel reaction time scales in the solution of 1.0 wt. % PS-b-PEO. (****a****): correlation profile; (****b****): corresponding size distribution profile.*

4.2.4.3 Impact of humidity on morphologies

It has been reported that the external humidity plays an important role on the morphology of the composite films. [108, 117, 129, 131, 273, 276-279] The samples are generally prepared in a climatized lab with a typical relative humidity of 35-45% and temperature of 21°C. In order to study the humidity effects in details, the same stock sample solutions are spin coated in ambient condition (relative humidity 41-42%) and glove box respectively (absolute humidity 0.0ppm) (lid is open during spin coating). **Figure 43** shows the corresponding morphologies of two sample series.

From the SEM images it can be seen that the morphologies are different for samples prepared under different humidity conditions. The films prepared under ambient conditions show nanowire structures of large size and there are also a small number of vesicle structures coexisting in the film (**Figure 43a1-u**, film thickness: 66nm). There is no FFT ring pattern indicating a broad size distribution of the structures. However, the sample spin coated in the glove box is composed of smalll nanowire structures and the nanowire structures are packed densely (**Figure 43a2-u**, film thickness: 71nm). The clear ring like FFT pattern (corresponding feature size: 24nm) indicates that the spacing between nanowires is uniform. Generally, after calcination both films exhibit nanowire morphologies (**Figure 43a1-c** and **43a2-c**). However, the film prepared in air shows a mesoscale open framework composed of nanowires and junction points. The weak FFT ring pattern corresponds to a size of 54nm.

The sample prepared in the glove box shows a finer nanowire network. Compared to **Figure 43a1-c**, there is a clear ring like FFT pattern, which corresponds to a spacing of 24nm between nanowires. For the **b** sample series, the size of the nanowire structures in the film prepared in glove box is again smaller than that prepared in air (**Figure 43b2-u**, film thickness, 71nm and Figure 14b1-u, film thickness, 69nm). Both SEM images show ring like FFT patterns with feature sizes of 39 and 24nm respectively. Therefore the nanowires in **Figure 43b2-u** are packed more densly than that in **Figure 43b1-u**. After calcination, the mesoscale network of the sample prepared in air is more porous than the one prepared in the glove box, which is in agreement with the structures before calcination (**Figure 43b1-c** and **43b2-c**). There are still ring-like FFT patterns in both images and the feature sizes are 44 and 26nm respectively.By comparing the morphologies of the two sample series spin coated in air and glove box, it can be concluded that the external humidity influences the size scales of the structures present after spin coating. The external humidity in air may enhance the hydrolysis and condensation process during spin coating and as a result, the structures formed after spin coating have a large size scale and are loosely packed. It seems that the external humidity influences sample **a1** stronger than

sample **b1**. The reason for this phenomenon can be rationalized by analyzing the role of HCl solution. The weight ratio of HCl solution in sample **a1** is higher than that in sample **b1**, which means there is more water in sample **a** than in sample **b**. As a result, the solution is dried more slowly and therefore the time available for internal condensation and coagulation is longer for sample **a** than for sample **b**.

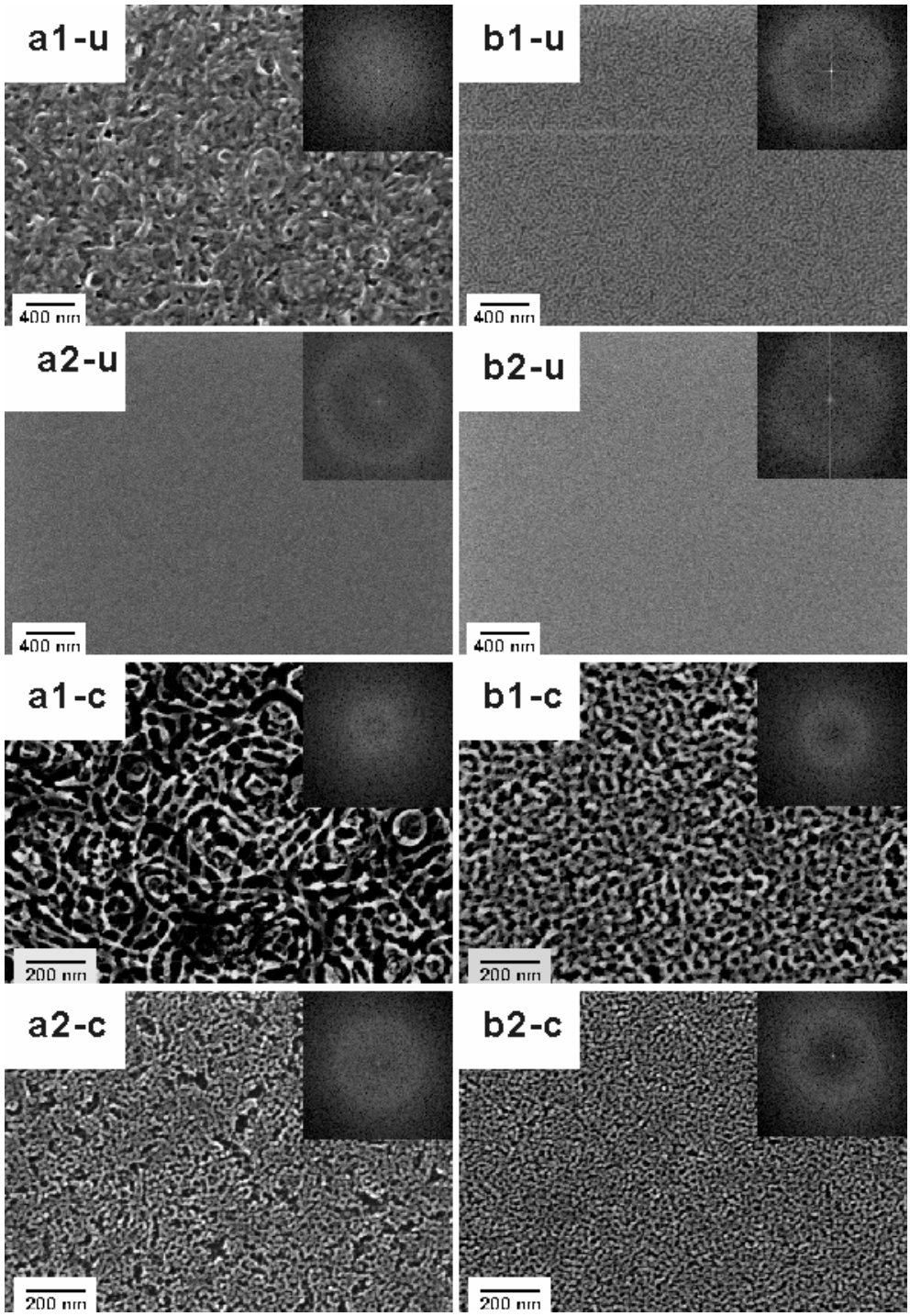

***Figure 43**. SEM images of samples prepared under different humidity conditions (**a1-u**, **b1-u**, spin coated under ambient conditions with a relative humidity of 41%-42% and temperature of 21.3℃; **a2-u**, **b2-u**, spin coated in glove box with an absolute humidity of 0.0ppm and temperature of 22.0℃; **a**, **b** series samples were spin coated from the same stock solution respectively; **a1-c** and **b1-c** are corresponding SEM images of samples **a1-u** and **b1-u** after calcination respectively; **a2-c** and **b2-c** are the corresponding SEM images of samples **a2-u** and **b2-u** after calcination respectively; calcination conditions: ramp rate, 6.25℃/min from 25 to 400℃, 400℃ for 4 hours; Composition ratios: **a** series:W_{TTIP}: 0.011; $W_{1,4\text{-}dioxane}$: 0.972; W_{HCl}:0.016; **b** series: W_{TTIP}: 0.025; $W_{1,4\text{-}dioxane}$: 0.971; W_{HCl}:0.004. The insets are FFT profiles of the corresponding structures. The accelerating voltage of SEM measurement is 3kv for the samples after calcination.*

4.2.4.4 Calcination Temperature Effects

It has been reported that the mesostructures may undergo structure rearrangement up to complete collapse when calcined at elevated temperatures higher than 450°C. [116, 117, 273, 277, 279] In order to check the stability of the structures the calcination experiments were conducted at different temperatures ranging from 400 to 600°C. In **Figure 44** it shows the morphology evolution of two sample series with increasing calcination temperature.

For sample series **a**, it can be observed that all the films after calcination show nanowire structures. The morphologies in the samples calcined at 400°C show similarities with those of as-prepared films (**Figure 44a2** and **44a1**). The feature size from FF is 54nm. Compared to the sample calcined at 400°C, there is almost no structural rearrangement in the films calcined at 500°C (**Figure 44a3**). And the spacing size between nanowires derived from FFT is 57nm, which is in agreement with the value of sample calcined at 400°C. However, for the films calcined at 600°C, the porous mesoscale network collapses into agglomerated nanowire structures (**Figure 44a4**) (FFT feature size: 55nm).

For sample series **b**, the structures of films calcined at 400°C are again in good aggrement with the sample before calcination (**Figure 44b2** and **44b1**) (FFT feature size: 39nm for sample **b2** and 44nm for sample **b1**). There is also no significant difference between the films calcined at 400 and 500°C (**Figure 44b3**) (size from FFT: 47nm). For the films calcined at 600°C (**Figure 44b4**), the connectivity between nanowires is severely destroyed and isolated nanowire aggregates are formed (size from FFT: 47nm).

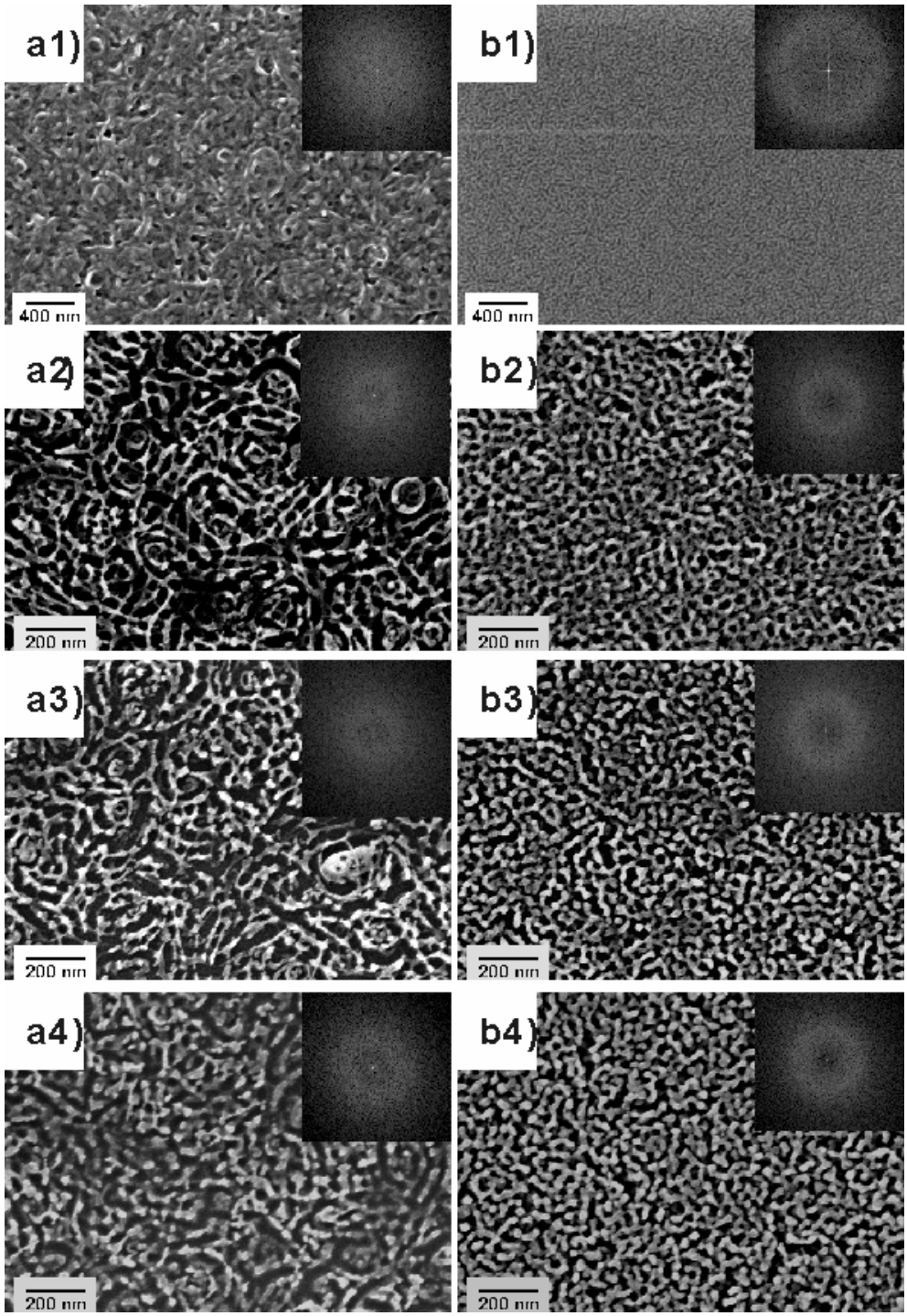

***Figure 44**. SEM images of films calcined at different temperatures. **a1**, **b1** as-prepared; **a2**, **b2**, calcined at 400℃; **a3**, **b3**, calcined at 500℃; **a4**, **b4**, calcined at 600℃. Ramp rate: 6.25℃ per minute starting from 25°C; calcination time: 4 hours. Composition ratios: **a** series:W_{TTIP}: 0.011; $W_{1,4\text{-dioxane}}$: 0.972; W_{HCl}: 0.016; **b** series: W_{TTIP}: 0.025; $W_{1,4\text{-dioxane}}$: 0.971; W_{HCl}:0.004. The insets are FFT profiles*

of the corresponding structures. The accelerating voltage of SEM measurement is 3kv for the samples after calcination.

From the comparison of the morphologies of two sample series calcined at different temperatures, it can be concluded that the films calcined at 400°C exhibit morphologies similar to the samples before calcination. Calcination at 500°C only induces slight nanostructure rearrangement. However, there is a severe structure rearrangement upon calcination at 600°C, where mesoscale networks collapse into isolated nanowire agglomerates.

Compared to the reported results, where mesostructures were destroyed at comparable temperatures, our samples remain almost intact at temperatures up to temperatures as high as 500°C. The relative high stability is probably because our films are ultrathin. On one hand, the absolute thermal induced contraction normal to the substrate in ultrathin film is smaller compared to thicker films. On the other hand, the substrate surface mechanically fixes the titania structures at the interface; however, in the thick films prepared by dip-coating, only the structures close to the substrate surface would remain fixed, while structures further away from the interface suffer reorganization due to anisotropic stresses during calcination.

4.3. PMMA-b-PEO Templating System

4.3.1 Overview

In the previous section a concept using an amphiphilic block copolymer of PS-b-PEO as a templating agent, coupled with a good-poor solvent pair induced phase separation process has been developed to control the morphology of TiO_2-block copolymer composite films. However, the general validity of this concept to other amphiphilic system needs to be further proved. Therefore a new amphiphilic block copolymer of PMMA-b-PEO is synthesized and applied as a templating agent to control the morphologies of the titania-block copolymer composite films based on the same concept. To simplify the strategy, several specific points in the ternary phase diagram were chosen to have a general picture about the templating effect of PMMA-b-PEO as shown in **Figure 45**.

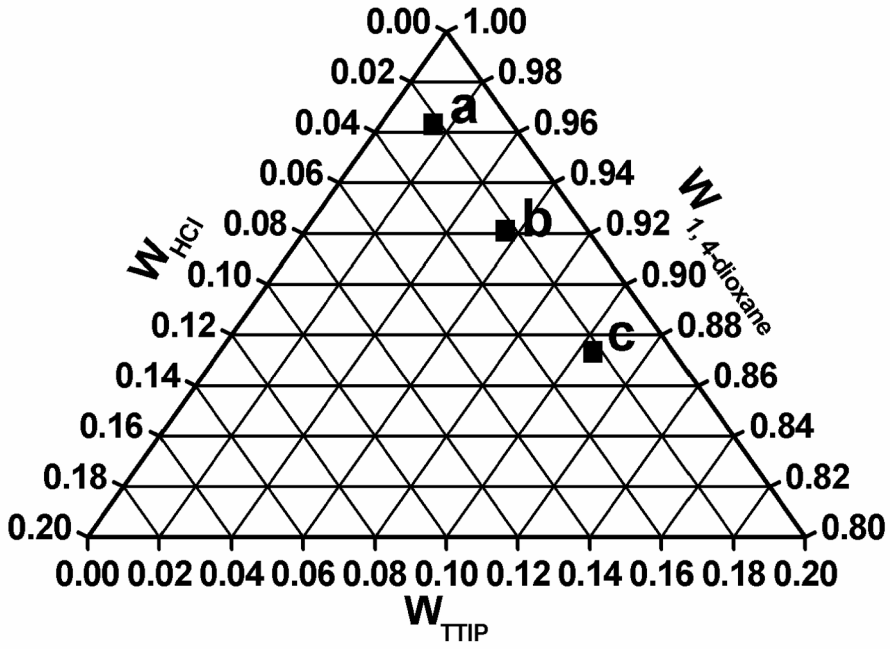

***Figure 45**. Three specific weight ratio combinations applied to prove the templating effects of PMMA-b-PEO*

4.3.2 Nanovesicles

The structures of the as-prepared "**a**" film are shown in **Figure 45** (weight ratios: $W_{1,\ 4\text{-dioxane}}$: 0.963; W_{HCl}: 0.022; W_{TTIP}: 0.015). The AFM height image (**Figure 45a**), suggests a seemingly mesoporous structure on the free film surface. However, instead of "holes" the structure is composed of vesicles, which is confirmed by a closer inspection of the phase image (**Figure 45b**). In the phase image, the bright dots have comparable hardness to the background, which is the soft continuous PMMA phase. Around the bright dots are dark regions, which are assumed to be a harder Ti-O-PEO phase. It can therefore be deduced that the structures are vesicles composed of hard Ti-O-PEO walls and soft PMMA interior pocket regions, as sketched in **Figure 45c**. In the height image, the average overall size of the vesicles is about 50nm and the average center-to-center distance indicated by the power spectral density (PSD) peak is 76nm, which is in agreement with the value (76nm) obtained from the phase image (bottom right insets in **Figure 45a** and **45b** respectively). However, there are multiple peaks present in the PSD profile of the phase image. The presence of an additional peak with an index value of 38nm is ascribed to the nature of vesicle structures. The vesicle structure is confirmed by the SEM top view image (**Figure 45d**). The inner ring of the SEMs FFT pattern corresponds to the center-to-center distance of the nanovesicles (81nm). The second ring corresponds to a structural size of 41nm. Since no other structural features of this length scale are visible in the SEM and AFM images, the second ring is interpreted as a higher order if the 81nm signal, indicating a higher degree of lateral order between the nanovesicles. The SEM side view image (**Figure 45e**) shows that the vesicle structure is a monolayer film on the Si substrate.

After calcination the as-prepared amorphous TiO_2 nanovesicles are converted to anatase phase (**Figure S-11** in appendix**)**. In **Figure 46a** the height difference between the vesicle wall and interior region is visible and in **Figure 46b** there is a clear mechanical property contrast between the interior and wall region. The TiO_2 wall has a similar hardness to the substrate and in contrast, the interior region is much soft. The average overall size of the vesicles is 47nm, which is slightly smaller than the size before calcination. Both height and phase images have double-ring FFT patterns. The double PSD peak in **Figure 46a** corresponds to 72nm and 36nm and in **Figure 46b** 70 and 35nm respectively. It's noteworthy that the bearing, correlation and depth profiles are all bimodal, which further proves the existence of a vesicle structures (**Figure S-12** in appendix). The SEM top view image (**Figure 46d**) shows the vesicle structure in agreement with the AFM image. Again as in the case of the unannealed films the double-ring FFT pattern corresponds to the center-to center distance (75 nm), and second

higher order (30nm). The SEM side view image (**Figure 46e**) further confirms a monolayer of TiO_2 vesicles on top of a thin titania layer, in agreement with the AFM phase image. Further proof of the thin layer is obtained from the x-ray reflectivity experiments.

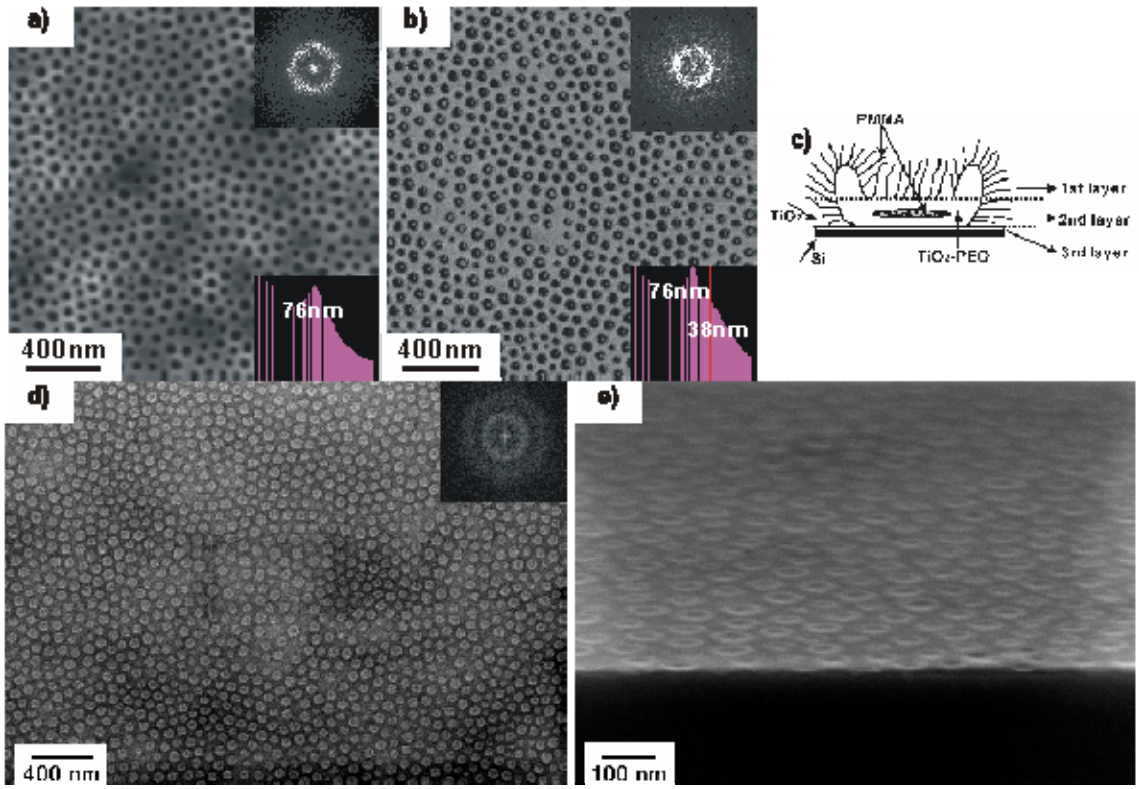

***Figure 45**: AFM and SEM images of the titania-block copolymer composite film before calcination. **a**: AFM height image, height scale: 20nm; **b**: AFM phase image, phase scale: 20°; **c**: side-view sketch of the nanovesicle strcuture; **d**: SEM image top view; **e**: SEM image side view. The upper right inset is a FFT pattern of each image (AFM image: FFT over the whole image; SEM image: 512×512 pixels, 1838nm×1838nm); the lower right inset is a power spectral density profile of each AFM image over 2μm×2μm. The double-ring FFT pattern of the SEM image corresponds to 81 (inner ring) and 41nm (outer ring) respectively.*

The x-ray reflectivity measurement enables it possible to study the structure gradient throughout the film in the direction normal to the substrate surface. [210, 214] **Figure 47** shows the x-ray reflectivity profile of the film before (**Figure 47a**) and after (**Figure 47b**) calcination. **Figure 47a** indicates a

multiple layer structure with a total thickness of *ca*. 26nm. The topmost layer (15.5nm thickness) has a low scattering length density and it is supposed to be composed of air, PMMA corona, and part TiO_2-PEO core (as indicated in the sketch **Figure 45c**). Compared to the first layer, the second layer indicated in figure 1c consists of PMMA corona, more PEO-titania components and the vesicle pocket region composed of PMMA (thickness: 10.8nm), leading to a higher scattering length density. The bottom thin layer (0.6nm) is composed of titania with a scattering length density even higher than that of the bulk Silicon substrate. Furthermore, the assignment of the titania thin layer in the model is also in agreement with the AFM and SEM results. The formation of the thin titania layer is likely due to a preferential wetting of the silicon oxide surface by the sol-gel solution and a subsequent reaction between the titania precursor and water molecules attached to the SiO_x surface.

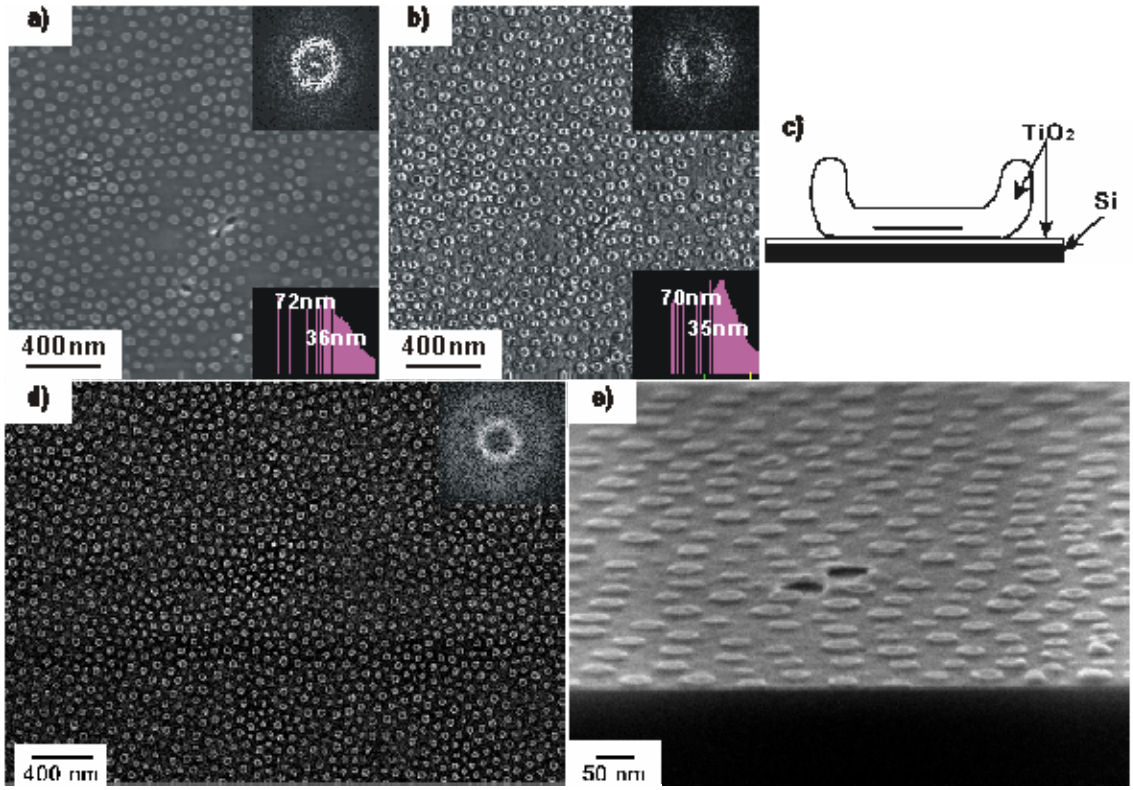

Figure 46: *AFM and SEM images of the film after calcination.* ***a****: AFM height image, height scale: 20nm;* ***b****: AFM phase image, phase scale: 20°;* ***c****: side view sketch of the nanovesicles;* ***d****: SEM image top view;* ***e****: SEM image side view. The upper right inset is a FFT pattern of each image (AFM image: FFT over the whole image; SEM image: 512×512 pixels, 1838nm×1838nm); the lower right inset is a power spectral density profile of each AFM image over 2μm×2μm.*

The x-ray reflectivity profile of the film after calcination does not show similar oscillation patterns compared to the profile before calcination because the roughness of the surface is high (1.9nm σ_{RMS} from AFM analysis and 1.6nm σ_{RMS} from the model of x-ray reflectivity).

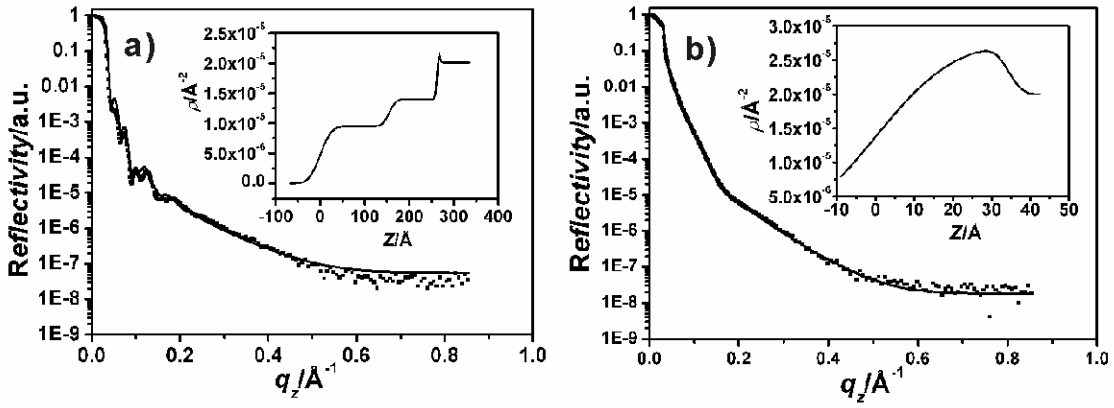

Figure 47. *X-ray reflectivity profiles and corresponding fitting curves of the films before (**a**) and after (**b**) calcination.*

As a complementary method to x-ray reflectivity, GISAXS is conducted to study the lateral structure of the TiO_2 film parallel to the substrate. [148, 149] **Figure 48** shows the 2D scattering images and corresponding out-of-plane (OOP) cuts along the Yoneda peak position of TiO_2 (parallel to q_y). The peaks in the OOP profile refer to the characteristic lateral dimensions of the TiO_2 nanovesicles over large length scale. The first-order maximum of the as-prepared sample is located at 73nm, which is in agreement with the inter particle distance obtained from the imaging analysis. The second peak indicating a structure of 18nm size is attributed to the diameter of the depressed region of the nanovesicles and the third peak indicating 4nm structures 4nm is probably due to domains of PEO inside the titania wall. The profile of the calcined film is very similar. It shows a first-order maximum at 72nm，consistent with the imaging analysis results，indicating that the nanovesicles remained fixed on the surface during calcination. The second peak indicating 25nm structures again corresponds to the depressed region of the calcined nanovesicles. Compared to the uncalcined vesicles, the size of the depression was enlarged, since the PMMA corona was burned away. The 4nm structural peak present in the uncalcined sample however has vanished during calcination, indication a fusion of the nanopores inside the titania wall upon thermal treatment.

The formation of the vesicles can be understood as following: The block copolymer is fully dissolved in pure 1, 4-dioxane at the used concentration of 1 wt. % since 1, 4-dioxane is a good solvent for both PMMA and PEO blocks. The addition of concentrated HCl solution increases the surface energy between the PMMA block and the solvent because it is a poor solvent for PMMA. In order to minimize the surface energy, the block copolymer self-assembles into a vesicle structure with a core of PEO and a corona of PMMA HCl solution and TTIP are incorporated into the hydrophilic PEO cores, where TTIP is hydrolyzed and condensed into Ti-O- nanostructures. With the composition ratio applied in this paper (weight ratios: $W_{1,\ 4\text{-dioxane}}$: 0.963; W_{HCl}: 0.022; W_{TTIP}: 0.015), the resulting morphology is a vesicle structure. The structure is similar to that templated by PS-b-PEO. Especially, the vesicle morphology can be further tuned by changing the relative ratios among 1, 4-dioxane, con. HCl, and TTIP as shown in the following **b** and **c** samples in the ternary phase diagram. During spin coating, there is a solvent evaporation induced particle rearrangement process and as a result the vesicles in the solution are transformed into an ordered pattern on the substrate.

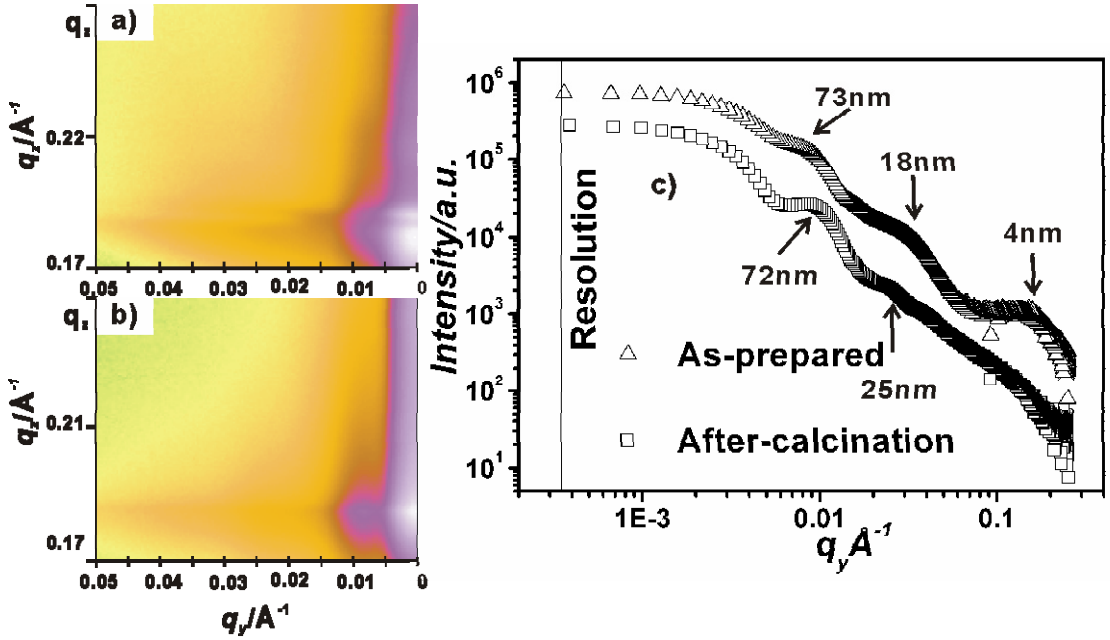

***Figure 48**. GISAXS 2D images and corresponding out of plane (OOP) scan profiles of the films before (**a**) and after calcination (**b**). Beam line: A2.*

4.3.3 Nanoplatelets

The SEM and AFM images in **Figure 49** show the structures of the film "**c**" in the ternary phase diagram ($W_{1,\ 4\text{-dioxane}}$: 0.873, W_{HCl}: 0.022 and W_{TTIP}: 0.105). The low magnification SEM images indicate that the film covers the Si substrate homonegenously (**Figure 50**). The morphology obtained is called nanoplatelet. The SEM image **Figure 49a** shows that the nanoplatelets composed of different polygons are closely packed together. The polygon pattern resembles the typical six corner voronoi pattern found for energy minimization pattern in 2D. It thus indicates that the block copolymer indeed acts both as a templating agent and as a surfactant, which minimizes the surface energy of the individual titania diomains. After calcination, the shape of nanoplatelets are still retained, however, gaps are formed among neighboring nanoplatelets because of the removal of the polymer template. This prooves that before calcination a continuous PMMA matrix exists within the film. The FFT patterns of the images show broad ring-like patterns with several weak but visible radial patterns. The presence of the radial patterns could probably be ascribed to the intrinsic polygon nature of the nanoplatelets. The AFM images (**Figure 49c** and **49d**) correspond to the SEM images and thus enhance the perevious structural analysis with an additional height information. The image before calcination (**Figure 49c**) shows that the the periphery region of the nanoplatelets is higher (*ca.* 13nm) than the centeral region. In the AFM image after calcination (**Figure 49d**), the difference between the periphery and central region is significantly reduced. This phenomenon can be explained by the formation mechanism of the nanoplatelets and will be discussed later on.

Figure 51 shows the SEM side view images of the nanoplatelets before (**a**) and after calcination (**b**). From the side view iamges it can be concluded that the film is composed of multilayer nanoplatelet structures. Besides, from **Figure 51a** it can be seen that the centeral region of the nanoplatelet is deeper compared to the periphery part, which is in agreement with the AFM image.

Since AFM and SEM are intrincally local characterizaiton methods, in order to obtain the structure information over large length scales, Grazing incidence small angle x-ray scattering (GISAXS) experiment is conducted to study the lateral structure parallel to the substrate (**Figure 52**). Before calcination the GISAXS profile only shows a weak structure correlation peak, resembling a shoulder rather than a peak. At first glance this may be surprising since the SEM and AFM images indicate a highly ordered patern. In contrast, the GISAXS profile after calcination shows a peak corresponding to a center-to-center disatance of 308nm. It is worth noting that the film after calcination is less ordered

than before calcination, so the lack of peak in the profile before calcination is probably due to a very low low electron density contrast and not due to a lack of order.

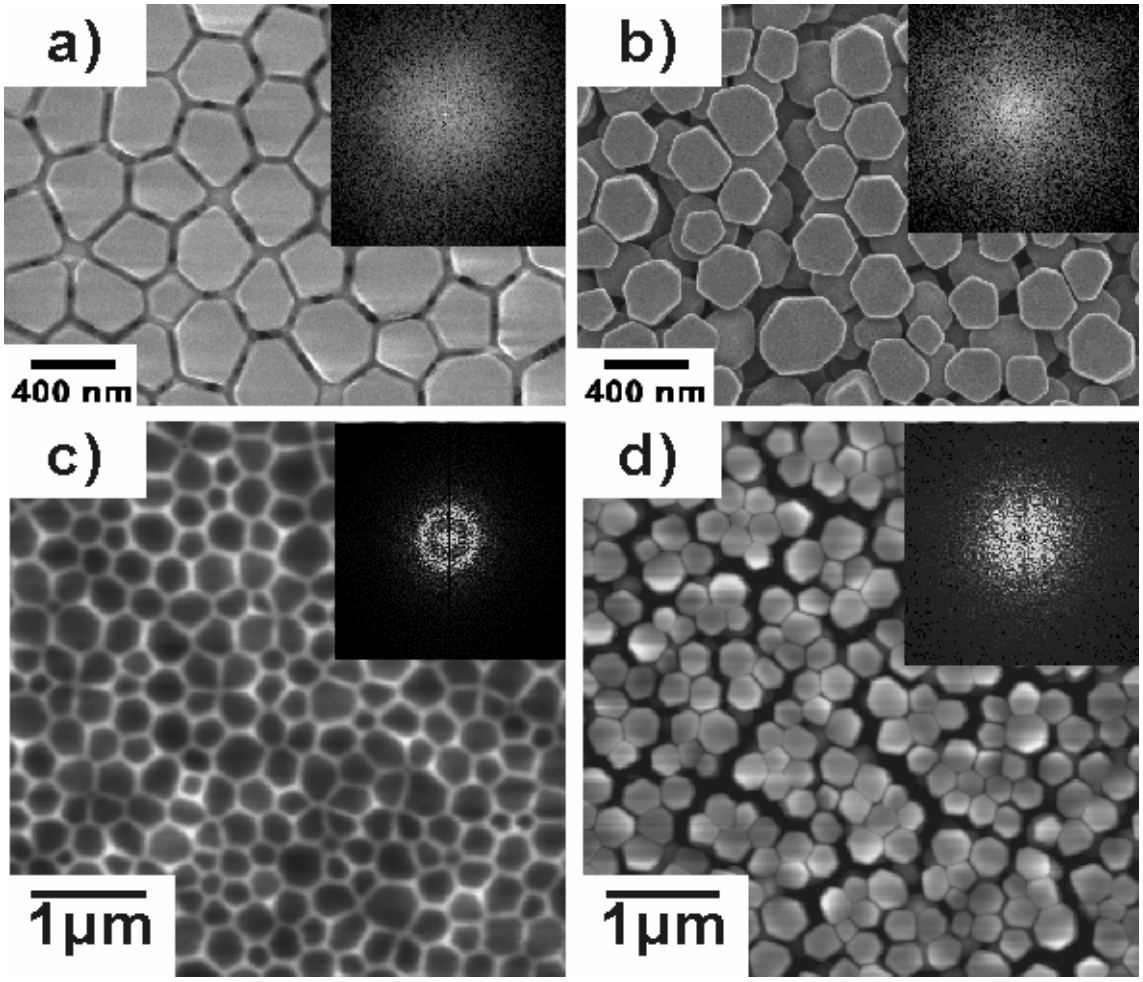

***Figure 49**. SEM images (**a** and **b**) and AFM height images (c and d) of titania nanoplatelets before (**a** and **c**) and after (**b** and **d**) calcination. Height scale: (**c**), 30nm; (**d**), 100nm. The insets are corresponding FFT patterns of each image. Weight ratios: $W_{1,\ 4\text{-dioxane}}$: 0.873; W_{HCl}: 0.022; W_{TTIP}: 0.105.*

The TiO_2 nanoplatelet is supposed to be of anatase phase because the same calcination recipe is applied as our previously reported results, where the anatase phase was obtained after calcination. The formation mechanism of the nanoplatelets can be explained by the good-poor solvent pair induced phase separation process.[11] Because 1,4-dioxane is a good solvent for both PMMA and PEO blocks, with the concentration of 1.wt%, the block copolymer is assumed to have no agreegates in the solution;

however, with the addition of concentrated HCl, which is a poor solvent for PMMA, the block copolymer tends to form nanoscale microphase separated structures in the solution. The titania precursor of TTIP is incorporated into the hydrohphilic PEO domain, where is is hydrolyzed and condensed into amorphous inorganic Ti-O- networks using HCl as a catalyst. Besides, TTIP is also a poor solvent for the hydrophobic PMMA block. Various different morphologies including nano vesicles can be formed when the relative weight ratios among 1, 4-dioxane, HCl, and TTIP are varied systematically. It can be proved by the sample "**b**" in the ternary phase diagram ($W_{1,\ 4\text{-dioxane}}$: 0.920, W_{HCl}: 0.023 and W_{TTIP}: 0.056), whose structures are shown in **Figure 53**.

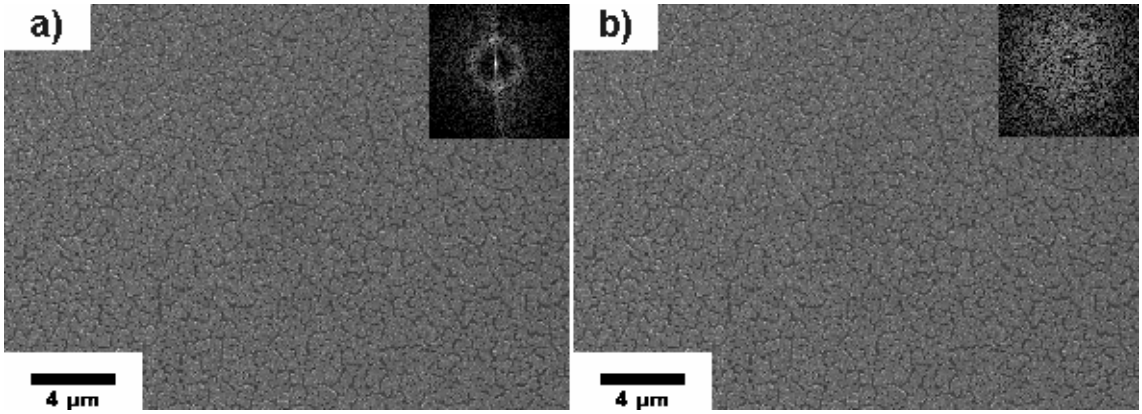

Figure 50. *SEM images of the titania nanoplatelets before (**a**) and after (**b**) calcination with low magnifications. The insets are FFT patterns of each image.*

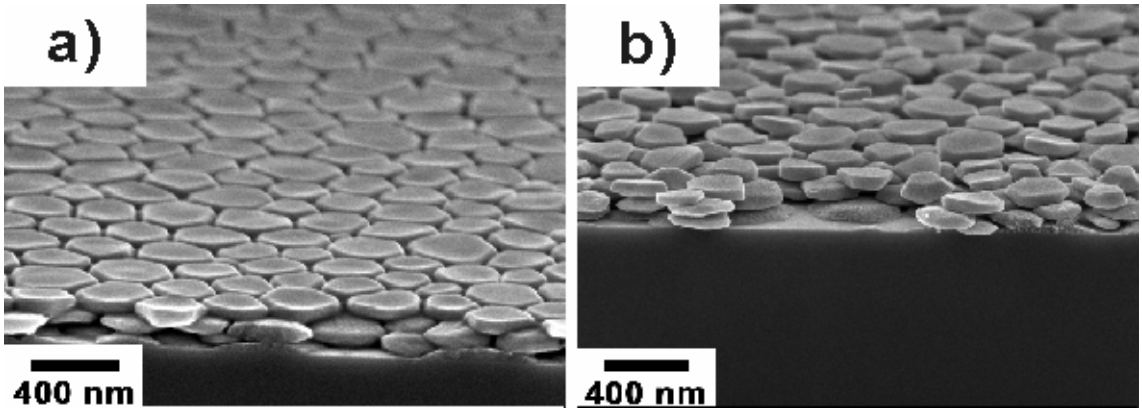

Figure 51. *Side view of the nanoplatelets before (**a**) and after (**b**) calcination*

The wall of the vesicle is composed of titania-PEO domain and the inner and outer regions are formed by PMMA block. The ratio of the wall thickness to diameter can be increased with increasing amount of TTIP in the solution, while keeping the amount of HCl constant. As a result, when W_{TTIP} is promoted to the limit where the block copolymer can still undergo nanoscale microphase separation, vesicles with fairly high wall-to-diameter ratios are formed ($W_{1,4\text{-dioxane}}$: 0.873, W_{HCl}: 0.022 and W_{TTIP}: 0.105). Through the squash process during spin coating, nanoplatelete is formed in the film with the central region slightly deeper compared to the outer periphery region composed of PMMA block. After calcination, the PMMA block is burned off; therefore the height difference between the periphery and centrer is significantly reduced. Besides, the PMMA block forms a matrix to link the neighboring nanoplatelets together, which leads to the formation of gap between neighboring nanoplatelets after calcination.

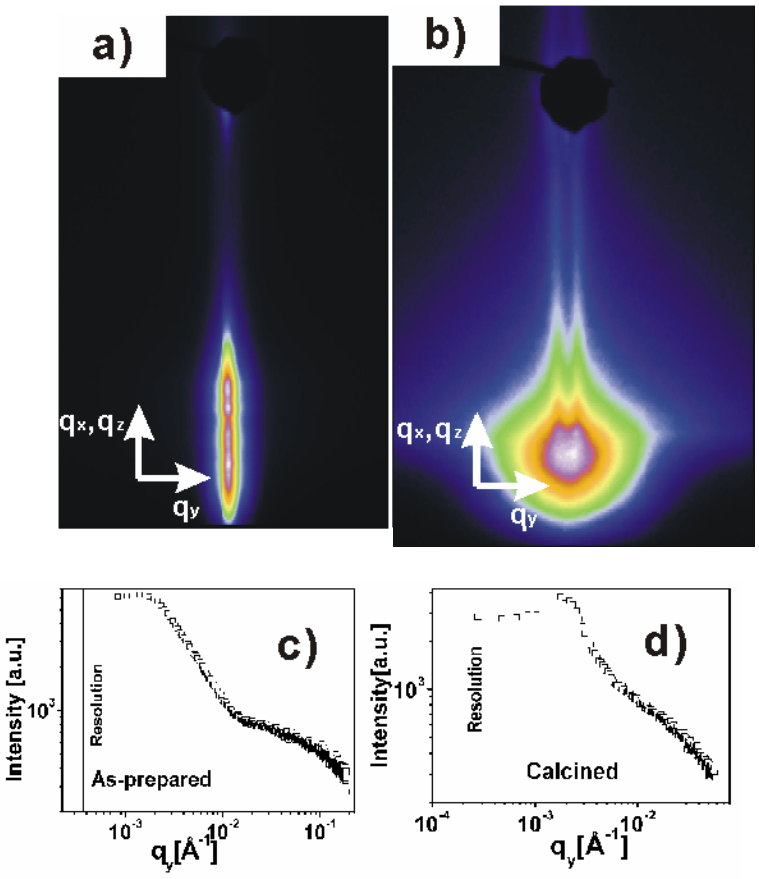

***Figure 52**. GISAXS profiles of the nanoplatelets before (**b**, **d**) and after (**a**, **c**) calcination. GISAXS 2D image cut region: q_y from –0.0210 to 0.0210Å^{-1}. Beam line: BW4.*

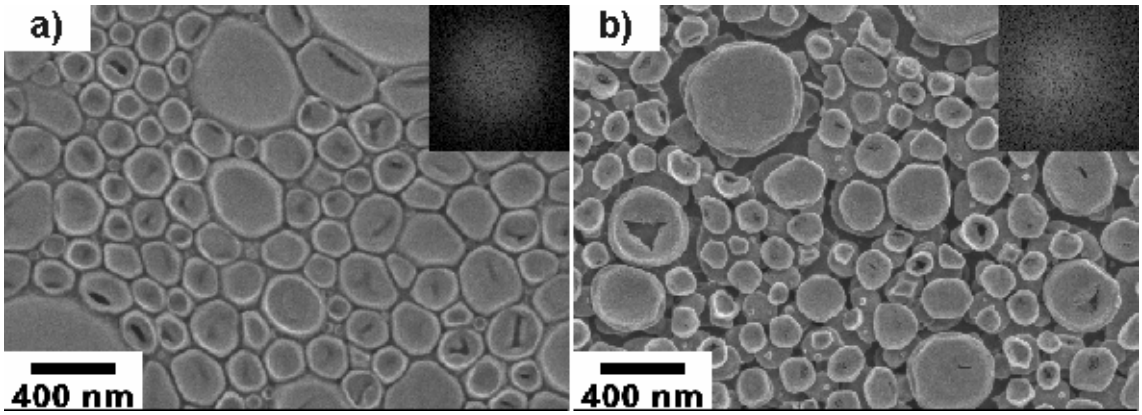

Figure 53. *SEM images of titania nanovesicles and nanoplatelets before (**a**) and after (**b**) calcination. The insets are corresponding FFT patterns of each image. Weight ratios:* $W_{1,\ 4\text{-dioxane}}$*: 0.920;* W_{HCl}*: 0.023;* W_{TTIP}*: 0.056.*

In summary, the morphology evolution of the films **a**-**c** with increasing weight ratio of TTIP is studied by AFM, SEM, x-ray reflectivity, and GISAXS. When the weight ratio of TTIP is increased from 0.056 to 0.105, the morphology is evolved from nanovesicles to nanoplatelet. This phenomenon is similar to that found in the system of PS-b-PEO, where the morphology evolves from so-called nanodoughnuts to nanogranulas with increasing amount of TTIP. Therefore the results confirm that the concept developed in the amphiphilic system of PS-b-PEO is also applicable to other amphiphilic block copolymers, like PMMA-b-PEO.

4.4. PEO-b-PS-b-PEO Templating System

Besides the diblock copolymer, amphiphilic triblock copolymer is also an interesting type of potential templating agent to control the morphology of nanostructured inorganic metal oxides like SiO_2, TiO_2, ZrO_2, and so on. Among the triblock copolymers used, pluronic triblock copolymer of PEO-PPO-PEO has been intensively used as a templating agent to produce inorganic metal oxides with different morphologies when sol-gel chemistry is coupled, for example, lamellae, cubic mesoporous, and hexagonal mesoporous structures. [92, 100, 108, 123, 124, 126-130, 132, 278] However, the strategy based on pluronic triblock copolymer can only produce mesoporous structures with a pore size in the range of 2-50 nm; [123] it is hard to achieve ordered macroporous materials with the pore size larger than 50nm. [280] This is mainly due to restrictions in accessible molecular weights of PEO-PPO-PEO block copolymers which are often too low to form nano structures with the size of hundreds of nanometers. Also there is only one methyl group difference between the PEO and PPO structural repeating unit, leading to a small hydrophobicity/hydrophilicity difference. Furthermore, even in cases where mesoporous structures were prepared the obtained mesoporous TiO_2 began to collapse at temperatures above 450°C because the wall thickness was commonly too thin. [116, 117, 281] However, in most of cases, the crystalline anatase modification can only be fully converted from initially amorphous TiO_2 at temperatures around 400°C. [117] Due to the above-mentioned restrictions, different strategies based on colloidal crystal templates are typically applied to synthesize macroporous TiO_2 materials. [63, 282, 283] These strategies however are complicated multi-step processes, in which first organic polymer or SiO_2 spheres need to be synthesized and self-assembled into colloidal crystal packing, followed by incorporation of titania precursors and removal of the templates. Especially, when SiO_2 is used as a colloid template, HF is needed to etch away SiO_2 to produce macroporous TiO_2, which is a dangerous substance. [63, 282] To simplify the colloidal templating process, herein a new strategy is used to achieve crystalline ordered macroporous TiO_2 thin films in a convenient one-step way. If prepared as a thin film, the resulting macroporous TiO_2 structure exhibits an unusual stabilities, retaining its structural integrity during calcination at temperature of up to 1000°C, which makes it possible to obtain both anatase and rutile phase at different calcination temperatures.

Instead of synthesizing a separate colloidal polystyrene template, a symmetric tri-block copolymer of PEO-PS-PEO was designed and synthesized. [266] The middle PS block can potentially self-assemble into polystyrene spheres as a core of the spherical micelles; however, the corona

composed of PEO block can incorporate titania precursor via coordination bonds, where it can be hydrolyzed and condensed into amorphous titania networks. During spin coating, the coronal of PEO and primary titania sol-gel particles are still soft and thus able fill the gaps present between densely packed polystyrene spheres. Consequently, the PS block will function in a similar way to the isolated polystyrene colloids and a porous structure can be formed after removal of the polystyrene core. The key step to fulfill the aim is to adopt an appropriate strategy through which the triblock copolymer can undergo microphase separation in the size range of hundreds nanometers. Therefore, the concept of good-poor solvent pair induced phase separation process is introduced into the PEO-PS-PEO system to control the morphologies. Instead of 1, 4-dioxane, N, N-dimethyl formamide (DMF) is used as a good solvent for both PS and PEO blocks. HCl and TTIP are used as poor solvents for PS block to induce the phase separation and control the sol-gel reaction. The slow addition of HCl and TTIP into the DMF solution will therefore cause the PS block to form a core of the spherical micelle and PEO as a corona, where TTIP is incorporated. [156, 177] Because there is a significant hydrophilicity and hydrophobicity difference between the PS and PEO block, micelles with the size of hundreds nanometers are formed in the solution (Dynamic light scattering result in **Figure 54**).

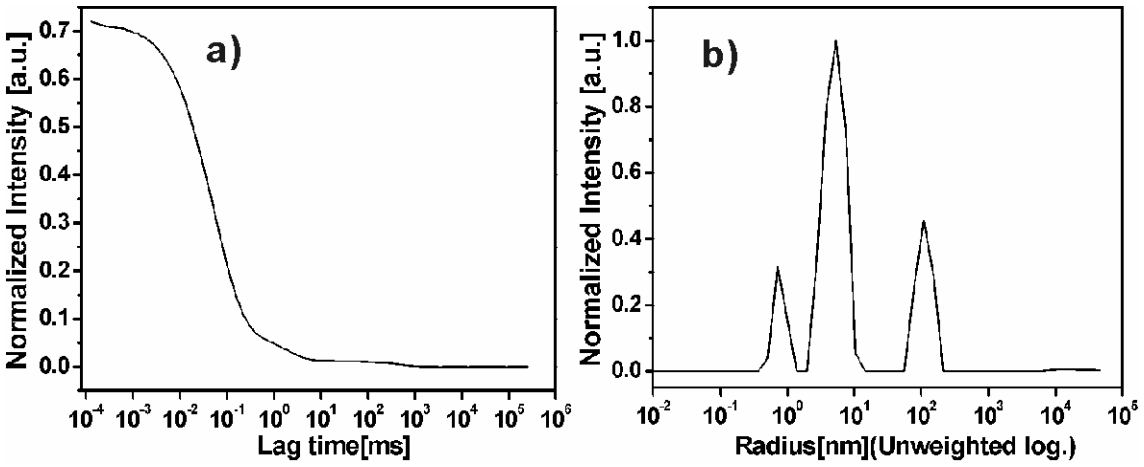

***Figure 54**. Dynamic light scattering (DLS) profile (**a**) and corresponding size distribution of the aggreagtes (**b**) in solution.*

These micelles are decorated at their surface with small primary titania sol-gel particles. During spin coating, the spherical micelles self assemble in a close-packing fashion. After calcination, the core composed of the PS block is burned away and a macroporous titania structure is remains. At the same

time the structural integrity of the close packed micelles is preserved, since they are fixed to the substrate via hydrolysis of surface hydroxyl groups to the sol-gel particles. **Figure 55** shows the SEM images of the macroporous film obtained by calcination at 550°C (**a**, **c**) and 1000°C (**b**, **d**) respectively. The macroporous film is produced by the removal of polystyrene core through calcination, which is confirmed when compared to the SEM image of the as-prepared sample (**Figure 56**). The SEM image of the as-prepared film suggests that the self-assembled structures are forming sub-monolayer coverage and are therefore distributed on the Si wafer in patches. Furthermore **Figure 56** clearly shows that the primary sol gel particles attached to the PEO-PS-PEO micelles have moved to fill the gap between the micellar cores, thereby leaving the top of the micellar core uncoated.

The FFT pattern of **Figure 55a** indicates that the macroporous TiO_2 calcined at 550° is of high order hexagonal packing. The gaussian pore size distribution profile shown in **Figure 57a** is centered at 278nm and the average wall thickness is 81nm. In contrast to the mesoporous TiO_2 structure templated by PEO-PPO-PEO, where the periodic property is usually to be deteriorated above 450°C, here the macroporous TiO_2 film has a rather strong stability.

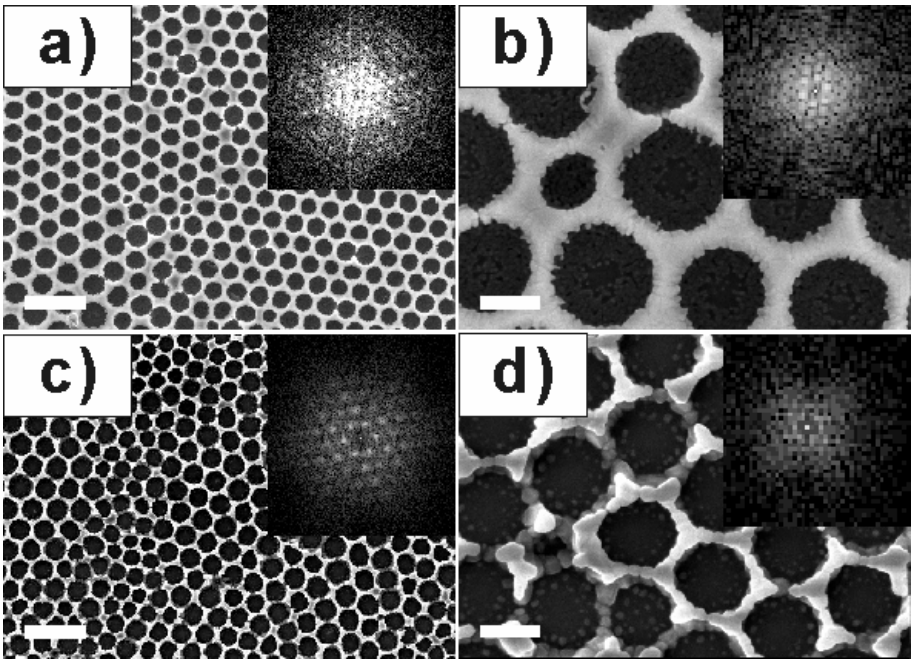

***Figure 55**. SEM images of the macroporous TiO_2 film calcined at 550 (**a** and **b**) and 1000℃ (**c** and **d**) respectively; Scale bar: 400nm for **a**, **c**; 200nm for **b**, **d**.*

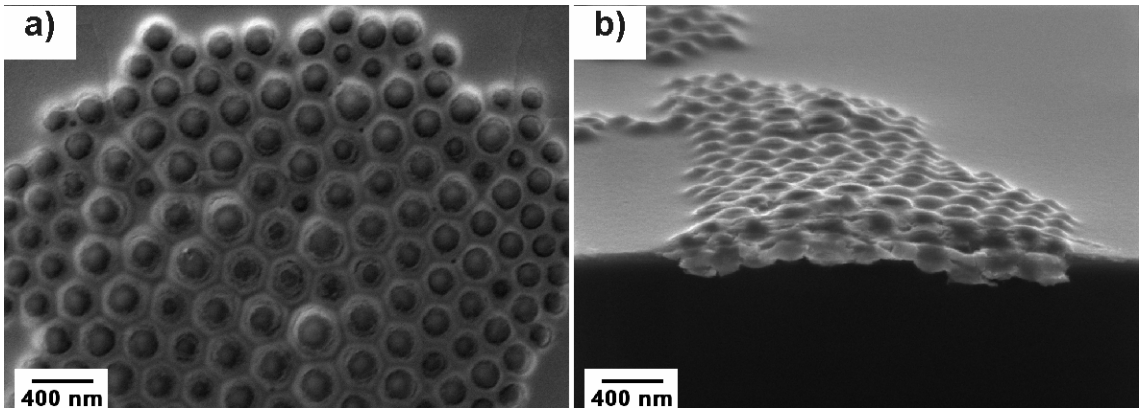

***Figure 56**. SEM image of the as-prepared sample.*

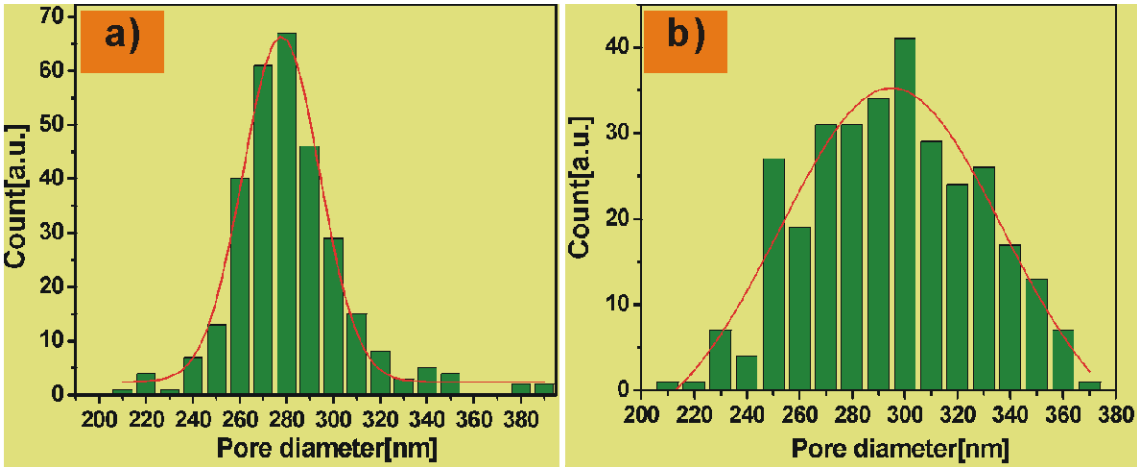

***Figure 57.** Pore size distribution of the macroporous TiO_2 film calcined at 550℃ (**a**) and 1000℃ (**b**) for 4 hours respectively.*

The SEM image with higher magnification (**Figure 55b**) shows that there are tiny TiO_2 nanoparticles beneath the macroporous framework. It's obvious that the macroporous structure is still retained after calcination at 1000°C for 4 hours (**Figure 55c)**. The pore size distribution is widened and centered at 289nm (**Figure 57b**). The average wall thickness is reduced to 43nm due to crystallization. The FFT shows fewer higher orders than that of the sample calcined at 550°C, however the presence of a 6^{th} higher order, indicates tha the macroporous film retains its highly ordered hexagonal packing. The SEM image with higher magnification (**Figure 55d**) again shows that the wall of the macroporous structure is composed of crystalline TiO_2 grains. The side view image of the 550°C calcination sample further confirms the macroporous characteristic of the TiO_2 film (**Figure 58a**). It shows that there is a

strong anisotropic shrinkage due to calcination at 1000°C (**Figure 58b**). However, it should be pointed out that the rutile phase can be formed above 800°C, so in principle, the calcination can be conducted below 1000°C to limit shrinkage. High-resolution TEM images prove that after caclcination the amorphous TiO_2 has been converted to crystalline phase. The film calcined at 550°C is of anatase phase and the sample calcined at 1000°C exhibits rutile phase (**Figure 59**).

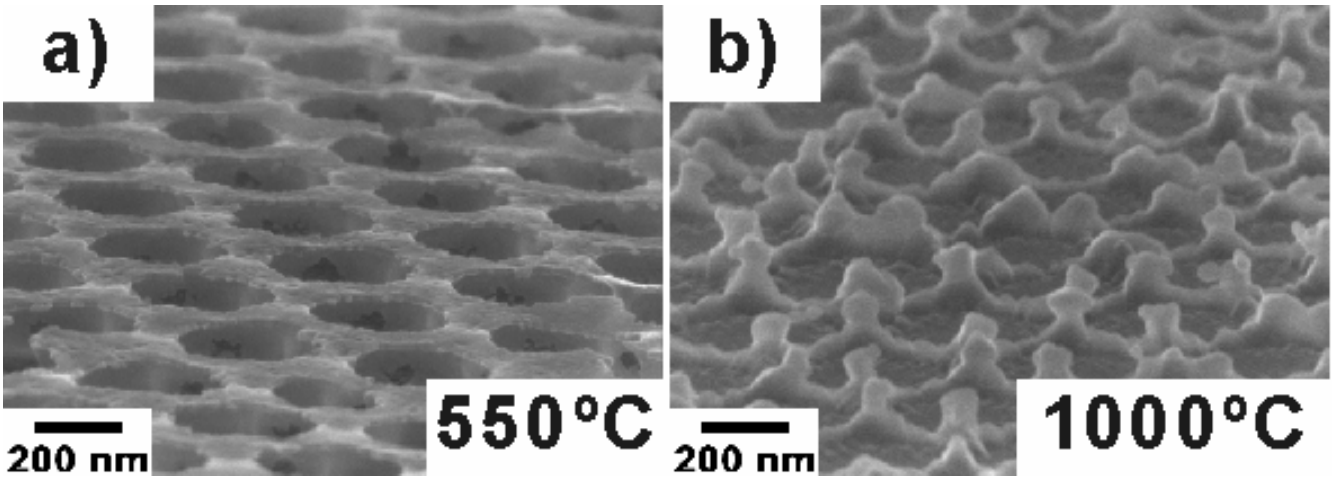

***Figure 58**. SEM images of the macroporous TiO_2 film calcined at 550 (**a**) and 1000℃ (**b**) respectively.*

Considering that TEM is intrinsically a highly local characterization method, complementary XRD measurement is conducted to prove the crystallographic phase of the film over the substrate. The XRD profiles clearly show that the film calcined at 550°C is of anatase phase and that calcined at 1000°C is of rutile phase (**Figure 60**).

In summary, macroporous crystalline TiO_2 film has been achieved via a new concept based on the triblock copolymer of PEO-PS-PEO, coupled with good-poor solvent pair induced phase separation process and sol-gel chemistry. The macroporous film can survive calcination at high temperatures such as 550 and 1000°C, at which the TiO_2 film is converted to either anatase or rutile phase.

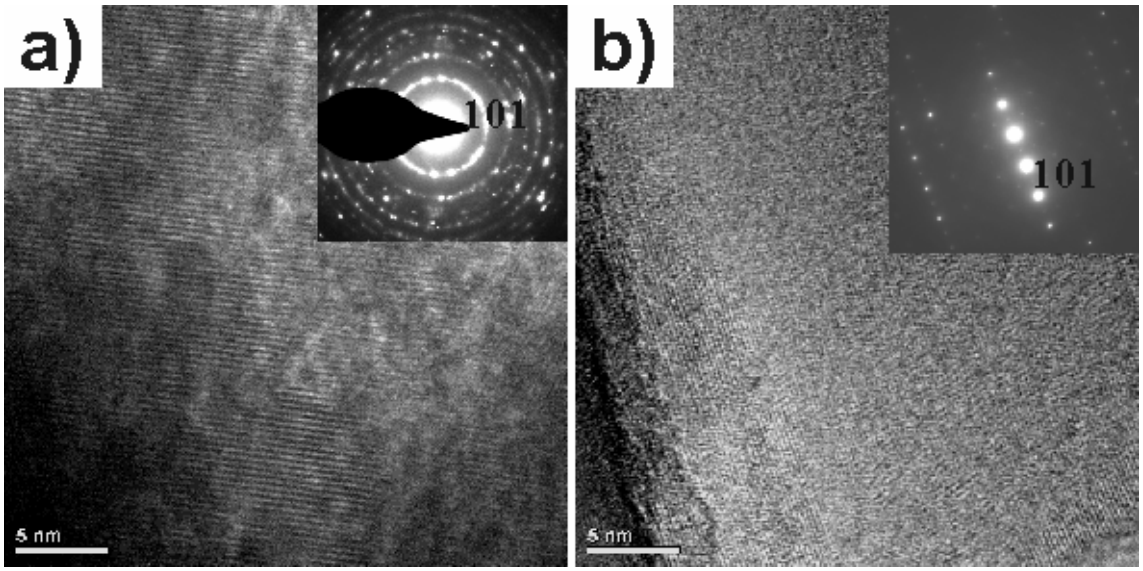

Figure 59. *TEM images of the macroporous TiO_2 films calcined at 550℃ (**a**) and 1000℃ (**b**) (insets are selected area diffraction patterns). The crystalline plane distance is 0.353 (**a**) and 0.250nm (**b**) respectively. The scale bars correspond to 5nm.*

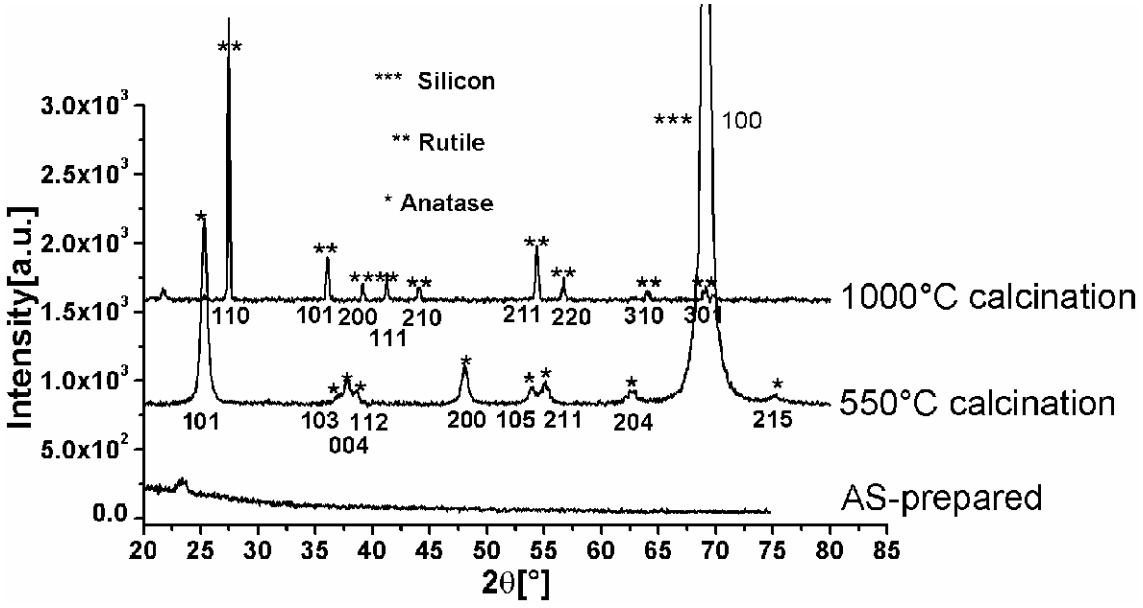

Figure 60. *XRD profiles of the as-prepared film and films calcined at 550℃ and 1000℃.*

4.5. Application of Nanostructured Titania Thin Films in Solid State Dye-sensitized Solar Cells

4.5.1 Solar Cell Device Structure

The structural component of the dye-sensitized solar cells is exhibited in **Scheme 11**. On the surface of normal soda-lime glass is deposited with a layer of FTO with a thickness ca. 600nm (**Figure 61**). A barrier layer of compact TiO_2 with a thickness around 40nm is prepared on the FTO surface via spin coating, which can prevent the short-cuts of the solar cells (**Figure 62**). The barrier layer possesses a good blocking ability, which is confirmed by the cyclovoltammetry measurement (**Figure 63**). On the surface of the barrier layer the nanostructured TiO_2 thin films with various different morphologies are deposited by spin coating the block copolymer-sol gel solution. The crystalline nanostructured TiO_2 thin film acts as a substrate for the adsorption of the monolayer dye molecules. A further layer of P3HT with a thickness of 56.0nm is spin coated on the titania surface and further annealed at 200°C for 2 hours acting as a hole conductor matrix (**Figure 64**).

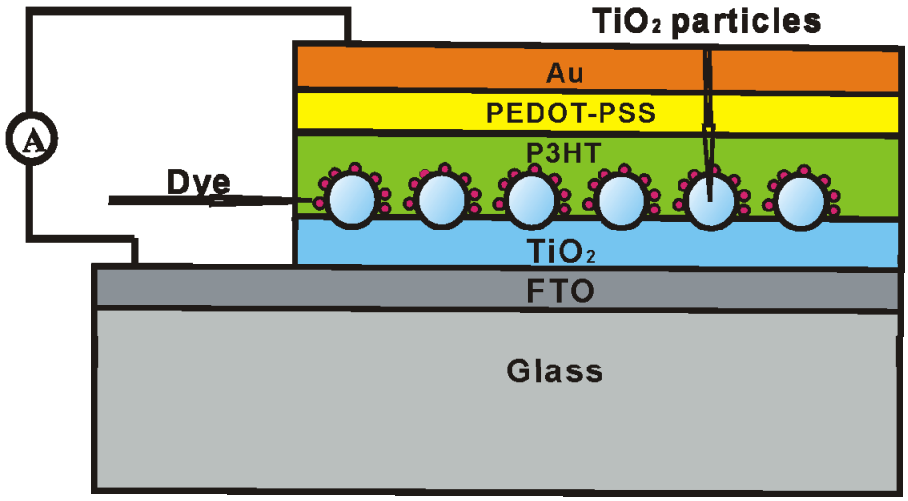

***Scheme 11**. The structural model of the solid state dye-sensitized solar cells*

The height difference in the AFM image indicates the formation of some random domains on the surface of the film; however, the AFM phase image only show a very weak phase contrast over the film, which means that the surface of the substrate is homogeneously covered with P3HT.

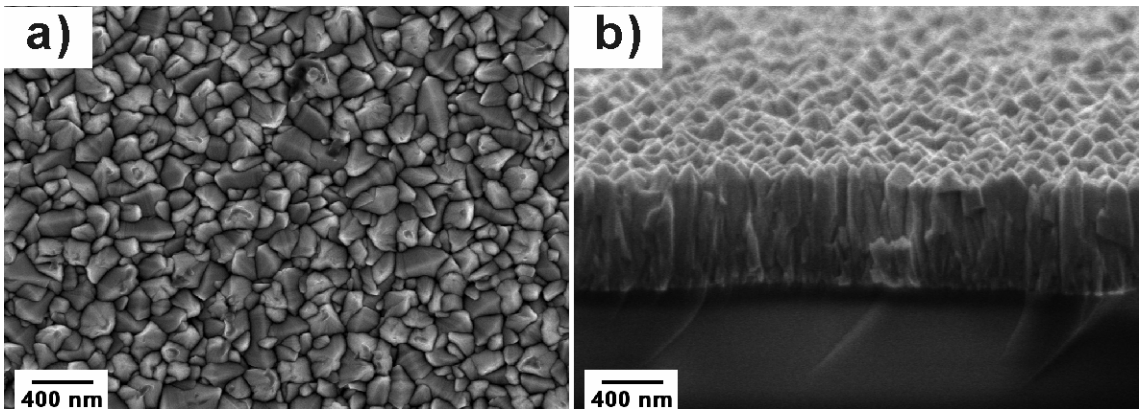

***Figure 61**. SEM top view (**a**) and side view (**b**) images of the FTO layer*

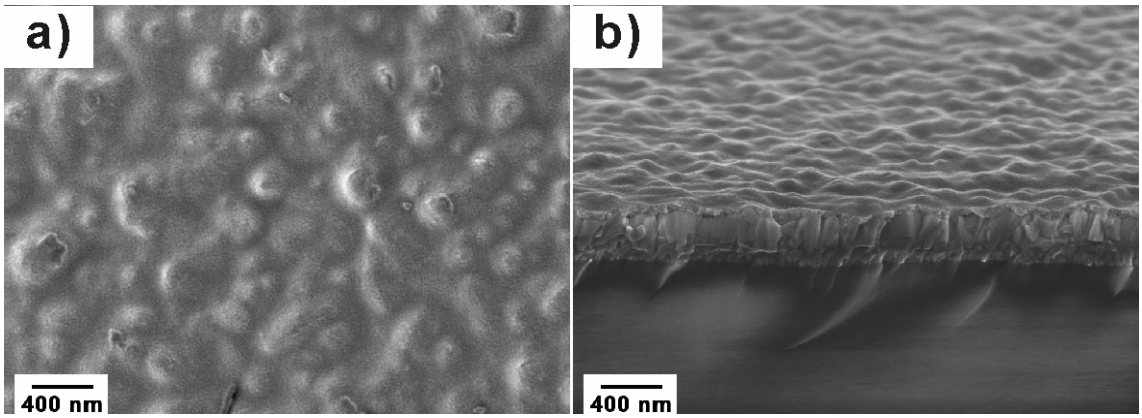

***Figure 62**. SEM top view and side images of the TiO_2 barrier layer*

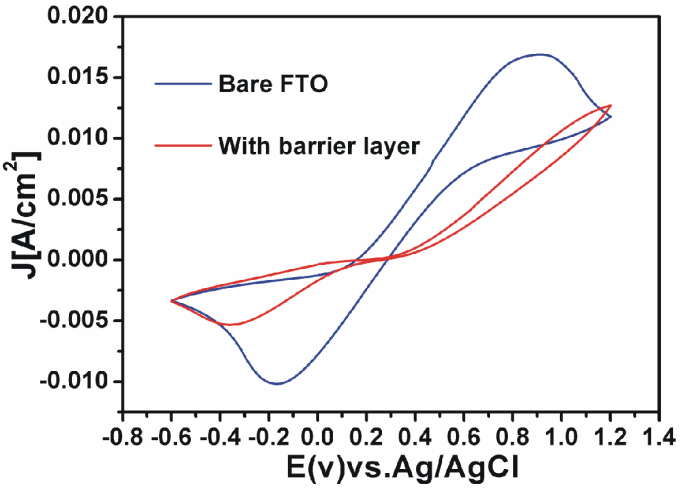

***Figure 63**. Cyclovoltammetry measurement of the bare and TiO_2 covered FTO layer*

An additional PEDOT-PSS layer of 67.8nm is deposited on the surface of P3HT and annealed at 100°C for 15min to block the electron migration to the counter Gold electrode, which can potentially improve the solar cell efficiency (**Figure 65**). [268] Both the AFM height and phase images prove that the PEDOT/PSS is homogeneous over the substrate. Finally, the top of the solar cell is covered with gold electrode with a thickness of 100nm.

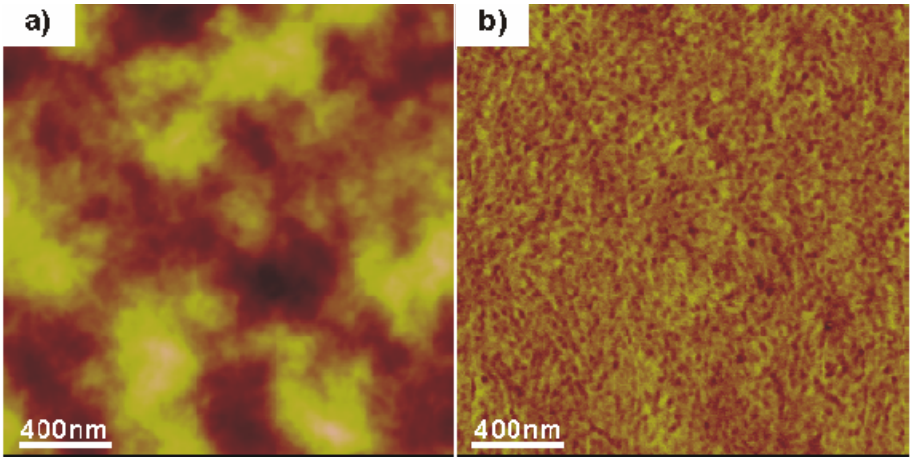

***Figure 64**. AFM height (**a**) and phase (**b**) images of the P3HT layer annealed at 200℃ for 2 hours. Height scale: 40nm; phase scale: 2°.*

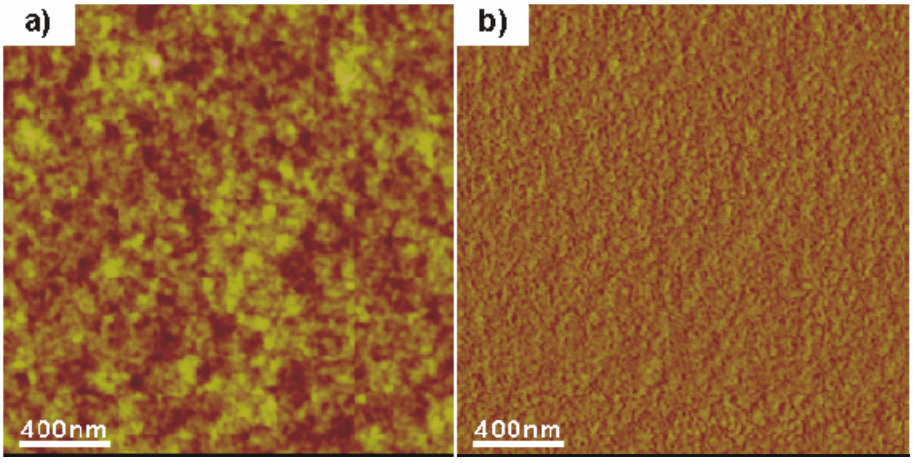

***Figure 65**. AFM height (**a**) and phase (**b**) images of the PEDOT/PSS layer annealed at 100℃ for 15min. Height scale: 15nm; phase scale: 2°.*

4.5.2 Role of the Nanostructured TiO_2 Thin films in Solar Cells

4.5.2.1 Control Device-only with TiO_2 Barrier Layer

In order to clarify the impact of the nanostructured TiO_2 layer on the solar cell performance, control devices with only TiO_2 barrier layer are fabricated and the performance is measured.

To exhibit the characteristic open circuit voltage (V_{oc}) in a pronounced way, *I-V* curves with log-scale current density vs. linear-scale voltage are plotted. [247] **Figure 66a** shows the *I-V* profile of the control device with a maximum global efficiency of 0.06%. The corresponding parameters are as following: short circuit current (I_{sc}): 72μA/cm^2, open circuit voltage (V_{oc}): 0.26V, filling factor (FF): 0.35. The maximum EQE in **Figure 66b** is 1.15%. The average parameter values of the devices are obtained from 5 pixels, which are as following: I_{sc}, 44.8±16.7μA/cm^2, V_{oc}, 0.274±0.025V, FF, 0.352±0.022, global efficiency of 0.038±0.015%, and EQE 0.82±0.31%. The whole data set of the five pixels is listed in **Table S-1** in appendix.

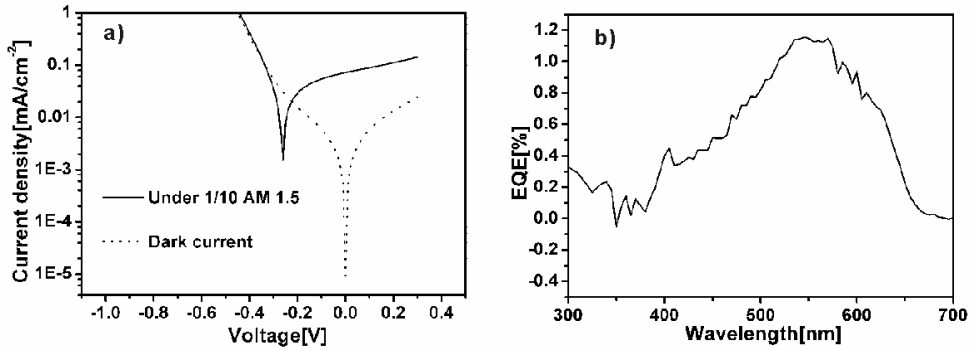

***Figure 66**. The peak performance of the solar cell with only barrier layer. **(a)** I-V curve, **(b)** EQE profile.*

4.5.2.2 Clustered Nanoparticles

The morphologies of the TiO_2 layer shown in **Figure 67** confirm that the TiO_2 thin films on both bare Si wafer and TiO_2 barrier layer coated Si wafer possess similar clustered nanoparticles. It means that the presence of the TiO_2 barrier layer does not modify the morphology significantly. The

maximum global efficiency of 0.12% is shown in **Figure 68** with a short-circuit (I_{sc}) of 76μA/cm^2, open circuit voltage (V_{oc}) of 0.35V, and filling factor (FF) of 0.36. The maximum EQE is 2.07% at wavelength of 540nm. Average performance parameters obtained from 8 pixels are as following, I_{sc}: 55.1±11.7μA/cm^2, V_{oc}: 0.239±0.052V, FF: 0.346±0.013, global efficiency η: 0.059±0.028%, and EQE 2.08±0.31%. The whole set of the solar cell performance data is listed in **Table S-2** in the appendix.

The maximum global efficiency is improved by 100% (from 0.06% to 0.12%) when the clustered nanoparticles layer is introduced into the device. In the sense of the average value, the efficiency is also improved by 55% compared to the control device (0.059% vs.0.038%), which is mainly due to the enhancement of the I_{sc} value (55.1 vs. 44.8μA/cm^2).

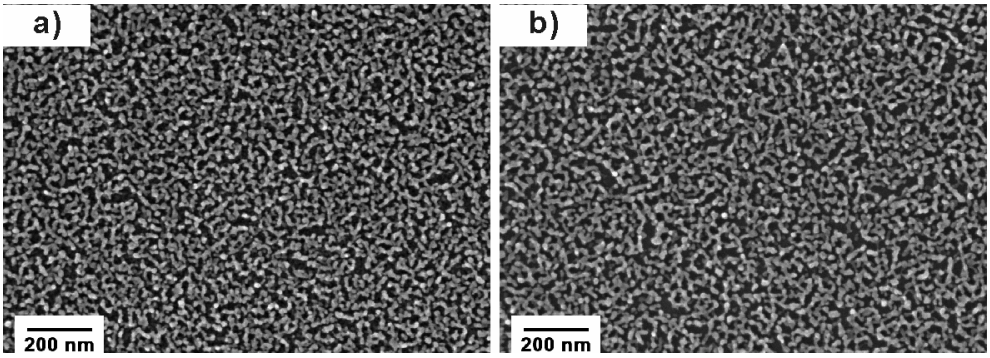

***Figure 67**. SEM image of the TiO_2 film with clustered nanoparticles on bare Si wafer (**a**) and TiO_2 barrier coated Si wafer (**b**).*

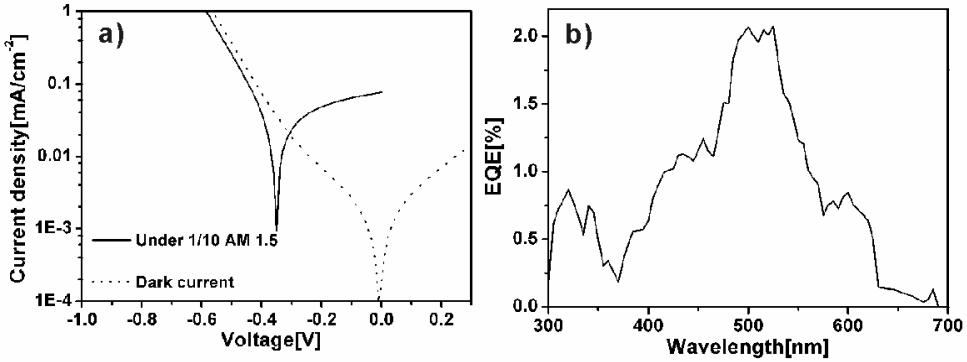

***Figure 68**. The maximum performance of the solar cell with clustered TiO_2 nanoparticles (**a**) I-V curve, (**b**) EQE profile.*

4.5.2.3 Worm like structures

The SEM images of the worm like structures shown in **Figure 69** indicates that the TiO_2 barrier layer has modified the morphology compared to the film on bare Si wafer, however, both structures are still in the category of worm-like structures. The solar cell devices consisting of worm structured TiO_2 layer has a maximum global efficiency of 0.11% with I_{sc} 99μA/cm^2, V_{oc} 0.27V, FF 0.34, and maximum EQE of 3.66% (**Figure 70**). Average performance data is obtained from 12 pixels as following: global efficiency η 0.062±0.028%, I_{sc} 59.4±22.2μA/cm^2, V_{oc} 0.248±0.043V, FF 0.339±0.031, and maximum EQE 2.81±0.50%. The whole data set of the data is shown in **Table S-3** in appendix. Compared to the control device, both the global efficiency (0.062% vs. 0.038%) and I_{sc} value (59.4 vs. 44.8μA/cm^2), and EQE (2.81% vs. 0.82%) are improved.

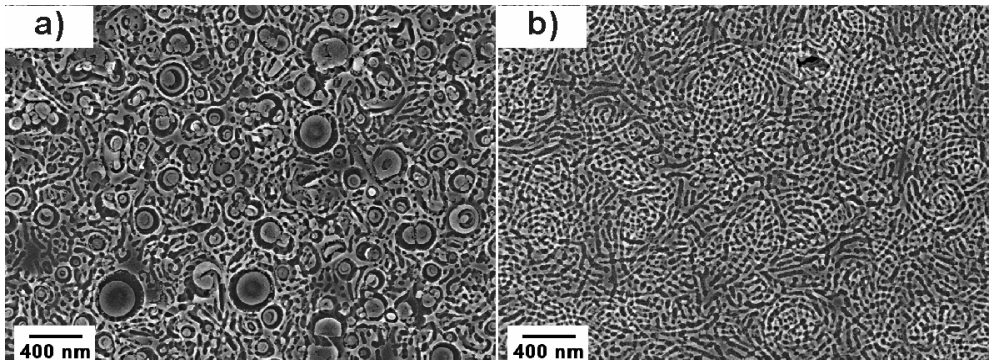

***Figure 69**. SEM image of the TiO_2 worm structures on bare Si wafer (**a**) and TiO_2 barrier coated Si wafer (**b**).*

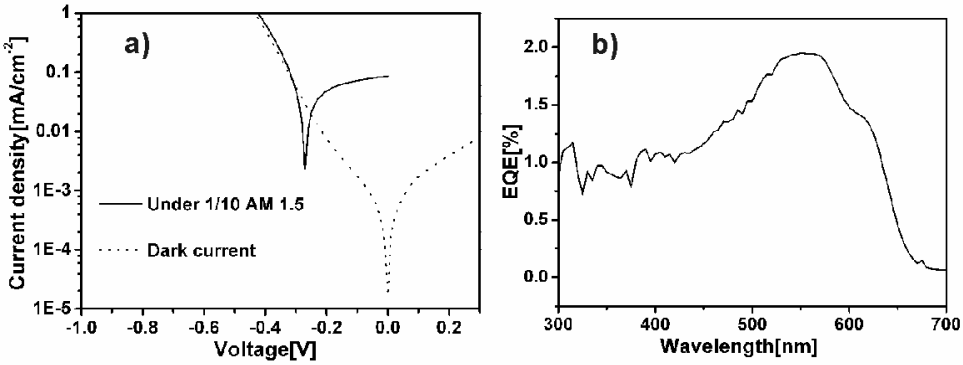

***Figure 70**. The maximum performance of the solar cell with worm structured TiO_2 film (**a**) I-V curve, (**b**) EQE profile.*

4.5.2.4 Foam

Figure 71 shows the structures of the TiO_2 foam on both bare Si wafer (**a**) and TiO_2 barrier layer coated Si wafer (**b**), where similar morphologies are observed. The *I-V* profile with a maximum global efficiency is shown in **Figure 72** with an I_{sc} of 63μA/cm^2, V_{oc} 0.21V, FF 0.36, global efficiency of 0.06%, and maximum EQE 3.17%. The average performance data is obtained from four individual pixels as following: I_{sc}, 67.5±7.59μA/cm^2, V_{oc}, 0.180±0.024V, FF, 0.332±0.019, global efficiency η, 0.050±0.008%, and maximum EQE 2.89±0.28% (Whole data set seen in **Table S-4** in appendix). Compared to the control device, the short-circuit-current I_{sc} is increased dramatically by 51% (67.5 vs. 44.8μA/cm^2) and the maximum EQE is also increased significantly (2.89% vs. 0.82%). However, due to relatively low V_{oc} compared to the control device, the global efficiency is not improved significantly. The reason of low V_{oc} can be due to technical problems in the solar cell fabrication process, not because of the TiO_2 layer itself.

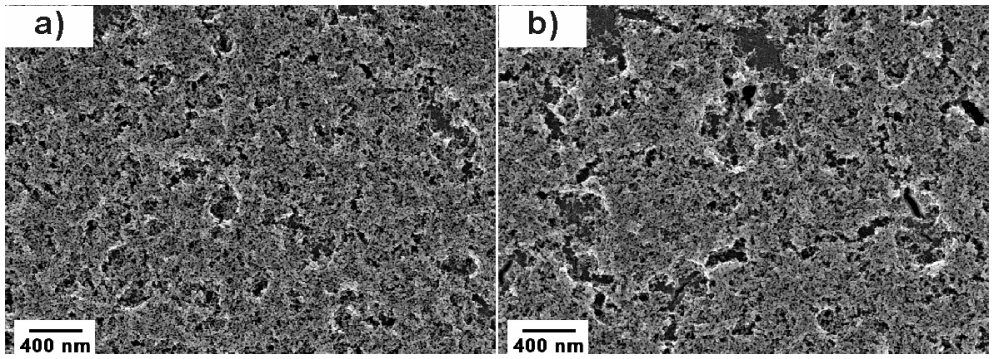

***Figure 71**. SEM image of the TiO_2 foam on bare Si wafer (**a**) and TiO2 barrier coated Si wafer (**b**).*

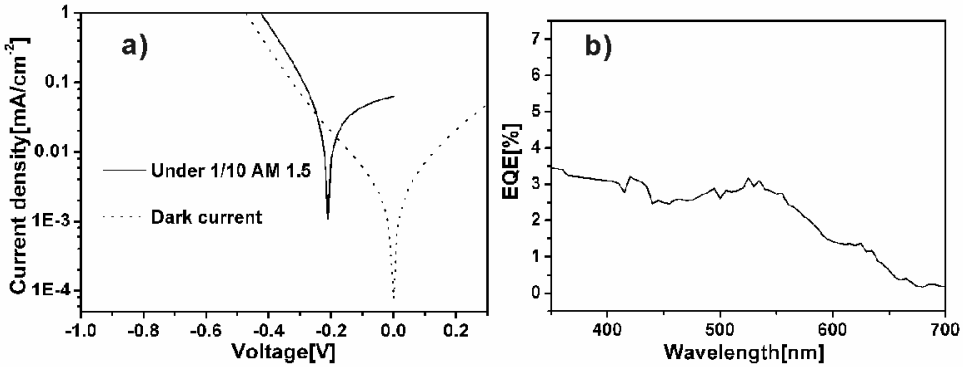

***Figure 72**. The Maximum performance of the solar cell with TiO_2 foam (**a**) I-V curve, (**b**) EQE profile.*

4.5.2.5 Large Collapsed Vesicles

Although the large collapsed vesicles do not provide nicely ordered structural pattern on both bare and barrier layer coated Si wafer (**Figure 73a** and **b** respectively), it still can make contribution to improve the solar cell performance. **Figure 74** shows the *I-V* curve with maximum efficiency of 0.09% and corresponding I_{sc} 87μA/cm^2, V_{oc} 0.27V, and FF 0.42. The maximum EQE% is 1.95%. Average performance data is calculated from 10 pixels as following: I_{sc}, 57.8±13.9μA/cm^2, V_{oc} 0.249±0.037V, FF 0.378±0.027, and global efficiency of 0.048±0.019%, and maximum EQE 1.45±0.38% (whole data set seen in **Table S-5** in appendix). Compared to the control devices, the average I_{sc} value are increased by 29%, which means that the presence of the TiO_2 large collapsed vesicles has a positive impact to improve the performance of the solar cells.

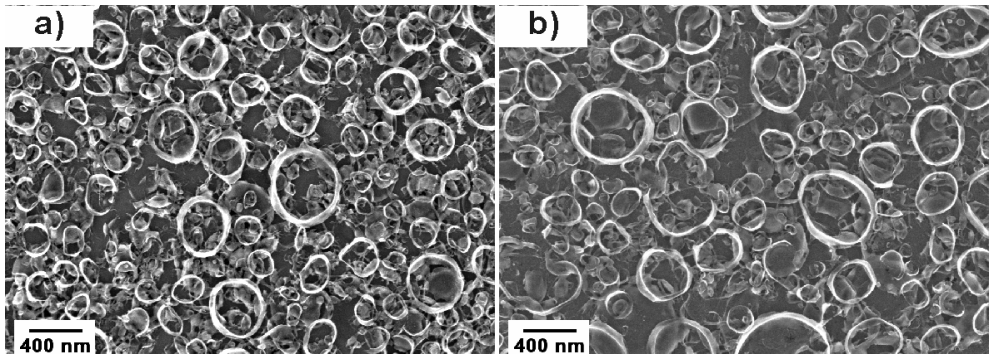

***Figure 73**. SEM image of the TiO_2 collapsed nanodoughts on bare Si wafer (**a**) and TiO_2 barrier coated Si wafer (**b**).*

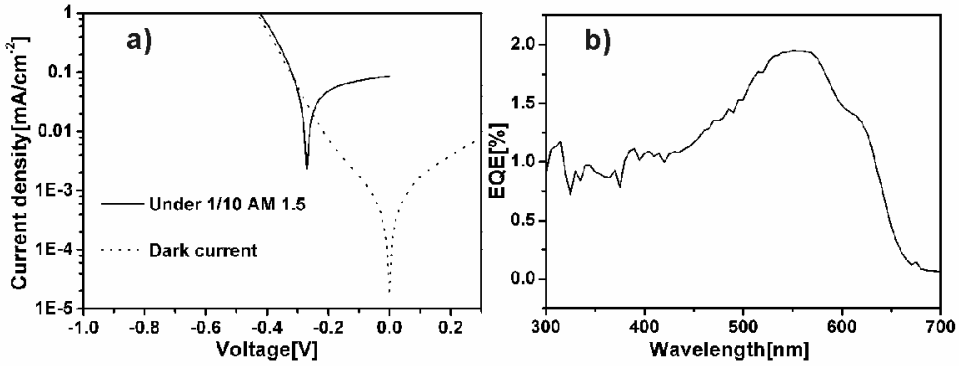

***Figure 74**. The maximum performance of the solar cell with TiO_2 large collapsed vesicles (**a**) I-V curve, (**b**) EQE profile.*

4.5.2.6 Small Vesicles

Figure 75 shows similar TiO_2 small vesicles structures on both bare (**a**) and barrier layer coated Si wafers (**b**). The *I-V* profile with a maximum global efficiency of 0.08% is exhibited in **Figure 76a**. Other corresponding performance parameters are as following: I_{sc}, 61μA/cm^2, Voc, 0.26V, FF, 0.38%, and maximum EQE 17.89%. The average performance data obtained from six individual pixels is as following: I_{sc}, 54.2±10.1μA/cm^2, V_{oc}, 0.225±0.023V, FF, 0.377±0.019%, and global efficiency, 0.058±0.015%, and maximum EQE 13.58±4.06% (whole data set seen **Table S-6** in appendix). Compared to the control device, the improvement of the solar cell performance is not obvious; however, it is worth noticing that the maximum EQE value is much higher than the control devices (13.58% vs. 0.82%), which suggests that the presence of the additional TiO_2 small vesicles layer provide more specific surface area for the adsorption of the dye molecules.

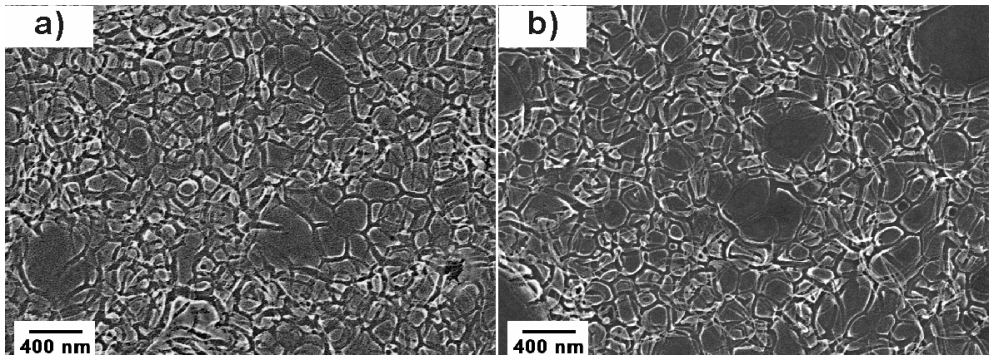

***Figure 75**. SEM image of the TiO_2 small vesicles on bare Si wafer (**a**) and TiO_2 barrier coated Si wafer (**b**).*

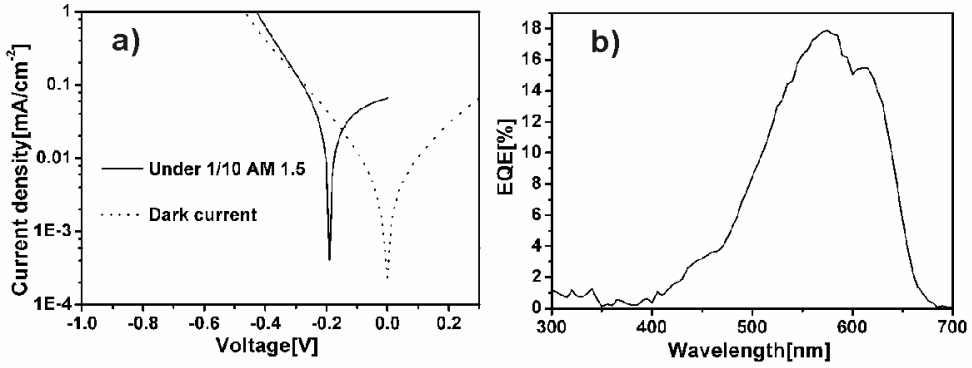

***Figure 76**. The maximum performance of the solar cell with TiO_2 small vesicles (**a**) I-V curve, (**b**) EQE profile.*

4.5.2.7 Control Sample from Different Batch

It has been found that the control devices prepared from different batches can have very different performance. The results to be addressed in the following are based on different batches from the devices addressed above. Therefore to make a reasonable comparison to clarify the impact of the additional nanostructured TiO_2 layer, the results of the control devices are presented in the following first. **Figure 77** exhibits the *I-V* profile with a maximum global efficiency of 0.02%, I_{sc}, 25μA/cm^2, V_{oc}, 0.21V, FF, 0.36, and maximum EQE 0.77%. The average data calculated from four pixels are as following: I_{sc}, 19.0±5.35μA/cm^2, V_{oc}, 0.225±0.013V, FF, 0.357±0.019, global efficiency η 0.015±0.006%, and maximum EQE% 0.58±0.18% (whole data set shown in **Table S-7** in appendix). Both the average and maximum data of the control devices show poorer performance than the previous control device. The reason for the poorer performance is probably due to the technical aspects during the solar cell device fabrication process.

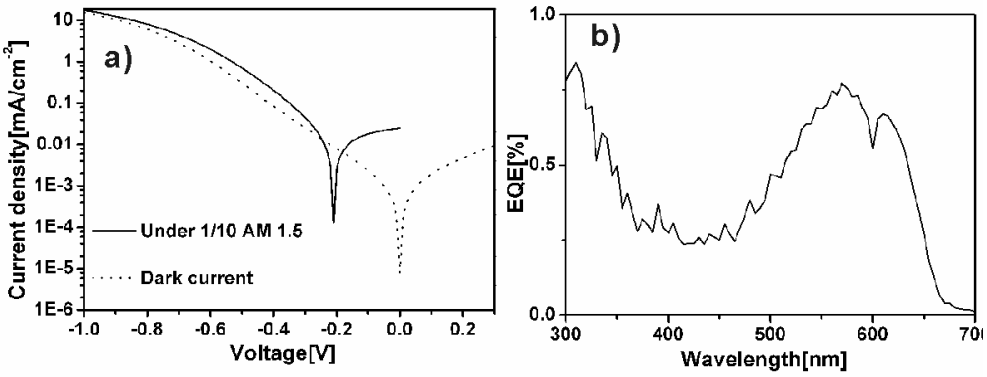

***Figure** 77. The peak performance of the solar cell with only barrier layer. **(a)** I-V curve, **(b)** EQE profile.*

4.5.2.8 Nanowires

Figure **78** shows the morphologies of the nanowire structures on both bare (**a**) and TiO_2 barrier layer coated Si wafers (**b**). The structures are different between bare Si wfer and barrier layer coated Si wafer. The structure on barrier layer coated Si wafer is composed of nanowires linked by large sized

junction plane as addressed in the previous section. The *I-V* curve of the device with a maximum efficiency 0.04% is shown in **Figure 79a** and a maximum EQE% is 1.39% (**Figure 79b**). The corresponding performance parameters with highest global efficiency are as following: I_{sc}, 35μA/cm^2, V_{oc}, 0.36V, FF, 0.37. The average values of the parameters calculated from four pixels are as following: I_{sc}, 27.2±9.57μA/cm^2, V_{oc}, 0.355±0.039V, FF, 0.352±0.013, global efficiency η, 0.030±0.012%, and maximum EQE 1.06±0.30% (whole data set shown in **Table S-8** in appendix). Compared to the control device, the short-circuit-current I_{sc} (27.2 vs.19.0μA/cm^2), global efficiency η(0.030% vs. 0.015%), and maximum EQE (1.06 vs. 0.58%) are all improved.

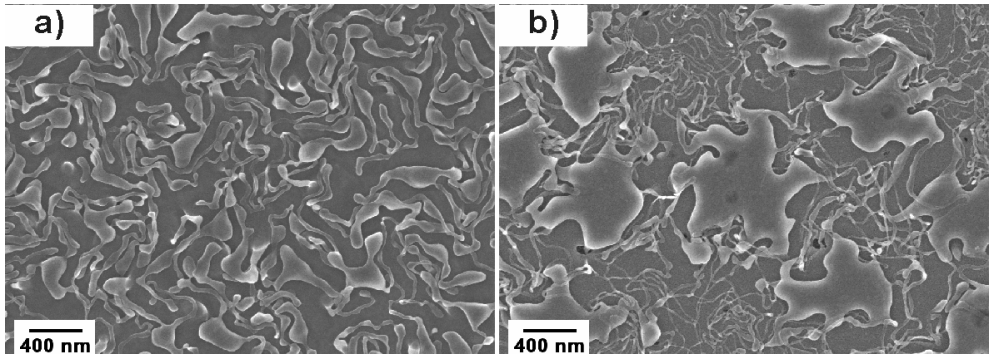

Figure 78. *SEM image of the TiO_2 nanowires on bare Si wafer (**a**) and TiO_2 barrier coated Si wafer (**b**).*

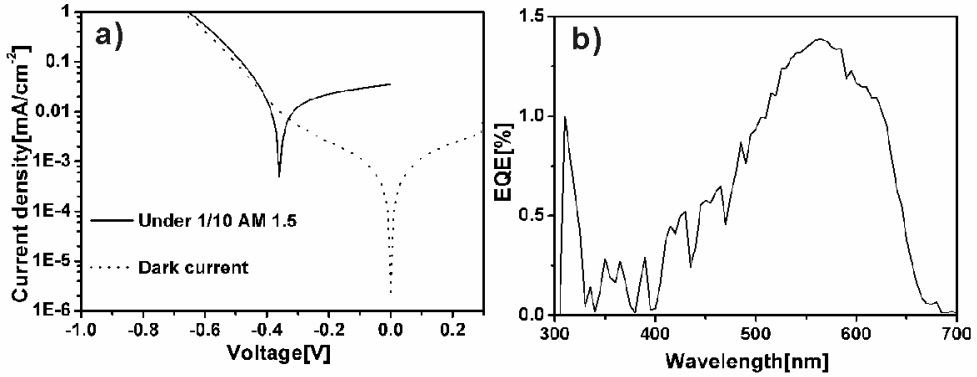

Figure 79. *The maximum performance of the solar cell with TiO_2 nanowires (**a**) I-V curve, (**b**) EQE profile.*

4.5.2.9 Nanogranular

The TiO_2 nanogranular structures on both bare (**Figure 80a**) and TiO_2 barrier layer coated Si wafer (**Figure 80b**) are shown in the SEM images, where very similar morphologies are present on both substrates. The *I-V* profile of the solar cell device composed of TiO_2 nanogranulars is exhibited in **Figure 81a**, where a maximum global efficiency of 0.02%, I_{sc} 23μA/cm^2, Voc 0.24V, FF 0.34, and maximum EQE 1.44% (**Figure 81b**) are recorded. Average performance obtained from five pixels is as following: I_{sc}, 19.6±3.29μA/cm^2, V_{oc}, 0.280±0.034V, FF, 0.346±0.029,η, 0.02±0.00%, and maximum EQE 1.12±0.27% (whole data set seen in **Table S-9** in appendix). Even though the performance of the devices with nanogranulars is very low, a slight improvement compared to the control deices with only TiO_2 barrier layer is still observed. For example, the global efficiency is improved from 0.015% to 0.02% and EQE is increased from 0.58% to 1.12%.

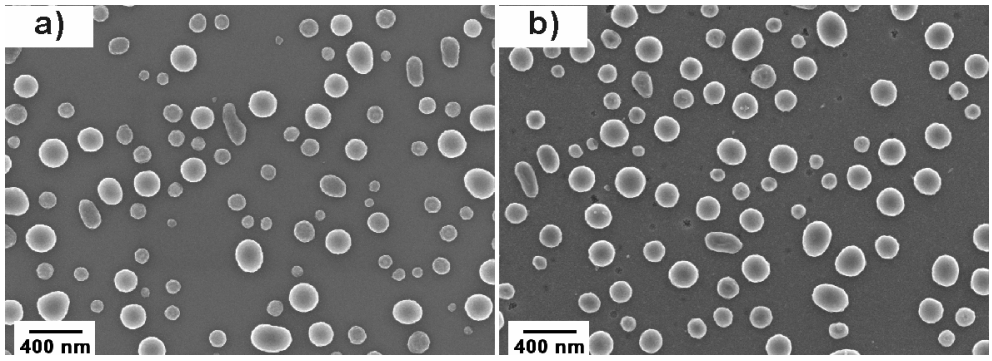

***Figure 80**. SEM image of the TiO_2 nanogranular on bare Si wafer (**a**) and TiO_2 barrier coated Si wafer (**b**).*

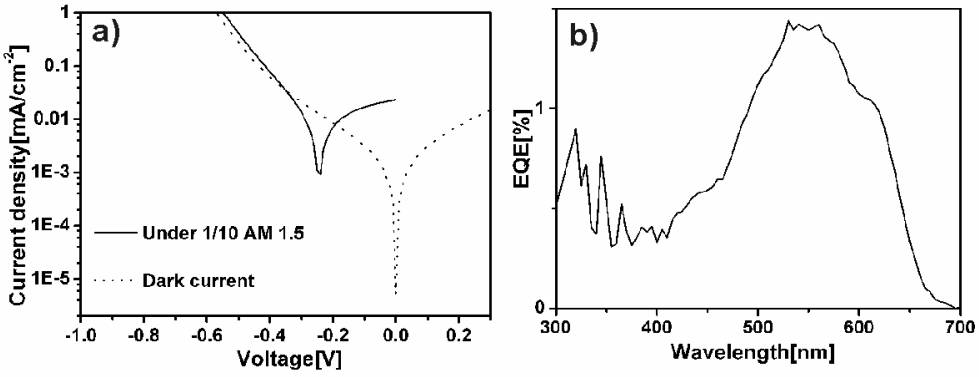

***Figure 81**. The maximum performance of the solar cell with TiO_2 nanogranulars (**a**) I-V curve, (**b**) EQE profile.*

4.5.2.10 Flakes

Figure 82 shows the structures of the TiO_2 flakes on both bare (**a**) and TiO_2 barrier layer coated Si wafers (**b**). A morphology modificantion is observed from the SEM images; however, both structures can still be defined as flakes. The *I-V* profile of the solar cell device with TiO_2 flakes is presented in **Figure 81a** and corresponding maximum EQE in **Figure 81b**. The maximum global efficiency is 0.03% with an I_{sc} value of 15μA/cm^2, V_{oc} of 0.40V, FF of 0.45, and maximum EQE of 0.87%. The average performance data obtained from eight pixels are as following: I_{sc}, 10.2±2.71μA/cm^2, V_{oc}, 0.312±0.047, FF, 0.459±0.141, and η, 0.014±0.007%, and maximum EQE 0.54±0.20% (whole data set seen in **Table S-10** in appendix). Compared to the performance of the control devices, there is a slight improvement with the maximum global efficiency (0.03% vs. 0.02%), and maximum EQE is also improved (0.87% vs. 0.77%). However, generally the degree of the performance improvement is not as prominent as those in other nanostructured solar cells.

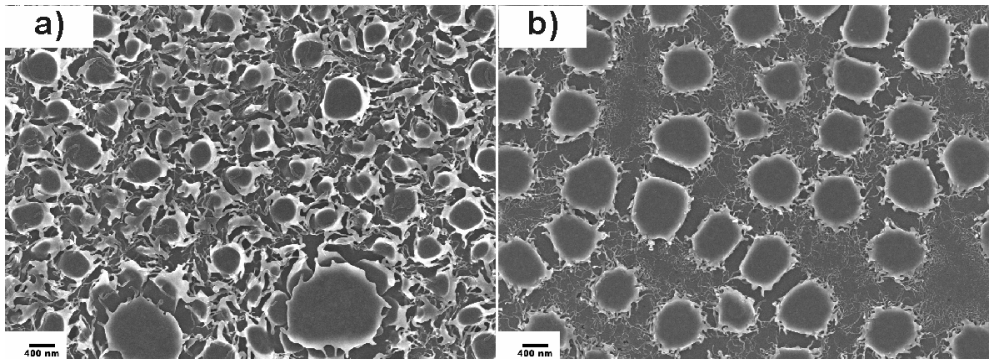

Figure 82. *SEM image of the TiO_2 flakes on bare Si wafer (**a**) and TiO2 barrier coated Si wafer (**b**).*

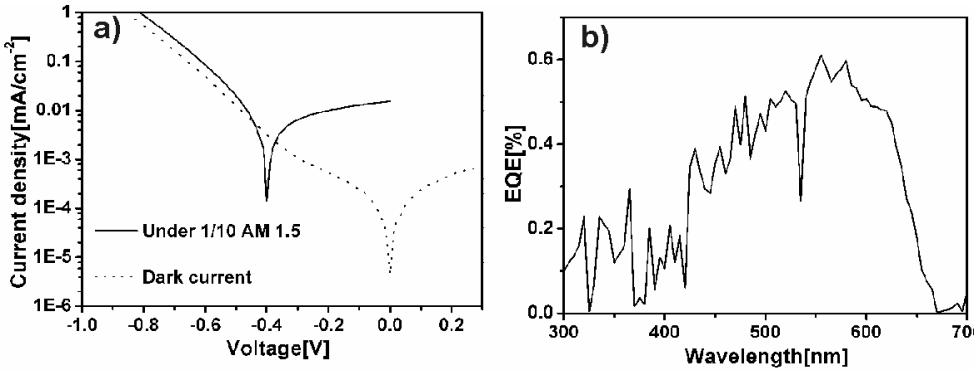

Figure 83*. The maximum performance of the solar cell with TiO_2 flakes (**a**) I-V curve, (**b**) EQE profile.*

4.5.2.11 Summary

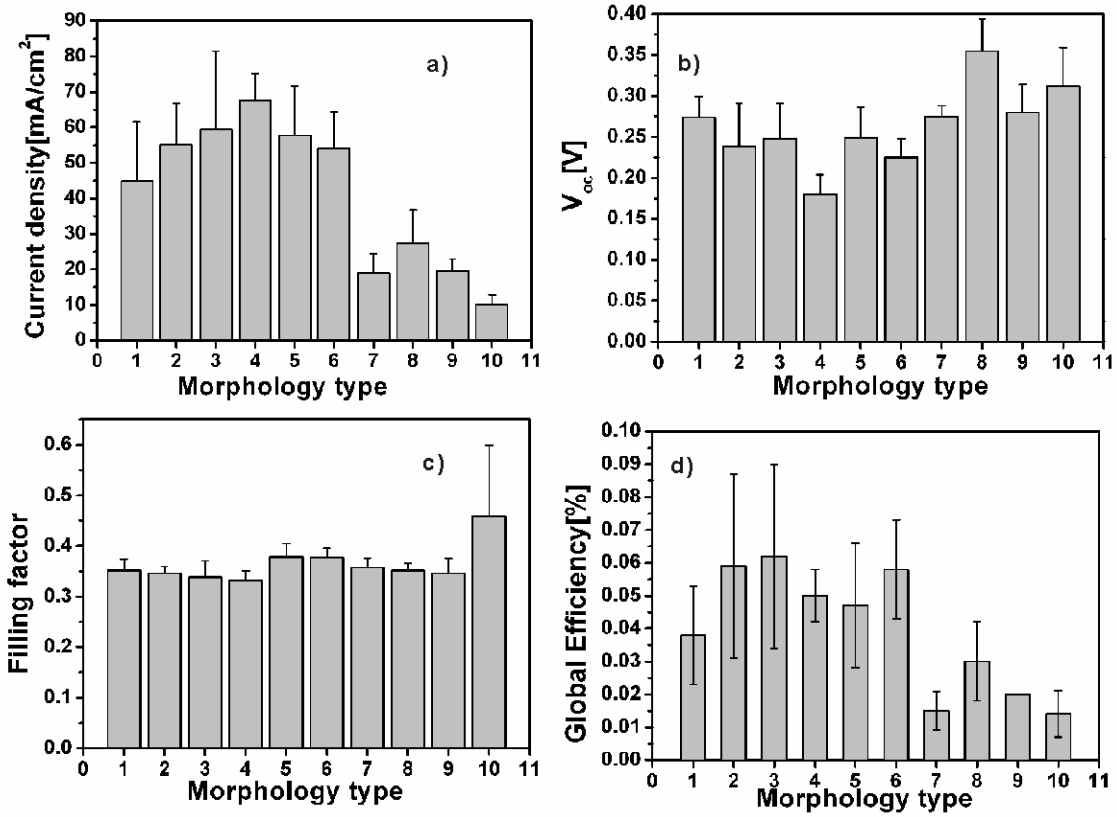

***Figure 84**. Summary of the performance parameters of the solar cell devices (a: short-circuit current density I_{sc}; b: open-circuit voltage V_{oc}; c: filling factor FF; d: global efficiency η) with different morphologies. 1. Control device with only TiO_2 barrier layer; 2. Clustered nanoparticles; 3. Worm like structures; 4. Foam; 5. Large collapsed vesicles; 6. Small vesicles; 7. Control device with only TiO_2 barrier layer from different batch;*

Figure 84 summarizes the mean values of the solar cell characteristic performance parameters with different morphologies. Due to the device fabrication difficulty, the distribution of the data is broad, especially the short-circuit current (I_{sc}) and consequently the global efficiency because the open-circuit voltage V_{oc}, filling factor FF have a relative narrow data distribution. For the devices from the first batch, the TiO_2 films composed of clustered nanoparticles, worm-like structures, foam structures, large collapsed vesicles, and small vesicles yield an evident enhancement of the short-circuit current

compared to the control device with only titania barrier layer (**Figure 84a**). In the second batch device, even though generally the short-circuit current is decreased compared that of the first batch device, a slight increase of the short-circuit current is still observed for the device with nanowires and nanogranular titania films (**Figure 84a**). Compared to I_{sc}, the open circuit voltage V_{oc} does not show a clear modification when the additional nanostructured titania layer is introduced into the solar cell devices. Furthermore, there is no a clear evident correlation between V_{oc} and the type of morphology. This phenomenon is reasonable because V_{oc} is mainly dependent on the Fermi level of TiO_2, which is influenced by the crystallinity rather than the morphology of TiO_2. In the fabrication process the same calcination recipe is applied on all of the as-prepared titania-block copolymer composite films, as a result, the crystallographic lattices of the TiO_2 films are generally all of anatase without a big difference in crystallinity. Therefore the open circuit voltage does not show an evident change along with the morphology. The fluctuation of the V_{oc} value is mainly due to the technique details in the device fabrication. The filling factors of the devices do not show big change from morphology to morphology except the flakes (**Figure 84c**). As a result, first, the devices with additional nanostructured TiO_2 layers exhibit an improved global efficiency compared to the control device with only barrier layer (**Figure 84d**) in both two batches; second, it seems that the morphologies of clustered nanoparticles, worm like structures, foam, large collapsed vesicles, and small vesicles can yield a better performance compared to nanowires, small vesicles, and flakes.

Generally, TiO_2 thin films with different morphologies have been successfully introduced into dye-sensitized solar cells. Compared to the control solar cell devices with only TiO_2 barrier layer, all of the TiO_2 nanostructured thin films help to improve the performance of the solar cell devices no matter what the specific morphology is. The origin of the performance improvement comes from the enhancement of the short-circuit current. This is reasonable because the presence of the TiO_2 nanostructured layer provide additional surface area for the adsorption of dye molecules and further electron transport paths compared to compact TiO_2 barrier layer itself. Among all of the morphologies, clustered nanoparticles, worm like structures, foam, large collapsed vesicles, and small vesicles exhibit a relatively more pronounced improvement of the performance than the morphologies of nanowires, small vesicles, and flakes. This makes the above mentioned morphologies potentially interesting candidates for further studies on the correlation between morphology and solar cell performance.

Chapter5. Conclusions

A new strategy based on good-poor solvent pair induced phase separation process has been developed to control the morphology of TiO_2 thin films, when anphiphilic block copolymer is used as a templating agent, coupled with sol-gel chemistry. The amphiphilic block copolymer exploited as templating agents include diblock copolymers of PS-b-PEO and PMMA-b-PEO, and triblock copolymer of PEO-b-PS-b-PEO. 1, 4-dioxane (in PS-b-PEO and PMMA-b-PEO systems) or DMF (in PEO-b-PS-b-PEO system) has been applied a good solvent for both hydrophobic and hydrophilic blocks; concentrated HCl was used as a poor solvent for the hydrophobic block and catalyst for the sol-gel chemistry process as well, and TTIP was used the precursor of sol-gel chemistry to introduce the titania species. The relative composition ratios of the solution components control the shape and size of the polymer micells in the solution.

Especially in the case of PS-b-PEO templating system, a ternary morphology phase diagram of TiO_2-block copolymer composite films has been mapped where a systematic variation of the relative ratios among 1, 4-dioxane, HCl, and TTIP lead to a variety of different morphologies with a copolymer concentration fixed at 1.wt %. The influence of different parameters on the morphologies of the composite films have been investigated including the copolymer concentration, sol-gel reaction time, external humidity, calcination temperature. It has been found a morphology evolution from nanovesicles to lamella with increasing block copolymer concentration from 0.25 to 4.0 wt. %, which further proves the lyotropic templating effect of the block copolymer. The sol-gel reaction time experiment proved that there is no significant morphology change within 5 hours and nevertheless, an obvious morphology change was observed after 25 hours and even more evident after 50 hours, which have been confirmed by both imaging characterization and dynamic light scattering experiment. The calcination studies show that the nanostructured films are robust enough to survive calcination up to 500°C, which is more stable than reports from other groups. The reason is probably due to the limited anisotropic shrinkage originating from the nature of the thin film. The humidity investigation shows that within the frame studied, the humidity does not really change the type of the morphologies, even though details of the structures can be changed. Further detailed structure analysis of the films with different morphologies has been conducted by the combination of imaging analysis and x-ray scattering techniques. Where three-dimension structural pictures of the films containing the vertical

structures normal to the substrate and corresponding horizontal structures parallel to the substrate have been built.

X-ray reflectivity experiments revealed the existence of an additional thin titania layer beneath the nanostructured layer due to the preferential wetting of sol-gel solution on the substrate. GISAXS measurements provide further long range lateral structure information of the nanostructured films. Concerning the crystallinity, the amorphous as-prepared titania-block copolymer composite films are converted to anatase phase at temperatures above 400°C.

The studies on the templating system of PMMA-b-PEO have proved that the strategy of good-poor solvent pair induced phase separation process is generally applicable not only to PS-b-PEO, but also to other amphiphilic diblock copolymers. A morphology evolution from nanovesicles to nanoplatelets has been observed when the weight ratio of TTIP is systematically increased, which is in agreement with the results from the PS-b-PEO templating system. Further detailed structure analysis of the films by x-ray reflectivity and GISAXS were also conducted to build a three-dimensional structural picture of the film.

The use of triblock ampiphilic block copolymer of PEO-PS-PEO coupled with the strategy has provided a new route to achieve macroporous TiO_2 film, which has an extraordinary stability to survive calcination up to 1000°C. Therefore it allows possible to achieve ordered macroporous TiO_2 films of both anatase and rutile phases under calcination temperatures at 550 and 1000°C respectively.

Based on the knowledge how to control the morphologies, TiO_2 nanostructured thin films with different morphologies in the ternary morphology phase diagram have been successfully introduced into dye-sensitized solar cells. It has been found that the presence of an additional nanostructured TiO_2 layer helps to improve the solar cell performance including the short-circuit-current and global efficiency, and maximum external quantum efficiency, no matter what the morphology it is. Especially, these studies have revealed that the TiO_2 films composed of clustered nanoparticles, worm, foam, and small vesicles improve the solar cell performance more prominent than other morphologies, which makes these morphologies interesting for further structure tuning to optimize the solar cell performance.

Literature

[1] M. Ni, M. K. H. Leung, D. Y. C. Leung, K. Sumathy, *Renewable & Sustainable Energy Reviews* **2007**, *11*, 401.

[2] C. McCullagh, J. M. C. Robertson, D. W. Bahnemann, P. K. J. Robertson, *Research on Chemical Intermediates* **2007**, *33*, 359.

[3] J. Blanco-Galvez, P. Fernandez-Ibanez, S. Malato-Rodriguez, *Journal of Solar Energy Engineering-Transactions of the Asme* **2007**, *129*, 4.

[4] H. M. Yates, M. G. Nolan, D. W. Sheel, M. E. Pemble, *Journal of Photochemistry and Photobiology a-Chemistry* **2006**, *179*, 213.

[5] Y. Shen, F. J. Ren, H. J. Liu, *Rare Metal Materials and Engineering* **2006**, *35*, 1841.

[6] D. G. Shchukin, D. V. Sviridov, *Journal of Photochemistry and Photobiology C-Photochemistry Reviews* **2006**, *7*, 23.

[7] V. Augugliaro, M. Litter, L. Palmisano, J. Soria, *Journal of Photochemistry and Photobiology C-Photochemistry Reviews* **2006**, *7*, 127.

[8] J. C. Zhao, C. C. Chen, W. H. Ma, *Topics in Catalysis* **2005**, *35*, 269.

[9] I. P. Parkin, R. G. Palgrave, *Journal of Materials Chemistry* **2005**, *15*, 1689.

[10] K. Hashimoto, H. Irie, A. Fujishima, *Japanese Journal of Applied Physics Part 1-Regular Papers Brief Communications & Review Papers* **2005**, *44*, 8269.

[11] P. Cheng, M. Y. Gu, Y. P. Jin, *Progress in Chemistry* **2005**, *17*, 8.

[12] V. M. Aroutiounian, V. M. Arakelyan, G. E. Shahnazaryan, *Solar Energy* **2005**, *78*, 581.

[13] B. L. Abrams, J. P. Wilcoxon, *Critical Reviews in Solid State and Materials Sciences* **2005**, *30*, 153.

[14] H. L. Zheng, J. H. Zhang, W. Q. Xiong, *Spectroscopy and Spectral Analysis* **2004**, *24*, 1003.

[15] X. H. Zhang, W. Z. Li, H. Y. Xu, *Progress in Chemistry* **2004**, *16*, 728.

[16] V. Ryabchuk, *International Journal of Photoenergy* **2004**, *6*, 95.

[17] K. Kabra, R. Chaudhary, R. L. Sawhney, *Industrial & Engineering Chemistry Research* **2004**, *43*, 7683.

[18] D. Hufschmidt, L. Liu, V. Selzer, D. Bahnemann, *Water Science and Technology* **2004**, *49*, 135.

[19] O. Carp, C. L. Huisman, A. Reller, *Progress in Solid State Chemistry* **2004**, *32*, 33.

[20] D. Bahnemann, *Solar Energy* **2004**, *77*, 445.

[21] J. Zhao, X. D. Yang, *Building and Environment* **2003**, *38*, 645.

[22] L. Q. Jing, X. J. Sun, J. Shang, W. M. Cai, Z. L. Xu, Y. G. Du, H. G. Fu, *Solar Energy Materials and Solar Cells* **2003**, *79*, 133.

[23] S. Anandan, M. Yoon, *Journal of Photochemistry and Photobiology C-Photochemistry Reviews* **2003**, *4*, 5.

[24] S. C. Ameta, R. Chaudhary, R. Ameta, J. Vardia, *Journal of the Indian Chemical Society* **2003**, *80*, 257.

[25] K. Pirkanniemi, M. Sillanpaa, *Chemosphere* **2002**, *48*, 1047.

[26] D. S. Bhatkhande, V. G. Pangarkar, A. Beenackers, *Journal of Chemical Technology and Biotechnology* **2002**, *77*, 102.

[27] A. Sobczynski, A. Dobosz, *Polish Journal of Environmental Studies* **2001**, *10*, 195.

[28] K. Rajeshwar, N. R. de Tacconi, C. R. Chenthamarakshan, *Chemistry of Materials* **2001**, *13*, 2765.

[29] D. A. Tryk, A. Fujishima, K. Honda, *Electrochimica Acta* **2000**, *45*, 2363.

[30] D. M. Blake, P. C. Maness, Z. Huang, E. J. Wolfrum, J. Huang, W. A. Jacoby, *Separation and Purification Methods* **1999**, *28*, 1.

[31] J. Peral, X. Domenech, D. F. Ollis, *Journal of Chemical Technology and Biotechnology* **1997**, *70*, 117.

[32] D. Y. Goswami, *Journal of Solar Energy Engineering-Transactions of the Asme* **1997**, *119*, 101.

[33] M. I. Litter, J. A. Navio, *Journal of Photochemistry and Photobiology a-Chemistry* **1996**, *98*, 171.

[34] B. Li, L. D. Wang, B. N. Kang, P. Wang, Y. Qiu, *Solar Energy Materials and Solar Cells* **2006**, *90*, 549.

[35] M. Gratzel, *Chemistry Letters* **2005**, *34*, 8.

[36] A. Fujishima, X. T. Zhang, *Proceedings of the Japan Academy Series B-Physical and Biological Sciences* **2005**, *81*, 33.

[37] B. S. Richards, *Progress in Photovoltaics* **2004**, *12*, 253.

[38] M. Gratzel, *Journal of Photochemistry and Photobiology a-Chemistry* **2004**, *164*, 3.

[39] A. J. Frank, N. Kopidakis, J. van de Lagemaat, *Coordination Chemistry Reviews* **2004**, *248*, 1165.

[40] M. Gratzel, *Journal of Photochemistry and Photobiology C-Photochemistry Reviews* **2003**, *4*, 145.

[41] M. Gratzel, *Journal of Sol-Gel Science and Technology* **2001**, *22*, 7.

[42] M. Gratzel, *Nature* **2001**, *414*, 338.

[43] A. Hagfeldt, M. Gratzel, *Accounts of Chemical Research* **2000**, *33*, 269.

[44] M. Gratzel, *Progress in Photovoltaics* **2000**, *8*, 171.

[45] M. Gratzel, *Current Opinion in Colloid & Interface Science* **1999**, *4*, 314.

[46] K. Kalyanasundaram, M. Gratzel, *Coordination Chemistry Reviews* **1998**, *177*, 347.

[47] A. Hagfeldt, M. Gratzel, *Chemical Reviews* **1995**, *95*, 49.

[48] A. Slaoui, R. T. Collins, *Mrs Bulletin* **2007**, *32*, 211.

[49] F. Dimroth, S. Kurtz, *Mrs Bulletin* **2007**, *32*, 230.

[50] L. Schmidt-Mende, W. M. Campbell, Q. Wang, K. W. Jolley, D. L. Officer, M. K. Nazeeruddin, M. Gratzel, *Chemphyschem* **2005**, *6*, 1253.

[51] A. J. Chatten, S. M. Tuladhar, S. A. Choulis, D. D. C. Bradley, J. Nelson, *Journal of Materials Science* **2005**, *40*, 1393.

[52] S. Akbar, P. Dutta, C. H. Lee, *International Journal of Applied Ceramic Technology* **2006**, *3*, 302.

[53] C. A. Grimes, *Journal of Materials Chemistry* **2007**, *17*, 1451.

[54] Y. K. Jun, H. S. Kim, J. H. Lee, S. H. Hong, *Sensors and Actuators B-Chemical* **2006**, *120*, 69.

[55] Y. Shimizu, T. Hyodo, M. Egashira, *Sensors and Actuators B-Chemical* **2007**, *121*, 219.

[56] O. K. Varghese, C. A. Grimes, *Journal of Nanoscience and Nanotechnology* **2003**, *3*, 277.

[57] M. Wagemaker, W. L. H. Borghols, E. R. H. van Eck, A. P. M. Kentgens, G. L. Kearley, F. M. Mulder, *Chemistry-a European Journal* **2007**, *13*, 2023.

[58] M. K. Nazeeruddin, R. T. Wegh, Z. Zhou, C. Klein, Q. Wang, F. De Angelis, S. Fantacci, M. Gratzel, *Inorganic Chemistry* **2006**, *45*, 9245.

[59] V. Subramanian, A. Karki, K. I. Gnanasekar, F. P. Eddy, B. Rambabu, *Journal of Power Sources* **2006**, *159*, 186.

[60] L. J. Fu, H. Liu, H. P. Zhang, C. Li, T. Zhang, Y. P. Wu, H. Q. Wu, *Journal of Power Sources* **2006**, *159*, 219.

[61] H. S. Zhou, D. L. Li, M. Hibino, I. Honma, *Angewandte Chemie-International Edition* **2005**, *44*, 797.

[62] A. R. Armstrong, G. Armstrong, J. Canales, P. G. Bruce, *Journal of Power Sources* **2005**, *146*, 501.

[63] J. W. Long, B. Dunn, D. R. Rolison, H. S. White, *Chemical Reviews* **2004**, *104*, 4463.

[64] M. Hibino, K. Abe, M. Mochizuki, M. Miyayama, *Journal of Power Sources* **2004**, *126*, 139.

[65] Y. K. Zhou, L. Cao, F. B. Zhang, B. L. He, H. L. Li, *Journal of the Electrochemical Society* **2003**, *150*, A1246.

[66] M. Wagemaker, A. P. M. Kentgens, F. M. Mulder, *Nature* **2002**, *418*, 397.

[67] C. R. Sides, N. C. Li, C. J. Patrissi, B. Scrosati, C. R. Martin, *Mrs Bulletin* **2002**, *27*, 604.

[68] B. Oregan, M. Gratzel, *Nature* **1991**, *353*, 737.

[69] Z. P. Zhang, S. Ito, B. O'Regan, D. B. Kuang, S. M. Zakeeruddin, P. Liska, R. Charvet, P. Comte, M. K. Nazeeruddin, P. Pechy, R. Humphry-Baker, T. Koyanagi, T. Mizuno, M. Gratzel, *Zeitschrift Fur Physikalische Chemie-International Journal of Research in Physical Chemistry & Chemical Physics* **2007**, *221*, 319.

[70] J. M. Kroon, N. J. Bakker, H. J. P. Smit, P. Liska, K. R. Thampi, P. Wang, S. M. Zakeeruddin, M. Gratzel, A. Hinsch, S. Hore, U. Wurfel, R. Sastrawan, J. R. Durrant, E. Palomares, H. Pettersson, T. Gruszecki, J. Walter, K. Skupien, G. E. Tulloch, *Progress in Photovoltaics* **2007**, *15*, 1.

[71] H. J. Snaith, M. Gratzel, *Applied Physics Letters* **2006**, *89*.

[72] L. Schmidt-Mende, M. Gratzel, *Thin Solid Films* **2006**, *500*, 296.

[73] M. Zukalova, A. Zukal, L. Kavan, M. K. Nazeeruddin, P. Liska, M. Gratzel, *Nano Letters* **2005**, *5*, 1789.

[74] L. Schmidt-Mende, S. M. Zakeeruddin, M. Gratzel, *Applied Physics Letters* **2005**, *86*.

[75] L. Schmidt-Mende, U. Bach, R. Humphry-Baker, T. Horiuchi, H. Miura, S. Ito, S. Uchida, M. Gratzel, *Advanced Materials* **2005**, *17*, 813.

[76] P. Wang, S. M. Zakeeruddin, J. E. Moser, M. K. Nazeeruddin, T. Sekiguchi, M. Gratzel, *Nature Materials* **2003**, *2*, 402.

[77] P. Wang, S. M. Zakeeruddin, R. Humphry-Baker, J. E. Moser, M. Gratzel, *Advanced Materials* **2003**, *15*, 2101.

[78] P. Wang, S. M. Zakeeruddin, P. Comte, R. Charvet, R. Humphry-Baker, M. Gratzel, *Journal of Physical Chemistry B* **2003**, *107*, 14336.

[79] M. Law, L. E. Greene, J. C. Johnson, R. Saykally, P. D. Yang, *Nature Materials* **2005**, *4*, 455.

[80] M. C. Yan, F. Chen, J. L. Zhang, M. Anpo, *Journal of Physical Chemistry B* **2005**, *109*, 8673.

[81] M. J. Cass, A. B. Walker, D. Martinez, L. M. Peter, *Journal of Physical Chemistry B* **2005**, *109*, 5100.

[82] J. B. Baxter, E. S. Aydil, *Applied Physics Letters* **2005**, *86*.

[83] Z. S. Wang, H. Kawauchi, T. Kashima, H. Arakawa, *Coordination Chemistry Reviews* **2004**, *248*, 1381.

[84] P. D. Cozzoli, A. Kornowski, H. Weller, *Journal of the American Chemical Society* **2003**, *125*, 14539.

[85] A. F. Wells, *Structural Inorganic Chemistry*, Clarendon Press: Oxford, **1975**.

[86] B. Peng, G. Jungmann, C. Jager, D. Haarer, H. W. Schmidt, M. Thelakkat, *Coordination Chemistry Reviews* **2004**, *248*, 1479.

[87] P. C. A. Alberius, K. L. Frindell, R. C. Hayward, E. J. Kramer, G. D. Stucky, B. F. Chmelka, *Chem Mater* **2002**, *14*, 3284.

[88] G. Armstrong, A. R. Armstrong, J. Canales, P. G. Bruce, *Chemical Communications* **2005**, 2454.

[89] N. Bai, S. G. Li, H. Y. Chen, W. Q. Pang, *Journal of Materials Chemistry* **2001**, *11*, 3099.

[90] F. Carn, A. Colin, M. F. Achard, H. Deleuze, C. Sanchez, R. Backov, *Advanced Materials* **2005**, *17*, 62.

[91] Y. H. Cho, G. Cho, J. S. Lee, *Advanced Materials* **2004**, *16*, 1814.

[92] S. Y. Choi, M. Mamak, S. Speakman, N. Chopra, G. A. Ozin, *Small* **2005**, *1*, 226.

[93] D. Grosso, E. L. Crepaldi, G. J. D. Illia, F. Cagnol, N. Baccile, F. Babonneau, P. A. Albouy, H. Amenitsch, C. Sanchez, *Stud Surf Sci Catal* **2003**, *146*, 281.

[94] X. P. Gao, H. Y. Zhu, G. L. Pan, S. H. Ye, Y. Lan, F. Wu, D. Y. Song, *Journal of Physical Chemistry B* **2004**, *108*, 2868.

[95] M. S. Doescher, J. J. Pietron, B. M. Dening, J. W. Long, C. P. Rhodes, C. A. Edmondson, D. R. Rolison, *Analytical Chemistry* **2005**, *77*, 7924.

[96] D. L. Liao, B. Q. Liao, *Journal of Photochemistry and Photobiology a-Chemistry* **2007**, *187*, 363.

[97] D. O. de Zarate, C. Boissiere, D. Grosso, P. A. Albouy, H. Amenitsch, P. Amoros, C. Sanchez, *New Journal of Chemistry* **2005**, *29*, 141.

[98] T. A. Crowley, B. Daly, M. A. Morris, D. Erts, O. Kazakova, J. J. Boland, B. Wu, J. D. Holmes, *Journal of Materials Chemistry* **2005**, *15*, 2408.

[99] M. Pal, J. G. Serrano, P. Santiago, U. Pal, *Journal of Physical Chemistry C* **2007**, *111*, 96.

[100] P. D. Yang, D. Y. Zhao, D. I. Margolese, B. F. Chmelka, G. D. Stucky, *Nature* **1998**, *396*, 152.

[101] M. H. Bartl, S. P. Puls, J. Tang, H. C. Lichtenegger, G. D. Stucky, *Angew Chem Int Edit* **2004**, *43*, 3037.

[102] C. Boissiere, D. Grosso, S. Lepoutre, L. Nicole, A. B. Bruneau, C. Sanchez, *Langmuir* **2005**, *21*, 12362.

[103] F. Cagnol, D. Grosso, G. J. D. A. S. Soler-Illia, E. L. Crepaldi, F. Babonneau, H. Amenitsch, C. Sanchez, *J Mater Chem* **2003**, *13*, 61.

[104] E. L. Crepaldi, D. Grosso, G. J. D. A. Soler-Illia, P. A. Albouy, H. Amenitseh, C. Sanchez, *Chem Mater* **2002**, *14*, 3316.

[105] A. Gibaud, D. Grosso, B. Smarsly, A. Baptiste, J. F. Bardeau, F. Babonneau, D. A. Doshi, Z. Chen, C. J. Brinker, C. Sanchez, *J Phys Chem B* **2003**, *107*, 6114.

[106] D. Grosso, F. Babonneau, C. Sanchez, G. J. D. A. Soler-Illia, E. L. Crepaldi, P. A. Albouy, H. Amenitsch, A. R. Balkenende, A. Brunet-Bruneau, *J Sol-Gel Sci Techn* **2003**, *26*, 561.

[107] D. Grosso, C. Boissiere, B. Smarsly, T. Brezesinski, N. Pinna, P. A. Albouy, H. Amenitsch, M. Antonietti, C. Sanchez, *Nat Mater* **2004**, *3*, 787.

[108] D. Grosso, F. Cagnol, G. J. D. A. Soler-Illia, E. L. Crepaldi, H. Amenitsch, A. Brunet-Bruneau, A. Bourgeois, C. Sanchez, *Advanced Functional Materials* **2004**, *14*, 309.

[109] W. B. Hong, M. Bersani, G. Stucky, *Abstr Pap Am Chem S* **2004**, *227*, U1427.

[110] J. Livage, C. Sanchez, *Actual Chimique* **2005**, 72.

[111] T. A. Ostomel, G. D. Stucky, *Chem Commun* **2004**, 1016.

[112] C. Sanchez, B. Julian, P. Belleville, M. Popall, *J Mater Chem* **2005**, *15*, 3559.

[113] C. Sanchez, F. Ribot, L. Rozes, B. Alonso, *Mol Cryst Liq Cryst* **2000**, *354*, 731.

[114] C. Sanchez, G. J. D. A. Soler-Illia, F. Ribot, D. Grosso, *Cr Chim* **2003**, *6*, 1131.

[115] C. Sanchez, G. J. D. A. Soler-Illia, F. Ribot, T. Lalot, C. R. Mayer, V. Cabuil, *Chem Mater* **2001**, *13*, 3061.

[116] B. Smarsly, D. Grosso, T. Brezesinski, N. Pinna, C. Boissiere, M. Antonietti, C. Sanchez, *Chem Mater* **2004**, *16*, 2948.

[117] E. L. Crepaldi, G. Soler-Illia, D. Grosso, M. Sanchez, *New Journal of Chemistry* **2003**, *27*, 9.

[118] G. J. A. A. Soler-Illia, E. L. Crepaldi, D. Grosso, D. Durand, C. Sanchez, *Chem Commun* **2002**, 2298.

[119] G. J. D. A. Soler-Illia, A. Louis, C. Sanchez, *Chem Mater* **2002**, *14*, 750.

[120] N. Steunou, S. Forster, P. Florian, C. Sanchez, M. Antonietti, *J Mater Chem* **2002**, *12*, 3426.

[121] J. Tang, Y. Y. Wu, E. W. McFarland, G. D. Stucky, *Chem Commun* **2004**, 1670.

[122] P. D. Yang, D. Y. Zhao, D. I. Margolese, B. F. Chmelka, G. D. Stucky, *Chem Mater* **1999**, *11*, 2813.

[123] G. J. D. Soler-illia, C. Sanchez, B. Lebeau, J. Patarin, *Chemical Reviews* **2002**, *102*, 4093.

[124] P. C. Angelome, S. Aldabe-Bilmes, M. E. Calvo, E. L. Crepaldi, D. Grosso, C. Sanchez, G. Soler-Illia, *New Journal of Chemistry* **2005**, *29*, 59.

[125] S. Y. Choi, B. Lee, D. B. Carew, M. Mamak, F. C. Peiris, S. Speakman, N. Chopra, G. A. Ozin, *Advanced Functional Materials* **2006**, *16*, 1731.

[126] K. X. Wang, M. A. Morris, J. D. Holmes, *Chemistry of Materials* **2005**, *17*, 1269.

[127] D. Grosso, C. Boissiere, C. Sanchez, *Abstracts of Papers of the American Chemical Society* **2005**, *229*, U720.

[128] M. H. Bartl, S. W. Boettcher, K. L. Frindell, G. D. Stucky, *Accounts Chem Res* **2005**, *38*, 263.

[129] G. Soler-Illia, E. L. Crepaldi, D. Grosso, C. Sanchez, *Current Opinion in Colloid & Interface Science* **2003**, *8*, 109.

[130] H. M. Luo, C. Wang, Y. S. Yan, *Chemistry of Materials* **2003**, *15*, 3841.

[131] D. Grosso, G. Soler-Illia, E. L. Crepaldi, F. Cagnol, C. Sinturel, A. Bourgeois, A. Brunet-Bruneau, H. Amenitsch, P. A. Albouy, C. Sanchez, *Chemistry of Materials* **2003**, *15*, 4562.

[132] J. C. Yu, L. Z. Zhang, J. G. Yu, *Chemistry of Materials* **2002**, *14*, 4647.

[133] B. K. Cho, A. Jain, S. M. Gruner, U. Wiesner, *Science* **2004**, *305*, 1598.

[134] B. K. Cho, A. Jain, S. Mahajan, H. Ow, S. M. Gruner, U. Wiesner, *Journal of the American Chemical Society* **2004**, *126*, 4070.

[135] B. K. Cho, A. Jain, J. Nieberle, S. Mahajan, U. Wiesner, S. M. Gruner, S. Turk, H. J. Rader, *Macromolecules* **2004**, *37*, 4227.

[136] A. C. Finnefrock, R. Ulrich, G. E. S. Toombes, S. M. Gruner, U. Wiesner, *Journal of the American Chemical Society* **2003**, *125*, 13084.

[137] C. Garcia, Y. M. Zhang, F. DiSalvo, U. Wiesner, *Angewandte Chemie-International Edition* **2003**, *42*, 1526.

[138] C. B. W. Garcia, Y. M. Zhang, S. Mahajan, F. DiSalvo, U. Wiesner, *Journal of the American Chemical Society* **2003**, *125*, 13310.

[139] A. Jain, G. E. S. Toombes, L. M. Hall, S. Mahajan, C. B. W. Garcia, W. Probst, S. M. Gruner, U. Wiesner, *Angewandte Chemie-International Edition* **2005**, *44*, 1226.

[140] A. Jain, U. Wiesner, *Macromolecules* **2004**, *37*, 5665.

[141] M. Kamperman, C. B. W. Garcia, P. Du, H. S. Ow, U. Wiesner, *Journal of the American Chemical Society* **2004**, *126*, 14708.

[142] S. Renker, S. Mahajan, D. T. Babski, I. Schnell, A. Jain, J. Gutmann, Y. M. Zhang, S. M. Gruner, H. W. Spiess, U. Wiesner, *Macromolecular Chemistry and Physics* **2004**, *205*, 1021.

[143] A. Thomas, H. Schlaad, B. Smarsly, M. Antonietti, *Langmuir* **2003**, *19*, 4455.

[144] S. C. Warren, F. J. Disalvo, U. Wiesner, *Nature Materials* **2007**, *6*, 156.

[145] U. Wiesner, in *Nanotechnology in Mesostructured Materials*, Vol. 146, **2003**, 407.

[146] D. H. Kim, Z. C. Sun, T. P. Russell, W. Knoll, J. S. Gutmann, *Advanced Functional Materials* **2005**, *15*, 1160.

[147] C. C. Oey, A. B. Djurisic, H. Wang, K. K. Y. Man, W. K. Chan, M. H. Xie, Y. H. Leung, A. Pandey, J. M. Nunzi, P. C. Chui, *Nanotechnology* **2006**, *17*, 706.

[148] Z. Sun, M. Wolkenhauer, G. G. Bumbu, D. H. Kim, J. S. Gutmann, *Physica B-Condensed Matter* **2005**, *357*, 141.

[149] Z. C. Sun, D. H. Kim, M. Wolkenhauer, G. G. Bumbu, W. Knoll, J. S. Gutmann, *Chemphyschem* **2006**, *7*, 370.

[150] H. Wang, C. C. Oey, A. B. Djurisic, M. H. Xie, Y. H. Leung, K. K. Y. Man, W. K. Chan, A. Pandey, J. M. Nunzi, P. C. Chui, *Applied Physics Letters* **2005**, *87*.

[151] C. Wnag, Q. Wnag, G. H. Qiu, *Acta Polymerica Sinica* **2006**, 1038.

[152] M. Groenewolt, T. Brezesinski, H. Schlaad, M. Antonietti, P. W. Groh, B. Ivan, *Advanced Materials* **2005**, *17*, 1158.

[153] D. H. Kim, S. H. Kim, K. Lavery, T. P. Russell, *Nano Letters* **2004**, *4*, 1841.

[154] J. Wu, A. Eisenberg, *J Am Chem Soc* **2006**, *128*, 2880.

[155] X. Y. Liu, J. Wu, J. S. Kim, A. Eisenberg, *Langmuir* **2006**, *22*, 419.

[156] P. L. Soo, A. Eisenberg, *J Polym Sci Pol Phys* **2004**, *42*, 923.

[157] I. C. Riegel, F. M. de Bittencourt, O. Terrau, A. Eisenberg, C. L. Petzhold, D. Samios, *Pure Appl Chem* **2004**, *76*, 123.

[158] E. A. Lysenko, P. S. Chelushkin, T. K. Bronich, A. Eisenberg, V. A. Kabanov, A. V. Kabanov, *J Phys Chem B* **2004**, *108*, 12352.

[159] A. A. Choucair, A. H. Kycia, A. Eisenberg, *Langmuir* **2003**, *19*, 1001.

[160] A. Choucair, A. Eisenberg, *J Am Chem Soc* **2003**, *125*, 11993.

[161] A. Choucair, A. Eisenberg, *Eur Phys J E* **2003**, *10*, 37.

[162] I. C. Riegel, A. Eisenberg, C. L. Petzhold, D. Samios, *Langmuir* **2002**, *18*, 3358.

[163] E. A. Lysenko, T. K. Bronich, E. V. Slonkina, A. Eisenberg, V. A. Kabanov, A. V. Kabanov, *Macromolecules* **2002**, *35*, 6351.

[164] D. E. Discher, A. Eisenberg, *Science* **2002**, *297*, 967.

[165] T. K. Bronich, O. Y. Ming, V. A. Kabanov, A. Eisenberg, F. C. Szoka, A. V. Kabanov, *J Am Chem Soc* **2002**, *124*, 11872.

[166] L. F. Zhang, A. Eisenberg, *J Polym Sci Pol Phys* **1999**, *37*, 1469.

[167] H. W. Shen, L. F. Zhang, A. Eisenberg, *J Am Chem Soc* **1999**, *121*, 2728.

[168] H. W. Shen, A. Eisenberg, *J Phys Chem B* **1999**, *103*, 9473.

[169] Y. S. Yu, L. F. Zhang, A. Eisenberg, *Macromolecules* **1998**, *31*, 1144.

[170] M. Moffitt, H. Vali, A. Eisenberg, *Chem Mater* **1998**, *10*, 1021.

[171] E. A. Lysenko, T. K. Bronich, A. Eisenberg, V. A. Kabanov, A. V. Kabanov, *Macromolecules* **1998**, *31*, 4516.

[172] J. X. Zhao, C. Allen, A. Eisenberg, *Macromolecules* **1997**, *30*, 7143.

[173] L. F. Zhang, H. W. Shen, A. Eisenberg, *Macromolecules* **1997**, *30*, 1001.

[174] Y. S. Yu, A. Eisenberg, *J Am Chem Soc* **1997**, *119*, 8383.

[175] K. Yu, A. Eisenberg, *Macromolecules* **1998**, *31*, 3509.

[176] L. F. Zhang, A. Eisenberg, *Macromolecules* **1996**, *29*, 8805.

[177] L. F. Zhang, A. Eisenberg, *Polymers for Advanced Technologies* **1998**, *9*, 677.

[178] S. E. Burke, A. Eisenberg, *Langmuir* **2001**, *17*, 8341.

[179] K. Yu, A. Eisenberg, *Macromolecules* **1996**, *29*, 6359.

[180] F. T. Liu, A. Eisenberg, *Journal of the American Chemical Society* **2003**, *125*, 15059.

[181] L. B. Luo, A. Eisenberg, *Langmuir* **2001**, *17*, 6804.

[182] F. S. Bates, *Science* **1991**, *251*, 898.

[183] P. J. Flory, *Principles of Polymer Chemistry*, Cornell Univ. Press, Ithaca, NY, **1953**.

[184] P.-G. deGennes, *Scaling Concepts in Polymer Physics*, Cornell Univ. Press, Ithaca, NY, **1979**.

[185] P. J. Flory, *Journal of the American Chemical Society* **1965**, *87*, 1833.

[186] L. P. McMaster, *Macromolecules* **1973**, *6*, 760.

[187] I. C. Sanchez, *in Polymer blends*, Vol. 1, Academic Press, New York, **1978**.

[188] F. S. Bates, G. H. Fredrickson, *Annual Review of Physical Chemistry* **1990**, *41*, 525.

[189] H. Hasegawa, H. Tanaka, K. Yamasaki, T. Hashimoto, *Macromolecules* **1987**, *20*, 1651.

[190] D. S. Herman, D. J. Kinning, E. L. Thomas, L. J. Fetters, *Macromolecules* **1987**, *20*, 2940.

[191] Y. H. Wei, C. Y. Pan, B. Y. Li, Y. C. Han, *Journal of Chemical Physics* **2007**, *126*.

[192] J. Holoubek, J. Baldrian, J. Lal, *Macromolecular Chemistry and Physics* **2007**, *208*, 739.

[193] I. Gunkel, S. Stepanow, T. Thurn-Albrecht, S. Trimper, *Macromolecules* **2007**, *40*, 2186.

[194] M. A. Adachi, F. Takazawa, N. Tomikawa, M. Tokita, J. Watanabe, *Polymer Journal* **2007**, *39*, 155.

[195] R. A. Segalman, *Materials Science & Engineering R-Reports* **2005**, *48*, 191.

[196] M. Q. Li, C. A. Coenjarts, C. K. Ober, in *Block Copolymers Ii*, Vol. 190, **2005**, 183.

[197] T. Grigorova, S. Pispas, N. Hadjichristidis, T. Thurn-Albrecht, *Macromolecules* **2005**, *38*, 7430.

[198] J. DeRouchey, T. Thurn-Albrecht, T. P. Russell, R. Kolb, *Macromolecules* **2004**, *37*, 2538.

[199] F. Ebert, T. Thurn-Albrecht, *Macromolecules* **2003**, *36*, 8685.

[200] T. Thurn-Albrecht, J. DeRouchey, T. P. Russell, R. Kolb, *Macromolecules* **2002**, *35*, 8106.

[201] T. Thurn-Albrecht, J. Schotter, C. A. Kastle, N. Emley, T. Shibauchi, L. Krusin-Elbaum, K. Guarini, C. T. Black, M. T. Tuominen, T. P. Russell, *Science* **2000**, *290*, 2126.

[202] E. A. Guggenheim, *Thermodynamics*, Elsevier, New York, **1985**.

[203] L. Leibler, *Macromolecules* **1980**, *13*, 1602.

[204] E. Helfand, Z. R. Wasserman, *in developments in block and graft copolymers-1*, Applied Science, New York, 1982.

[205] G. H. Fredrickson, E. Helfand, *Journal of Chemical Physics* **1987**, *87*, 697.

[206] http://en.wikipedia.org/wiki/Atomic_force_microscopy.

[207] http://en.wikipedia.org/wiki/Tapping_AFM.

[208] http://www.mpip-mainz.mpg.de/groups/butt/spmlab/introduction.

[209] M. A. Vandijk, R. Vandenborg, *Macromolecules* **1995**, *28*, 6773.

[210] M. Birkholz, *Thin Film Analysis by X-ray Scattering*, WILEY-VCH Verlag GmbH& Co. KGaA, Weinheim, **2006**.

[211] www1.chm.colostate.edu/Files/XRR.pdf.

[212] www.ias.ac.in/currsci/jun252000/GIBAUD.PDF.

[213] www.mint.ua.edu/Research/ResearchTools/XRRnote_FengHuang-05.pdf.

[214] T. P. Russel, *Materials Science Reports* **1990**, *5*, 171.

[215] http://www.gisaxs.de/.

[216] P. Fratzl, *Journal of Applied Crystallography* **2003**, *36*, 397.

[217] P. Muller-Buschbaum, *Analytical and Bioanalytical Chemistry* **2003**, *376*, 3.

[218] P. Muller-Buschbaum, E. Bauer, S. Pfister, S. V. Roth, M. Burghammer, C. Riekel, C. David, U. Thiele, *Europhysics Letters* **2006**, *73*, 35.

[219] P. Muller-Buschbaum, N. Hermsdorf, S. V. Roth, J. Wiedersich, S. Cunis, R. Gehrke, *Spectrochimica Acta Part B-Atomic Spectroscopy* **2004**, *59*, 1789.

[220] P. Muller-Buschbaum, S. V. Roth, M. Burghammer, E. Bauer, S. Pfister, C. David, C. Riekel, *Physica B-Condensed Matter* **2005**, *357*, 148.

[221] P. Muller-Buschbaum, S. V. Roth, M. Burghammer, A. Diethert, P. Panagiotou, C. Riekel, *Europhysics Letters* **2003**, *61*, 639.

[222] S. V. Roth, R. Dohrmann, M. Dommach, M. Kuhlmann, I. Kroger, R. Gehrke, H. Walter, C. Schroer, B. Lengeler, P. Muller-Buschbaum, *Review of Scientific Instruments* **2006**, *77*.

[223] S. V. Roth, P. Muller-Buschbaum, M. Burghammer, H. Walter, P. Panagiotou, A. Diethert, C. Riekel, *Spectrochimica Acta Part B-Atomic Spectroscopy* **2004**, *59*, 1765.

[224] M. Rauscher, R. Paniago, H. Metzger, Z. Kovats, J. Domke, J. Peisl, H. D. Pfannes, J. Schulze, I. Eisele, *Journal of Applied Physics* **1999**, *86*, 6763.

[225] http://en.wikipedia.org/wiki/Dynamic_light_scattering.

[226] R. L. Xu, M. A. Winnik, F. R. Hallett, G. Riess, M. D. Croucher, *Macromolecules* **1991**, *24*, 87.

[227] B. J. Berne, R. Pecora, *Dynamic Light Scattering: : with Applications to Chemistry, Biology and Physics*, Courier Dover, **2000**.

[228] R. Pecora, *Dynamic Light Scattering: applications of photon correlation spectroscopy* Springer, **1985**.

[229] M. Biancardo, K. West, F. C. Krebs, *Journal of Photochemistry and Photobiology a-Chemistry* **2007**, *187*, 395.

[230] V. Jovanovski, E. Stathatos, B. Orel, P. Lianos, *Thin Solid Films* **2006**, *511*, 634.

[231] F. J. Li, F. Y. Cheng, J. F. Shi, F. S. Cai, M. Liang, J. Chen, *Journal of Power Sources* **2007**, *165*, 911.

[232] H. Matsui, K. Okada, T. Kawashima, T. Ezure, N. Tanabe, R. Kawano, M. Watanabe, *Journal of Photochemistry and Photobiology a-Chemistry* **2004**, *164*, 129.

[233] X. Pan, S. Y. Dai, K. J. Wang, L. H. Hu, C. W. Shi, L. Guo, F. T. Kong, *Chinese Journal of Chemistry* **2005**, *23*, 1579.

[234] H. Paulsson, L. Kloo, A. Hagfeldt, G. Boschloo, *Journal of Electroanalytical Chemistry* **2006**, *586*, 56.

[235] H. Santa-Nokki, S. Busi, J. Kallioinen, M. Lahtinen, J. Korppi-Tommola, *Journal of Photochemistry and Photobiology a-Chemistry* **2007**, *186*, 29.

[236] P. K. Singh, K. I. Kim, J. W. Lee, H. W. Rhee, *Physica Status Solidi a-Applications and Materials Science* **2006**, *203*, R88.

[237] K. Suzuki, M. Yamaguchi, M. Kumagai, N. Tanabe, S. Yanagida, *Comptes Rendus Chimie* **2006**, *9*, 611.

[238] H. Usui, H. Matsui, N. Tanabe, S. Yanagida, *Journal of Photochemistry and Photobiology a-Chemistry* **2004**, *164*, 97.

[239] L. Wang, S. B. Fang, Y. Lin, X. W. Zhou, M. Y. Li, *Chemical Communications* **2005**, 5687.

[240] P. Wang, S. M. Zakeeruddin, J. E. Moser, M. Gratzel, *Journal of Physical Chemistry B* **2003**, *107*, 13280.

[241] S. Yanagida, *Comptes Rendus Chimie* **2006**, *9*, 597.

[242] M. Gratzel, *Inorganic Chemistry* **2005**, *44*, 6841.

[243] L. Kavan, J. Rathousky, M. Gratzel, V. Shklover, A. Zukal, *Microporous and Mesoporous Materials* **2001**, *44*, 653.

[244] F. Fleischhaker, A. C. Arsenault, Z. Wang, V. Kitaev, F. C. Peiris, G. von Freymann, I. Manners, R. Zentel, G. A. Ozin, *Advanced Materials* **2005**, *17*, 2455.

[245] C. Grasso, M. Nanu, A. Goossens, M. Burgelman, *Thin Solid Films* **2005**, *480*, 87.

[246] M. Nanu, J. Schoonman, A. Goossens, *Advanced Functional Materials* **2005**, *15*, 95.

[247] A. C. Arango, L. R. Johnson, V. N. Bliznyuk, Z. Schlesinger, S. A. Carter, H. H. Horhold, *Advanced Materials* **2000**, *12*, 1689.

[248] U. Bach, D. Lupo, P. Comte, J. E. Moser, F. Weissortel, J. Salbeck, H. Spreitzer, M. Gratzel, *Nature* **1998**, *395*, 583.

[249] A. J. Breeze, Z. Schlesinger, S. A. Carter, P. J. Brock, *Physical Review B* **2001**, *6412*.

[250] D. Gebeyehu, C. J. Brabec, F. Padinger, T. Fromherz, S. Spiekermann, N. Vlachopoulos, F. Kienberger, H. Schindler, N. S. Sariciftci, *Synthetic Metals* **2001**, *121*, 1549.

[251] D. Gebeyehu, C. J. Brabec, N. S. Sariciftci, D. Vangeneugden, R. Kiebooms, D. Vanderzande, F. Kienberger, H. Schindler, *Synthetic Metals* **2001**, *125*, 279.

[252] D. Gebeyehu, C. J. Brabec, N. S. Sariciftci, *Thin Solid Films* **2002**, *403*, 271.

[253] A. Petrella, M. Tamborra, P. D. Cozzoli, M. L. Curri, M. Striccoli, P. Cosma, G. M. Farinola, E. Babudri, F. Naso, A. Agostiano, *Thin Solid Films* **2004**, *451-52*, 64.

[254] G. K. R. Senadeera, K. Nakamura, T. Kitamura, Y. Wada, S. Yanagida, *Applied Physics Letters* **2003**, *83*, 5470.

[255] H. Wang, C. T. Yip, K. Y. Cheung, A. B. Djurisic, M. H. Xie, Y. H. Leung, W. K. Chan, *Applied Physics Letters* **2006**, *89*.

[256] D. Gebeyehu, C. J. Brabec, F. Padinger, T. Fromherz, J. C. Hummelen, D. Badt, H. Schindler, N. S. Sariciftci, *Synthetic Metals* **2001**, *118*, 1.

[257] Y. Saito, T. Kitamura, Y. Wada, S. Yanagida, *Chemistry Letters* **2002**, 1060.

[258] K. M. Coakley, M. D. McGehee, *Applied Physics Letters* **2003**, *83*, 3380.

[259] C. D. Grant, A. M. Schwartzberg, G. P. Smestad, J. Kowalik, L. M. Tolbert, J. Z. Zhang, *Synthetic Metals* **2003**, *132*, 197.

[260] P. A. van Hal, M. M. Wienk, J. M. Kroon, W. J. H. Verhees, L. H. Slooff, W. J. H. van Gennip, P. Jonkheijm, R. A. J. Janssen, *Advanced Materials* **2003**, *15*, 118.

[261] K. M. Coakley, M. D. McGehee, *Chemistry of Materials* **2004**, *16*, 4533.

[262] L. H. Slooff, M. M. Wienk, J. M. Kroon, *Thin Solid Films* **2004**, *451-52*, 634.

[263] Q. Q. Qiao, J. T. McLeskey, *Applied Physics Letters* **2005**, *86*.

[264] M. Gratzel, *Mrs Bulletin* **2005**, *30*, 23.

[265] http://www.oberlin.edu/physics/Scofield/p414/primers/solar%20cell%20primer.pdf.

[266] G. Floudas, C. Tsitsilianis, *Macromolecules* **1997**, *30*, 4381.

[267] P. Wang, S. M. Zakeeruddin, I. Exnar, M. Gratzel, *Chemical Communications* **2002**, 2972.

[268] P. Ravirajan, D. D. C. Bradley, J. Nelson, S. A. Haque, J. R. Durrant, H. J. P. Smit, J. M. Kroon, *Applied Physics Letters* **2005**, *86*.

[269] D. Papoutsi, P. Lianos, P. Yianoulis, P. Koutsoukos, *Langmuir* **1994**, *10*, 1684.

[270] Y. Murakami, T. Matsumoto, Y. Takasu, *Journal of Physical Chemistry B* **1999**, *103*, 1836.

[271] E. Hosono, S. Fujihara, K. Kakiuchi, H. Imai, *Journal of the American Chemical Society* **2004**, *126*, 7790.

[272] S. Dourdain, J. F. Bardeau, M. Colas, B. Smarsly, A. Mehdi, B. M. Ocko, A. Gibaud, *Applied Physics Letters* **2005**, *86*.

[273] A. Gibaud, S. Dourdain, O. Gang, B. M. Ocko, *Physical Review B* **2004**, *70*.

[274] W. Bao, C. Broholm, G. Aeppli, S. A. Carter, P. Dai, C. D. Frost, J. N. Honig, P. Metcalf, *Journal of Magnetism and Magnetic Materials* **1998**, *177*, 283.

[275] L. F. Zhang, A. Eisenberg, *Macromolecular Symposia* **1997**, *113*, 221.

[276] S. Y. Choi, M. Mamak, N. Coombs, N. Chopra, G. A. Ozin, *Advanced Functional Materials* **2004**, *14*, 335.

[277] E. L. Crepaldi, G. Soler-Illia, D. Grosso, P. A. Albouy, H. Amenitsch, C. Sanchez, in *Nanoporous Materials Iii*, Vol. 141, **2002**, 235.

[278] E. L. Crepaldi, G. Soler-Illia, D. Grosso, F. Cagnol, F. Ribot, C. Sanchez, *Journal of the American Chemical Society* **2003**, *125*, 9770.

[279] D. Grosso, G. Soler-Illia, F. Babonneau, C. Sanchez, P. A. Albouy, A. Brunet-Bruneau, A. R. Balkenende, *Advanced Materials* **2001**, *13*, 1085.

[280] P. C. Angelome, M. C. Fuertes, G. Soler-Illia, *Advanced Materials* **2006**, *18*, 2397.

[281] F. Schuth, *Chemistry of Materials* **2001**, *13*, 3184.

[282] A. Stein, R. C. Schroden, *Current Opinion in Solid State & Materials Science* **2001**, *5*, 553.

[283] M. E. Turner, T. J. Trentler, V. L. Colvin, *Advanced Materials* **2001**, *13*, 180.

Acknowledgment

This thesis is the result of two and half years of work whereby I have been accompanied and supported by many people. It is my great pleasure to have this opportunity to express my gratitude for all of them.

First of all I would like to express my sincere and deep gratitude to Prof. Dr., who has given me a treasure chance to start my master studies in University Siegen, Germany, and thereafter the Ph. D studies in the Max-Planck Institute for Polymer Research, a worldwide famous academic institute.

I am also deeply indebted to my thesis supervisor, for his kind advices, inspiring discussions, and great patience during my Ph. D studies. Because I also did the practice and master thesis under his supervisor, it is he who has shaped my academic picture and established a good start for my future career.

Special thanks also go to for his kind and warm-hearted help with dynamic light scattering and numerous nice scientific and non-scientific suggestions.

I am grateful to, and to show and teach me how to fabricate and characterize solar cells. Great generosity from and to share solar cell experience is also greatly appreciated.

I would like to thank and Sebastian Nett, for the help with GISAXS measurement at HASYLAB.

I want to express my gratitude to, and for their great help with the synthesis of the chemicals, with the x-ray measurement, and for their kind help and great patience teaching me how to operate AFM, for the help with SEM measurement, for transition electron microscopy measurement, for help with thermal gravity analysis, and with GISAXS measurement and the provision of beamtime by the HASYLAB, for the cyclovoltammetry measurement, for teaching me how to use the glove box, profilemeter, and gold deposition set-up, for the DSC experiment, for the photoluminescence measurement, and for many things. Without help from those people mentioned above, it's hard to carry out the experiment successfully successfuly.

Finally I appreciate the great support from my family during my Ph. D studies. Their strong support is always one of my most important driving forces to strive to be my best.

Curriculum Vitae

Personal Data

Name: Ya-Jun Cheng

Gender: Male

Nationality: Chinese

Birth date: 08. Nov. 1977

Birth place: Jiangsu, P. R. China

Education

2004 .Oct-2007. Jun: **Ph.D in chemistry**

Max-Planck Institute for Polymer Research, Mainz,Germany

Johannes Gutenberg Universität, Mainz, Germany

2002. Oct-2004. Apr: **Master in chemistry**

University Siegen, Germany

1996. Sep-2000. Jun: **Bachelor in chemistry**

Peking University, P. R. China

Publications

Publications Based on This Thesis

1. **Cheng Y.-J**., Gutmann, J. S.; ***J. Am. Chem. Soc.***, **2006**, *128*, 4658-4674.
2. **Cheng, Y. -J**.; Memesa, M.; Nett, S.; Gutmann, J. S.; ***Mater. Res. Soc. Symp. Proc.*** **2006**, Vol. 974, CC10-29.
3. **Cheng, Y. -J**.; Müller-Buschbaum, P.; Gutmann, J. S.; ***Small***, *DOI: 10.1002*/smll200600712.
4. **Cheng, Y. -J**.; Zhou, S. Y.; Gutmann, J. S. ***Macromol. Rapid. Comm.***, **2007**, *28*, 1392-1396.
5. **Cheng, Y. -J**.; Li, J. L.; Sun, Z. C.; Gutmann, J. S.; ***Eur. Phys. J. Appl. Phys.***, *revised*.

6. **Cheng, Y. -J**.; Gutmann, J. S.; **Annual HASYLAB Report, 2005**.
7. **Cheng, Y. -J**.; Zhi, L. J.; Gutmann, J. S.; A New Concept to Achieve Ordered Macroporous TiO_2 Films of Anatase and Rutile Phases. ***Adv. Funct. Mater.***, *submitted*.

Collaboration Publications Generated from This Thesis

8. Müller-Buschbaum, P.; Perlich, J.; Kashem, M. M. A.; Schulz, L.; Roth, S. V.; **Cheng, Y.-J**.; Gutmann, J. S.; ***Phys Stat Sol.***, **2007**, *1*, 119-121.
9. M. Memesa, **Y. J. Cheng**, J. Perlich, *et.al,* ***Synthetic and Reactivity in Inorganic, Metal-Organic, and Nano-Metal Chemistry,*** **2007***, 37, 315-320.*
10. Farshchi-Tabrizi, M.; Kappl, M.; **Cheng, Y. -J**.; Gutmann, J. S.; Butt, H.-J.; ***Langmuir***, **2006**, *22*, 2171-2184.
11. J. Perlich, L. Schulz, M. M. Abul Kashem, **Y.-J. Cheng**, M. Memesa1, J. S. Gutmann, S. V. Roth, P. Müller-Buschbaum.; ***Langmuir***, *submitted*

Other Collaboration Publications

12. Berger, R.; **Cheng, Y**.; *et.al*.; ***Langmuir***, **2007**, 23, 3150-3156.
13. Wolkenhauer, M.; Bumbu, G.-G.; **Cheng, Y.-J**.; Roth, S. V.; Gutmann, J. S.; ***Appl. Phys. Lett.*** **2006**, *89*, 054101.

---

14. **Cheng, Y.-J**., Renker, S.; Sun, Z. C.; Gutmann, J. S.; ***Macromol. Rapid. Comm.,*** **2005**, *26*, 613-619.

---

15. **Cheng, Y. -J**.; Wang, Z. M.; Liao, C. S.; Yan, C. H.; ***New Journal of Chemistry*** **2002**, *26*, 1360-1364.
16. Wang, Z. M.; **Cheng, Y.-J**.; Liao, C. S.; Yan, C. H.; ***CrystEngcomm*** **2001**.

Conference and Workshop Contributions

1. **German Physical Society Meeting**, Regensburg, Germany. Mar. 2007, Poster.
2. **Materials Research Society 2006 Fall Meeting**, Boston, USA. Nov. 2006, Poster and proceedings; **Best Poster Award Nominated**
3. **European Conference on Hybrid and Organic Solar Cells**, Paris, France. June.2006, Poster and proceedings
4. **German Physical Society Meeting**, Dresden, Germany. Mar. 2006, **15min oral talk**.
5. **First MicroSAXS/WAXS Beamline Workshop for PETRA III**, Hamburg, Germany. May.2006, Poster.
6. **Workshop on Grazing Incidence Small Angle Scattering at HASYLAB**, Hamburg, Germany. May. 2005, Poster.
7. **German Physical Society Meeting**, Berlin, Germany. Mar. 2005, Poster.

Awards

1. **Award for outstanding Chinese overseas Ph. D student** from **China Government** in 2006.
2. **Student Prize** for excellent studies at **University Siegen** in 2003-2004 semester.
3. **Excellent Bachelor Thesis Award** at **Peking University** in 2000.
4. **Sony Scholarship** for excellent studies at **Peking University** in 2000.

Social Activities

Member of the **Ph. D committee** in the Max-Planck Institute for Polymer Research since **May. 2005**.

Appendix

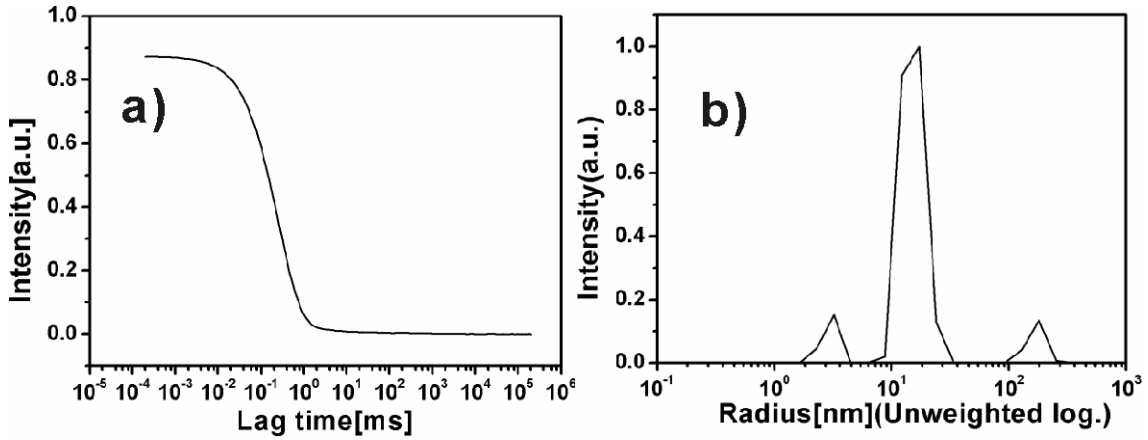

Figure S-1. *Dynamic light scattering results of the solution which yields clustered nanoparticles in the film through spin coating.* ***a****: lag time curve;* ***b****: size distribution curve. Composition ratios:* W_{TTIP}*, 0.020;* $W_{1,\ 4\text{-}dioxane}$*, 0.976;* W_{HCl}*, 0.004.*

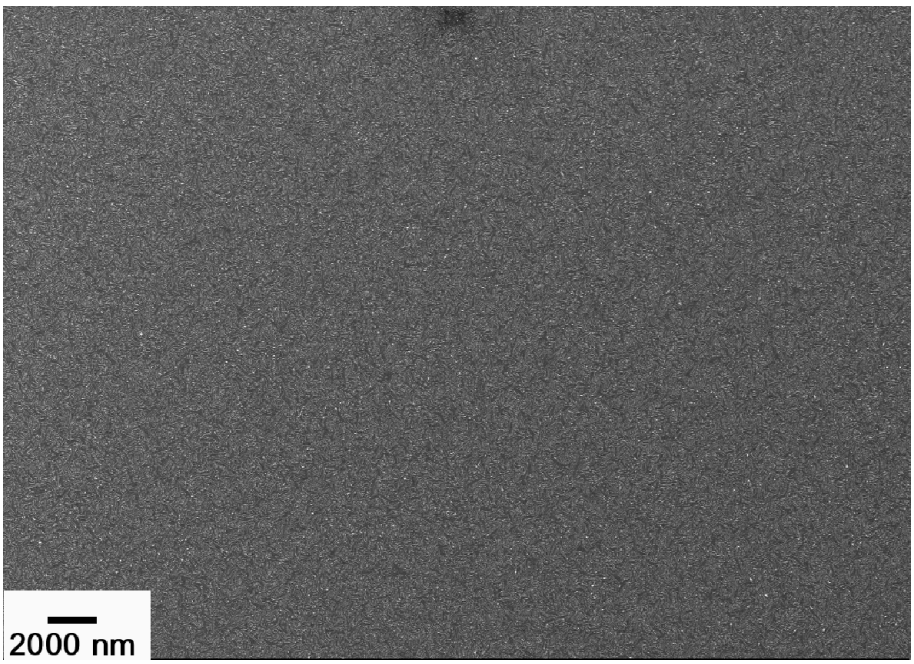

Figure S-2. *SEM image of the nanowire structure with a low magnification*

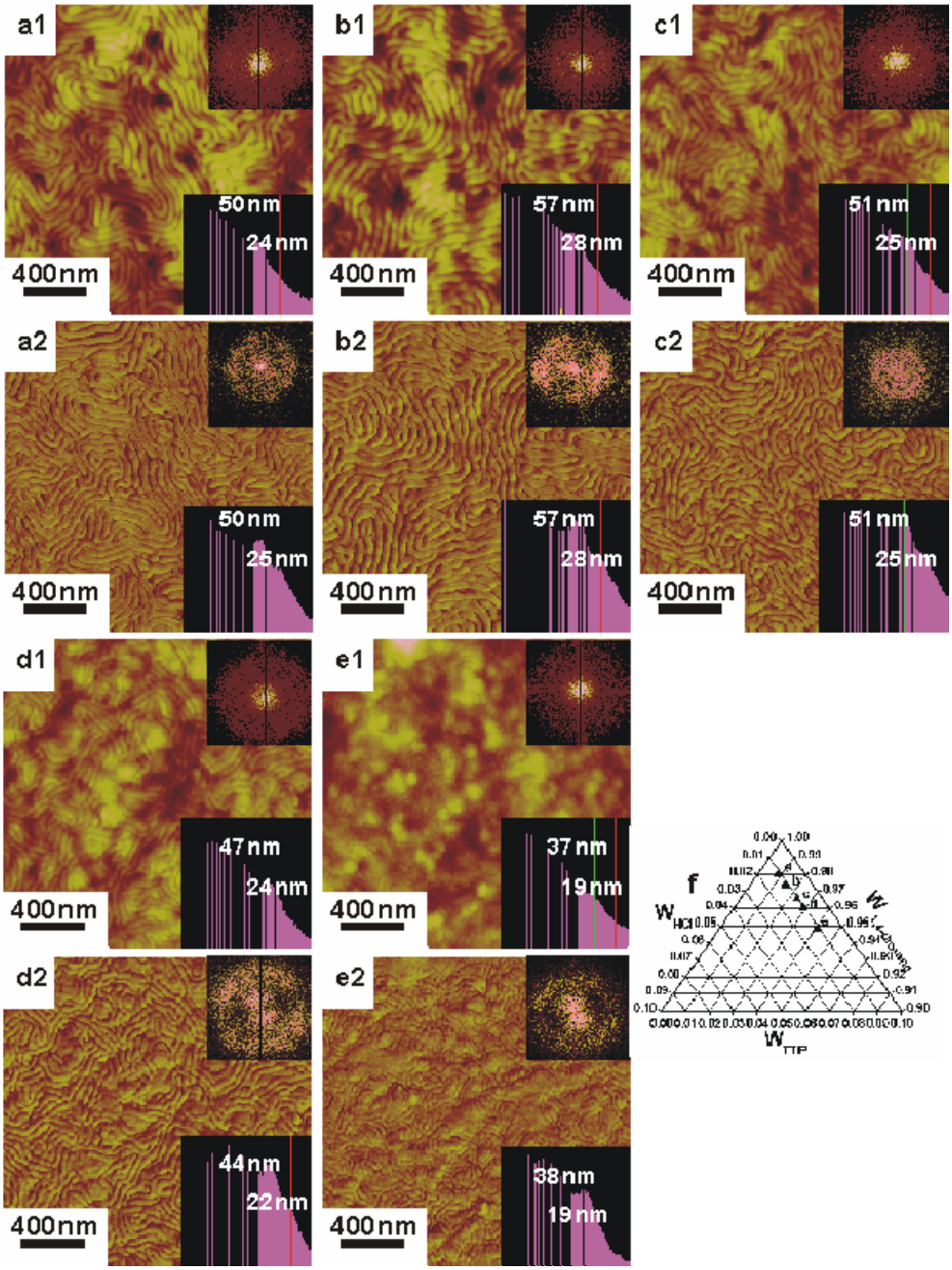

Figure S-3. *AFM height and phase images of structure evolution with increasing weight fractions of TTIP in TiO_2 nanowire films before calcination.* ***a1***, ***b1***, ***c1***, *d1, and* ***e1****: AFM height images;* ***a2***, ***b2***, ***c2***, ***d2***, *and* ***e2****: AFM phase images; f: compositional existence points in the phase diagram with increasing TTIP weight fractions from* ***a*** *to* ***e*** *(W: weight fraction). The insets in the images are FFT patterns of the corresponding structures. Height scale: 20nm; Phase scale: 20°.*

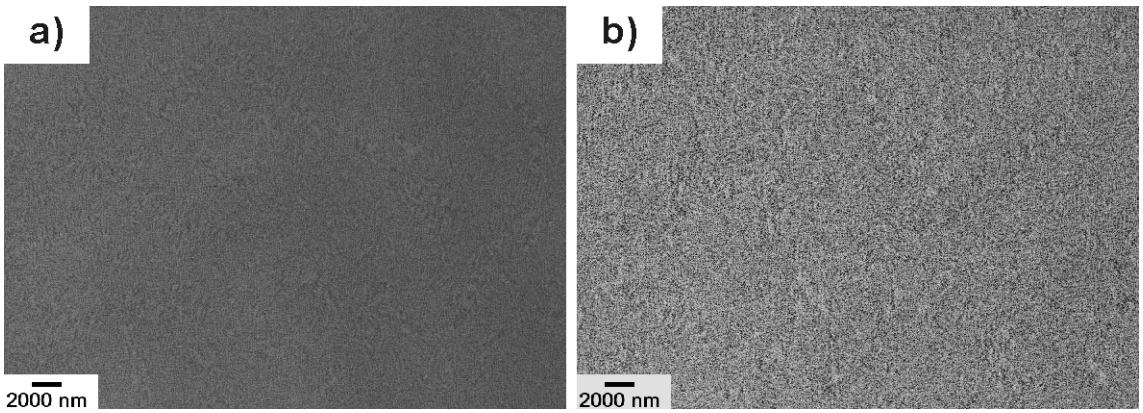

Figure S-4. *Low magnification SEM images of the titania film before(**a**) and after (**b**) calcination with a copolymer concentration of 0.25%.*

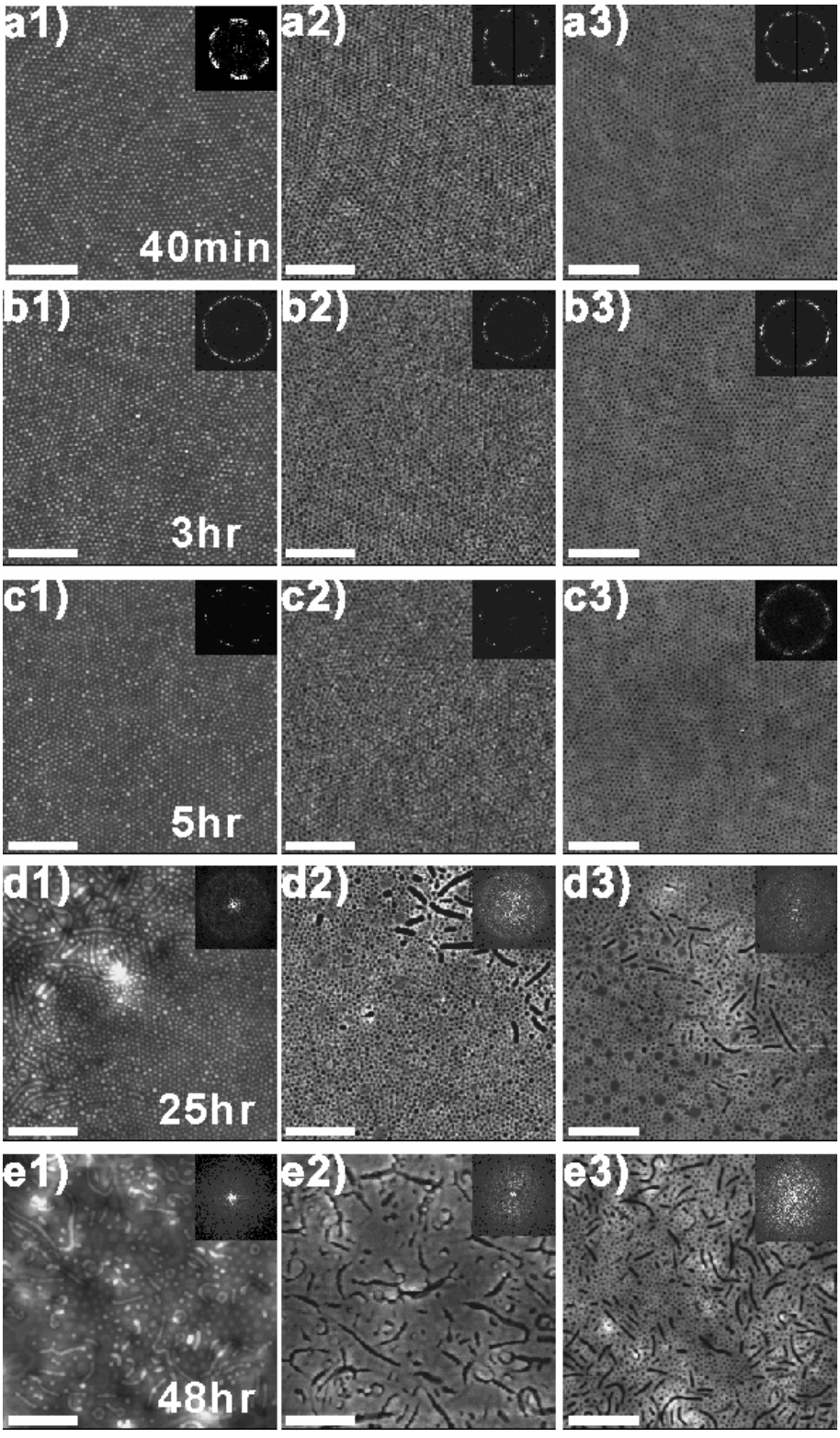

***Figure S-5**. AFM height images of the nanovesicles prepared with different sol-gel reaction time from a stock solution of 0.25 wt. % PS-b-PEO. As-prepared film: **a1**, **b1**, **c1, d1, and e1**; calcined at 400℃:*

***a2**, **b2**, **c2, d2, and e2**; UV degraded: **a3**, **b3**, **c3, d3, and e3**. Insets are corresponding FFT patterns of each image. Height scale: 10nm. Scale bar: 400nm.*

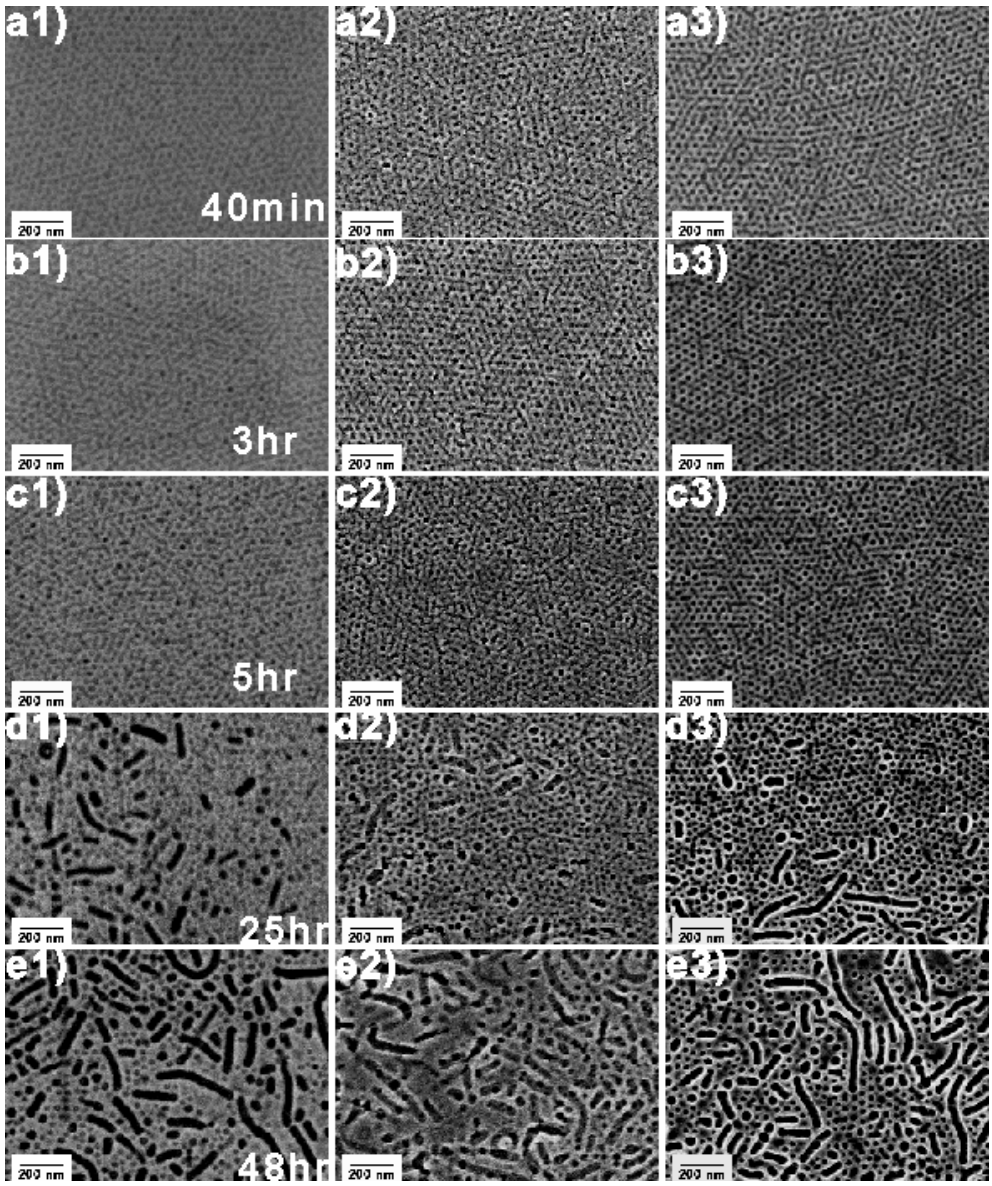

***Figure S-6.** SEM images of the nanovesicles prepared with different sol-gel reaction time from a stock solution of 0.25 wt. % PS-b-PEO. As-prepared film: **a1**, **b1**, **c1, d1, and e1**; calcined at 400℃: **a2**, **b2**, **c2, d2, and f2**; UV degraded: **a3**, **b3**, **c3**, **d3**, and **e3**.*

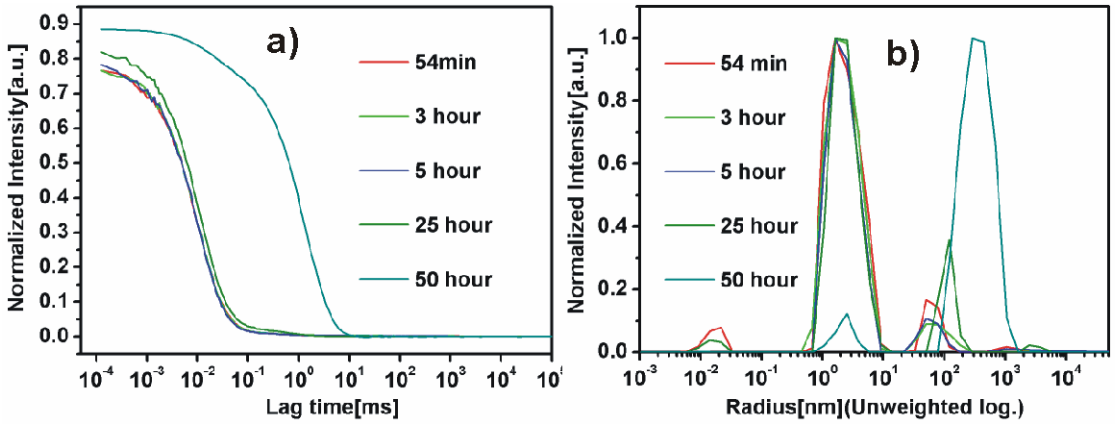

Figure S-7*. Dynamic light scattering results of the aggregate size evolution with different sol-gel reaction time scales in the solution of 0.25 wt. % PS-b-PEO.* ***(a)****: correlation profile;* ***(b)****: corresponding size distribution profile.*

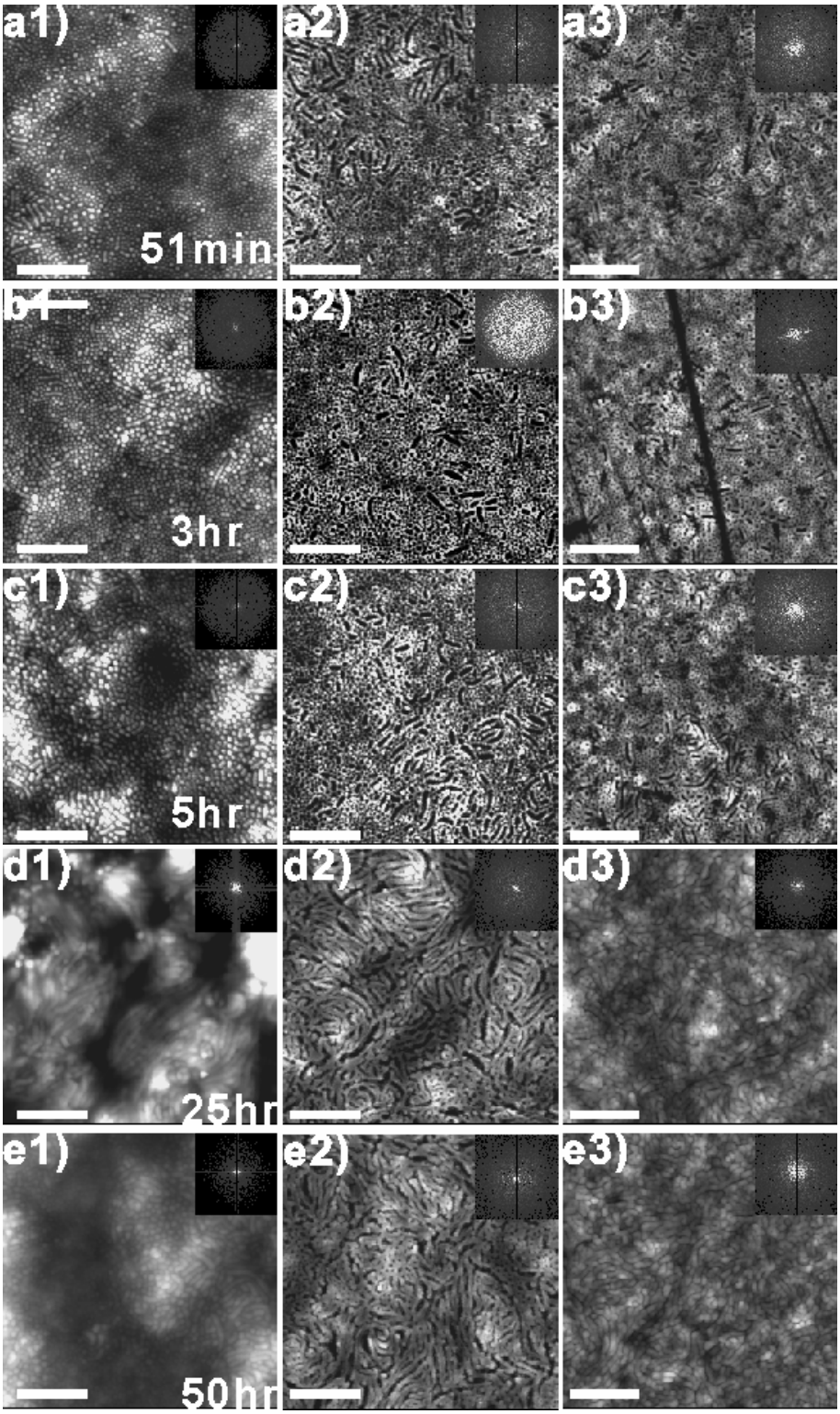

Figure S-8. *AFM height images of the nanovesicles prepared with different sol-gel reaction time from a stock solution of 1.0 wt. % PS-b-PEO. As-prepared film:* ***a1***, ***b1***, ***c1, d1, and e1****; calcined at 400℃:*

***a2**, **b2**, **c2, d2, and e2**; UV degraded: **a3**, **b3**, **c3, d3, and e3**. Insets are corresponding FFT patterns of each image. Height scale: 10nm. Scale bar: 400nm.*

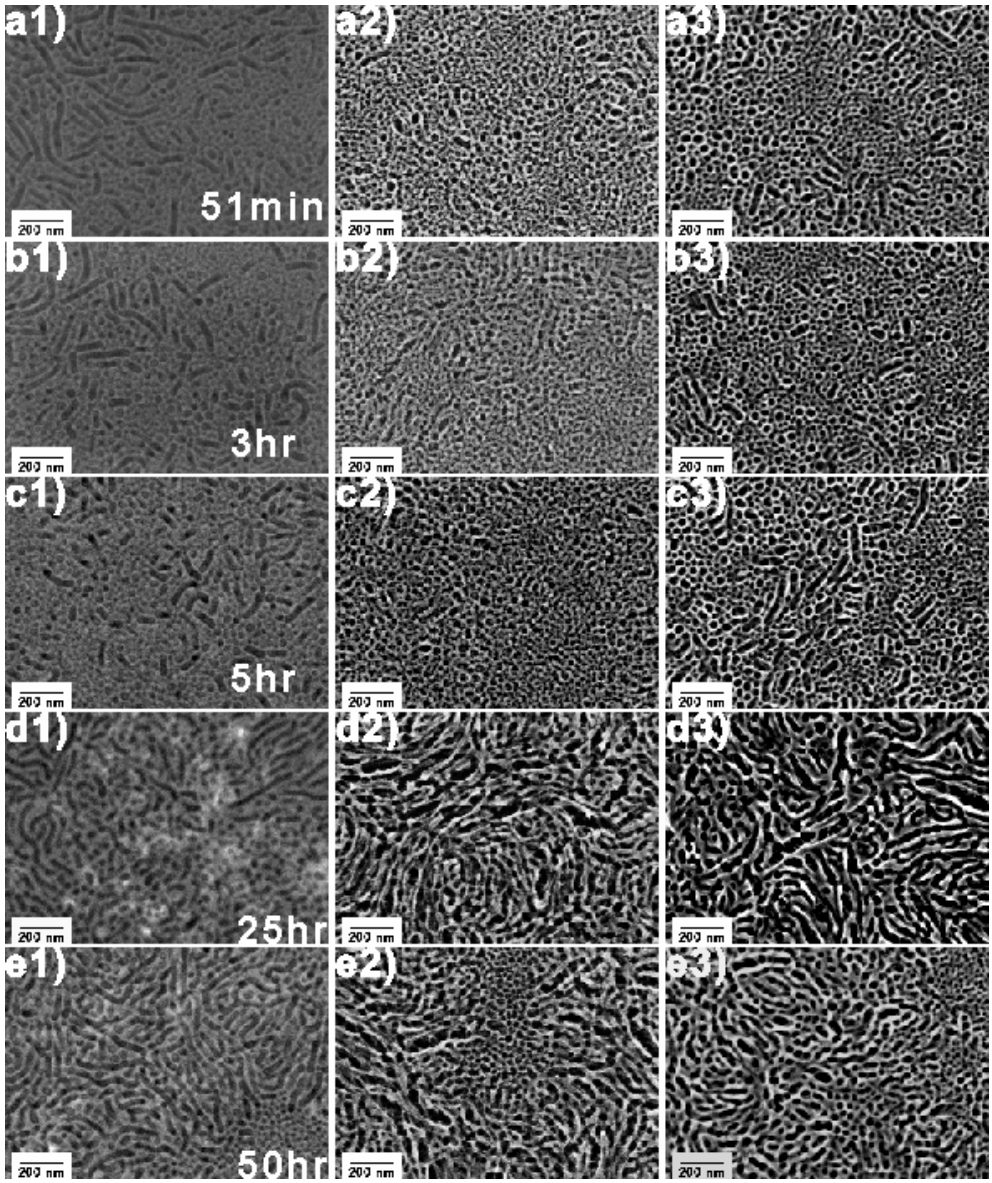

***Figure S-9.** SEM images of the nanovesicles prepared with different sol-gel reaction time from a stock solution of 1.0 wt. % PS-b-PEO. As-prepared film: **a1**, **b1**, **c1, d1, and e1**; calcined at 400℃: **a2**, **b2**, **c2, d2, and f2**; UV degraded: **a3**, **b3**, **c3**, **d3**, and **e3**.*

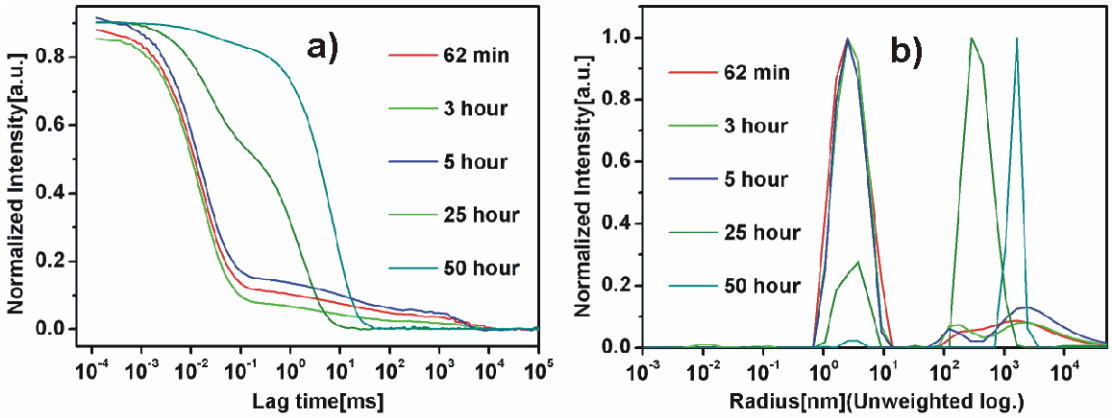

Figure S-10. *Dynamic light scattering results of the aggregate size evolution with different sol-gel reaction time scales in the solution of 1.0 wt. % PS-b-PEO.* (***a***)*: correlation profile;* (***b***)*: corresponding size distribution profile.*

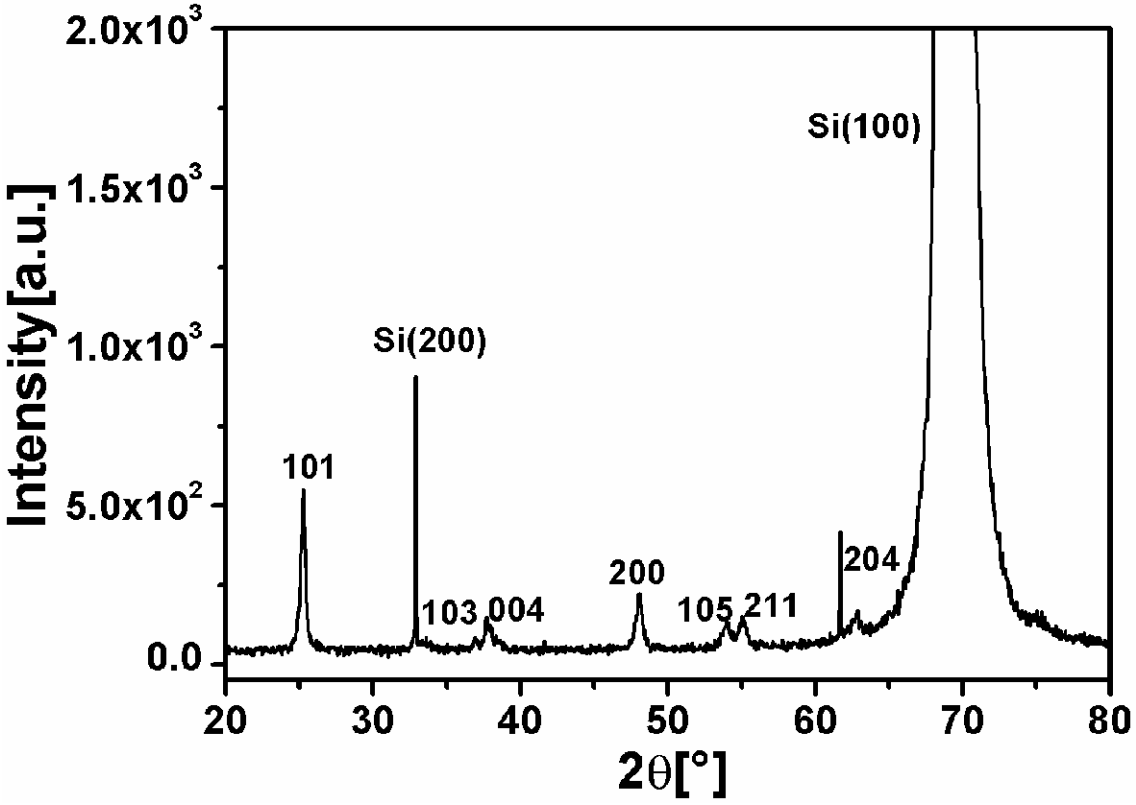

Figure S-11. *XRD result of the TiO_2 films on Si (100) substrate.*

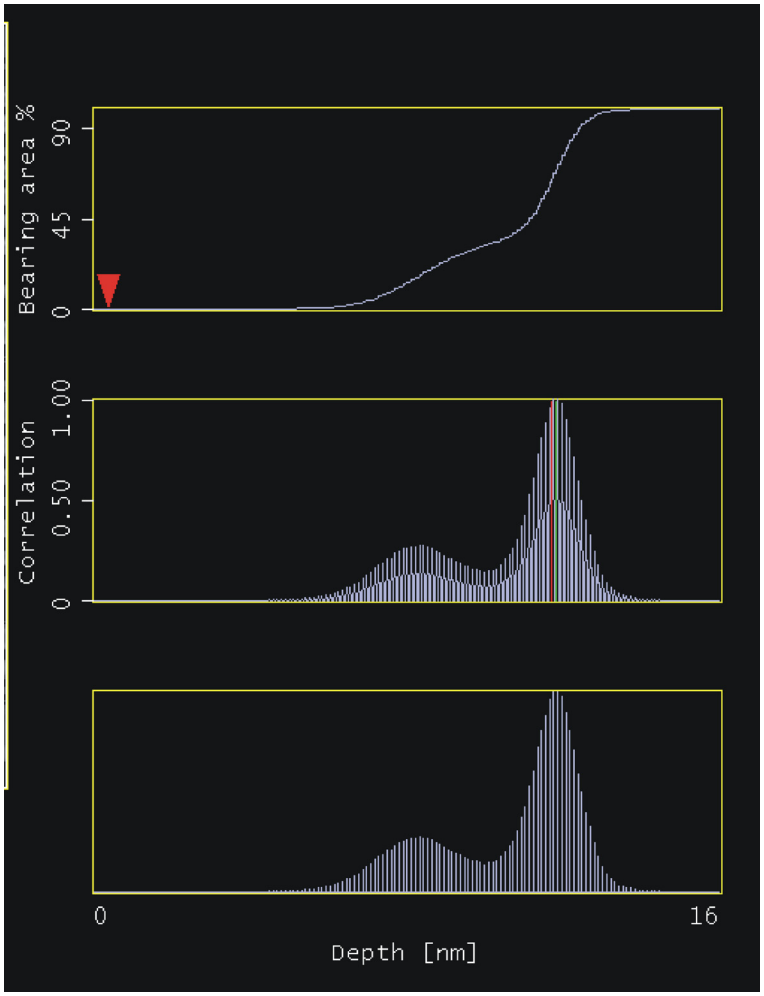

***Figure S-12**. Particle analysis profiles of the AFM height image after calcination.*

***Table S-1**. The whole data set of the solar cell performance with only barrier layer*

Isc ($\mu A/cm^2$)	Voc (V)	FF	η(%)	EQE_{max} (%)
40	0.29	0.36	0.04	-
46	0.26	0.32	0.03	0.97
72	0.26	0.35	0.06	1.15
27	0.25	0.38	0.02	0.45
39	0.31	0.35	0.04	0.7
44.8	**0.274**	**0.352**	**0.038**	**0.82**

Note: The highlighted data in the last row is the average value from the individual data in all of the above rows.

***Table S-2**.The whole data set of the solar cell performance with TiO_2 clustered nanoparticles film*

I_{sc} ($\mu A/cm^2$)	V_{oc} (V)	FF	η (%)	EQE_{max} (%)
63	0.27	0.35	0.07	2.82
76	0.35	0.36	0.12	2.07
64	0.23	0.36	0.07	2.06
56	0.22	0.34	0.05	1.85
46	0.24	0.36	0.05	2.05
43	0.21	0.34	0.04	2.05
47	0.21	0.33	0.04	1.87
46	0.18	0.33	0.03	1.9
55.1	**0.239**	**0.346**	**0.059**	**2.08**

Note: The highlighted data in the last row is the average value from the individual data in all of the above rows.

Table S-3. *The whole data set of the solar cell performance with TiO_2 worm-like structured film*

I_{sc} (μA/cm^2)	V_{oc} (V)	FF	η (%)	EQE_{max} (%)
93	0.15	0.26	0.04	-
36	0.23	0.36	0.04	-
45	0.23	0.36	0.05	2.6
47	0.20	0.33	0.04	3.03
79	0.28	0.33	0.09	3.37
99	0.27	0.34	0.11	3.66
78	0.28	0.38	0.11	2.47
55	0.28	0.35	0.07	2.77
38	0.31	0.37	0.05	2.22
37	0.23	0.31	0.03	2.03
54	0.27	0.34	0.06	2.91
52	0.25	0.34	0.05	3.06
59.4	**0.248**	**0.339**	**0.062**	**2.81**

Note: The highlighted data in the last row is the average value from the individual data in all ofthe above rows.

Table S-4. *The whole data set of the solar cell performance with TiO_2 foam structured film*

I_{sc} (μA/cm^2)	V_{oc} (V)	FF	η (%)	EQE_{max} (%)
63	0.21	0.36	0.06	3.17
60	0.16	0.33	0.04	3.09
70	0.19	0.32	0.05	2.57
77	0.16	0.32	0.05	2.75
67.5	**0.180**	**0.332**	**0.050**	**2.89**

Note: The highlighted data in the last row is the average value from the individual data in all of the above rows.

***Table S-5**. The whole data set of the solar cell performance with TiO2 large collapsed vesicles*

I_{sc} (μA/cm^2)	V_{oc} (V)	FF	η (%)	EQE_{max} (%)
32	0.29	0.35	0.03	0.84
52	0.30	0.39	0.05	1.37
60	0.26	0.42	0.06	1.87
87	0.27	0.42	0.09	1.95
55	0.21	0.38	0.04	1.34
61	0.19	0.34	0.03	1.55
53	0.21	0.36	0.03	0.82
50	0.23	0.38	0.04	1.56
64	0.26	0.36	0.05	1.57
64	0.27	0.38	0.06	1.6
57.8	**0.249**	**0.378**	**0.048**	**1.45**

Note: The highlighted data in the last row is the average value from the individual data in all of the above rows.

***Table S-6**. The whole data set of the solar cell performance with TiO_2 small vesicle film*

I_{sc} (μA/cm^2)	V_{oc} (V)	FF	η (%)	EQE_{max} (%)
46	0.23	0.39	0.05	10.12
61	0.23	0.39	0.07	10.12
61	0.26	0.38	0.08	
48	0.23	0.38	0.05	
67	0.19	0.34	0.06	17.89
42	0.21	0.38	0.04	16.19
54.2	**0.225**	**0.377**	**0.058**	**13.58**

Note: The highlighted data in the last row is the average value from the individual data in all of the above rows.

Table S-7*.The whole data set of the solar cell performance with only TiO_2 barrier layer*

I_{sc} ($\mu A/cm^2$)	V_{oc} (V)	FF	η (%)	EQE_{max} (%)
14	0.23	0.37	0.01	0.57
15	0.22	0.33	0.01	0.34
25	0.21	0.36	0.02	0.77
22	0.24	0.37	0.02	0.64
19.0	**0.225**	**0.357**	**0.015**	**0.58**

Note: The highlighted data in the last row is the average value from the individual data in all of the above rows.

Table S-8*. The whole data set of the solar cell performance with TiO_2 nanowire film*

I_{sc} ($\mu A/cm^2$)	V_{oc} (V)	FF	η (%)	EQE_{max} (%)
36	0.3	0.35	0.04	0.8
35	0.36	0.37	0.04	1.39
20	0.37	0.35	0.02	1.24
18	0.39	0.34	0.02	0.82
27.2	**0.355**	**0.352**	**0.030**	**1.06**

Note: The highlighted data in the last row is the average value from the individual data in all of the above rows.

Table S-9*. The whole data set of the solar cell performance with TiO_2 nanogranular film*

I_{sc} ($\mu A/cm^2$)	V_{oc} (V)	FF	η (%)	EQE_{max} (%)
23	0.24	0.34	0.02	1.44
23	0.26	0.39	0.02	1.37
17	0.28	0.35	0.02	1.03
19	0.29	0.34	0.02	0.94
16	0.33	0.31	0.02	0.84
19.6	**0.280**	**0.346**	**0.02**	**1.12**

Note: The highlighted data in the last row is the average value from the individual data in all of the above rows.

***Table S-10**. The whole data set of the solar cell performance with TiO_2 flakes film*

I_{sc} ($\mu A/cm^2$)	V_{oc} (V)	FF	η (%)	EQE_{max} (%)
9	0.33	0.54	0.01	0.57
10	0.26	0.47	0.01	0.79
12	0.27	0.36	0.01	0.53
15	0.4	0.45	0.03	0.87
9	0.27	0.27	0.01	0.37
9	0.31	0.34	0.01	0.44
6	0.32	0.72	0.01	0.49
12	0.34	0.52	0.02	0.28
10.2	**0.312**	**0.459**	**0.014**	**0.54**

Note: The highlighted data in the last row is the average value from the individual data in all of the above rows.